Luminescent properties of YOF phosphor for solar cell application

By

Nadir Azhari Mustafa Saeed

(M.Sc)

A thesis submitted in fulfilment of the requirements for the degree of

PHILOSOPHIAE DOCTOR

in the

Faculty of Natural and Agricultural Sciences

Department of Physics

at the

University of the Free State

Republic of South Africa

Supervisor: Prof. E. Coetsee

Co-Supervisor: Prof. H.C. Swart

January 2019

Declaration

To: Registrar: Academic Student Services

I, N.A.M. Saeed (2016107118), declare that the thesis for the degree Philosophiae Doctor (Ph.D) in Physics, submitted by me to the University of the Free State, is my own independent work and was not submitted by me to another university/faculty. I further forgo copyright of the thesis in favour of the University of the Free State.

Student Name: N.A.M. Saeed
Student Number: 2016107118

Signature: 

Date: 10/12/2019

I, E. Coetsee-Hugo, declare that I approve the submission of N.A.M. Saeed's (2016107118) thesis and that the thesis was not formerly submitted to examiners partially or altogether.

Supervisor Name: Prof. E. Coetsee-Hugo
Institute: Department of Physics, University of the Free State, Bloemfontein ZA9300, South Africa.

Signature: 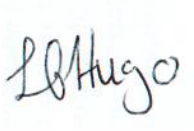

Date:

Co-Supervisor Name: Prof. H.C. Swart

Institute: Department of Physics, University of the Free State, Bloemfontein ZA9300, South Africa.

Signature:

Date:

This thesis is dedicated to my lovely parents, family and friends.

Acknowledgements

I would like to thank the following individuals and institutions:

- Prof. E. Coetsee for being my supervisor, her help, guidance and suggestions throughout this study.
- Deep thanks goes to Prof. H.C. Swart and Prof. J.J. Terblans, for giving me this opportunity to be part of the Department of Physics family and for Prof. Swart for his guidance and professional suggestions throughout this thesis as my co-supervisor.
- Prof. R.E. Kroon for his assistance with PL laser measurements as well as fruitful discussions and great suggestions.
- Prof. M. Bettinelli for his great help, assistant and valuable opinions throughout our work.
- I am indebted to my lovely family, my parents for their support, encouragement, love and constant assistance throughout my life. National Research Foundation (NRF), South African Research Chairs Initiative (SARChI) chair and the University of the Free State for financial support.
- But above all, I would like to thank the Almighty Allah for everything that he has given to me, for his blessing and guidance to finish this work.

List of Abbreviations

AES – Auger electron spectroscopy

Bi^{3+} – trivalent bismuth

Bi_2O_3 – bismuth oxide

BSE – back scattered electron

Ce_2O_3 – cerium oxide

CF_3COO – trifluoroacetate

CF_3COOH – trifluoroacetic acid

CIE – Commission Internationale de l'Eclairage

CL – cathodoluminescent

c-Si – crystalline silicon

CT – charge transfer

DC – down-conversion

DS – down-shifting

E_g – band gap

EDS – energy dispersive x-ray spectroscopy

EELS – electron energy loss spectroscopy

e-h – electron-hole

F^- – fluorine

FEDs – field emission displays

FWHM – full width at half maximum

Ho^{3+} – holmium

Ho_2O_3 – holmium oxide

I-H – Inokuti-Hirayama

IR – infrared

LED – light emitting diode

Ln^{3+} – lanthanide

MMCT – metal to metal charge transfer

NIR – near-infrared

O^{2-} – oxygen

PCE – photon cascade emission

PL – photoluminescence

Pr^{3+} – praseodymium

Pr_2O_3 – praseodymium (III) oxide

RE – rare earth

SE – secondary electron

Si – silicon

SC – solar cell

SPARC – scalable processor architecture

STEM – scanning transmission electron microscopy

TEM – transmission electron microscopy

QC – quantum cutting

UC – up-conversion

UV – ultraviolet

VIS – visible

VUV – vacuum ultraviolet

XPS – X-ray photoelectron spectroscopy

XRD – X-ray diffraction

Y^{3+} – yttrium

Y_2O_3 – yttrium oxide

Yb^{3+} – ytterbium

Yb_2O_3 – ytterbium (III) oxide

$Y(CF_3COO)_3$ - yttrium trifluoroacetate

YF_3 – yttrium fluoride

YOF – yttrium oxyfluoride

Abstract

The luminescent properties of yttrium oxyfluoride (YOF) phosphor doped and co-doped with different ions (praseodymium (Pr^{3+}), cerium (Ce^{3+}), ytterbium (Yb^{3+}), bismuth (Bi^{3+}) and holmium (Ho^{3+})) were investigated for c-Si solar cell application. The pyrolysis method with trifluoroacetate (CF_3COO) as precursor was used to synthesize all the powders. Investigations were done on the crystal structure, the surface morphology, surface and optical properties. The X-ray diffraction patterns exhibited a crystalline phase of stoichiometric rhombohedral YOF (space group: $R\bar{3}m$ (166)) after annealing at 900 ^{0}C. The crystallite sizes for the YOF:Pr^{3+} sample, decreased with an increase in Pr^{3+} doping concentrations. During thermal decomposition from CF_3COO to YOF (600 ^{0}C to 900 ^{0}C), the scanning electron spectroscopy (SEM) images showed an agglomeration of small particles (< 100 nm) that started to melt and agglomerate to form bigger particles with sizes > 500 nm.

X-ray photoemission spectroscopy (XPS) high-resolution peak fits for the high Pr^{3+} doped sample (YOF: 0.5 % Pr^{3+}) revealed two Pr oxidation states, Pr^{3+} and Pr^{4+}. Annealing in air caused the formation of a small amount of Pr^{4+}. The photoluminescent (PL) excitation spectra showed an intense band at 250 nm with weaker bands at 456, 470 and 483 nm. The weaker bands were ascribed to the 4f-4f $^3H_4$-$^3P_2$, $^3H_4$-$^1I_6$, $^3P_1$ and $^3H_4$-$^3P_0$ transition bands of the Pr^{3+} ion, respectively. The green Pr^{3+} PL emission was ascribed to the 4f-4f [$^3P_0$-$^3H_4$] and [$^3P_0$-$^3F_2$] transitions at 498 nm and 659 nm, respectively. A YOF:Ce^{3+} sample was synthesized in order to predict the value of the Pr^{3+} 4f-5d level in the YOF host. The PL excitation and emission results obtained showed that the lowest 4f-5d excitation of Pr^{3+} in this host has to peak around 250 nm. The 250 nm band was therefore ascribed to the 4f-5d band of Pr^{3+} in the YOF host.

The optimum Pr^{3+} concentration for the PL emission was recorded for the sample doped with 0.3 % of Pr^{3+}. Concentration quenching occurred through a cross relaxation process due to dipole-quadrupole interactions. Near infra-red (NIR) emission for the 0.3 % Pr^{3+} doped sample during excitation of 250 nm showed multi narrow peaks in the range between 885 nm and 1120 nm that corresponded to the $^3P_0 \rightarrow {}^1G_4$ and the $^1D_2 \rightarrow {}^3F_3$, $^3F_4$ transitions. The decay lifetimes were calculated to be in the μs range.

YOF:Pr^{3+}, Yb^{3+} samples were investigated for down-conversion applications for c-Si solar cells. The SEM images showed an agglomeration and melting of small particles to form bigger

particles. XPS's high-resolution peak fits for the high Pr^{3+} co-doped Yb^{3+} sample (YOF: 0.3 % Pr^{3+}, 6 % Yb^{3+}) revealed two Pr oxidation states, Pr^{3+} and Pr^{4+}. The presence of Pr^{4+} was due to the annealing in ambient air. The deconvolution of the Yb 4d peak showed only the $4d_{5/2}$ peak that was ascribed to Yb^{3+}. The Pr^{3+} visible (VIS) emission's excitation spectra showed an intense 4f-5d band of Pr^{3+} at 250 nm accompanied with weaker 4f-4f peaks at 456, 470 and 483 nm. These weaker 4f-4f peaks were ascribed to the $^3H_4$-$^3P_2$, $^3H_4$-$^1I_6$, $^3P_1$ and $^3H_4$-$^3P_0$ transition of Pr^{3+}, respectively. The VIS green PL emission was due to the 4f-4f [$^3P_0 \rightarrow {}^3H_4$] and [$^3P_0 \rightarrow {}^3F_2$] transitions at 498 nm and 659 nm, respectively. Quenching of the Pr^{3+} green emission was due to the energy transfer to Yb^{3+} ions through the cross-relaxation mechanism with a dipole-dipole interaction. The Yb^{3+} IR emission's excitation spectrum revealed a new band at 225 nm that overlapped with the 4f-5d band of Pr^{3+}. The band at 225 nm was ascribed to the charge transfer band of Yb^{3+} due to electron transfers from the O^{2-} $3p^6$ level to the $4f^{13}$ level of Yb^{3+}. Excitation with 225 nm showed the typical Pr^{3+} VIS emission and this confirmed the nature of the 225 nm band as a charge transfer band. Excitation with 250 nm showed multi-narrow peaks in the IR range between 885 nm and 1120 nm that corresponded to the Pr^{3+} $^3P_0 \rightarrow {}^1G_4$ and $^1D_2 \rightarrow {}^3F_3$, $^3F_4$ transitions and to the $^2F_{7/2} \rightarrow {}^2F_{5/2}$ transition of Yb^{3+}. Upon excitation of 225 nm, the IR emission showed only emission of Yb^{3+} transitions with almost no traces of Pr^{3+} emission. The optimum IR emission for both excitations was recorded with a Yb^{3+} content of 2 % and a constant Pr^{3+} content of 0.3 %. The decay times for VIS and IR emissions were calculated to be in the microseconds range.

The investigations of YOF:Bi^{3+} were done at room temperature. Auger electron spectroscopy results showed that Bi was homogeneously distributed on the surface of the sample. XPS showed two doublet peaks for the Bi 4f region which were attributed to Bi^{3+} ions and Bi metal. PL studies revealed an asymmetric broad ultraviolet (UV) emission band centered at 314 nm that originated from the $^3P_1 \rightarrow {}^1S_0$ A band of Bi^{3+}. The excitation band was a symmetric broad band centered at 267 nm and corresponded to the $^1S_0 \rightarrow {}^3P_1$ A band with a Stokes shift of 47 nm. This excitation overlapped with a metal to metal charge transfer band of Bi^{3+}. The optimum concentration for maximum luminescence intensity was 0.4 mol % of Bi^{3+} and the quantum yield of this sample was about 60 %. The decay curves of the prepared samples were also investigated and the lifetimes were found to be in the microsecond range.

Bi^{3+} was investigated as sensitizer for Ho^{3+} emission in the YOF:Bi^{3+}, Ho^{3+} phosphor in the VIS and IR regions. The PL studies of YOF:Bi^{3+}, Ho^{3+} were investigated for energy transfer

possibilities for IR emission. The morphology investigations revealed agglomerations of small particles into bigger particles that developed during annealing. XPS high resolution peak fits for the high concentration co-doped sample (YOF: 0.4 mol % Bi^{3+}, 5 mol % Ho^{3+}) revealed overlapping of Bi 4f and Ho 4d peaks with the Y 3d peak. PL excitation spectra showed an intense $^1S_0 \rightarrow {}^3P_1$ Bi^{3+} band at 265 nm that dominated the 4f-4f Ho^{3+} peaks at 360 nm and 449 nm. VIS PL emission was done upon 449 nm and 265 nm excitation. The UV emission that peaked at 314 nm upon 265 nm excitation was ascribed to the $^3P_1 \rightarrow {}^1S_0$ transition of Bi^{3+}. The emissions at 538 nm and 753 nm were ascribed to the $^5F_4,{}^5S_2 \rightarrow {}^5I_8$ and $^5F_4,{}^5S_2 \rightarrow {}^5I_7$ transitions of Ho^{3+} with the optimum concentration of Ho^{3+} obtained at 2 mol %. IR emission occurred for both the 449 nm and 265 nm excitations, respectively. The IR emissions that peaked at 1014 nm and 1200 with weak emission at 1400 nm were ascribed to the $^5F_4,{}^5S_2 \rightarrow {}^5I_6$, $^5I_6 \rightarrow {}^5I_8$ and $^5F_4,{}^5S_2 \rightarrow {}^5I_5$ transitions of Ho^{3+}, respectively. The decay times for both Bi^{3+} and Ho^{3+} in the VIS and IR regions were calculated to be in the microseconds range. A great enhancement of the emission in the IR and VIS regions have been achieved. Despite the efficient energy conversion in the Bi^{3+}, Ho^{3+} system, enhancement of the energy flow from Bi^{3+} to Ho^{3+} needs to be considered. This will reduce the dissipated energy into many unnecessary manifolds of Ho^{3+} and direct it to the range of spectral absorption of Si-SC.

Tunable emission was achieved through Ho^{3+} co-doped Bi^{3+} doped YOF for optoelectronic applications. Cathodoluminescent (CL) studies were investigated under electron beam irradiation (5 keV) for both YOF: x mol % Bi^{3+} (x = 0.3, 0.4, 0.5, 0.6, 0.8) and YOF: 0.4 mol % Bi^{3+}, x mol % Ho^{3+} (x = 0.8, 1.4, 2, 3, 4, 5) samples. The morphology investigations revealed agglomerations of small particles into bigger particles that developed during annealing. XPS's surveys for the YOF: 5 mol % Bi^{3+} and the YOF: 0.4 mol % Bi^{3+}, 5 mol % Ho^{3+} samples revealed the presence of all elemental compositions. UV CL emission for the YOF:Bi^{3+} samples were ascribed to the $^3P_1 \rightarrow {}^1S_0$ transition of Bi^{3+} at 314 nm and the VIS emission at 624 nm to the $^2P_{3/2}$ (1) $\rightarrow {}^2P_{1/2}$ transition of Bi^{2+}. Bi^{2+} were created during CL excitation as a result of ionization. The CL emission of the YOF:Bi^{3+}, Ho^{3+} samples in the UV and VIS regions peaked at 316 nm, 540 nm and 624 nm and were ascribed to the $^3P_1 \rightarrow {}^1S_0$, $^5F_4,{}^5S_2 \rightarrow {}^5I_8$ and $^2P_{3/2}$ (1) $\rightarrow {}^2P_{1/2}$ transitions of Bi^{3+}, Ho^{3+} and Bi^{2+}, respectively. The fitted International commission on Illumination (CIE) coordinates of the YOF:Bi^{3+}, Ho^{3+} samples showed a tunable CL emission from green to yellow and orange.

Contents

Chapter 1

Introduction

This chapter gives a general overview on thermalization and transparency losses of solar cells (SC), spectral conversion and the yttrium oxyfluoride (YOF) host. It also gives the research problem, the aims and the thesis layout.

1.1 Overview

The vast progress of the population on earth demands more energy and this gave rise to the importance of solar energy. In the past few decades' energy research has been focused on solar energy as a suitable replacement for the current energy resources. According to literature, the energy that reaches the earth, from the sun, is about 10 000 times more than what we benefit from [1]. There is therefore still a wide field of research to be done to obtain high efficiency solar energy. One mechanism that can assist in good energy conversion is photovoltaic devices [2, 3].

A SC is a photovoltaic device that converts solar energy into useful energy like electricity [2]. A lot of research have been done on SCs as a solar converter by applying the photovoltaic effect [4-8]. Single-junction monocrystalline and polycrystalline silicon (Si) systems currently account for about 95 % of the photovoltaic market. The bandgap (E_g) of this kind of semiconductor is 1.1 eV and this is equal to the energy of a photon with a wavelength of about 1100 nm [7]. The theoretical maximum efficiency of c-Si SC, according to the Shockley-Queisser's model with an E_g of 1.1 eV, is about 30 % [9]. This model is based on the principle of the balance between the incident and escaping photons and extracted electrons [9]. Up to date, the efficiency of the commercial SCs is not yet exceeding the Shockley-Queisser model's limit and the highest efficiency was recorded to be around 25 % for c-Si SC [10, 11]. The major energy loss accounted for the SCs is due to lattice thermalization and transparency due to sub-bandgap photons [8]. In figure 1, process (1) demonstrates lattice thermalization as a result of a high energy incoming photon that created an electron-hole (e-h) pair. This photo-excited pair lost its energy rapidly as heat within the cell [8]. Process (2) demonstrates the transparency of the cell to the sub-bandgap photons. Process (3) shows the loss of energy through the recombination of the photo-excited e-h pairs. Processes (4) and (5) show the energy lost due to the junction and contact voltage.

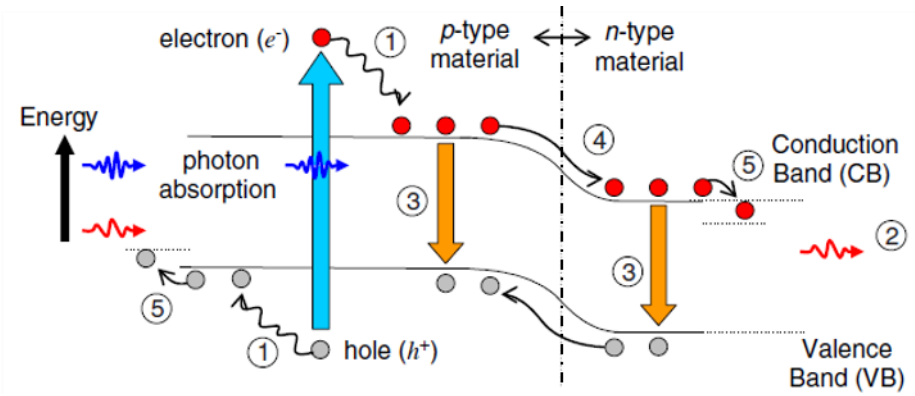

Figure 1: Energy-loss processes in a single-junction solar cell demonstrated by Richards [8], (1) lattice thermalization, (2) transparency, (3) recombination, (4) junction and (5) contact voltage loss.

Enhancement of the spectral response of the SC through certain mechanisms is considered to be a major part of the recent SC research. The application of a suitable luminescent material to the SC can convert the absorbed energy towards the energy range where the SC can absorb. The down-conversion (DC) mechanism (also known as quantum cutting (QC)) was adopted to reduce the energy loss caused by lattice thermalization. DC is where one absorbed high energy photon like ultraviolet (UV) or a blue photon can be converted into two lower-energy photons [10]. The downshifting (DS) mechanism is where one high energy photon is shifted to one lower energy photon [11]. It is well known that for the DC mechanism the external quantum efficiency can exceed unity, while for the DS mechanism it cannot exceed unity and the SC will not overcome the Shockley-Queisser limit [8]. Both DC and DS mechanisms are mainly used to overcome lattice thermalization losses by placing a suitable spectral converter layer on top of the SC. The up-conversion (UC) mechanism was utilized to minimize the transparency losses by applying a spectral converter to the bottom of the SC. UC is where two low energy photons are absorbed and added together to emit one high energy photon [4]. This process is based on using the non-absorbed photons [8].

A luminescent converter that is able to convert the absorbed photons to the SCs' absorption ranges is based on different types of inorganic materials [7]. The commonly used materials are fluorides and oxides [7]. Luminescence of the material is based on suitable activator center ions such as lanthanide (Ln^{3+}) and transition metals ions [7]. The praseodymium ion (Pr^{3+}) has unique properties that result in emission in the spectral response range of about 1000 nm [7]. Enhancement of the Pr^{3+} emission can be obtained through a suitable co-dopant ion such as

ytterbium (Yb^{3+}) [12-15]. A combination of different lanthanides with Yb^{3+} in the form of Ln^{3+}-Yb^{3+} (Ln^{3+} = holmium (Ho^{3+}), Eu^{3+}, Er^{3+}, Tb^{3+}, Nd^{3+}, $Dy^{3+,}$ and Tm^{3+}) was used in different hosts and showed a high conversion efficiency [12-15]. The lanthanides act as a sensitizer that transfers its energy to two Yb^{3+} ions that act as activators. The transition metals can also be used in combination with Yb^{3+} or other lanthanide ions. Trivalent bismuth (Bi^{3+}) shows promising properties as a suitable sensitizer when combined with other lanthanides [16]. Fluoride hosts such as YOF has good potential as a suitable host for luminescent centers that might show the DC mechanism [17, 18]. A theoretical prediction done on fluoride hosts used as down-converters showed that the efficiency can be increased up to 39 % [5, 6].

1.2 Research problem

Which host and luminescent co-dopant pair is the ideal spectral converter to apply to c-Si SC? Would YOF doped with Pr^{3+} or Bi^{3+} and co-doped with Yb^{3+} or Ho^{3+} be potential spectral converters? Systematic investigations on the crystal structures and luminescent properties will therefore be done. YOF has combined properties of fluorides and oxides and is therefore considered as a suitable host material for SC applications [17, 18]. Some of these properties are low phonon energies (400 cm^{-1}), low probability of multiphonon quenching and a wide bandgap that is favorable for activator ions [17, 18]. These properties are also favorable for near-infrared emission (NIR). Application of the fluoride hosts as luminescent converters has been established by Piper et al. [19] in 1974. It is well known that the forbidden 4f-4f transitions of Pr^{3+} has a low absorption cross-section while the dipole allowed 4f-5d transitions have intense and broad absorption cross-sections [5]. An enhancement of the Pr^{3+} emission has also been done by co-doping with Yb^{3+} that yielded a high efficiency close to 200 % [7]. The co-doping of Pr^{3+}-Yb^{3+} has been investigated in multiple hosts where an energy transfer has occurred from the sensitizer Pr^{3+} to two activator ions Yb^{3+} [12-15]. Investigation of Bi^{3+} as a sensitizer for SC application was mainly done by co-doping either with Yb^{3+} or other different ions such as Ho^{3+} [20, 21, 22]. Bi^{3+} is considered a favorable ion as a sensitizer due to the broadband emission that originates from unique energy levels that allow Bi^{3+} to emit in the absorption range of most of the lanthanide ions [16]. Amongst these ions, Ho^{3+} is considered a good choice as activator for NIR emission which emits in a wide range (1030 nm, 1200 nm and 1350 nm) with a wide range of absorption [23]. The intense infrared (IR) emission of Ho^{3+} also depends on the host [24, 25].

This study focusses on investigations on the Pr^{3+} and Bi^{3+} ions in the YOF host. Investigations of Pr^{3+} has been done in YOF basically on its behavior as a DS layer [26]. The luminescence behavior of the Pr^{3+} ion in the NIR region for YOF host, will give a deep insight into its suitability as a DC layer by selecting a proper activator ion. The Pr^{3+}-Yb^{3+} pair was selected to improve the NIR emission of Pr^{3+} through energy transfer from Pr^{3+} to Yb^{3+}. Research has also been done on the luminescence of Bi^{3+} [27]. Sensitization of Ho^{3+} emission by using the broad emission of Bi^{3+} through energy transfer was also investigated since most researches focused on the DS behavior of this pair [20, 21].

1.3 The aim of the study:

- Synthesizing YOF:Pr^{3+}, YOF:Bi^{3+}, YOF:Pr^{3+}-Yb^{3+} and YOF:Bi^{3+}-Ho^{3+} by using the pyrolysis method.
- Characterization and photoluminescent (PL) investigation of YOF:Pr^{3+} for application as a suitable DS layer.
- Systematic investigations on the position of the allowed 4f-5d transitions of Pr^{3+}.
- Characterization and luminescent investigation on the origin of the UV luminescence of Bi^{3+} in the YOF host.
- Characterization and luminescent investigation on the the effect of the Pr^{3+}-Yb^{3+} co-doping pair as a DC pair.
- Characterization and luminescent investigation on the application of Bi^{3+} as a sensitizer for Ho^{3+} emission focusing on the NIR emission and the nature of the energy transfer.
- Utilization of Ho^{3+} cathodoluminescent (CL) emission with different concentrations of Ho^{3+} in the Bi^{3+}-Ho^{3+} system.

1.4 Thesis Organization

This thesis will be organized into nine chapters. Chapter 1 contains a brief description regarding the overview and the explanation of the research problem. Chapter 2 contains the theoretical basics and concepts based on the background of the research and research problem. Synthesis method and characterization techniques will be addressed and shown with their principles in chapter 3. Chapter 4 contains the systematic studies of Pr^{3+} ions doped in the YOF host with different concentrations and investigations on the position of the allowed 4f-5d transitions of Pr^{3+}. Chapter 5 contains DC investigations of the YOF:Pr^{3+}-Yb^{3+} co-doped phosphor for SC enhancement as well as the energy transfer mechanism. Chapter 6 describes the PL

investigations of Bi^{3+} in the YOF structure in order to explain the origin of the UV emission. Chapter 7 contains NIR enhancement PL studies and the nature of the energy transfer mechanism of Ho^{3+} co-doped YOF:Bi^{3+}. CL excitation and tunement of Ho^{3+} emission as well as the energy transfer mechanism controlling the quenching of the emission are investigated in chapter 8. Chapter 9 contains the conclusion and the future work and Appendix A shows a description of the Inokuti-Hirayama (I-H) model. Appendix B shows the published papers and conference participation.

References

[1] H. Aguas, S.K. Ram, A. Araujo, D. Gaspar, A. Vicente, S.A. Filonovich, E. Fortunato, R. Martins and I. Ferreira, Energy Environ. Sci. 4 (2011) 4620 - 4632.

[2] D.M. Chapin, C.S. Fuller and G.L. Pearon, J. Appl. Phys. 25 (1954) 676 - 677.

[3] V.S. Arunachalam and E.L. Fleischer, MRS Bulletin, 33 (2008) 264 - 276.

[4] X. Huang, S. Han, W. Huang and X. Liu, Chem. Soc. Rev. 42 (2013) 173 - 201.

[5] B.M. Van der Ende, L. Aarts and A. Meijerink, Phys. Chem. Chem. Phys. 11 (2009) 11081 - 11095.

[6] T. Trupke, M. A. Green and P. Wurfel, J. Appl. Phys. 92 (2002) 1668 - 1674.

[7] Q.Y. Zhang and X.Y. Huang, Prog. Mater. Sci. 55 (2010) 353 - 427.

[8] B.S. Richards, Sol. Energy Mater. Sol. Cells, 90 (2006) 2329 - 2337.

[9] H. Lian, Z. Hou, M. Shang, D. Geng, Y. Zhang and J. Lin, Energy, 57 (2013) 270 - 283.

[10] B. Ahrens, Down- and Up-Conversion in Fluorozirconate-Based Glasses and Glass Ceramics for Photovoltaic Application, University of Paderborn, PhD Thesis, (2009).

[11] M.A. Green, K. Emery, Y. Hishikawa and W.Warta, Prog. Photovolt: Res. Appl. 16 (2008) 435 - 440.

[12] B.M van der Ende, L. Aarts and A. Meijerink, Adv. Mater. 21 (2009) 3073 - 3077.

[13] P. Vergeer, T.J.H. Vlugt, M.H.F. Kox, M.I. den Hertog, J.P.J.M. van der Eerden and A. Meijerink, Phys. Rev. B, 71 (2005) 014119-1 - 014119-11.

[14] Y. Song, Z. Bin, C. Jingxin, L. Jin and Q. Jian Rong, Appl. Phys. Lett. 92 (2008) 141112-1 - 141112-3.

[15] Q.Y. Zhang, G.F. Yang and Z.H. Jiang, Appl. Phys. Lett. 91 (2007) 051903-1 - 051903-3.

[16] H.T. Sun, J. Zhou and J. Qiu, Prog. Mater. Sci. 64 (2014) 1 - 72.

[17] G. Chai, G. Dong, J. Qiu, Q. Zhang and Z. Yang, Sci. Rep. 3 (2013) 1 - 10.

[18] H. He, Q. Liu, D. Yang, Q. Pan, J. Qiu and G. Dong, Sci. Rep. 6 (2016) 1 - 10.

[19] W.W. Piper, J.A. DeLuca, and F.S. Ham, J. Lumin. 8 (1974) 344 - 348.

[20] T.K.V. Rao, Ch.S. Kamal, T. Samuel, V.S. Rao, V.S. Rao, P.V.S.S.S.N. Reddy and K.R. Rao, J. Mater Sci: Mater Electron. DOI 10.1007/s10854-017-8000-5.

[21] X. Zhang, G. Zhou, J. Zhou, H. Zhou, P. Kong, Z. Yu and J. Zhan, RSC Adv. 4 (2014) 13680 - 13686.

[22] R.V. Yadav, R.S. Yadav, A. Bahadur, A.K. Singh and S.B. Rai, Inorg. Chem. 55 (2016) 10928 - 10935.

[23] J. Xu, D. Murata, B. So, K. Asami, J. Ueda, J. Heo and S. Tanabe, J. Mater. Chem. C, 6 (2018) 11374 - 11383.

[24] Sk. Mahamuda, K. Swapna, P. Packiyaraj, A.S. Rao and G.V. Prakash, Opt. Mater. 36 (2013) 362 - 371.

[25] G. Gupta, S. Balaji, K. Biswas and K. Annapurna, AIP Adv. 9(2019) 045201-1 - 045201-11.

[26] S. Fujihara, S. Koji, Y. Kadota and T. Kimura, J. Am. Ceram. Soc. 87 (2004) 1659 - 1662.

[27] G. Blasse and A. Bril, J. Chern. Phys. 47 1920 (1967) 217 - 222.

Chapter 2

Literature Review

In this chapter the concepts necessary to understand the theoretical principles in this study are addressed and explained.

2.1 Solar cells

The solar energy that reaches the earth in one hour is larger than the entire human energy consumption in one year [1]. The challenges to replace fossil fuel with renewable energy opened up a wide area of research for researchers to benefit from solar energy. Therefore, a vast amount of research on renewable energy has been done on solar energy. Generating electricity out of solar energy can be obtained through photo-voltaic cells [2, 3]. The main principle of SC is therefore based on the photo-voltaic effect [2, 3]. In semiconductor materials, excitation of electrons occurs from the valence band to the conduction band that is separated with a E_g [4], see figure 1. An excited electron leaves a hole behind in the valence band that moves towards the anode and the electron moves towards the cathode [5].

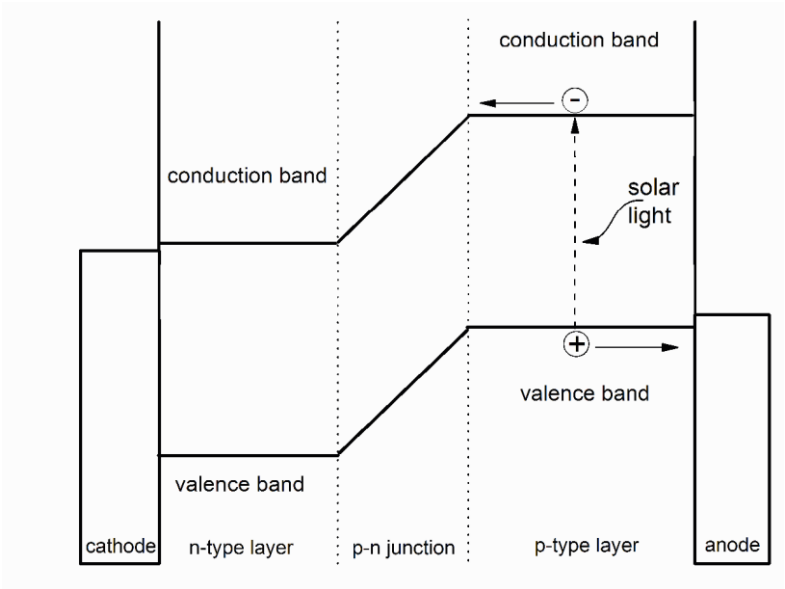

Figure 1: Illustration of the production of current during irradiance of solar light [5].

SCs can be designed from many types of materials but the most commonly used material now-days is c-Si and it holds about 87 % shares of the SC market [5]. The E_g of c-Si is around 1.1 eV and can be modified through doping. When Si is doped with positive ions, like boron, it

forms a p-type semiconductor whereas when it is doped with negative ions, like phosphorous, it forms a n-type semiconductor [5]. A p-n junction is formed when a p-type and a n-type is brought into contact. This causes diffusion of the electrons from the n-type to the p-type across the p-n junction and creates an electric field. The achieved lab scale energy conversion efficiency of c-Si SCs is about 25 % [6] and for solar panels the efficiency is only about 20 % [5]. With these limited efficiencies there is still requirements to produce high purity Si SC and this is making the production costly and the solar energy expensive. As a result, solar electricity is very expensive in comparison to the other sources of energy to produce electricity.

A high energy conversion efficiency is essential for a good SC. The ratio of the maximum power (P_m) generated by a SC to the incident power (P_{in}) gives the maximum conversion efficiency (η), eq. 1. P_{in} is equivalent to the AM 1.5 irradiance spectrum whereas P_m is the voltage at P_m (V_m) multiplied by the maximum current density (J_m) [7],

$$\boldsymbol{\eta = \frac{P_m}{P_{in}} = \frac{J_m V_m}{P_{in}} = \frac{J_{sc} V_{oc}\, FF}{P_{in}}} \quad \textbf{.....(1).}$$

J_{sc} are the short circuit current density, V_{oc} the open circuit voltage and FF is the fill factor describing the squireness of the current-voltage curve. High thermalization losses, where both V_{oc} and V_m are low, refer to low band gap materials. For high band gap materials, the values J_m and J_{sc} are low due to sub-band gap losses [8]. The incident power can theoretically be calculated with the following equation [8]:

$$\mathbf{P_{in} = \int_0^{\infty} \emptyset(\lambda)\, \frac{hc}{\lambda}\, d\lambda} \quad \textbf{.....(2).}$$

$\emptyset\,(\lambda)$ is the photon flux density, the term $\emptyset(\boldsymbol{\lambda})\ \frac{\mathbf{hc}}{\boldsymbol{\lambda}}$ is equal to the spectral power density ($P(\lambda)$)**,** c is the speed of light and h is Plank's constant.

Generation of e-h pairs mainly occurs through photons having energy higher than the E_g of the material. The part of the absorbed incident energy, by the single junction SC, that is utilized in energy conversion is given by equation [8]:

$$\mathbf{P_{abs} = \frac{\int_0^{\lambda_G} \emptyset(\lambda) \frac{hc}{\lambda} d\lambda}{\int_0^{\infty} \emptyset(\lambda) \frac{hc}{\lambda} d\lambda}} \quad \textbf{.....(3).}$$

λ_G is the wavelength of the photons that correspond to the E_g of the SC. The rest of the photons are lost due to thermalization of the absorber material. The part of the absorbed energy that is accounted for as useful energy is given by:

$$\mathbf{P_{use}} = \frac{\mathbf{E_G}\int_0^{\lambda_G} \emptyset(\lambda)\,\mathbf{d\lambda}}{\int_0^{\lambda_G} \emptyset(\lambda)\frac{\mathbf{hc}}{\lambda}\mathbf{d\lambda}} \quad \textbf{……..(4).}$$

E_G is the energy of the band gap. The total conversion efficiency combined with the spectral mismatch is then written as [7, 8]:

$$\mathbf{\eta = P_{abs}\,P_{use}} = \underbrace{\frac{\int_0^{\lambda_G} \emptyset(\lambda)\frac{\mathbf{hc}}{\lambda}\mathbf{d\lambda}}{\int_0^{\infty} \emptyset(\lambda)\frac{\mathbf{hc}}{\lambda}\mathbf{d\lambda}}}_{\mathbf{1}} \underbrace{\frac{\mathbf{E_G}\int_0^{\lambda_G} \emptyset(\lambda)\,\mathbf{d\lambda}}{\int_0^{\lambda_G} \emptyset(\lambda)\frac{\mathbf{hc}}{\lambda}\mathbf{d\lambda}}}_{\mathbf{2}} \quad \textbf{……..(5).}$$

Part (1) of the above equation is the transmission loss and part (2) is the thermalization loss. Both these losses are responsible for the spectral mismatch losses [7]. For small E_g the dominant loss is the thermalization loss whereas, for wide E_g the dominant loss is the transmission loss. The theoretical model proposed by Shockley-Queisser [9] suggested that the conversion efficiency limit for single junction SCs is about 30 %. This means that almost 70 % accounts for transmission and thermalization loss.

2.2 Photon conversion processes

Photon conversion in general is a concept aiming to convert the solar spectrum to match the absorption edge of SC devices. This is a different concept from the other concepts that only focus on developing a semiconductor device to match the solar spectrum such as space-separated QC and multiple exciton generation [10, 11]. Photon conversion processes can be divided into three major types; DS, DC or QC and UC, see figure 2 [12]. UC in simplicity occurs when two lower energy photons combine to form one high energy photon [12]. It reduces transmission losses and it utilizes the principle of anti-stoke shifts. Stoke's law states that "the wavelength of the emitted light should be greater than the wavelength of the excited spectrum" [12]. Recently, Trupke et al. [13] reported a maximum efficiency of about 47 % with UC through the absorption of the SC and the generation of e-h pairs. We are not going to focus on UC but more details can be found elsewhere [14]. DC and DS mechanisms are both utilized to enhance the SC efficiency by placing a converter layer on top of the SC. DC is where one high energy photon is converted into two lower energy photons and DS is where one high energy photon is converted to one lower energy photon. More detailed information is given in section 2.8 and 2.9 below.

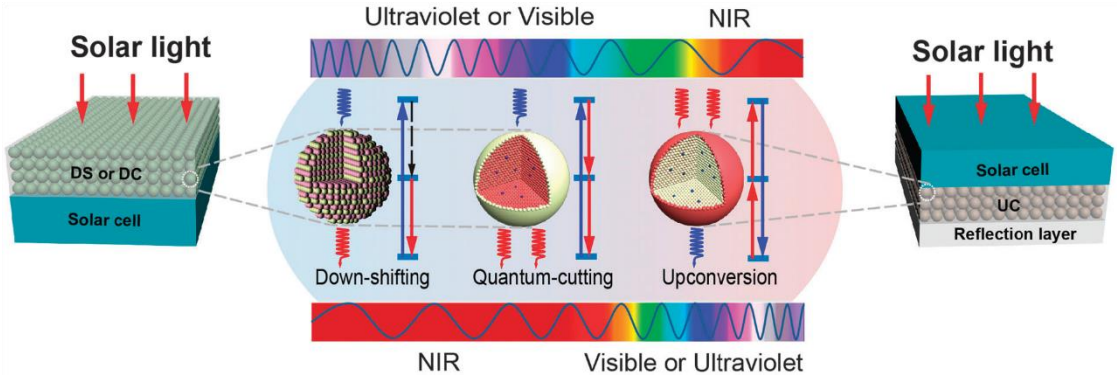

Figure 2: Illustration of the three basic photon conversion processes [12].

2.3 Luminescent materials

Luminescence is a general term describing the glow of a material when exposed to an external source of energy [12]. The type of luminescence is dependent on the type of the external excitation source. A few examples are PL from electromagnetic radiation and CL from an electron beam excitation. The phenomenon of luminescence can further be divided into two general types named as fluorescence and phosphorescence. The main difference between both types is related to their decay curves. Fluorescence materials have fast decay curves (< 0.1 s) and phosphorescence materials have slower decay curves (> 10 ms) [15]. The emission rate of a fluorescent material is very fast (about 10^8 s^{-1}). For phosphorescence (emission after excitation) the energy is not immediately radiated but instead it gets transferred to the triplet with the same spin orientation as the ground state. The result is then a very slow emission (in the order of seconds) [12, 15].

Luminescence can occur from inorganic or organic hosts [16]. The inorganic hosts in some cases can emit due to some characteristics related to the host itself like the existence of vacancies or defects [16]. Introducing some impurity ions as a dopant in the inorganic hosts can also lead to an emission representing the electronic properties of these ions with different emission characteristics. The selected dopants can be Ln^{3+} ions or transition metal ions. To yield the desired emission, the optimization of the dopant distribution is necessary to prevent non-radiative processes and concentration quenching. Luminescence of the YOF host with different dopant ions is addressed in this research study with the highlight on the possible applications for c-Si SC.

2.4 Lanthanides (Ln^{3+})

The Ln^{3+} ions are a set of elements in the periodic table characterized by 4f orbitals [12]. In total there are 15 elements characterized with similar chemical nature starting from lanthanum to lutetium. The term rare earth (RE) is also applicable to describe these elements (including yttrium (Y^{3+}). In their most stable oxidation state they exist as trivalent ions. Extensive investigations have been done on the Ln^{3+} ions for their optical properties for many possible applications [12]. The electronic configuration of the Ln^{3+} ions are characterized by the arrangement of electrons as $4f^n5s^25p^6$ ($0 < n < 14$). The electronic configuration of the 4f orbital can be occupied by electrons according to the 14! = [n! (14 - n)!] distribution [17]. The 4f orbital electrons are weakly affected by the crystal field of the ligand due to the shielding of the outer 5s and 5p electrons. As a consequence, the electronic transitions of the 4f-4f levels of the Ln^{3+} ions will show sharp peaks in the absorption and emission spectra. The Laporte selection rules explain that "the states with even parity can only be connected by electric dipole transitions with states of odd parity, and odd states only with even ones" [17]. Transitions within the 4f levels are forbidden with respect to the electric dipole transitions and allowed in respect to the magnetic dipole or electric quadrupole radiation. Electric dipole transition as a forbidden transition may occur but with low probability [17].

Perturbation of the $^{2S+1}L_J$ states of the RE^{3+} ions by weak crystal interactions can cause further splitting of the energy levels (stark levels), see figure 3. This type of splitting is weaker than the spin-orbit splitting caused by the atomic forces and as a consequence, the optical absorption and emission is similar to that of the free ions [17]. This similarity is the same even if doped in different inorganic hosts or glass matrixes.

Systematic studies of the energy of the 4f levels of the Ln^{3+} ions have been done by Dieke et al. [18, 19]. A prediction of the energy levels of the Ln^{3+} ions was depicted in a diagram, shown in figure 4. This diagram allowed more investigation and studies on the Ln^{3+} ions in recent years. According to Dieke's diagram, the thickness of the levels explains the degree of the crystal field splitting as well as the location of the $^{2S+1}L_J$ free ions approximated from the center of the multiplet level.

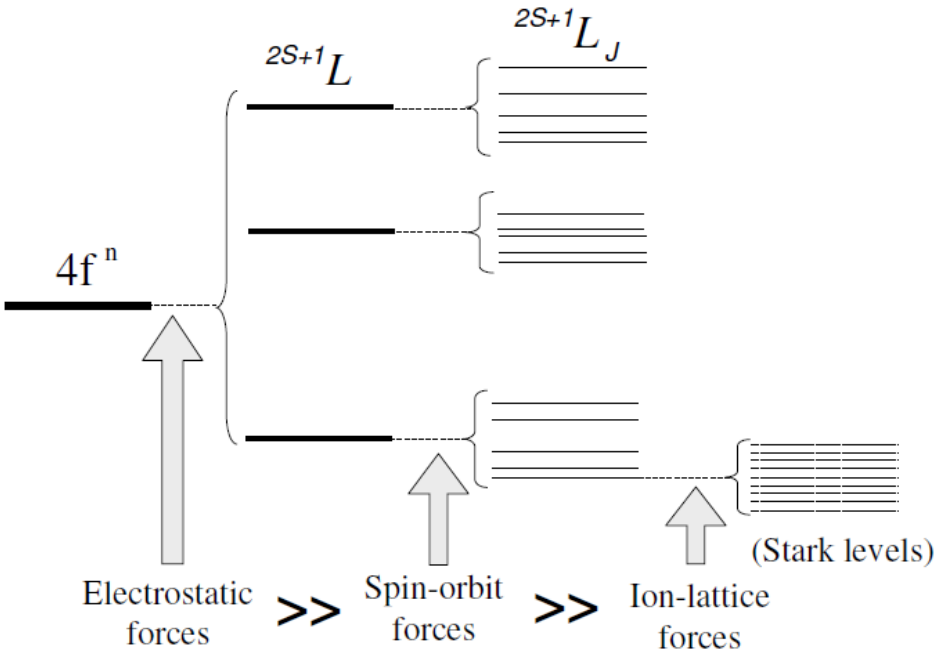

Figure 3: Schematic explanation of the splitting of the Ln^{3+}:$4f^n$ electronic configuration as a result of the atomic and the crystal field forces, adopted from [7].

On the other hand, the splitting of the 5d orbitals by the crystal field splitting is large if compared to the spin-orbit splitting. The 5d levels interact with neighboring anion ligands and this degenerates the 5d levels and shifts the whole 5d configuration (centroid shift) towards lower energy. The 5d splitting therefore depends on the site symmetry of the crystal system. The crystal field splitting and the centroid shift therefore determines the energy of the lowest 5d level. This phenomenon is known as a redshift or depression D. The D value determines the color and the position of the 4f-5d transitions [8].

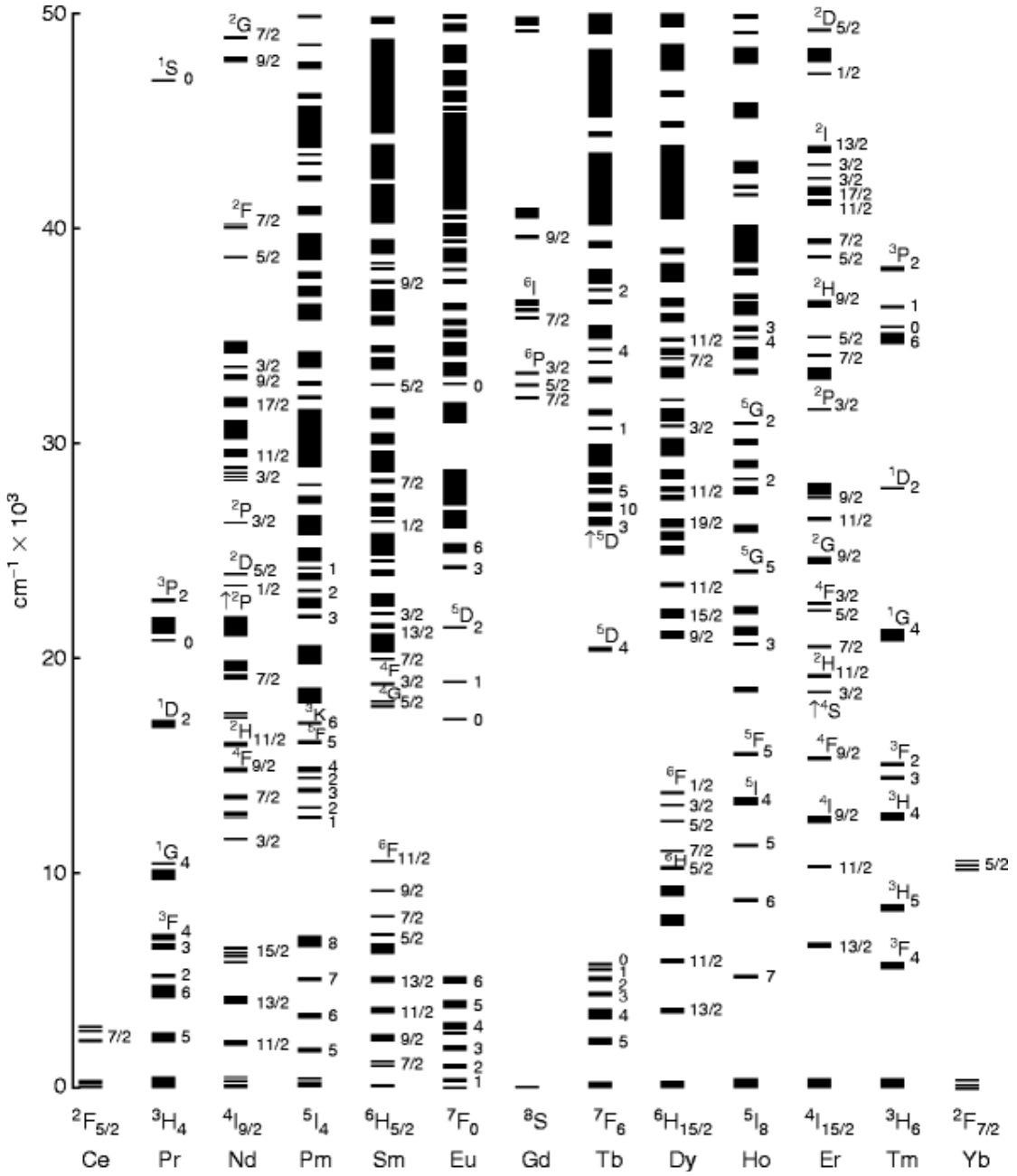

Figure 4: Dieke energy-levels diagram of Ln^{3+} ions [19].

2.5 Ions with s^2 outer shell

This class of elements is considered as heavy metals. They easily form crystalline compounds that can be applied in various applications. Among this class of s^2 elements, the elements with $6s^2$ shell, as Hg, Tl, Pb, and Bi, have an interesting configuration that allows them to be applied as luminescent centers. These elements have an intense interconfigurational $s^2 \rightarrow sp$ structure in the vacuum ultraviolet (VUV) region. Its luminescence is not observed due to quenching by the underlying excited states ($^1P_1$, $^3P_2$, $^3P_1$ and $^3P_0$) of the s^2 configuration [20]. Within these

elements, Bi, with an electronic configuration of $[Xe]4f^{14}5d^{10}6s^26p^3$, can be introduced in different hosts with different oxidation states such as 0, +1, +2, +3, +4 and +5. The nature of different oxidation states of Bi arises from losing the p electrons and by forming the ns^2 configuration in the valence shell [21]. We applied Bi^{3+} as a luminescent center in our project.

2.6 Trivalent bismuth (Bi^{3+}) and its optical properties

Bi^{3+} ions have been investigated extensively for many applications such as phosphors or scintillation detectors as well as a spectroscopic probes for covalency [22]. The luminescence of Bi^{3+} is mainly in the UV and visible (VIS) regions so it attracted attention for various applications. The optical features of the excitation and emission spectra of Bi^{3+} are broader in comparison to the well-known f-f elements. The energy levels of Bi^{3+} are characterized with a $^1S_0$ ground state from the $6s^2$ configuration. The 6s6p excited state is characterized with four excited energy levels known as one singlet level, $^1P_1$, and three triplet levels, $^3P_2$, $^3P_1$ and $^3P_0$, see figure 5 [22]. The energy transitions to the $^1S_0$ ground state consist of two forbidden transitions, $^1S_0 \rightarrow {}^3P_2$ (B band) and $^1S_0 \rightarrow {}^3P_0$ (D band). The first one can be allowed by coupling with the asymmetric lattice vibrations whereas the later one is strongly forbidden. The $^1S_0 \rightarrow {}^1P_1$ (C band) transition is an allowed electric dipole transition and the $^1S_0 \rightarrow {}^3P_1$ (A band) transition becomes allowed due to the spin-orbit coupling [22].

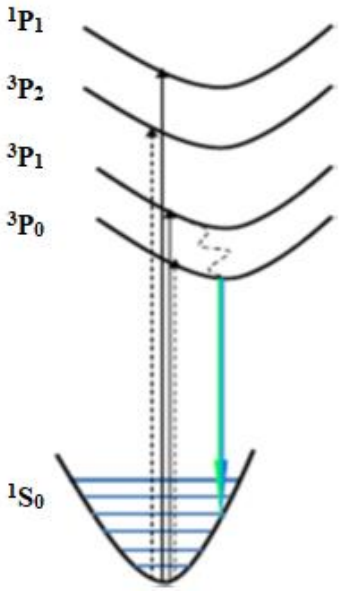

Figure 5: Energy-levels diagram of Bi^{3+} [22].

The absorption (excitation) and emission characteristics of Bi^{3+} occur as broad bands. The excitation occur in the UV region and the emission might occur in the UV and in the VIS

regions. The excitation is usually ascribed to the $^1S_0 \rightarrow {}^3P_1$ transition. The allowed $^1S_0 \rightarrow {}^1P_1$ level occurs at high energy and vary depending on the type of the ligand of the host. The energy difference between the $^1S_0 \rightarrow {}^1P_1$ levels is approximately 45 700 cm^{-1}. This transition has an energy separation of about 10 000 cm^{-1} if compared to the $^1S_0 \rightarrow {}^3P_1$ transition. The position and the energy separation is highly dependent on the host due to the sensitivity of Bi^{3+} to the environment of the host ligand [22]. Although the emission of Bi^{3+} mainly occur from the $^3P_1$ level, in some cases emission might also occur from the forbidden $^3P_0$ level [23]. Emission from the $^3P_0$ level dominates at low temperature (10 K) with a long decay time (e.g. 390 μs) whereas, at high temperature (room temperature) the emission is dominated by the $^3P_1$ level [21]. The radiative $^3P_1 \rightarrow {}^1S_0$ emission has a typical decay time in the 10^{-6} to 10^{-8} s range. A shorter decay time in the nano-second range may also occur in some systems [14].

2.7 Energy transfer mechanisms

Energy transfer is a process where the excitation energy absorbed by an ion called a donor is transferred to a second ion called an acceptor. An emitted photon will be released after a certain time. Generally, energy transfer mechanisms can be divided into four main types, see figure 6. Process (a) is the resonant radiative energy transfer where the photons emitted by a donor is re-absorbed by an acceptor and (b) is the non-radiative energy transfer between an absorber and an emitter. Process (c) is the phonon-assisted energy transfer and lastly process (d) is cross-relaxation between two identical ions [24]. The resonant radiative transfer implies a spectral overlap between a donor's emission and an acceptor's absorption region. If radiative energy transfer dominates in a system, the donor's decay time will not vary significantly with acceptor concentrations. In the case of non-radiative energy transfer a significant decrease in the decay time of the donor will occur with increasing the acceptor concentrations. The radiative energy transfer can be neglected in most inorganic systems as it requires a resonant condition between the donor and acceptor [24, 25]. This requires that the energy difference between the ground state and the excited state of the donor must be equivalent to that of the acceptor. With this condition, a suitable interaction may occur between the donor and the acceptor through either exchange or multipolar interaction [25].

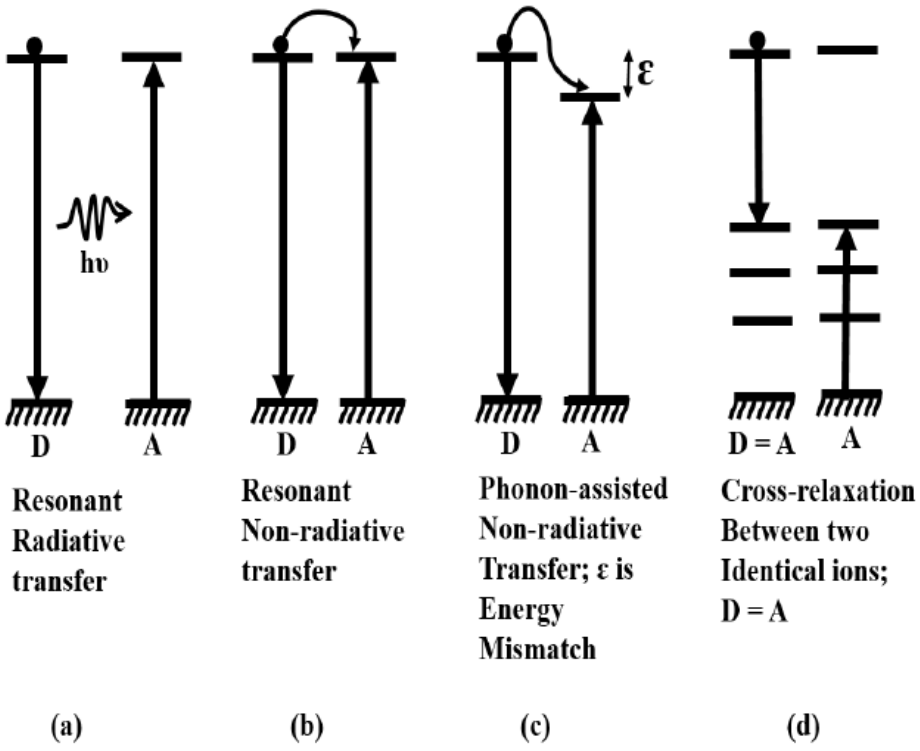

Figure 6: Illustration of different energy transfer mechanisms between two ions [24].

The exchange interaction, also known as Dexter energy transfer, depends on a sufficient overlap of the wave function and only occurs at short distances (> 5 Å). The multipolar interaction, also known as Forster energy transfer, depends on the strength of the optical transition and occurs at large distances (5 Å <). If the difference is not large between the ground state and the excited state of the donor and the acceptor, non-resonant energy transfer may occur through assisted phonons. In respect to the distance dependency, the transfer rate for the exchange interaction is exponential whereas, for the multipolar interaction it takes the expression of R^{-n} (n = 6, 8, 10 for electric interactions of dipole-dipole, dipole-quadrupole, and quadrupole-quadrupole, respectively) [26]. According to the Dexter model, the energy transfer rate between the donor and the acceptor can be written as:

$$W_{DA} = \frac{2\pi}{\hbar} |\langle DA^* \left| H_{DA} \right| D^*A\rangle|^2 \int g_D(E) g_A(E) dE \quad \text{...(6).}$$

$\langle DA^*|$ and $|D^*A\rangle$ are the final and the initial states, respectively. The integral represents the spectral overlap between the donor and the acceptor. The terms $\int g_D(E)$ and $g_A(E)$ are the normalized shape of the donor's emission and the acceptor's absorption spectra, respectively. The above equation implies the enery transfer probability should drop to zero when the spectral

overlap vanishes [26]. The square matrix element in the equation represents the distance-dependent energy transfer between the donor and acceptor.

If there's a high energy mismatch between the donor and the acceptor (≈ 100 cm^{-1}), the energy transfer may be assisted by one or more phonons [27]. According to Miyakawa-Dexter theory [28], the probability of phonon-assisted energy transfer is written as:

$$W_{PAT}(\Delta E) = W_{PAT}(0)\, e^{-\beta \Delta E} \quad \text{.....(7).}$$

ΔE is the E_g between the electronic levels of the donor and acceptor, β represents a parameter that is determined by the strength of the electron-lattice coupling and the nature of the phonon. The cross-relaxation process in process (d), occurs through a diffusion process between the activators' levels when the levels involved are identical or it can lead to self-quenching if the levels are different.

2.8 Down-conversion (DC)

DC in general occurs when a phosphor material is excited with a short wavelength photon and that the emission is then divided into two longer wavelength photons [12]. Currently, this process can refer to QC, quantum splitting, multiphoton emission or photon cascade emission (PCE). Theoretically, the first evidence of DC was proposed by Dexter [29] in 1950. The first experimental evidence of DC process was shown by Piper et al [30] and Somerdijk [31] in 1974 for a YF_3:Pr^{3+} system but not by using the Dexter model. The DC process was first proposed to minimize the energy loss of c-Si SC due to lattice thermalization and thus enhancing its efficiency [32]. The first DC couple was discovered for Gd^{3+}-Eu^{3+} in 1999 through a two-step energy transfer process [33]. The first experimental DC results for a SC was discovered for the Tb^{3+}-Yb^{3+} couple through cooperative energy transfer from Tb^{3+} to Yb^{3+} that corresponded to Dexter's model.

In general, the DC process can occur in different ways by utilizing one or different ions' centers as described in figure 7. A single QC process can occur in one ion through excitation to the highest level of the ion that consists of more than two levels, see figure 7(a). This process was investigated in a number of Ln^{3+} ions such as Pr^{3+}, $Ho^{3+,}$ and Er^{3+} through the absorption of VUV, UV and VIS photons that were converted to NIR photons. The main problem of single QC is the lack of high quantum yield through a combination of unwanted UV/VIS and non-radiative emissions competing with the wanted NIR emission [32]. The second type of DC

occurs through cross-relaxation or resonant energy transfer between two different ions as depicted in figures (b) to (e). Figure 7(b) shows the cross-relaxation process between two ions (process (1)) followed by the energy transfer from ion I to II (process (2)). Process (2) is then followed by the emission from ion II. Figures (c) and (d) demonstrate the DC mechanism with the onset of a single energy transfer between I and II that is followed by emission from both ions. Figure (e) represents the cooperative energy transfer between ion I to a pair of ion II and then emission occur from the II ion pair [32].

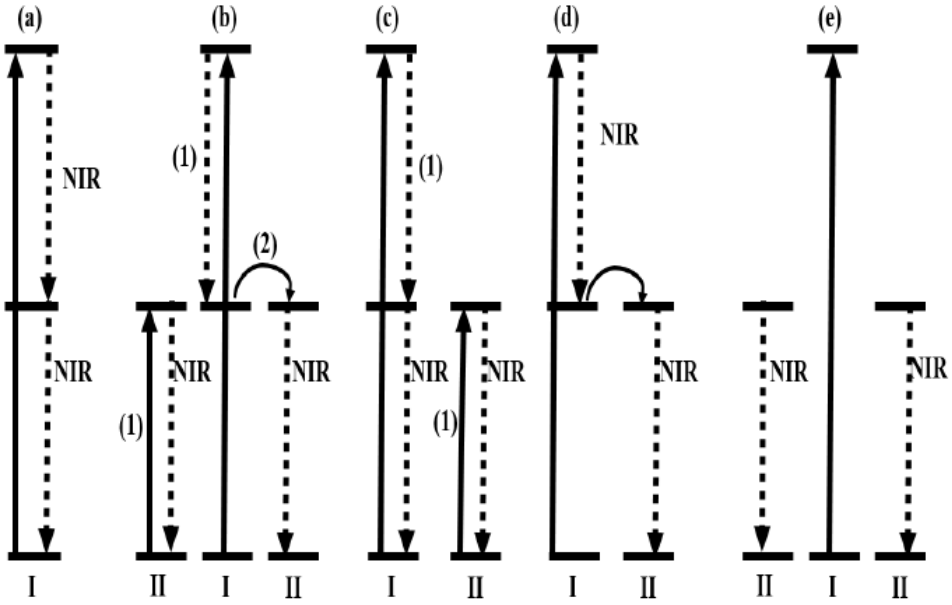

Figure 7: Illustration of the NIR QC mechanisms adopted from [8]. (a) Single ion QC through absorption of one photon and emission of two photons, (b) to (d) resonant energy transfer from donor to acceptor leading to NIR QC and (e) NIR QC through cooperative energy transfer.

The efficiency of energy transfer can be obtained through investigations by using the steady-state measurement of time-resolved spectroscopy [34]. The energy transfer could be obtained as a function of the dopant decay time as:

$$\eta_{ET} = \eta_{x\%Acc} = 1 - \frac{\int I_{x\%Acc}\, dt}{\int I_{0\%Acc} dt} = 1 - \frac{\tau_{x\%Acc}}{\tau_{0\%Acc}} \quad \text{.....(8)}$$

$$\eta_{QE} = \eta_{Don}\,(1 - \eta_{ET}) + 2\,\eta_{ET} \quad \text{.....(9).}$$

I and τ are the intensity and the decay time, respectively. $x\,\%Acc$ represents the acceptor concentration and η_{Don} is the donor efficiency (usually taken as 1) [12]. Another procedure can also be used to determine the quantum yield. It is a process called the integrating sphere

[35]. The obtained efficiency through the integrating sphere process is usually measured relevant to a known standard.

2.9 Downshifting (DS)

DS is a process that is very close to the DC process. Instead of converting the high absorbed energy photon to two lower energy photons, it converts it to one low energy photon [32]. The simple explanation of the process is that the absorbed high energy photon non-radiatively relaxes to a lower level and then radiatively relaxes further. In terms of quantum efficiency it will therefore not exceed unity [32]. The non-radiative relaxation process from the excited state to the emitted state is known as a stoke shift. DS materials normally absorb in the short wavelength range of 300 – 500 nm [36]. According to literature, the internal quantum efficiency of a SC can be enhanced up to ~ 10 % with a DS layer. The enhancement will not exceed the suggested Shockley-Queisser limit. It is known that the ideal DS material has a good external quantum efficiency that is close to unity and a large stoke shift. The advantage of a DS layer is that it also minimizes the lattice thermalization process in the SC [8].

2.10 Host material

Inorganic host's crystal structures for possible optical applications must consist of certain properties. Some of these properties are the large E_g and chemical and thermal stability. A pure host can also act as an emitting material through the E_g itself [16]. Some hosts can also emit as a result of defects or other functional groups such as VO^{3-}_4, WO^{2-}_4 or MoO_4^{-2} [16]. Large E_g materials are considered a good choice for doping with impurities such as Ln^{3+} ions or transition metal ions or s^2 ions. Doping can result in electronic levels of the ions inside the E_g that can act as luminescent centers [14, 16].

Fluoride hosts have been considered a good choice for many DC, DS and other optical applications [37]. Fluoride materials however have low chemical stability comparing to other systems such as oxides. Such a problem can be overcome by merging the properties of the fluorides and the oxides into the well-known oxyfluoride materials. RE oxyfluorides have attracted the attention for many applications due to intrinsic properties [38, 39, 40]. One of the RE oxyfluoride hosts is YOF.

The crystal structure of the YOF host (stoichiometric) exhibits a rhombohedral structure with a space group of $R\bar{3}m$ (166) (a = 3.797 Å, c = 18.89 Å). The structure contains one site for the

Y^{3+} ion that is surrounded with 4 oxygen ions (O^{2-}) and 4 fluorine ions (F^{-}), see figure 8. The coordination in the structure is in an arrangement of a bi-capped trigonal antiprism with 6c-Wyckoff positions and the symmetry of Y^{3+} as C_{3V} [41]. On the other side, there are other phases of YOF structures known as non-stoichiometric structures. The concept of non-stoichiometric comes from the non-equivalent number of O^{2-} and F^{-} ions inside the structure and takes the form of $Y_nO_{n-1}F_{n+2}$ (n = 5 - 7) leading to structures like $Y_5O_4F_7$, $Y_6O_5F_8$, and $Y_7O_6F_9$ [42]. In contrast to the YOF structure these phases have orthorhombic structures [42]. During the phase transition and formation of YOF, Guang Chai [43] and his group have explained how we can get different phases of stoichiometric and non-stoichiometric YOF starting from yttrium fluoride (YF_3). Eloussifi et al. [44] have studied the decomposition of a source of yttrium trifluoroacetate ($Y(CF_3COO)_3$) to form different phases of YOF accompanied by releasing different gases.

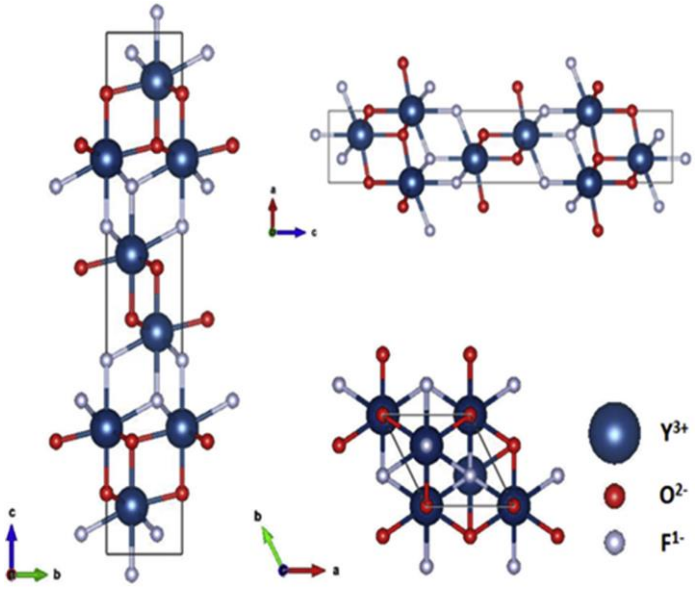

Figure 8: Crystal structure of YOF [41].

Studies of YOF for possible applications have been carried on for many years. Huilin He [45] and his group have investigated a set of YOF:Er^{3+} and GdOF:Er^{3+} for mid-IR fluorescence and as laser materials. Yang Zhang [46] and his group have extended their studies to more Ln^{3+} ions (Ln^{3+} = Tb^{3+}, Eu^{3+}, Tm^{3+}, Dy^{3+}, Ho^{3+}, Sm^{3+}) for field emission displays (FEDs). Fujihara et al. [47] have also studied YOF doped with Pr^{3+} thin films with an intense green emission at 498 nm for UV-light emitting diode (LED) optoelectronic applications. Studies of outer s^2 shells have also been done by Blasse and Brill [48] by doping with Bi^{3+} for UV emission and excitation.

References

[1] O. Morton, Nature, 443 (2006) 19.

[2] D.M. Chapin, C.S. Fuller and G.L. Pearon, J. Appl. Phys. 25 (1954) 676 - 677.

[3] V.S. Arunachalam and E.L. Fleischer, MRS Bulletin, 33 (2008) 264 - 276.

[4] T. Trupke, M.A. Green and P. Wurfel, J. Appl. Phys. 92 (2002) 1668 - 1674.

[5] O.M. Ten Kate, Lanthanide doped spectral conversion materials for solar cells, PhD Thesis, (2014).

[6] M.A. Green, K. Emery, Y. Hishikawa, W. Warta and E.D. Dunlop, Prog. Photovoltaics: Res. Appl. 22 (2014) 1 - 9.

[7] A. Shalav, Rare-Earth Doped Up-converting Phosphors for an Enhanced Silicon Solar Cell Response, University of New South Wales, PhD Thesis, (2006).

[8] M.Y.A Yagoub, H.C. Swart and E. Coetsee, Effect of broadband excitation ions in the luminescence of Ln^{3+} doped SrF_2 nanophosphor for solar cell application, PhD Thesis, (2015).

[9] W. Shockley and H.J. Queisser, J. Appl. Phys. 32 (1961) 510 - 519.

[10] D. Timmerman, I. Izeddin, P. Stallinga, I. N. Yassievich and T. Gregorkiewicz, Nat. Photonics, 2 (2008) 105 - 108.

[11] R.D. Schaller, V.M. Agranovich and V.I. Klimov, Nat. Phys. 1 (2005) 189 - 195.

[12] X. Huang, S. Han, W. Huang and X. Liu, Chem. Soc. Rev. 42 (2013) 173 - 201.

[13] T. Trupke, M. A. Green and P. Wurfel, J. Appl. Phys. 92 (2002) 1668 - 1674.

[14] R.S. Liu, Phosphors, Up Conversion Nano Particles, Quantum Dots and Their Applications, (Springer-Verlag Berlin Heidelberg), Vol. 1 (2017).

[15] C. Feldmann, T. Justel, C.R. Ronda and P.J. Schmidt, Adv. Funct. Mater. 13 (2003) 511-516.

[16] A. Edgar, Luminescent Materials. In: S. Kasap and P. Capper (eds) Springer Handbook of Electronic and Photonic Materials. Springer Handbooks. Springer, Cham (2017).

[17] Judd-Ofelt theory: principles and practices; available from: http://link.springer.com/chapter/10.1007/1-4020-4789-4-21page-1 (Accessed on 17-09-2019).

[18] G. Dieke, Spectra and Energy Levels of Rare Earth Ions in Crystals, Interscience Publishers, New York, (1968).

[19] G. Dieke and H. Crosswhite, Appl. Opt. 2 (1963) 675 - 686.

[20] P. Lecoq, M. Korzhik, A. Annenkov, C. Pedrini and A. Gektin, Inorganic Scintillators for Detector Systems, (Springer-Verlag Berlin Heidelberg), (2006).
[21] F. Kang and M. Peng, Dalton Trans. 43 (2014) 277 - 284.
[22] H.T. Sun, J. Zhou and J. Qiu, Prog. Mater. Sci. 64 (2014) 1 - 72.
[23] H.C. Swart and R.E. Kroon, Opt. Mater. X, 2 (2019) 100025 (22 pages).
[24] G. Liu and B. Jacquier, Spectroscopic Properties of Rare Earth in Optical Materials, Springer, China, (2005).
[25] Q.Y. Zhang and X.Y. Huang, Prog. Mater. Sci. 55 (2010) 353 - 427.
[26] A. Fabio, Energy transfer and charge transfer processes in luminescent materials, PhD Thesis, (2013).
[27] S. Ye, F. Xiao, Y.X. Pan, Y.Y. Ma and Q.Y. Zhang, Mater. Sci. Eng. R, 71 (2010) 1 - 34.
[28] T. Miyakawa and D.L. Dexter, Phys. Rev. B, 1 (1970) 2961 - 2969.
[29] D.L. Dexter, Phys. Rev. 108 (1957) 630 - 633.
[30] W.W. Piper, J.A. DeLuca, and F. S. Ham, J. Lumin. 8 (1974) 344 - 348.
[31] J.L. Sommerdijk, A. Bril and A.W. de Jager, J. Lumin. 8 (1974) 341 - 343.
[32] B.M. Van der Ende, L. Aarts and A. Meijerink, Phys. Chem. Chem. Phys. 11 (2009) 11081 - 11095.
[33] R.T. Wegh, H. Donker, K.D. Oskam and A. Meijerink, Science, 283 (1999) 663 - 666.
[34] J. Zhou, Y. Teng, G. Lin and J. Qiu, J. Non-Cryst. Solids, 357 (2011) 2336 - 2339.
[35] B.M van der Ende, L. Aarts and A. Meijerink, Adv. Mater. 21 (2009) 3073 - 3077.
[36] C. Strümpel, M. McCann, G. Beaucarne, V. Arkhipov, A. Slaoui, V. Švrčekc, C. del Cañizo and I. Tobias, Sol. Energ. Mat. Sol. C, 91 (2007) 238 - 249.
[37] J. Day, S. Senthilarasu and T.K. Mallick, Renew. Energy, 132 (2019) 186 - 205.
[38] E. Martinez-Castro, J. Garcia-Sevillano, F. Cusso and M. Ocana, J. Alloy Compd. 619 (2015) 44 - 51.
[39] R. Li, L. Li, W. Zi, J. Zhang, L. Liu, L. Zou and S. Gan, New J. Chem. 39 (2015) 115 - 121.
[40] Y. Zhang, D. Geng, X. Kang, M. Shang, Y. Wu, X. Li, H. Lian, Z. Cheng and J. Lin, Inorg. Chem. 52 (2013) 12986 - 12994.
[41] N.A.M. Saeed, E. Coetsee and H.C. Swart, Opt. Mater. 96 (2019) 109331 (12 pages).
[42] T. Wen, W. Luo, Y. Wang, M. Zhang, Y. Guo, J. Yuan, J. Ju, Y. Wang, F. Liao and B. Yang, J. Mater. Chem. C, 1 (2013) 1995 - 2001.
[43] G. Chai, G. Dong, J. Qiu, Q. Zhang and Z. Yang, Sci. Rep. 3 (2013) 1 - 10.

[44] H. Eloussifi, J. Farjas, P. Roura, J. Camps, M. Dammak, S. Ricart, T. Puig and X. Obradors, J. Therm. Anal. Calorim. 108 (2012) 589 - 596.

[45] H. He, Q. Liu, D. Yang, Q. Pan, J. Qiu and G. Dong, Sci. Rep. 6 (2016) 1 - 10.

[46] Y. Zhang, D. Geng, X. Kang, M. Shang, Y. Wu, X. Li, H. Lian, Z. Cheng and J. Lin, Inorg. Chem. 52 (2013) 12986 - 12994.

[47] S. Fujihara, S. Koji, Y. Kadota and T. Kimura, J. Am. Ceram. Soc. 87 (2004) 1659 - 1662.

[48] G. Blasse and A. Bril, J. Chern. Phys. 48 (1967) 217 - 222.

Chapter 3

Preparation method & Characterization techniques

This chapter gives a general overview on the preparation method used in this study to prepare the high quality powders. A brief description and principle of operation of the characterization techniques used in this study are also given.

3.1 Pyrolysis method

Pyrolysis is a terminology that describes the thermal decomposition of materials at elevated temperature in an inert gas or sometimes at ambient air. It has been widely used in synthesizing high quality powders in nanometer scale [1]. The first evidence for thermal decomposition of RE trifluoroacetate (CF_3COO) was done by Rillings during his investigation on Pr^{3+}, Er^{3+} and Sm^{3+} CF_3COO to prepare LnF_3 and LnOF (Ln = Pr^{3+}, Er^{3+} and Sm^{3+}) by annealing in air and in vacuum [2]. Complexes of CF_3COO precursors were also used to prepare high performance and high temperature superconductor coated layers for conductors and thin films using chemical solution decomposition [3-5]. Various studies were done on the decomposition of the CF_3COO precursor to get different high crystalline phases through single sources [6-8].

Eloussifi et al. [8] have studied the process of decomposition of a source of commercial $Y(CF_3COO)_3$. During their investigation on the decomposition process, different phases formed with increasing temperatures. Different gasses were released with increasing temperatures as different phases formed. The decomposition included four stages. The first stage was the dehydration process that was accompanied with a mass loss, and this stage occurred at low temperatures (> 200 ^oC). The second stage was the formation of YF_3 at a low temperature (~ 400 ^oC) that was accompanied with the release of $(CF_3CO)_2O$, CO and CO_2 gasses. The third stage occurred during an increase in temperature and it involved the formation of a mid-structure known as non-stoichiometric yttrium oxyfluoride. This mid-structure had an $Y_nO_{n-1}F_{n+2}$ (n = 5 - 7) form that lead to an $Y_6O_5F_8$ structure with an orthorhombic phase [9]. The fourth stage resulted in the formation of stoichiometric YOF and occurred at 900 ^oC. A further increase in temperature will however result in the replacement of fluorine ions with oxygen ions and therefore the decomposition of YOF into cubic yttrium oxide (Y_2O_3). Rare earth CF_3COO can be synthesized by using metal oxides or metal carbonates. The starting

oxides or carbonates react with trifluoroacetic acid (CF_3COOH) when it is mixed with distilled water. After evaporation of the excess solvents the remaining powder can act as a precursor that can decompose into different structures with annealing [10, 11].

For the purpose of this research study, we've first let Y_2O_3 react with a mixture of CF_3COOH and distilled water to form the $Y(CF_3COO)_3$ starting precursor as in figure 1. Pyrolysis of the prepared $Y(CF_3COO)_3$ then resulted in the decomposition into orthorhombic YF_3 at low temperature. Some compounds evaporated with increasing temperature such as $(CF_3CO)_2O$, CO, and CO_2, see the chemical reaction:

$$\mathbf{Y(CF_3COO)_3 \rightarrow YF_3 + (CF_3CO)_2O + CO + CO_2 \ldots\ldots\ldots 1.}$$

With a further increase in the temperature, more oxygen ions were introduced inside the YF_3 structure. This resulted in the decomposition of YF_3 into a non-stoichiometric structure of yttrium oxyfluoride known as $Y_6O_5F_8$, with an orthorhombic structure. The rhombohedral YOF structure therefore formed by incorporating more oxygen ions from air into the structure during increased temperatures. At higher temperatures (~1200 °C) the structure changed to cubic Y_2O_3.

We can therefore divide the pyrolysis of $Y(CF_3COO)_3$ to different structures into five stages [8]:

- Dehydration.
- Formation of YF_3 as a stable intermediate.
- Decomposition of YF_3 to form a non-stoichiometric yttrium oxyfluoride.
- Formation of stoichiometric YOF.
- Decomposition of YOF into cubic Y_2O_3. The complete transformation was obtained at 1200 °C.

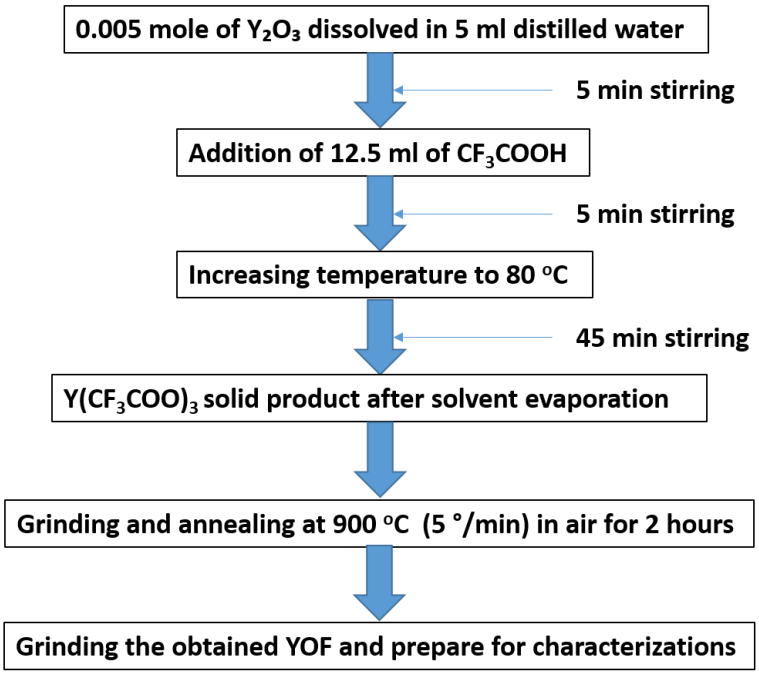

Figure 1: Flow chart explaining the synthesis of YOF by using pyrolysis of trifluoroacetate precursor.

3.2 X-ray diffraction (XRD)

3.2.1 Overview

XRD is a non-destructive technique used to analyze and to determine crystal phases, grain sizes and lattice parameters of materials [12]. Max Von Laue discovered in 1912 that a crystalline substance can act as a three-dimensional diffraction grating for x-rays with wavelengths similar to the spaces between planes of a crystal lattice [12, 13]. When incident monochromatic x-rays interact with the material, scattering of x-rays occur from the atoms of the material. This kind of behavior is called diffraction [13]. The scattered x-rays can also experience constructive and destructive interference. Almost 95 % of solid materials can be described as crystalline materials [14]. The wavelengths of the x-rays are normally between 0.07 – 0.23 nm, that is very close to the inter-planar spacing of most of the crystalline materials. The diffraction of x-rays in crystalline materials appears as individual peaks at certain angles that correspond to the inter-planar distances [15]. The XRD pattern can be described in terms of Bragg's law.

3.2.2 Bragg's law

Bragg's law was named after the contribution of both Sir W.H Bragg and his son W.L Bragg in 1913 [13]. Bragg's law connected the diffraction angles of the incident x-rays with the inter-

atomic distances. When the sample is bombarded with x-rays of a specific wavelength at a certain angle, intense reflected x-rays are produced when the wavelengths of the scattered x-rays interfere constructively. Constructive interference diffracts the x-rays with an angle equal to that of the incident beam, see figure 2. Bragg's law can be expressed as follow [13]:

$$n\lambda = 2d \sin\theta \quad \text{.....2.}$$

λ is the incident x-ray wavelength, d is the inter-planar space between crystal planes of atoms, ions or molecules. The integer number, n, represents the order of diffraction and 2θ is the angle between the diffracted and transmitted x-rays. The value of 2θ is obtained from the experimental measurement.

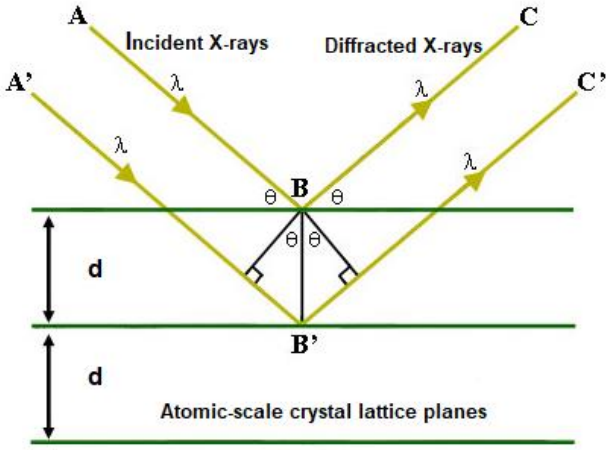

Figure 2: Schematic diagram showing Bragg's law, adopted from [13].

A XRD pattern is obtained by a diffractometer. A typical diffractometer consists of an x-ray tube, a sample holder and an x-ray detector, see figure 3(a). In the x-ray tube electrons are emitted from a heated tungsten filament and accelerated by an electric potential to impinge on a metal target. The interaction between the electrons and the metal target leads to the emission of x-rays. Some of these x-rays have a wavelength characteristic of the target and some have a continuous distribution of wavelengths between 0.05 nm and 0.5 nm [12]. This continuous distribution contains multiple wavelength components like K_α and K_β. K_α consists of two parts, $K_{\alpha1}$ and $K_{\alpha2}$, where $K_{\alpha1}$ has a shorter wavelength and twice the intensity of $K_{\alpha2}$. Copper is the most frequently used material for single crystal diffraction with CuK_α = 0.154 nm. Filtering of the monochromatic x-ray wavelengths by using a proper nickel filter for example, results in the absorbance of the wavelengths bellow 0.154 nm, see figure 3(b). The filtered wavelengths are focused towards the sample with an angle, θ, while the x-ray source and the detector are rotated with 2θ angles. The detector records the maximum intensities corresponding to each

diffraction angle [12, 13]. Further correction of the obtained XRD results is done by correcting the pattern with respect to K_α.

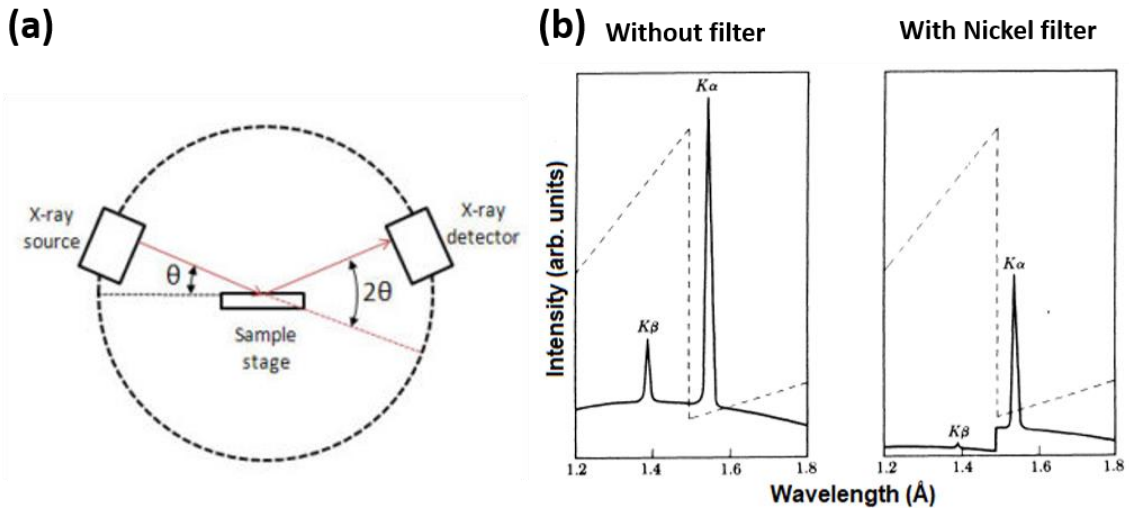

Figure 3: a) Schematic diagram showing different components of the diffractometer, adopted from [16] and b) a spectra of copper radiation with and without a nickel filter [12].

The crystallite size of the samples can be obtained by using the Scherer equation for the broadening of the diffraction peaks [17]. The broadening is a result from sample broadening as well as the instrument broadening. It is useful to identify the nature of the broadening by collecting the diffraction pattern from the line broadening of a standard material (e.g., silicon) to be able to determine the instrumental broadening. The corrected β_{hkl} is corresponding to the diffraction peak of the material and can be calculated by using the relation

$$(\beta_{hkl})^2 = (\beta_{hkl})^2_{measured} - (\beta_{hkl})^2_{instrumental} \quad \text{.....3}$$

$$\beta_{hkl} = \frac{k\lambda}{D\cos\theta} \quad \text{.....4.}$$

β_{hkl} represents the peak broadening or full width at half maximum (FWHM) corresponding to the diffraction angle θ and miller indices hkl. λ represents the wavelength of the CuK_α x-ray radiation (0.154 nm), D is the crystallite size in nanometer and k represents the shape factor for spherical shapes and is equivalent to 0.9 [18, 19]. All the XRD measurements of this study were collected by using a Bruker D8 Advance diffractometer equipped with a copper anode (λ = 0.154 nm). It was operated at a voltage of 40 kV and a current of 40 mA.

3.3 Scanning Electron Microscopy (SEM) and Cathodoluminescence (CL)

3.3.1 (SEM)

The SEM technique is used to study the morphology of a sample's surface. It produces an image using electrons instead of light. SEM has various advantages such as a wide scan area of the sample's surface with good spatial resolution (depending on the different systems). The principle of SEM is based on a beam of high energy electrons that are accelerated and focused on the sample while passing through a combination of lenses and apertures in a column, see figure 4. This generates a variety of signals from the surface of the specimen such as secondary electrons, backscattered electrons (determine the crystal structure and orientation of minerals), x-rays, visible photons, Auger electrons, diffracted backscattered electrons and heat [20]. These signals reveal information from the sample that includes topography (texture), morphology (particle size and shape), chemical composition, crystalline structure and orientation of the materials. The sample is placed on a holder in a vacuum chamber and both the column and the chamber are evacuated by various pumping. SEM scanning areas range from nanometers up to a few microns depending on the type of study. Some SEM systems are also capable of doing some element identification of samples by using Energy Dispersive X-ray Spectroscopy [20]. Secondary electrons are used to determine the morphology and topography of the sample.

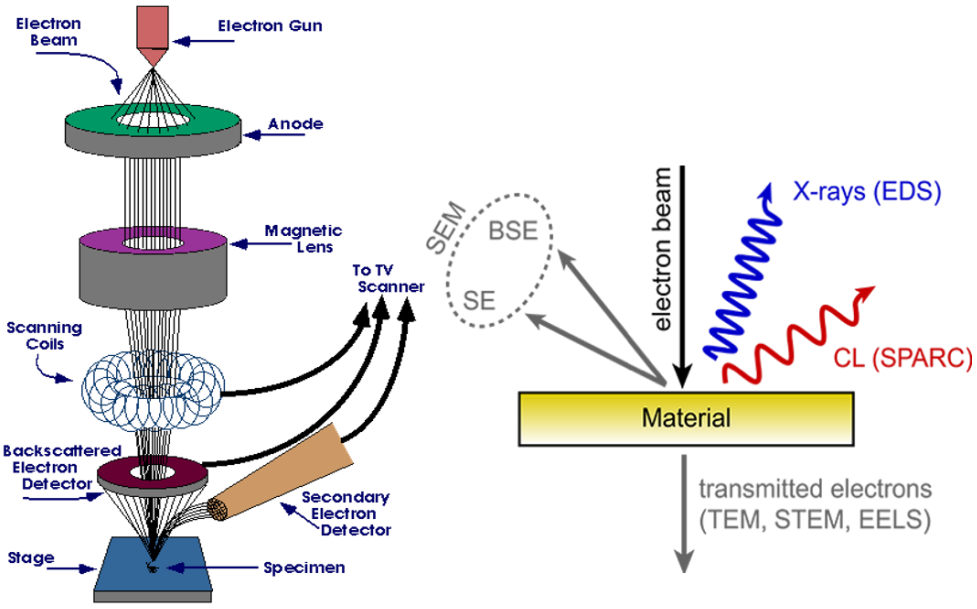

Figure 4: Schematic diagram of a SEM system and the generation of different signals after electron interaction [20, 21].

Backscattered electrons are important for showing the contrasts in composition for multiphase samples [20, 22]. The SEM images for this study was recorded by using a JEOL JSM-7800F SEM system.

3.3.2 CL

Emission of photons from the surface of a material after irradiation of high energy electrons is known as CL. These emitted photons cover a wide range of wavelengths in the UV, VIS and NIR ranges. CL is mainly used to characterize the optical properties of materials in the nanoscale. CL photons are a side product after irradiation of high energy electrons. In some kinds of microscopy, a CL detector is attached to detect the emitted photons after irradiation of high energy electrons. The recorded emission intensity is given as a function of the scanned wavelengths. For a better response of the recorded emission, cooling of the sample stage may be implied. The obtained emission of the sample gives intrinsic structural features of the sample that correspond to each individual peak [21, 23]. CL analysis in this study were done by using the same JEOL JSM-7800F SEM system equipped with a CL detector, Gatan Mono CL4. The photons were detected inside the chamber and cooling of the chamber by liquid nitrogen was necessary.

3.4 X-ray Photoemission Spectroscopy (XPS)

XPS, also known as Electron Spectroscopy for Chemical Analysis (ESCA), is mainly used to investigate the elemental and chemical composition of a sample's surface. The first development of XPS was in the mid- 1960's by Kai Siegbahn and his research group at the University of Uppsala, Sweden [24]. A full and detailed description of XPS can be found in various textbooks and literatures studies [25-28]. When a solid material is irradiated with photons having sufficient energy ($\hbar\upsilon$), photoelectrons will be released, based on the photoelectric effect, having a kinetic energy given by [24]:

$$\mathbf{E_k = h\upsilon - E_B - \phi} \quad \text{.....5.}$$

E_k is the kinetic energy of the released electrons, E_B is the binding energy of the state where the electrons eject from and ϕ is the sample's work function that is defined as the minimum energy required to remove an electron from the material [15]. The intensity of the photoemission peaks ($I(E_k)$) can also be determined as a function of the binding energy through [15]:

$$I(E_k) = DOS(h\upsilon - E_B - \phi) \text{ ……..…6.}$$

DOS(E) is the density of states as a function of the binding energy. The photoemission spectrum therefore represents the energy distribution of the electron states in a solid, see figure 5. The sample and the analyzer are grounded together during the experimental procedure in order to align their Fermi levels. It is then convenient to write the measured kinetic energy in respect to the Fermi energy levels as [15]:

$$E_k = h\upsilon - E_B - \phi_{sp} \text{ ……7.}$$

ϕ_{sp} is the spectrometer's work function. The binding energy can then be described as the energy difference between the initial and final states after the photoelectron left the atom. There is a dependency of the energy level of the core electron to the chemical state of the atom. Important information can therefore be obtained through understanding the XPS data and by distinguishing between the initial and the final state effects. The photoemission is due to the final state and its nature. A change in the oxidation states has an effect on the binding energies, which increase with increasing oxidation state and vice versa. The p, d and f levels of the atoms can split during the ionization process resulting in $p_{1/2}$, $p_{3/2}$, $d_{3/2}$, $d_{5/2}$ $f_{5/2}$ and $f_{7/2}$. The ratio of splitting for each orbital is 1:2, 2:3 and 3:4 for p, d and f, respectively [24].

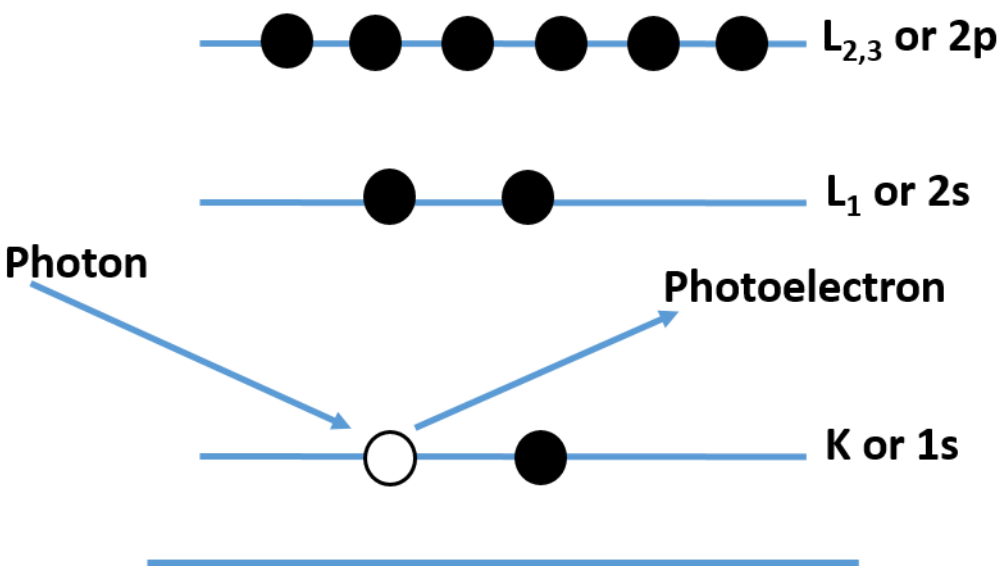

Figure 5: Schematic diagram of the production of a x-ray photoelectron [24].

In this research study high-resolution XPS was obtained with a PHI 5000 Versa-probe system. The samples were irradiated with a 100 μm diameter monochromatic Al K_α x-ray beam ($h\upsilon$ = 1486.6 eV) generated by a 25 W, 15 kV electron beam, in an ultra-high vacuum chamber (9 x 10^{-10} Torr), that resulted in the ejection of photo-electrons. Some of these photo-electrons

inelastically scattered through the sample towards the surface, while the rest of the electrons escaped from the surface into the vacuum without energy loss [29, 30]. The ejected photo-electrons were collected by an electron analyzer that measured their kinetic energy. The analyzer produces spectra of intensity (number of ejected electron versus time) versus binding energy (electron energy before leaving the atom). Each peak in the XPS spectrum corresponds to a specific element [29, 30]. The pass energy was set to 23.5 eV giving an analyzer resolution of ≤ 0.5 eV.

A low energy Ar^+ ion gun and low energy neutralizer electron gun were used to minimize charging on the surface. Multipack version 8.2 software was utilized to analyze the spectra to identify the chemical compounds and their electronic states using Gaussian-Lorentz fits.

3.5 Auger Electron Spectroscopy (AES)

AES is a phenomenon that was first introduced by Pierre Victor Auger in 1923 during his studies of electron induced x-ray excitation in a Wilson cloud chamber. He did experiments and theoretical explanations of the mechanism that were reported in his doctoral thesis in 1926 [31]. Later in 1953, Launder explained the possibility of doing surface analysis by determining the characteristics of Auger peaks. He successfully observed secondary electron emission during electron irradiation of solids [31], see figure 6. AES is an important surface analysis technique that provides elemental information of the material. The Auger electrons have relatively short inelastic mean free paths and the AES technique can detect all the elements except H and He.

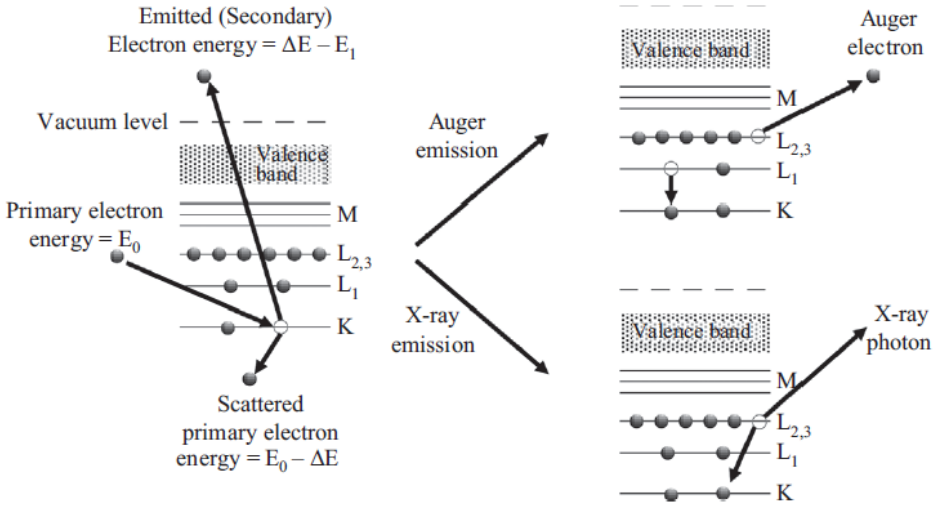

Figure 6: Schematic diagrams explaining the production of Auger electrons and of x-ray emission, adopted from [32].

The simplified description of the AES mechanism involves the removal of an electron from the core level, K, through an incident primary electron. A second electron from the upper level L_1 will relax to the K level to fill up this hole. The energy released during the relaxation will be transferred to a third electron that will be released from the upper level $L_{2,3}$, see figure 6. The Auger electron's kinetic energy is given by [15]:

$$\mathbf{E_{kin} = E_K - E_{L_1} - E_{L_{2,3}} - \phi} \text{ ..……..……8,}$$

where ϕ is the work function of the analyzer. The notation, K, represents the initial state whereas L_1 and $L_{2,3}$ are the final state transitions. According to Chung and Jenkins' approximation an accurate expression of kinetic energy of the ejected Auger electron is given by (Z+1) [32], where Z is the atomic number of a specific atom. This approach was based on the assumption that the binding energy of all the electrons will increase the moment one electron is removed. Thus, the properties are electrostatically similar to an atom that has an atomic number greater by unity and this gives an expression [15, 32]:

$$\mathbf{E_{kin} = E_K^Z - \frac{1}{2}\left[E_{L_1}^Z + E_{L_1}^{Z+1}\right] - \frac{1}{2}\left[E_{L_{2,3}}^Z + E_{L_{2,3}}^{Z+1}\right] - \phi \text{ …9.}}$$

The AES data of all the powder samples in this study and related SEM images were collected using a PHI 700 Scanning Auger Nanoprobe with a 20 kV 10 nA beam voltage and current, having a beam diameter of about 12 nm, in ultra-high vacuum at a pressure of 1.7 x 10^{-10} Torr. This high energy electron beam was focused on the sample surface through electric lenses and caused the ejection of the Auger electrons. A cylindrical mirror Auger analyzer was used to detect the Auger electrons. The measured electrons were then displayed in a spectrum that represented the intensity versus the kinetic energy of the emitted Auger electrons. Each peak of the spectrum correspond to an individual element [33].

3.6 Photoluminescence (PL)

PL is a technique used to study the optical properties of a material based on its excitation and emission. The optical properties depend on the electronic transitions of a certain material or ions (e.g. transition metals or lanthanide ions) [34]. PL measurements can be divided into steady state and time-resolved PL measurements. The main difference between the two types are based on the nature of the study. The steady state measurements involve excitation and emission spectra whereas time-resolved measurements obtain the decay curves [15, 34]. In PL measurements the intensity distribution is given as a function of the wavelength. The excitation

spectrum is recorded while monitoring a certain emission. The emission spectrum is recorded through exciting the material with the individual excitation wavelengths.

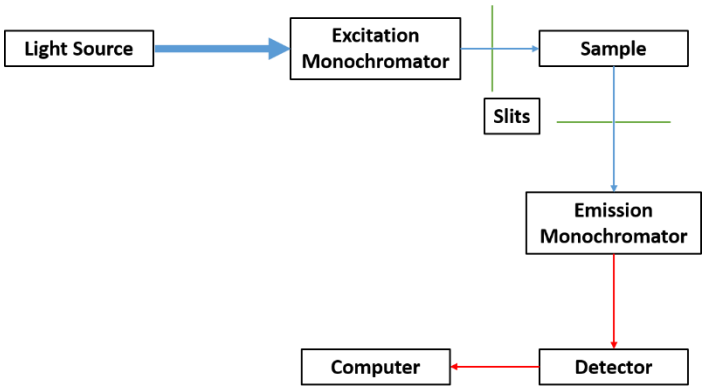

Figure 7: Schematic diagram of the typical components of spectrofluorometer.

Figure 7 shows the basic components of a PL spectrofluorometer. A beam of photons from a light source passes through the first monochromater that selectively transmit a specific excitation wavelength and is focused on the desired sample. The emitted light from the sample is directed towards the emission monochromater and then directed to a photodetector. The photodetector converts the emitted light to an analog electrical signal. This analog electrical signal is then converted into a digital signal by using analog to digital converters and further processing is done by using computer software. The obtained spectrum will be shown in terms of intensity of the emitted light (proportional to the electrical signal generated) as a function of the wavelength of the emitted light [15, 34, 35].

PL measurements for all the prepared samples in this study was done by using the Edinburgh FLS980 instrument. For the lifetime measurements the system was equipped with an EPLED 257.4 nm excitation source or uF2 Microsecond Xe flash lamp source depending on the measurement. The quantum yield measurements were done by using the same instrument equipped with an integrating sphere.

References

[1] Y.A. Opata and J.-C. Grivel, J Anal. Appl. Pyrol. 132 (2018) 40 - 46.

[2] K.W. Rillings and J.E. Roberts, Thermochim. Acta, 10 (1974) 285 - 298.

[3] Y. Zhao, W. Wu, X. Tang, N.H. Andersen, Z. Han and J.-C. Grivel, Cryst. Eng. Comm. 16 (2014) 4369 - 4372.

[4] Y.A. Opata, A.C. Wulff, J.O.B. Hansen, Y. Zhao and J.-C. Grivel, IEEE Trans. Appl. Supercond. 26 (3) (2016) 7500705 (5 pages).

[5] K. De Keukeleere, P. Cayado, A. Meledin, F. Vallès, J. De Roo, H. Rijckaert, G. Pollefeyt, E. Bruneel, A. Palau, M. Coll, S. Ricart, G. Van Tendeloo, T. Puig, X. Obradors and I. Van Driessche, Adv. Electron. Mater. 2 (2016) 1600161 (9 pages).

[6] M. Mosiadz, K.L. Juda, S.C. Hopkins, J. Soloducho and B.A. Glowacki, J. Fluor. Chem. 135 (2012) 60 59 - 67.

[7] J. Farjas, J. Camps, P. Roura, S. Ricart, T. Puig and X. Obradors, Thermochim. Acta, 544 (2012) 77 - 83.

[8] H. Eloussifi, J. Farjas, P. Roura, J. Camps, M. Dammak, S. Ricart, T. Puig and X. Obradors, J. Therm. Anal. Calorim. 108 (2012) 589 - 596.

[9] T. Wen, W. Luo, Y. Wang, M. Zhang, Y. Guo, J. Yuan, J. Ju, Y. Wang, F. Liao and B. Yang, J. Mater. Chem. C, 1 (2013) 1995 - 2001.

[10] C. Rüssel, J. Non-Cryst. Solids, 152 (1993) 161 - 166.

[11] U. Wagener and C. Rüssel, J. Non-Cryst. Solids, 152 (1993) 167 - 171.

[12] B.D. Cullity, Element of x-ray diffraction, Addison-Wesley Publishing Company, Inc. USA, (1956).

[13] https://serc.carleton.edu/research_education/geochemsheets/techniques/XRD.html (Accessed on 24.10.2019).

[14] http://old.vscht.cz/clab/RTG/dokumenty/thermo/xrd/Introduction%20to%20powder%20diffraction.pdf (Accessed on 24.10.2019).

[15] M.Y.A. Yagoub, E. Coetsee and H.C. Swart, Effect of broadband excitation ions in the luminescence of Ln^{3+} doped SrF_2 nanophosphor for solar cell application, PhD Thesis, (2015).

[16] http://xrd.co/component-parts-x-ray-diffractometer/ (Accessed on 24.10.2019).

[17] V.D. Mote, J.S. Dargad and B.N. Dole, J. Nanosci. Nanotechnol. 1 (2013) 116 - 122.

[18] Y.T. Prabhu, K.V. Rao, V.S.S. Kumar and B.S. Kumari, World Journal of Nano Science and Engineering, 4 (2014) 21 - 28.

[19] T. Many K. Thandavan, S. Meriam Abdul Gani, C. San Wong and R. Md Nor, J Nondestruct. Eval. 34 (2015) 1 - 14.

[20] https://www.purdue.edu/ehps/rem/laboratory/equipment%20safety/Research%20Equipment/sem.html (Accessed on 23-10-2019).

[21] https://www.nanoscience.com/techniques/cathodoluminescence/ (Accessed on 23-10-2019).

[22] https://serc.carleton.edu/msu_nanotech/methods/SEM.html (Accessed on 23-10-2019).

[23] https://serc.carleton.edu/research_education/geochemsheets/semcl.html (Accessed on 23-10-2019).

[24] J.F. Moulder, W.F. Stickle, P.W. Sobol and K.D. Bomben, Handbook of X-ray Photoelectron Spectroscopy, Perkin-Elmer, Eden Prairie, MN, (1992).

[25] S. Hüufner, photoelectron Spectroscopy Principles and Application, Springer, Berlin, Second Edition, (1995).

[26] D.W. Lynch and C.G. Olson, Photoemission Studies of High-Temperature Superconductors, Cambridge University Press, UK, (2005).

[27] F. de Groot and A. Kotani, Core Level Spectroscopy of Solids, CRC Press, New York, (2008).

[28] J. M. Hollas, Modern Spectroscopy, Wiley, UK, (2004).

[29] https://www.lanl.gov/orgs/nmt/nmtdo/AQarchive/04summer/XPS.html (Accessed on 08-11-2019).

[30] https://www.phi.com/surface-analysis-techniques/xps-esca.html (Accessed on 08-11-2019).

[31] S. Hofmann, Auger- and X-Ray Photoelectron Spectroscopy in Materials Science, Springer-Verlag Berlin Heidelberg (2013).

[32] J. Wolstenholme, Practical Application to Materials Analysis and Characterization of Surfaces, Interfaces and Thin Films, Momentum Press, LLC, New York, (2015).

[33] http://www.ocivm.com/_auger_electron_spectroscopy.html (Accessed on 08-11-2019).

[34] J.R. Lakowicz, Principles of Fluorescence Spectroscopy, Kluwer Academic/Plenum Publisher, New York, (1999).

[35] J.Z. Zhang, Optical Properties and Spectroscopy of nanomaterials, World Scientific, Singapore, (2009).

Chapter 4

Photoluminescence studies of a YOF phosphor synthesized by the pyrolysis method

In this chapter PL studies of Pr^{3+} doped YOF samples were investigated for SC applications. Investigations were done to show that the intense excitation peak obtained at 250 nm was due to the 4f-5d band of Pr^{3+}. These investigations were done in order to contradict previous results reported by other authors that attributed the 250 nm excitation peak to a charge transfer (CT) band of Pr^{4+}.

4.1 Introduction

The vast progress in the population and the demand for more energy with decreasing of available energy resources opened up a large field of research for a new energy source. The energy resources that are being used for the last decades are non-renewable energy such as fossil fuels, coal petroleum and natural gasses. These energy resources are of great importance to us since they can produce significant amounts of energy. One disadvantage is however that they produce carbon dioxide that has a bad impact on the planet. [1]. SC are considered to be a good resource of energy production that has faced many obstacles up until now in order to increase the energy efficiency. For a c-Si SC some of these obstacles are the loss of energy through thermalization, e-h recombination and transparency [2].

Single-junction monocrystalline and polycrystalline Si systems currently account for about 95 % of the photovoltaic market. The E_g of this kind of semiconductors is 1.1 eV and this is equal to the energy of a photon with a wavelength of about 1100 nm [2]. According to the Shockley-Queisser's model the theoretical maximum efficiency of c-Si SC, with an E_g of 1.1 eV, is about 30 % [1]. This model is based on the principle of the balance between the incident and escaping photons and extracted electrons [1].

The luminescence and spectroscopic properties of a Pr^{3+} ion is very dependent on the host. It can result in red emission from the $^1D_2$ level in Y_2O_3 [3], blue emission from the $^3P_0$ level in YF_3 [4] or green emission from the $^3P_0$ to $^3F_2$ and $^3H_4$ levels in YOF [5]. In all three cases the emission occurred via transitions to the $^3H_4$ ground state. The Pr^{3+} ion has been studied for various applications such as FED, laser devices, scintillator application and other optoelectronic devices [6]. It also has very promising potential as a DC and an UC material,

depending on the host, for SC applications [5, 7, 8]. The intrinsic properties and different emitting energy levels in the UV, VIS and IR regions make the Pr^{3+} ion a very suitable spectral converter material [9, 10].

DC or QC is a mechanism where one high energy photon is converted into two low energy photons. DC could result in energy efficiency above 100 % and it can reduce the thermalization effect [11]. The DC mechanism can occur through PCE from a single lanthanide ion or by energy transfer through different lanthanide centers [12, 13]. In the 1970's the QC effect was first observed in Pr^{3+}-doped YF_3 with a quantum efficiency of about 140 % under the excitation of 185 nm and up until now, QC had been reported in a variety of Pr^{3+}-doped fluorides and several oxides [2]. Highly efficient PCE for Pr^{3+} in the VIS region was reported in YF_3 by Piper et al. [14], Sommerdijk et al. [15] and S. Kuck et al. [16]. They have studied the luminescence of Pr^{3+} in different fluoride host crystals including YF_3, $KMgF_3$, LuF_3, $BaMgF_4$ and PrF_3. They've showed internal theoretical quantum efficiencies with excitation wavelengths below 200 nm between 1.2 and 1.6 by using the Judd-Ofelt model. In spite of the high quantum efficiency from a single Pr^{3+} ion it cannot be used as lamp phosphors because the first step of the photon cascade lies at about 400 nm and this is too far in the UV spectral region [16].

Oxyfluoride materials show promising host potential since they combine the main advantages of oxides with fluorides, such as low phonon energy and low probability of multiphonon quenching [17]. It is well known that the oxide materials are mechanically and chemically stable and that they also have high phonon energies (larger than 500 cm^{-1}. The fluoride materials however are chemically and mechanically unstable and they have lower phonon energies [18, 19]. The phonon energy of YOF is equal to 400 cm^{-1} comparing to that of YF_3 that is ~ 350 cm^{-1}. In addition, the YOF is chemically and thermally more stable than YF_3 [20]. YOF also has a wide band gap (~7.2 eV) that makes it suitable as a host lattice for optical applications [21]. YOF has a rhombohedral structure (space group: $R\bar{3}m$ (166)), where each Y^{3+} ion is surrounded by four F^- and four O^{2-} atoms with one available site of Y^{3+} that can be occupied by the dopants [5].

The luminescence of YOF doped with Pr^{3+} was investigated as it is considered to be a promising DC phosphor material for Si SC enhancement. There is no clear report on the

possible luminescent mechanisms for the YOF:Pr^{3+} phosphor and with this study the authors aimed to better understand the behavior of the Pr^{3+} ion in the YOF host.

4.2 Experimental

Pure YOF and Pr^{3+} doped YOF powder samples were prepared by the pyrolysis method with CF_3COO as precursor from a single source as described in chapter 3, section 3.1. The doped YOF: x mol % Pr^{3+} (x = 0.07, 0.1, 0.2, 0.3, 0.4 and 0.5) samples were prepared by the same method only by introducing praseodymium (III) oxide (Pr_2O_3) in the starting materials. An additional sample was also prepared by doping YOF with 1 mol % of cerium oxide (CeO_2).

The structure of the prepared samples was characterized by XRD using a Bruker Advance D8 diffractometer (40 kV, 40 mA) with Cu K_α x-rays (λ = 0.154 nm). SEM images were taken by using the JEOL JSM-7800F SEM. High-resolution XPS was obtained with a PHI 5000 Versa-probe system as was described in chapter 3, section 3.4. All measurements were performed at room temperature. PL, NIR emission and life time measurements were done by using the Edinburgh FLS980 instrument.

4.3 Results & Discussion

The crystal structure and phase formation were studied by using XRD. Figure 1(a) shows the XRD patterns of the starting precursor, $Y(CF_3COO)_3$, the standard data of YF_3 (space group Pnma (62) (ICSD No. 74-0911)), YOF (ICSD No. 71-2100) and for the precursor annealed at different temperatures. At 600 ^{0}C the precursor decomposed into crystalline orthorhombic YF_3 with small impurity peaks of orthorhombic yttrium oxyfluoride ($Y_5O_4F_7$). At 700 ^{0}C and 800 ^{0}C, these small impurity peaks developed into YOF. Finally at 900 ^{0}C a pure rhombohedral YOF structure (space group: $R\bar{3}m$ (166)) occurred without any noticeable impurities. The XRD patterns have successfully showed the formation of the YOF structure starting from $Y(CF_3COO)_3$. A further increase in the temperature will however result in small impurity peaks of cubic Y_2O_3. Figure 1(b) shows the XRD patterns of the standard YOF pattern (ICSD No. 71-2100), the different samples of YOF: x mol Pr^{3+} (x = 0, 0.07, 0.1, 0.2, 0.3, 0.4 and 0.5) and for the YOF: 1 mol % Ce^{3+} sample. There is a slight shift of the diffraction peaks of the doped samples towards the lower angles due to the difference of the ionic radii (Y^{3+} = 0.1019 nm, Pr^{3+} = 0.1126 nm and Ce^{3+} = 0.1143 nm). This confirmed that the Pr^{3+} and Ce^{3+} ions were successfully incorporated into the host lattice.

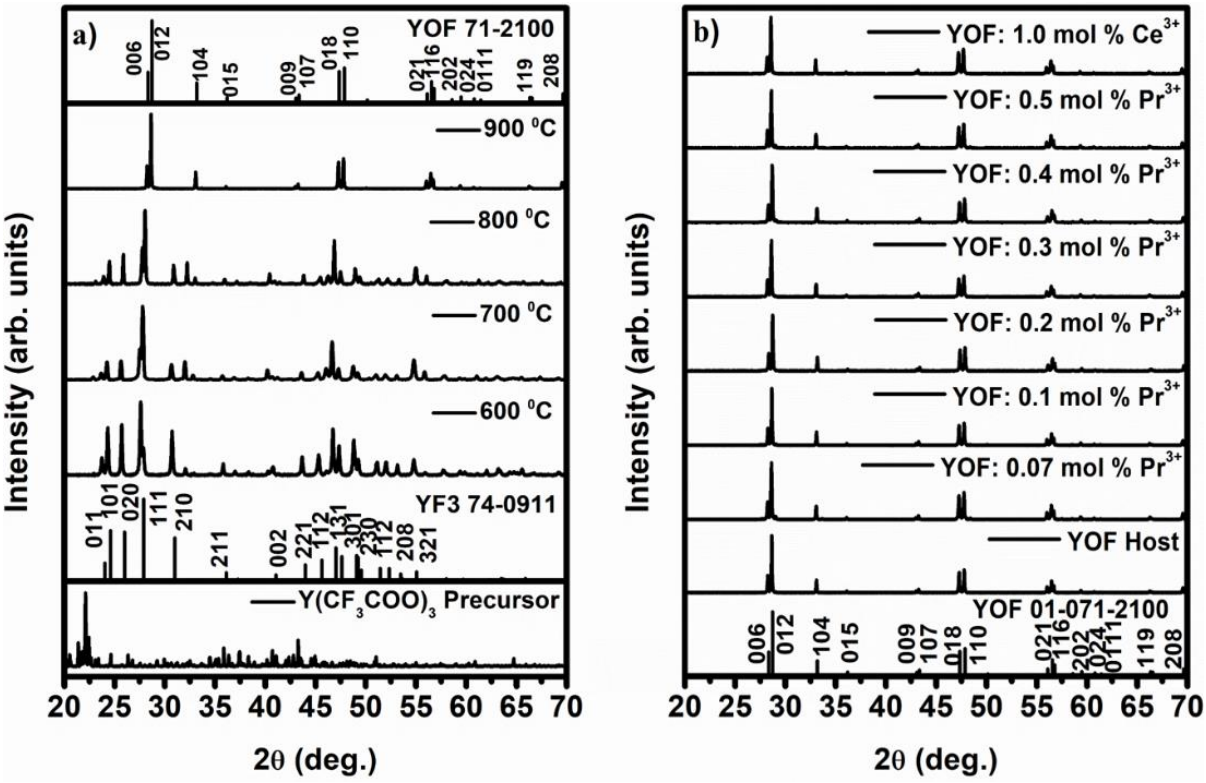

Figure 1: XRD patterns for the (a) $Y(CF_3COO)_3$ precursor annealed at different temperatures and (b) of the YOF: x mol % Pr^{3+} (x = 0, 0.07, 0.1, 0.2, 0.3, 0.4, and 0.5) and the YOF: 1.0 mol % Ce^{3+} phosphors.

The schematic illustration for the crystal structure of the YOF host is shown in figure 2. Each Y^{3+} ion is surrounded with four F^- and four O^{2-} ions that yields the 8 coordination Y^{3+} ion. The Y^{3+}, O^{2-} and F^- ions' coordination in the structure is in an arrangement of a bi-capped trigonal antiprism with 6c Wyckoff positions with the symmetry for the Y^{3+} cation as C_{3v} site symmetry. The crystal structure of YOF can be derived from the cubic calcium fluorite structure with a slight trigonal distortion [19, 22, 23].

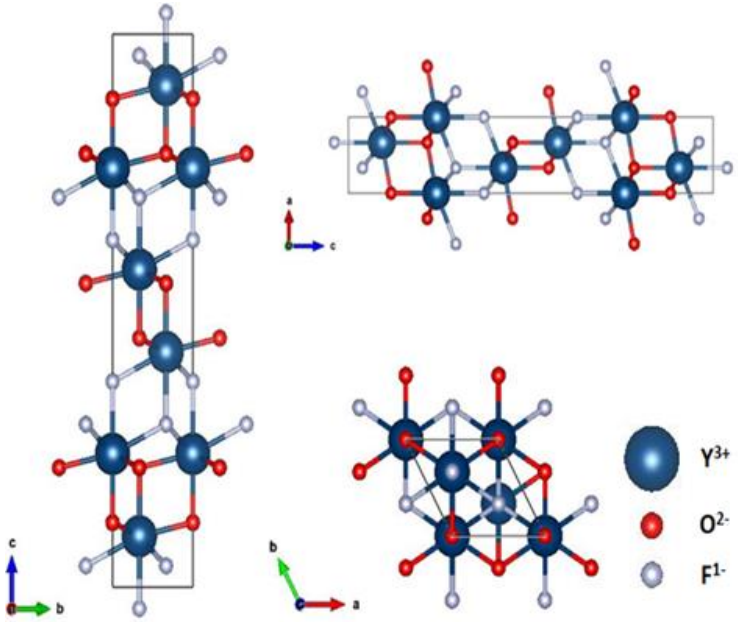

Figure 2: The schematic illustration for the crystal structure of the YOF host. Each Y^{3+} ion is surrounded with four F^{-} and four O^{2-} ions that yields the 8 coordination Y^{3+} ion. The crystal structure was drawn using Vesta software [24].

The estimation of the crystallite size of the prepared powders was done by using the Debye-Scherer equation for the broadening of the diffraction peaks [25]. The effect of broadening is a result from instrument broadening as well as the sample broadening. It is useful to identify the nature of the broadening by collecting the diffraction pattern from the line broadening of a standard material (e.g., Si) to be able to determine the instrumental broadening. The corrected β_{hkl} is corresponding to the diffraction peak of the material and can be calculated by using the relation,

$$\boldsymbol{\beta_{hkl} = \left[(\beta_{hkl})^2_{measured} - (\beta_{hkl})^2_{instrumental}\right]} \text{.....1}$$

$$\boldsymbol{\beta_{hkl} = \frac{k\lambda}{D\cos\theta}} \text{ .....2,}$$

where, β_{hkl} represents the peak broadening or FWHM corresponding to the diffraction angle θ and miller indices hkl, λ represents the wavelength of CuK_{α} of the x-ray radiation (1.54056 Å), D is the crystallite size in nanometer and k represents the shape factor for spherical shapes and is equivalent to 0.9 [26, 27].

The crystallite sizes of the prepared samples that were calculated by using the Debye-Scherer equation 2, for the diffraction peaks corresponding to the Miller indices, is given in table 1.

The variation of the crystallite sizes is depicted in figure 3. The pure host's crystallite size was 81.24 nm and it decreased with increasing doping concentration to 75.31, 73.32, 66.58, 65.22, 61.18 and 59.8 nm for the samples doped with 0.07, 0.1, 0.2, 0.3, 0.4 and 0.5 mol % of Pr^{3+} respectively. The decrease of the crystallite size with increasing doping concentrations indicated a successful incorporation of Pr^{3+} ions into the Y^{3+} sites of the host.

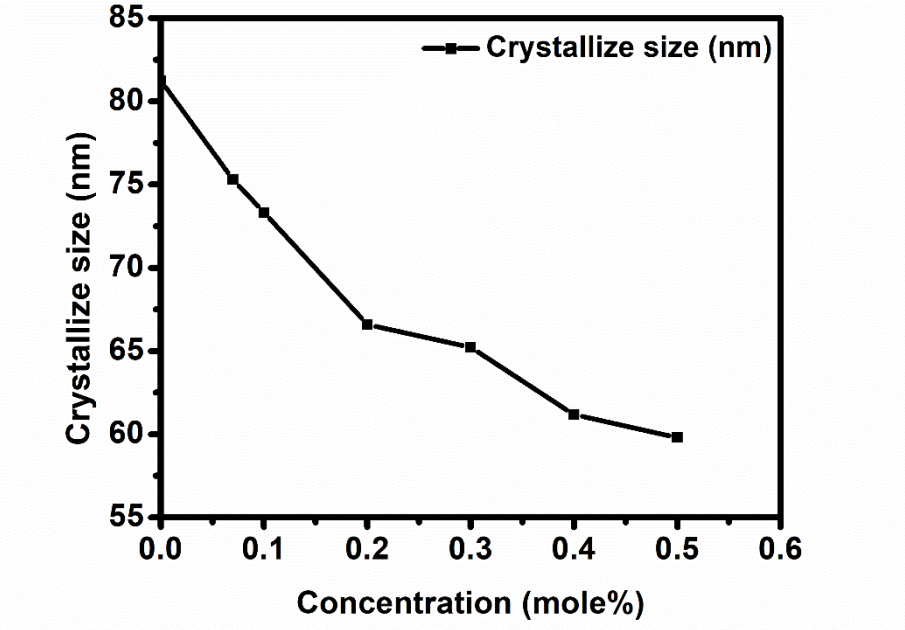

Figure 3: The variation of the crystallite size with Pr^{3+} concentrations calculated using Debye-Scherer equation of the crystallite size as a function of FWHM.

Table 1: The calculated crystallite sizes of the prepared samples by using the Debye-Scherer equation.

Sample	**Crystallite size (nm) (± 1)**
YOF: 0 mol % Pr^{3+}	81
YOF: 0.07 mol % Pr^{3+}	75
YOF: 0.1 mol % Pr^{3+}	73
YOF: 0.2 mol % Pr^{3+}	67
YOF: 0.3 mol % Pr^{3+}	65
YOF: 0.4 mol % Pr^{3+}	61
YOF: 0.5 mol % Pr^{3+}	60

The surface morphology was investigated with SEM. The precursor powder showed non-uniform morphology of big particles and flakes, see figure 4(a). During thermal decomposition at 600 ^{0}C, figure 4(b), the morphology shows an agglomeration of small particles, < 100 nm. At 700 ^{0}C these small particles started to melt and agglomerate more to form bigger particles with sizes > 100 nm, see figure 4(c). The morphology of the sample annealed at 800 ^{0}C, figure 4(d) shows an increase in particle agglomeration and melt into bigger particles with sizes > 500 nm. The sample annealed at 900 ^{0}C, figure 4(e), shows an increase in bigger melted particles having spherical and more longitudinal shapes with a width close to 500 nm and a length > 1 μm. This change in morphology was reported by Z. Li et al. [28] during investigations done on the pyrolysis method of YOF:Yb^{3+}, Er^{3+} thin films and also by H. Eloussifi et al. [29] during studies of thermal decomposition of the $Y(CF_3COO)_3$ precursor. They've reported that the big particles contain small grains that are randomly oriented. Figure 5 shows the SEM images for the doped samples of YOF:Pr^{3+}. There is no apparent change in the morphology except for a slight variation of the agglomerated particle's sizes.

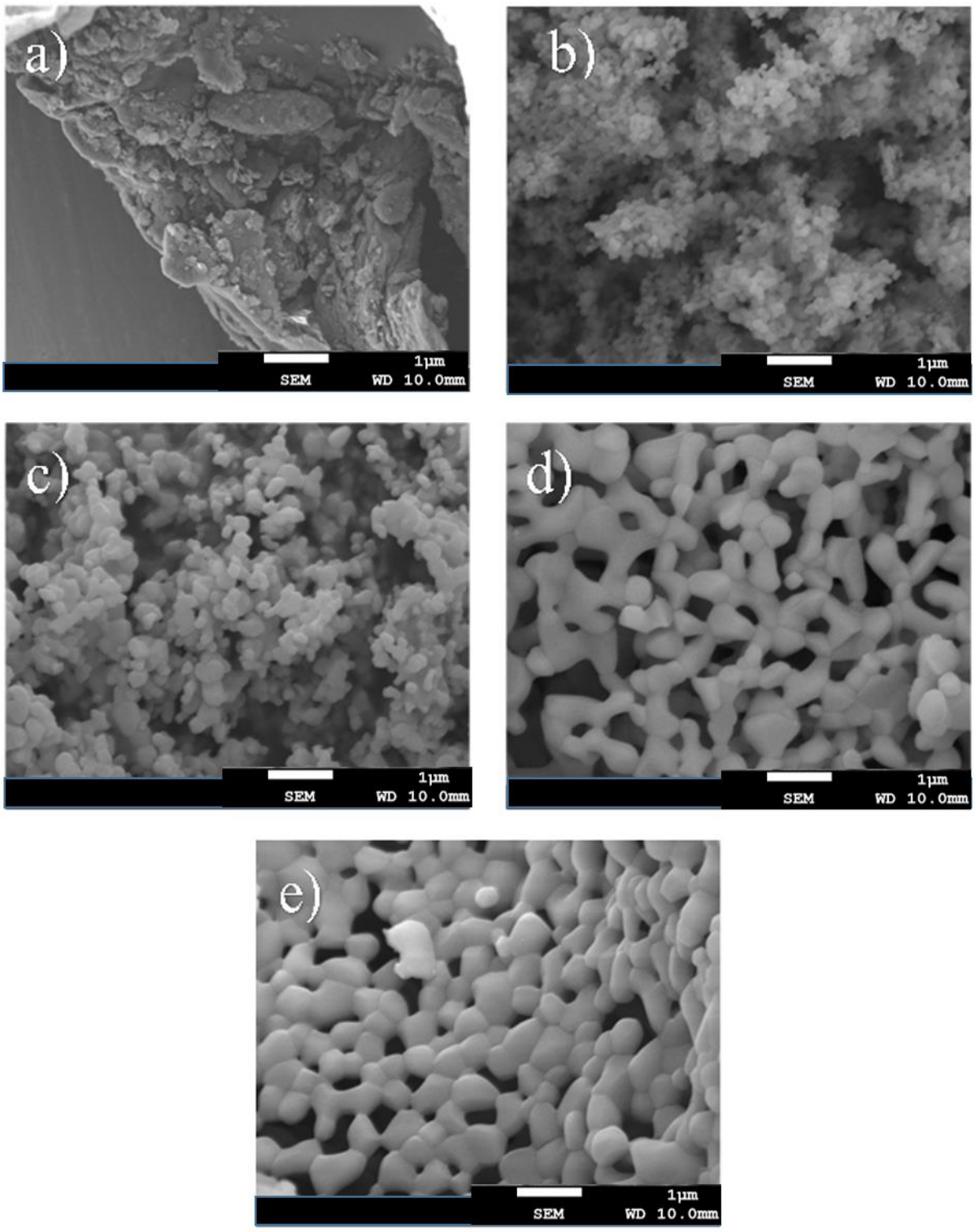

Figure 4: SEM images of the YOF host annealed at different temperature for a) the precursor powder, b) at 600 ^{0}C, c) at 700 ^{0}C, d) at 800 ^{0}C and e) at 900 ^{0}C.

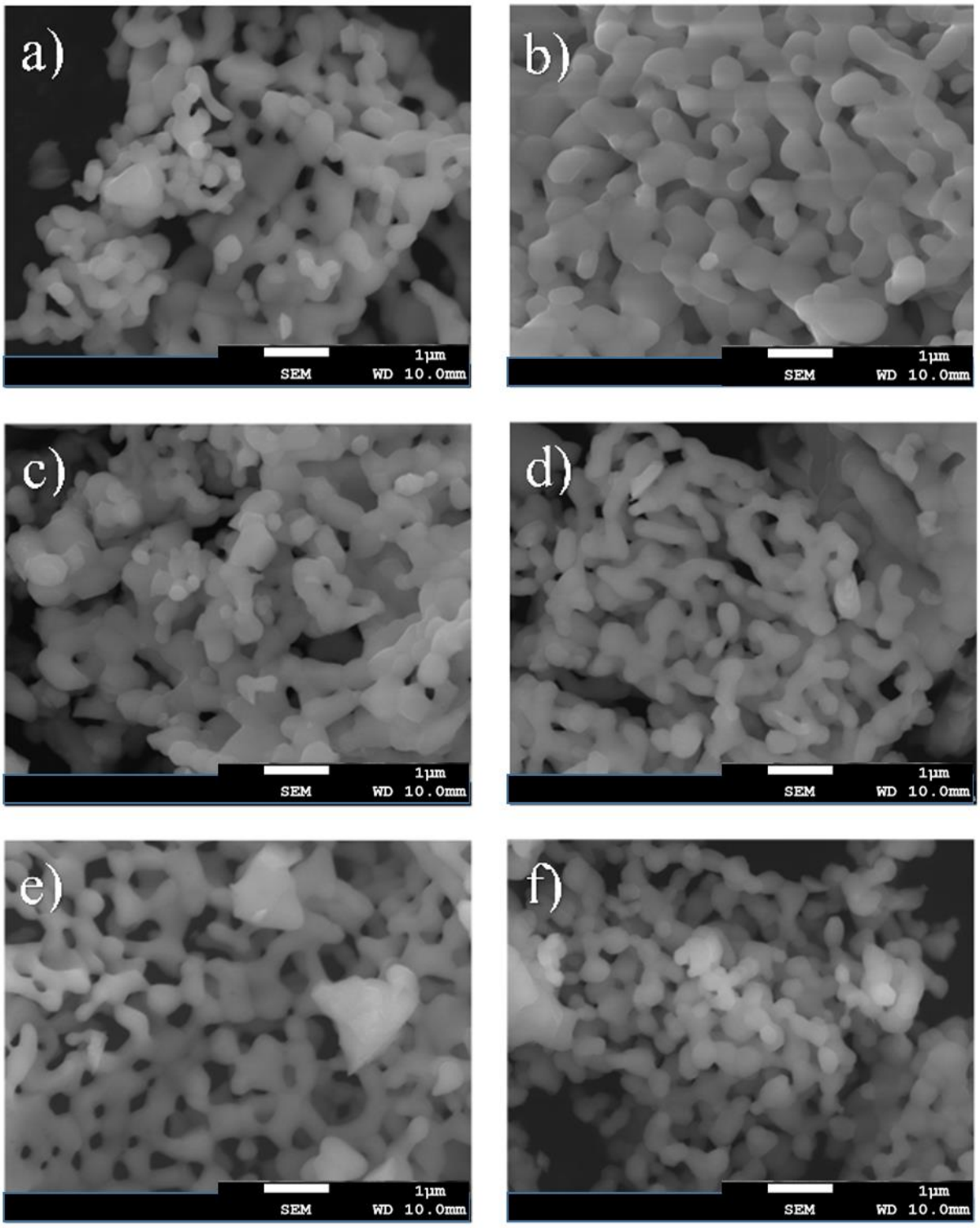

Figure 5: SEM images of YOF: Pr^{3+} for the samples doped with different concentrations of Pr^{3+} ion, a) 0.07, b) 0.1, c) 0.2, d) 0.3, e) 0.4 and f) 0.5 mol %.

XPS has been used to study the surface composition of the high concentration YOF: 0.5 mol % Pr^{3+} sample. All the XPS high-resolution peaks were corrected for charge compensation in respect to the C 1s peak at 284.8 eV. The C contamination was ascribed to adventitious

hydrocarbons on the surface [30]. Figure 6 shows the peak deconvolution of the a) Y 3d, b) O 1s, c) F 1s and d) Pr 3d peaks. The Y 3d peak, figure 6(a), can be deconvoluted into two binding energy peaks at 157.1 eV and 159.1 eV that are due to the spin orbit splitting into the $3d_{5/2}$ and $3d_{3/2}$ peaks respectively. The O 1s peak, figure 6(b), shows two peaks at 529.1 eV and 531.4 eV. The F 1s peak shows one peak at 684.9 eV (figure 6(c)) and the Pr 3d peak shows two sets of peaks for the $3d_{5/2}$ and $3d_{3/2}$ peaks due to the spin orbit splitting (figure 6(d)) at 933.4 eV and 953.8 eV and at 929 eV and 949.4 eV respectively.

The 157.1 eV peak of Y $3d_{5/2}$ correspond well with other reported values for the Y $3d_{5/2}$ peak in the YOF structure [31, 32]. The peak of O 1s at 529.1 eV correspond to the oxygen peak in the YOF structure and this was also reported by Rizhkof et al. [33]. The second peak at 531.4 eV can be ascribed to hydroxyl or carbonate groups [34]. The F 1s peak at 684.9 eV is also in correlation with reported data for the YOF structure [33]. The two sets of fitted peaks for the Pr 3d peak correspond to two different oxidation states of Pr^{3+} and Pr^{4+}. The 933.4 eV and 953.8 eV peaks correspond to the Pr $3d_{5/2}$ and Pr $3d_{3/2}$ peaks of Pr^{4+} respectively and the other pair at 929 eV and 949.4 eV correspond to the Pr $3d_{5/2}$ and Pr $3d_{3/2}$ peaks of Pr^{3+}. The separation between the spin orbit splitting peaks is 20.4 eV. The obtained values for the Pr 3d peak are in correlation with results obtained by Narula et al. [35], Matsumura et al. [36] and Sarma et al. [37]. It is also in correlation with results obtained for a $Pr_{0.60}Zr_{0.35}Y_{0.05}O_2$ system with the Pr 3d peak binding energies found at 933.9 and 953.5 eV for Pr^{4+} and at 929.5 and 949.8 eV for Pr^{3+} [38]. The presence of Pr^{4+} could have an effect on the PL results. The Pr^{4+} ions could have formed during the synthesis process or during annealing where the O^{2-} ions replaced the F^- ions to form the YOF structure. Schaefer et al. [6] and A. Guzik et al. [39] have ascribed a CT band to hybridization of the Pr ion where one electron from the Pr ion is localized and the other (delocalized) electron density is provided by the O 2p band through a Pr 4f – O 2p bond. The Pr $3d_{3/2}$ and Pr $3d_{5/2}$ split due to the final state configurations of the $4f^3L^2$ (L-hole on the O 2p valence band) level. The splitting could also arise from the coupling between the 3d hole and the outer unpaired 4f electron.

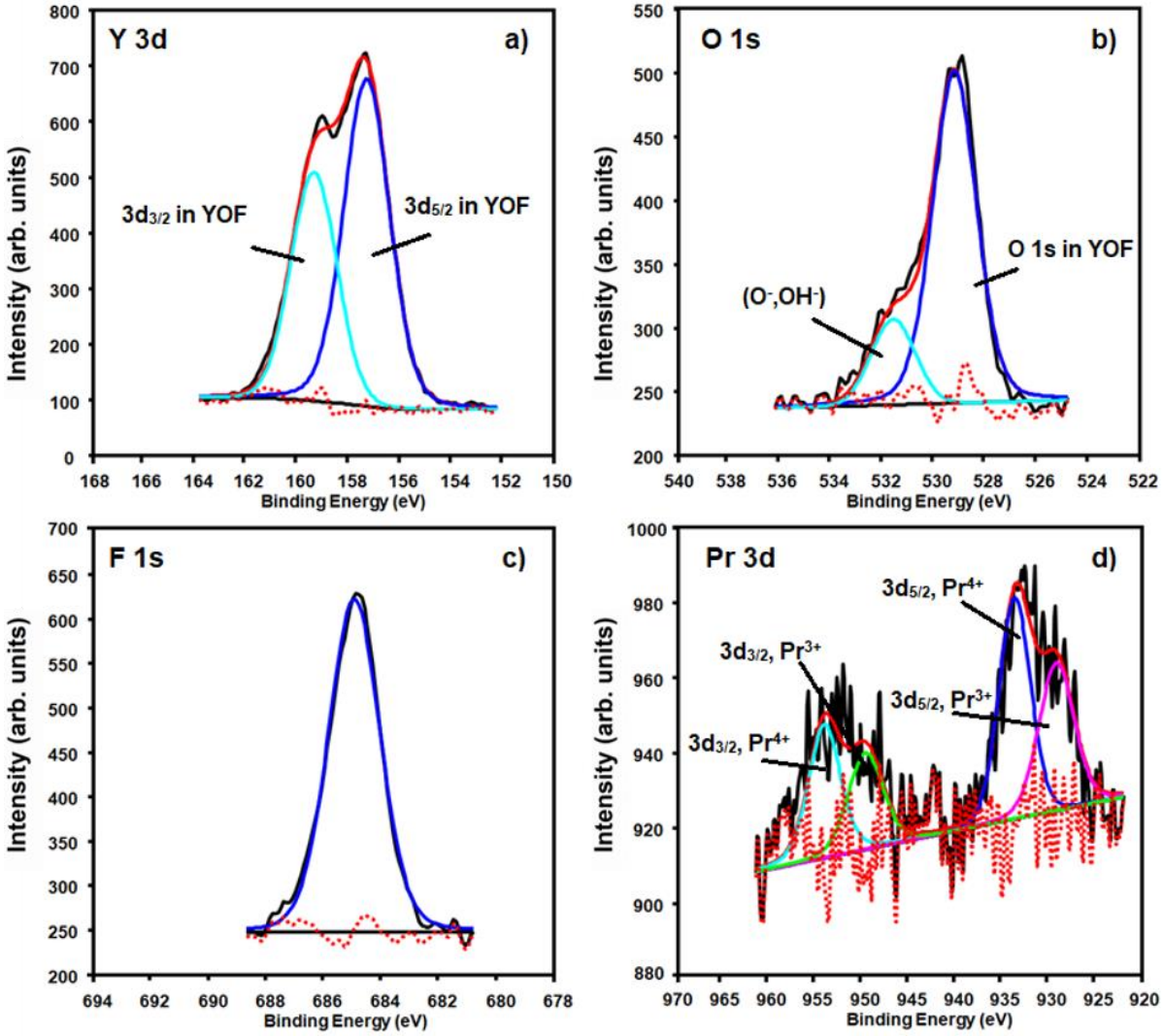

Figure 6: XPS high-resolution peak fits for the a) Y 3d, b) O 1s, c) F 1s and d) Pr 3d peaks in YOF: 0.5 mol % Pr^{3+}.

XPS measurements were also done on the prepared precursor $Y(CF_3COO)_3$ doped with 0.3 mol % of Pr^{3+}. The survey scan consisted of all the main elements of the structure without any contaminations (data not shown). All the XPS high-resolution peaks were also corrected for charge compensation in respect to the C 1s peak at 284.8 eV. The high-resolution deconvoluted peaks are shown in figure 7 for Y 3d, O 1s and F 1s. The Y 3d peak in figure 7(a) was deconvoluted into two peaks at 158.6 eV for Y $3d_{5/2}$ and 160.7 eV for Y $3d_{3/2}$. The O 1s peak was deconvoluted into five peaks at binding energies of 529 eV, 531 eV, 532.1 eV and 533.9 eV in figure 7(b). In figure 7(c) the F 1s peak was deconvoluted into three peaks with binding energy at 684.5 eV, 686.1 eV and 687.7 eV. The Pr 3d peak could not be detected due to nature of the amorphous as-prepared precursor.

The binding energies of the Y 3d peak at 158.6 eV for Y $3d_{5/2,}$ is ~1.6 eV higher than our recorded value for the YOF structure at 157 eV for Y $3d_{5/2}$, and is ~ 0.5 eV lower than the reported binding energy of YF_3 at 159.1 eV for Y $3d_{5/2}$ [40]. We can therefore estimate that our obtained binding energy for the Y 3d peak can be related to the yttrium ion in $Y(CF_3COO)_3$. Investigations on the deconvoluted F 1s peak revealed more information on the type of the species within the materials. J.H. Su et al. [32] reported on two F 1s peaks with binding energies at 687.7 eV and 684.5 eV that they've related to a $-CF_3$ group that represented a metal CF_3COO bond and a F-O bond respectively. We can therefore correlate our obtained 684.5 eV and 687.7 eV peaks to the CF_3 and F-O bonds in $Y(CF_3COO)_3$ respectively. The third fluorine component obtained at 686.1 eV can be ascribed to a C-F ionic bond according to Y.M. Shulga et al. [41]. They've explained this C-F ionic bond to the nature of the material with the existence of the carbon within it. Our sample is not strongly ionic since the true ionic bonds have binding energies of E_b (F 1s) = 684 eV – 686 eV. According to our data the C-F bond is therefore an intermediate between an ionic bond and a covalent bond. The deconvoluted O 1s peak at 529 eV might be due to the formation of O^{2-} bond on the surface [42]. Whereas, the peak at 531 eV can be ascribed to surface adsorbed oxygen species (O^-, OH^-) [43], while the peak at 532.1 eV was assigned to the oxygen peak in $Y(CF_3COO)_3$ which matched the reported value of 532.1 eV [32]. The higher binding energy peak at 533.9 eV is a representative of the oxygen peak of the heavily fluorinated material since we used CF_3COOH as a solvent. The acid de-fluorinated the $Y(CF_3COO)_3$ and formed volatile fluoro-phosgene (COF_2) during annealing [41].

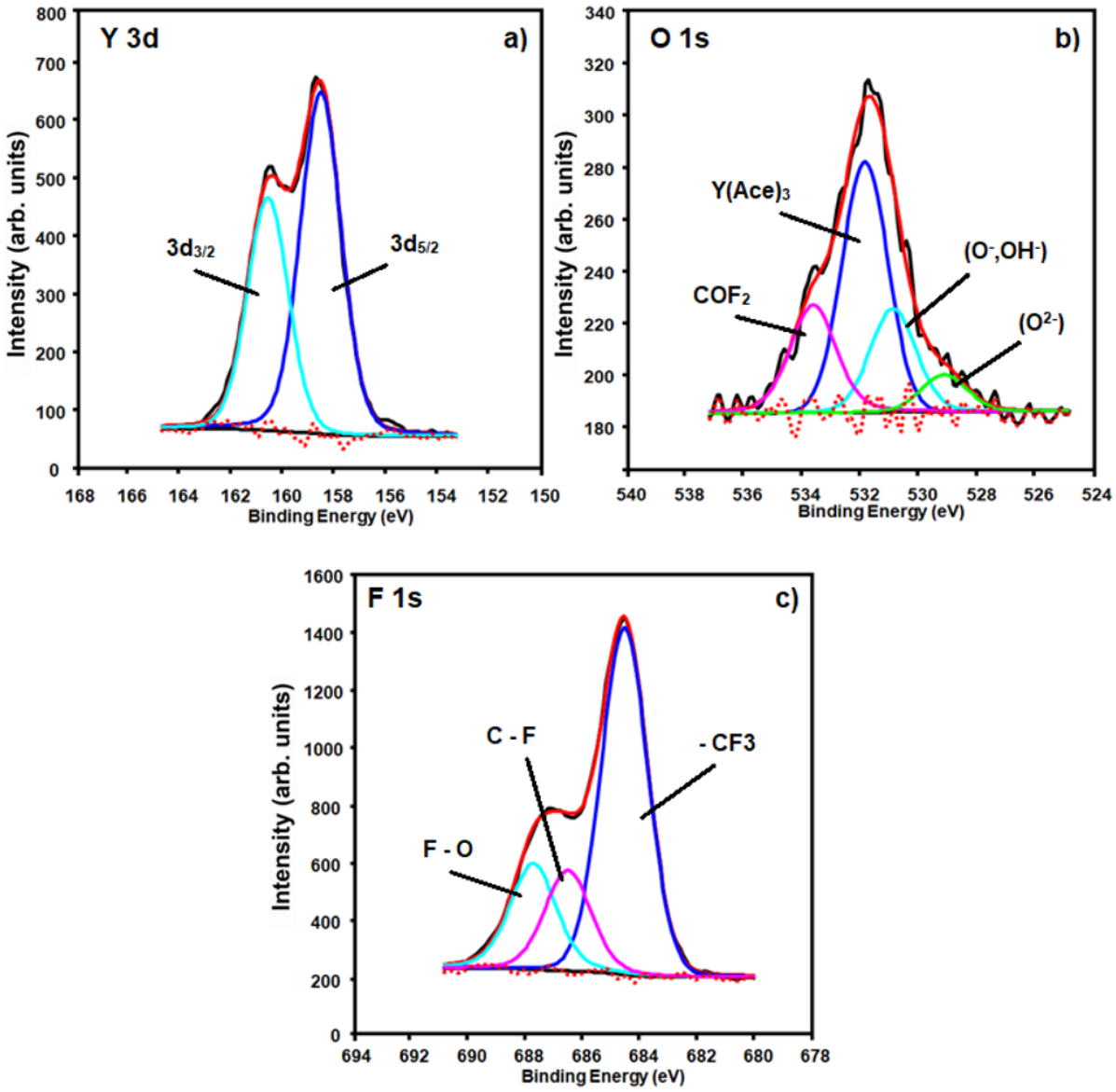

Figure 7: XPS high-resolution peak fits for the a) Y 3d, b) O 1s and c) F 1s in $Y(Ace)_3$: 0.3 mol % Pr^{3+}.

PL excitation and emission was done in order to investigate the possibility of a Pr^{4+} CT band in our system. The PL excitation spectrum was recorded for the two emissions at 498 nm and 659 nm in figure 8(a) and (c) respectively. The excitation spectrum contains two different types of transitions that correspond to a band around 250 nm and to the 4f-4f forbidden transition of the Pr^{3+} ion around 456 nm, 470 nm and 483 nm as depicted in the figures 8(b) and 8(d). The 4f-4f peaks correspond to the $^3H_4$-$^3P_2$, $^3H_4$-$^1I_6$, $^3P_1$ and $^3H_4$-$^3P_0$ transitions of the Pr^{3+} ion, respectively. From the excitation spectrum we can see that the band at 250 nm is located around 40 000 cm^{-1} which is lower than the Pr^{3+} 4f $^1S_0$ state, which is usually around 46 700 cm^{-1} in different hosts [44].

The nature of a CT band usually appears as an intense and broad peak in the absorption, excitation and reflection spectrum as a result of spin and dipole allowed transitions [45]. Fujihara et al. [5] reported on the position of the CT band for YOF:Pr^{3+} thin films synthesized by the pyrolysis method. They've reported that the CT band was located at 250 nm and that there was also an intense green emission at 498 nm. The possible explanation for the occurrence of the CT band, is the transition of an electron from a Pr^{4+} ion ligand in Pr^{4+}-O^{2-}, to the Pr^{3+} ion in Pr^{3+}-O^{1-} [44]. T. Balaji et al. [46] have done some fluorescence investigations on Ce^{3+} doped YOF in order to exclude the possibility of relating the band at 250 nm (40 000 cm^{-1}) to the 4f-5d band of Pr^{3+} in YOF. They've showed that the excitation band at 250 nm could be ascribed to the 4f-5d transition of Ce^{3+}. Dorenbos et al. [47, 48] have studied the spectral data for more than 450 hosts doped with Ce^{3+} and Pr^{3+} and concluded that we can predict the position of the 4f-5d level for any lanthanide ion doped in inorganic hosts based on the position of the 4f-5d band of Ce^{3+} when doped in the same host. He concluded that the difference between the 4f-5d levels of Pr^{3+} and of Ce^{3+} remained nearly constant (12 240 $\pm$ 750 cm^{-1}). A YOF:Ce^{3+} sample was synthesized to confirm Balaji et al.'s investigations on the existence of the 4f-5d Pr^{3+} band. The excitation and emission spectra are shown in figure 8(e). The broad excitation spectrum showed a maximum peak around 362 nm (27 624.31 cm^{-1}) and the broad emission spectrum showed two main peaks around 385 nm and 404 nm. The excitation band at 362 nm was assigned to the 4f-5d transition of Ce^{3+} and the two emission peaks to the 5d - $^2F_{5/2}$ and $^2F_{7/2}$ transitions at 385 nm and 415 nm respectively [49]. These results contradicted the values obtained by Balaji et al. The value of the Pr^{3+} 4f-5d band in YOF:Pr^{3+} can now be predicted to be around 251 nm (27 624.31 + 12 240 $\approx$ 39 864.31 $\pm$ 750 cm^{-1}); based on our excitation results for the Ce^{3+} ion (figure 8(e). The excitation band at 250 nm in our system was therefore attributed to the Pr^{3+} 4f-5d band. Previous interpretation of this 250 nm CT excitation band was therefore incorrect and a new well-founded interpretation is given. The 251 nm predicted value is below the forbidden $^1S_0$ (46 700 cm^{-1}) level. For efficient PCE to occur, the 4f-5d state should be situated above the $^1S_0$ state. [5, 14, 15, 16]. A.M. Srivastava [50] concluded that when the 4f-5d level of the Pr^{3+} ion doped in different hosts, appeared below the forbidden $^1S_0$ level, it could result to $4f^15d^1 \rightarrow 4f^2$ emission. Emission from the 4f-5d levels are not always possible. Fast non-radiative relaxation could occur to the forbidden 4f-4f transitions with narrow emission from the intra-configurational transitions.

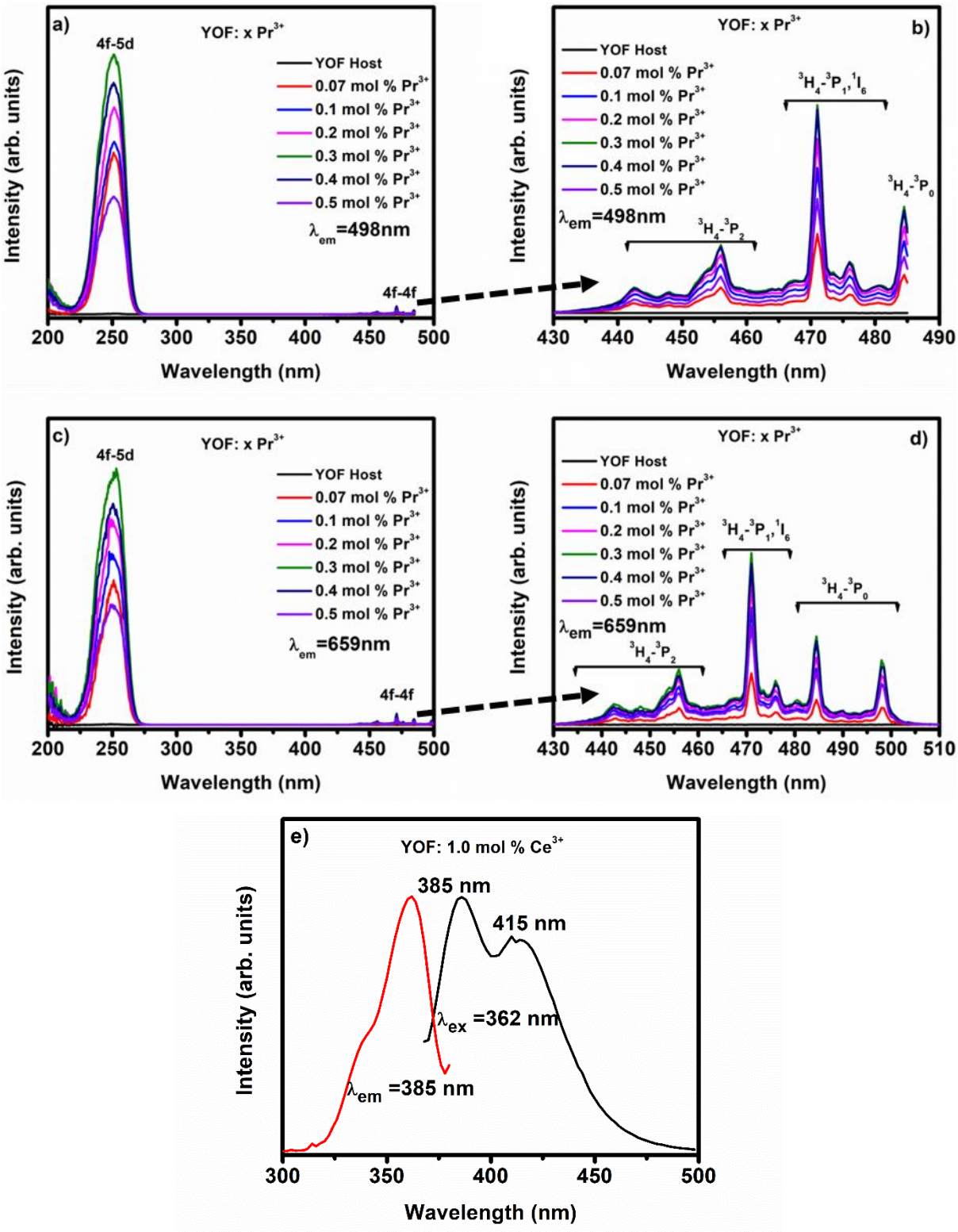

Figure 8: PL excitation of YOF: x mol % Pr^{3+} (x = 0, 0.07, 0.1, 0.2, 0.3, 0.4 and 0.5) monitored at a) 498 nm and c) 659 nm. b) and d) show the 4f-4f excitation parts and e) shows the excitation and emission of YOF: 1 mol % Ce^{3+}.

Emission of the Pr^{3+} ion in the YOF host consists of a combination of advantages from both YF_3 and Y_2O_3 hosts [17]. Figure 9(a) shows the PL emission for the YOF:Pr^{3+} phosphor doped with different concentrations, recorded in the 450 – 800 nm range upon 250 nm excitation. The emission of the samples occurred using only the excitation band at 250 nm due to the low gain emission from excitation using 4f-4f excitation. The emission spectrum originated from the $^3P_0 \rightarrow {}^3H_{4,5,6}$ and $^3P_0 \rightarrow {}^3F_{2,3,4}$ transitions and from the weaker $^1D_2 \rightarrow {}^3H_4$ and $^3P_0 \rightarrow {}^3H_6$ levels of Pr^{3+} [24]. The dominant emission around 498 nm and 659 nm therefore corresponded to the $^3P_0 \rightarrow {}^3H_4$ and $^3P_0 \rightarrow {}^3F_2$ transitions of Pr^{3+} respectively, see figure 9(c). Figure 9(b) shows the variation in intensity of the two dominating emissions ($^3P_0$-$^3H_4$ and $^3P_0$-$^3F_2$) as a function of Pr^{3+} concentration. The presence of the 4f-5d band below the $^1S_0$ level however also occurred in hosts as in Y_2O_3:Pr^{3+} [6] and $SrAlSi_4N_7$:Pr^{3+} [51] with emission also from the 4f-4f states of Pr^{3+}.

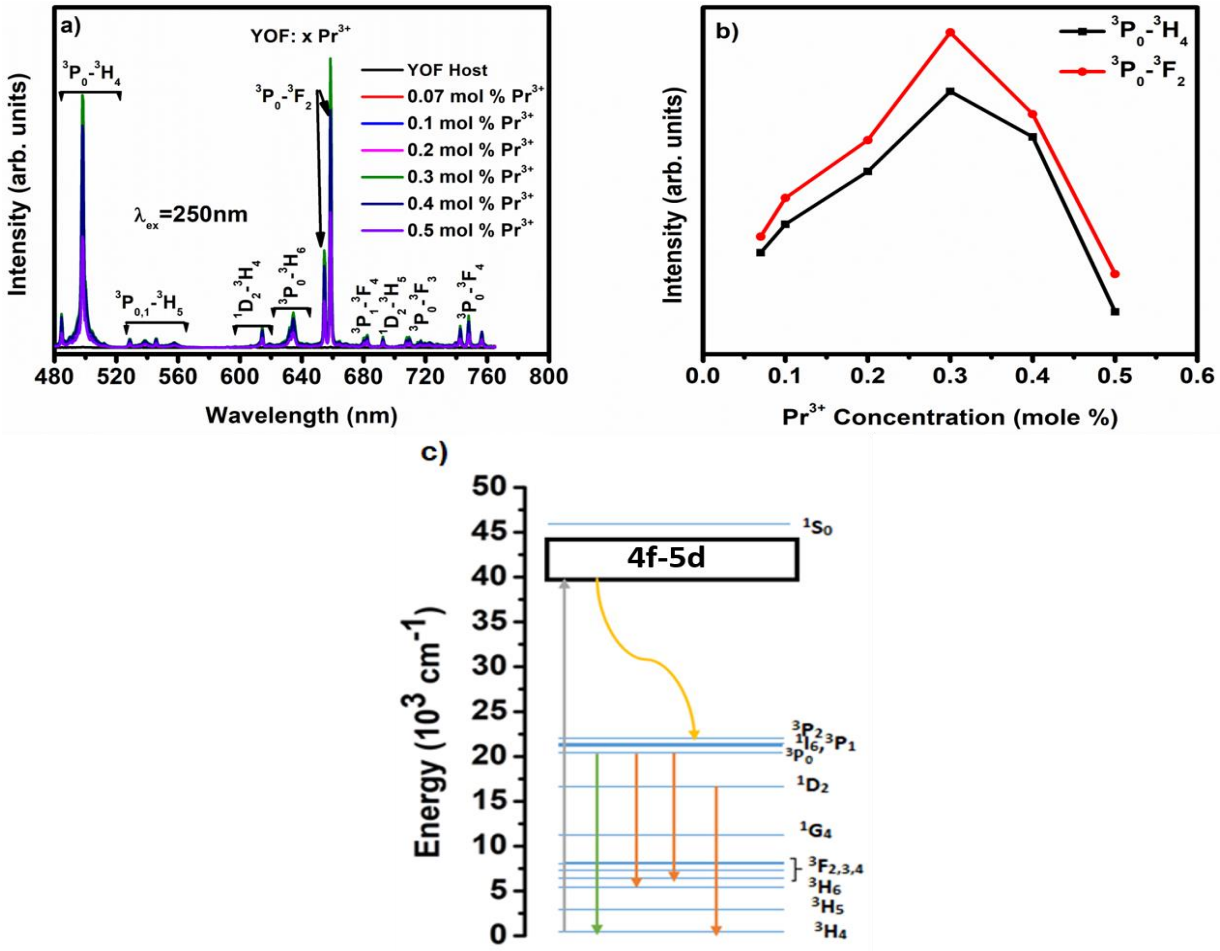

Figure 9: a) PL emission of YOF: x mol % Pr^{3+} (x = 0, 0.07, 0.1, 0.2, 0.3, 0.4 and 0.5) under 250 nm excitation, b) the variation of $^3P_0$ and $^3F_2$ emissions with Pr^{3+} concentrations and c) the schematic diagram of the possible luminescent transitions of Pr^{3+}, based on Pr^{3+} transition in YF_3 [4].

The Commission Internationale de l'Eclairage (CIE) color coordinates for the YOF: 0.3 mol % Pr^{3+} phosphor under excitation at 250 nm is shown in figure 10. The CIE coordinate was obtained using the Edinburgh FS5 fluorometer. The coordinates of the emitted phosphor are situated in the blue-green region with values for x = 0.29584 and y = 0.42989.

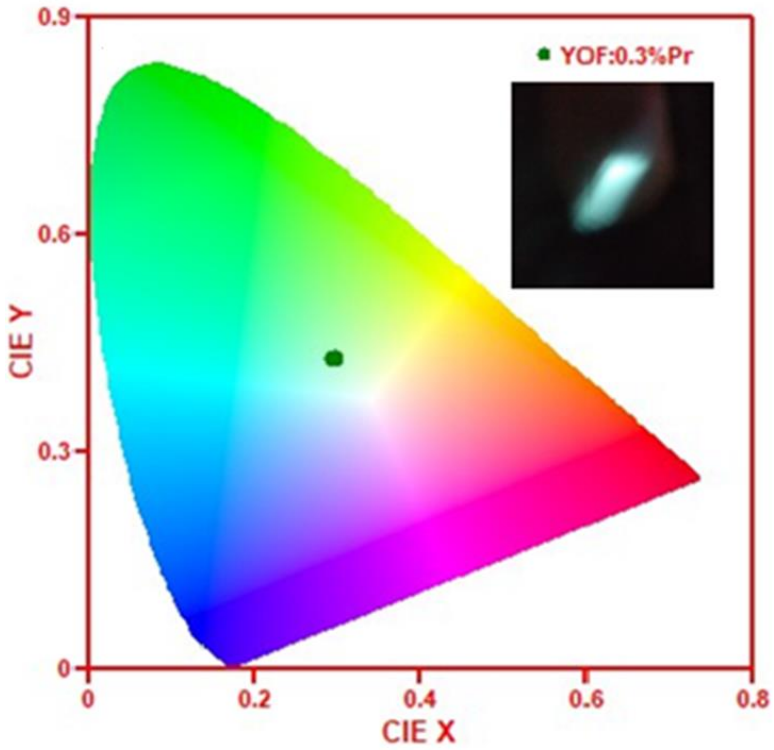

Figure 10: The plotted chromaticity coordinate for the YOF: 0.3 mol % Pr^{3+} sample (the inset shows the fluorescence emission of the sample under UV excitation (λ_{ex}=250 nm)).

The optimum intensity occurred at 0.3 mol % of Pr^{3+}, see figures 8(a) and (c). The decrease in intensity after 0.3 mol % can be ascribed to concentration quenching of the Pr^{3+} ion [52]. Concentration quenching is a well-known behavior for Pr^{3+} doped inorganic hosts [7, 53]. Concentration quenching usually occurs at low Pr^{3+} concentrations (maximum 0.4 mol %) due to the unique properties of the Pr^{3+} energy levels [54]. Concentration quenching can occur through three main mechanisms, 1) multi-phonon relaxation to the $^1D_2$ level, 2) cross-relaxation between Pr^{3+}-Pr^{3+} ion pairs and 3) energy transfer to the killer sites [55, 56]. For the multi-phonon relaxation process to occur the equivalent number of phonons required to bridge the energy gap between the $^3P_0$ and $^1D_2$ levels must be lower than 4-5 phonons, the primary emission will then act as a de-excitation mechanism [57]. It is well known that the phonon energy of YOF is about 400 cm^{-1} [22] and that the energy gap between the $^3P_0$ and $^1D_2$ levels

are approximately 3794 cm^{-1}. This implies that 9.5 phonons are required to bridge the energy gap between them. The multi-phonon relaxation process can however be neglected as the probability of the process to occur decreases when the phonon energy of the host decreases [58]. The second possibility for concentration quenching of the $^3P_0$ emission is a cross-relaxation process. This possibility suggests that there are cross-relaxation channels and that the $^1D_2$ level can be populated through the [$^3P_0$,$^3H_4$] → [$^3H_6$,$^1D_2$] levels. These levels show weak emissions at 614 nm and 692 nm and can also be found in other hosts like in $BaGd_2(MoO_4)_4$ [59] and in $KPb_2Cl_5:Pr^{3+}$ [8]. The dominating emission in these hosts are from the $^3P_0$→$^3H_4$,$^3F_2$ levels and these are the same levels as in our structure. The first cross-relaxation channel is where the electron relaxes to the lower $^3H_6$ level from the $^3P_0$ level and where a part of its energy is then transferred to the neighbor ion in the ground state $^3H_4$ to $^1D_2$ [60]. The population of the $^1D_2$ level can then yield the population of the $^1G_4$ and $^3F_{3,4}$ levels and quenching of the $^1D_2$ level therefore occurred through the cross-relaxation process with the [$^1D_2$, $^3H_4$] → [$^1G_4$, $^3F_{3,4}$] transitions [61]. We can therefore assume that concentration quenching in our system occurred through the cross relaxation process.

In order to explain the type of interaction that is responsible for concentration quenching in our system, it is necessary to calculate the critical distance between two activator ions. The critical distance is the distance that control the type of the energy transfer between two activators. According to Blasse et al. [62], concentration quenching resulted from the radiative energy transfer between two activators and can be expressed in terms of the critical concentration X_c and can be estimated using the following relation:

$$\boldsymbol{R_c = 2[\frac{3V}{4\pi X_C N}]^{\frac{1}{3}}} \text{ .....3.}$$

V is the volume of the host lattice and we assume that there is no change in the volume and that it is equal to 235.85 $Å^3$ [63]. X_c is the critical concentration and N is the number of the ions in the host that can be replaced by the dopant and it is equal to 6 [5]. For the present work the critical concentration was found to be X_c = 0 .003 and the critical distance was then calculated by using the above equation to be 29.25 Å. This value is different to the reported value of 31 Å for a $YOF:Pr^{3+}$ thin film structure [5] and this difference could be due to the nature of the powder comparing to the thin films. According to Dexter's theory, exchange interaction occur between activator ions at a distance of about 5 Å. It is therefore useful to obtain the critical distance between the activator ions since the exchange interaction is responsible for energy

transfer of forbidden interactions. Above this value the interaction is related to multipolar interaction [64]. According to our calculations of the critical distance, we can therefore conclude that the type of interaction in our YOF:Pr^{3+} structure is a multipolar interaction. The third type of concentration quenching can therefore be neglected in our system, since the critical distance is large and the transfer of energy to killer sites (one activator to another) would not occur [65].

We can now further investigate what type of multipolar interaction is responsible for the non-radiative energy transfer or concentration quenching in our system. Dexter's theory indicated that multipolar interactions were responsible for quenching of emission from the $^3P_0$ or $^1D_2$ levels [66]. The strength or the type of the multipolar interaction (Q) can be determined from the change of the emission intensity through the relation:

$$\frac{I}{C}=k(1+\beta(C)^{\frac{Q}{3}})^{-1} \quad \text{.....4.}$$

C is the activator concentration, Q = 6, 8 or 10 for dipole-dipole, dipole-quadrupole and quadrupole-quadrupole interactions, respectively, k and β are constants for the same excitation conditions for a given host material. This relation can be reduced for a high concentration beyond the critical concentration (C_C) to yield the relation below

$$\frac{I}{C}=\frac{k'}{\beta C^{\frac{Q}{3}}} \quad \text{.....5.}$$

k′ is a constant [67, 68] and C is the dopant concentration that is greater than the critical distance. Figure 11 shows the plot of log(I/C) versus log(C), the value of the slope (that is equal to -2.53566) and the estimated Q value is 7.6 which is close to 8. We can therefore predict that the quadrupole-dipole interaction is responsible for the concentration quenching. The same type of multipolar interactions between Pr^{3+} ions were also reported in other systems like in YPO_4:Pr^{3+}, where the quenching of the $^1D_2$ emission was due to the quadrupole-dipole interaction [69].

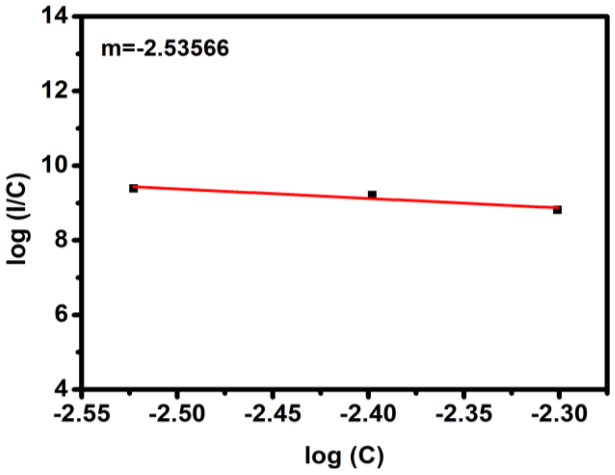

Figure 11: The plot of log(I/C) versus log(C) in the YOF:Pr^{3+} phosphor.

The prepared samples were also investigated for NIR emission. The NIR emission for the 0.3 mol % Pr^{3+} doped sample is shown in figure 12(a). The NIR emission is very low compared to the green emission (data not shown) and future investigations will be done in order to enhance the NIR emission. The emission of the sample during excitation of 250 nm shows multi narrow peaks in the range between 885 nm and 1120 nm that corresponded to the $^3P_0 \rightarrow {}^1G_4$ (most intense at 907 nm) and the $^1D_2 \rightarrow {}^3F_3$, $^3F_4$ transitions. J. Hölsa [24] theoretically investigated the emission of YOF:Pr^{3+} and attributed the narrow emission of the Pr^{3+} ion due to the crystal field splitting of the $^3P_{0\text{-}2}$, $^1I_6$, $^1D_2$, $^3F_{2\text{-}4}$ and $^3H_{4\text{-}6}$ levels into 39 sub-levels (crystal field has 58 components). It is therefore appropriate to ascribe these narrow peaks to originate from the $^3P_0$ and $^1D_2$ levels. This behavior of splitting of the NIR emission levels into narrow peaks was also investigated by E. Cavali et al. [70] for a YAG:Pr^{3+} system with an emission that originated from the $^1D_2$ level to the $^3F_{2\text{-}4}$ level. J. Cybińska et al. [71] explained the same behavior in a K_2PrCl_5 powder with a dominant emission that originated from the $^3P_0$ and $^1I_6$ levels to the $^1G_4$ level. Figure 12(b) shows the excitation of the sample monitored for the emission peak at 907 nm. The excitation spectrum contains the same broad band at 250 nm and it contains the 4f-4f transitions of the Pr^{3+} ion.

The NIR emission of YOF:Pr^{3+} is within the effective response range for Si SC and revealed a DS mechanism. DS is where a system absorbs a short wavelength photon (UV or blue) and convert it to a long wavelength photon without increasing the number of photons [72]. As a consequence, the quantum yield can therefore not be greater than 100 % [2]. YOF:Pr^{3+} is therefore an appropriate candidate to enhance the spectral response of Si SC.

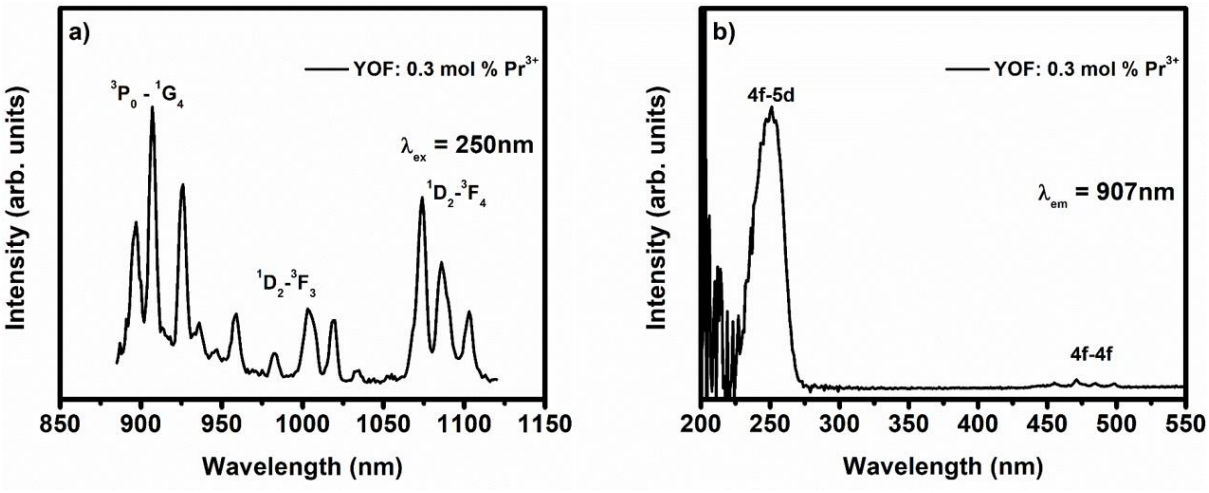

Figure 12: a) PL NIR emission of the doped sample with 0.3 mol % of Pr^{3+} under excitation of 250 nm and b) the excitation of the sample by monitoring the emission at 907 nm.

The fluorescence decay curves for the prepared YOF:Pr^{3+} samples were recorded under 250 nm excitation with a pulsed Xenon lamp. The emission of the $^3P_0 \rightarrow {}^3H_4$ transition was monitored and is shown in figure 13. The decay curves show a clear non-exponential curve behavior which is consistent with the suggested cross-relaxation process in our system. The non-exponential decay curves were fitted using a bi-exponential equation:

$$\mathbf{I(t) = A_0 + A_1 exp(-t/\tau_1) + A_2 exp(-t/\tau_2)}\ldots\ldots\ldots\ldots\ldots\ldots\ldots\ldots\mathbf{6,}$$

where I(t) is the PL intensity, $\boldsymbol{\tau_1}$ and $\boldsymbol{\tau_2}$ are emission decay times, and A_1 and A_2 are their relative weights [52]. The calculated lifetimes $\boldsymbol{\tau_1}$ and $\boldsymbol{\tau_2}$ were depicted in table 2 in order of μs. According to literature the lifetimes of Pr^{3+} doped materials are in the range of nanoseconds up to 50 μs [52]. In the present investigation the decay time is in the range of 26.9 μs to 16.7 μs for the 0.07 mol % doped concentration sample up to the 0.5 mol % doped sample. This is in good agreement with previously reported values for decay lifetimes calculated for $Gd_3Ga_5O_{12}$:Pr^{3+} [61] and $LaAlO_3$:Pr^{3+} [73].

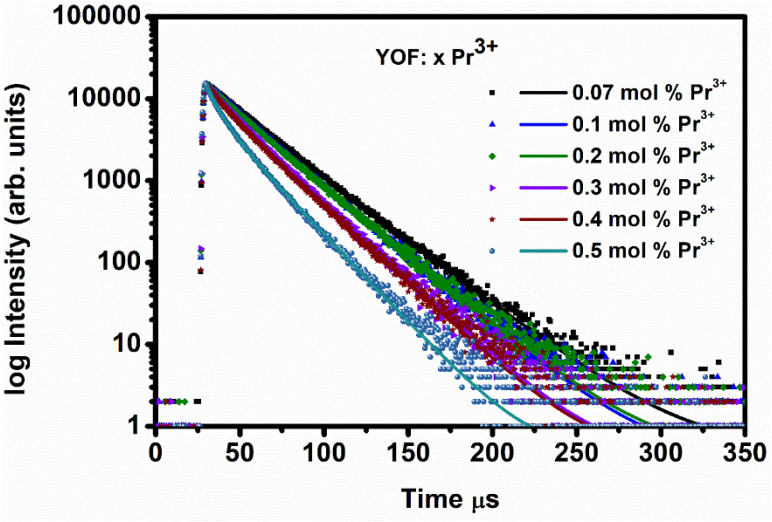

Figure 13: Emission decay curves of the $^3P_0 \rightarrow {}^3H_4$ transition for the YOF:Pr^{3+} doped samples (λ_{ex} = 250 nm, λ_{em} = 498 nm).

Table 2: The calculated lifetimes for the prepared YOF:Pr^{3+} samples.

Sample	τ_1/ μs	τ_2/ μs	τ/ μs
YOF: 0.07 mol % Pr^{3+}	23.25	30.68	26.9
YOF: 0.1 mol % Pr^{3+}	21.84	27.93	24.4
YOF: 0.2 mol % Pr^{3+}	19.12	27.25	24.6
YOF: 0.3 mol % Pr^{3+}	12.38	23.27	21.5
YOF: 0.4 mol % Pr^{3+}	10.45	23.10	20.8
YOF: 0.5 mol % Pr^{3+}	6.74	20.16	16.7

4.4 Conclusion

The YOF:Pr^{3+} phosphor was successfully synthesized using the pyrolysis method with trifluoroactate as precursor. XRD results showed a high crystallinity of the powder as rhombohedral YOF (space group: $R\bar{3}m$ (166)) after annealing at 900 ^{0}C. XPS investigations showed two sets of fitted peaks for the Pr 3d peak that correspond to two different oxidation states for Pr 3d, Pr^{3+} and Pr^{4+}. PL results showed 4f-4f emission of Pr^{3+} under excitation of a broad band around 250 nm. The 4f-4f emission confirmed that Pr^{3+} ions were successfully incorporated into the Y^{3+} ions' positions of the YOF host lattice. The nature of the broad excitation band at 250 nm was ascribed to the 4f-5d transition of Pr^{3+} based on PL excitation and emission results obtained from a YOF:Ce^{3+} sample. The YOF:Ce^{3+} sample was specifically

synthesized to confirm the existence of the Pr^{3+} 4f-5d level in order to contradict previous investigations that attributed the 250 nm excitation band to a Pr^{4+} CT band. The optimum Pr^{3+} concentration for PL emission was recorded for the sample doped with 0.3 % of Pr^{3+} as concentration quenching occurred at higher concentrations through cross relaxation processes. The low intensity NIR emission of YOF:Pr^{3+} is within the effective response range for Si SC and revealed a DS mechanism. YOF:Pr^{3+} is therefore an appropriate candidate to enhance the spectral response of Si SC. The decay life times revealed the order of the life times in the range of μs which is consistent with other reported values of Pr^{3+} doped materials. The current investigations done on the YOF:Pr^{3+} phosphor material revealed a promising material for optoelectronic applications such as for UV-LED, SC and scintillators [5, 6, 7, 8, 9].

References

[1] H. Lian, Z. Hou, M. Shang, D. Geng, Y. Zhang and J. Lin, Energy, 57 (2013) 270 - 283.

[2] Q.Y. Zhang and X.Y. Huang, Prog. Mater. Sci. 55 (2010) 353 - 427.

[3] D. Jia, X. Wang and W.M. Yen, Phys. Solid State, 50(9) (2008) 1674 - 1676.

[4] F. Pelle, M. Dhaouadi, L. Michely, P. Aschehoug, A. Toncelli, S. Veronesi and M. Tonelli, Chem. Chem. Phys. 13 (2011) 17453 - 17460.

[5] S. Fujihara, S. Koji, Y. Kadota and T. Kimura, J. Am. Ceram. Soc. 87 (2004) 1659 - 1662.

[6] A. Schaefer, S. Gevers, V. Zielasek, T. Schroeder,3 J. Falta, J. Wollschläger and M. Bäumer, the J. Chem. Phys. 134 (2011) 054701 - 054708.

[7] Y. Ji, J. Cao, Z. Zhu, J. Li, Y. Wang and C. Tu, Mater. Express, 1 (2011) 3.

[8] R. Balda, M. Voda, M. Al-Saleh and J. Fernandez, J. Lumin. 97 (2002) 190 -197.

[9] B. Zhou, L. Tao, Y. H. Tsang, W. Jin, and E. Yue-Bun Pun, Opt. Express, 20(4) (2012) 3803 - 3813.

[10] T. Passuello, F. Piccinelli, M. Trevisani, M. Giarola, G. Mariotto, L. Marciniak, D. Hreniak, M. Guzik, M. Fasoli, A. Vedda, V. Jary, M. Nikl, V. Causin, M. Bettinelli and A. Speghini, J. Mater. Chem. 22 (2012) 10639 - 10649.

[11] X. Huang, S. Han, W. Huang and X. Liu, Chem. Soc. Rev. 42 (2013) 173 - 201.

[12] A.M. Srivastava and S.J. Duclos, Chem. Phys. Lett. 275 (1997) 453 - 456.

[13] R.T. Wegh, E.V.D. van Loef and A. Meijerink, J. Lumin. 90 (2000) 111 - 122.

[14] W.W. Piper, J.A. DeLuca, and F. S. Ham, J. Lumin. 8 (1974) 344 - 348.

[15] J.L. Sommerdijk, A. Bril and A.W. de Jager, J. Lumin. 8 (1974) 341 - 343.

[16] S. Kuck, I. Sokolska, M. Henke, M. Doring and T. Scheffler, J. Lumin. 102–103 (2003) 176-181.

[17] E. Martinez-Castro, J. Garcia-Sevillano, F. Cusso and M. Ocana, J. Alloy Compd. 619 (2015) 44 - 51.

[18] R. Li, L. Li, W. Zi, J. Zhang, L. Liu, L. Zou and S. Gan, New J. Chem. 39 (2015) 115 - 121.

[19] Y. Zhang, D. Geng, X. Kang, M. Shang, Y. Wu, X. Li, H. Lian, Z. Cheng and J. Lin, Inorg. Chem. 52 (2013) 12986 - 12994.

[20] G. Chai, G. Dong, J. Qiu, Q. Zhang and Z. Yang, Sci. Rep. 3 (2013) 1 - 10.

[21] G. Shwetha, V. Kanchana and M.C. Valsakumar, J. Appl. Phys. 116 (2014) 1 - 9.

[22] Y. Zhang, X. Li, D. Geng, M. Shang, H. Lian, Z. Cheng and J. Lin, Cryst. Eng. Comm. 16 (2014) 2196 - 2204.

[23] J. Hölsä, E. Kestilä, P. Ylha, E. Antic-Fidancev, M. Lemaitre-Blaise, P. Porcher, P. Deren and W. Strek, J. App. Spect. 62 (1995) 697 - 705.

[24] K. Momma and F. Izumi, J. Appl. Crystallogr. 44 (2011) 1272 - 1276.

[25] V.D. Mote, J.S. Dargad and B.N. Dole, J. Nanosci. Nanotechnol. 1 (2013) 116 - 122.

[26] Y.T. Prabhu, K.V. Rao, V.S.S. Kumar and B.S. Kumari, World Journal of Nano Science and Engineering, 4 (2014) 21 - 28.

[27] T. Many K. Thandavan, S. Meriam Abdul Gani, C. San Wong and R. Md Nor, J Nondestruct. Eval. 34 (2015) 1 - 14.

[28] Z. Li, L. Zheng, L. Zhang and L. Xiong, J. Lumin. 126 (2007) 481 - 486.

[29] H. Eloussifi, J. Farjas, P. Roura, J. Camps, M. Dammak, S. Ricart, T. Puig and X. Obradors, J. Therm. Anal. Calorim. 108 (2012) 589 - 596.

[30] R.E. Kroon, H.C. Swart, O.M. Ntwaeaborwa and H.A.A. Seed Ahmed, Physica B, 439 (2014) 83 - 87.

[31] L. Sun, J. Pan, X. Zhang, H. Wang, L. Li and Y. Yu, RSC Adv. 5 (2015) 77673 - 77681.

[32] J.H. Su, P.P. Joshi, V. Chintamaneni and S. M. Mukhopadhyay, Appl. Surf. Sci. 253 (2007) 4652 - 4658.

[33] M. Rizhkov, V.A. Gubanov and M.P. Bytzman, J. Electron Spectrosc. Relat. Phenom. 18 (1980) 227 - 233.

[34] J.F. Moulder, W.F. Stickle, P.W. Sobol and K.D. Bomben, Handbook of X-ray Photoelectron Spectroscopy (Perkin-Elmer, Eden Prairie, MN, 1992).

[35] C.K. Narula, L.P. Haack, W. Chun, H.W. Jen and G.W. Graham, J. Phys. Chem. B, 103 (1999) 3634 - 3639.

[36] Y. Matsumura, S. Sugiyama and J.B. Moffat, in: S.T. Oyama and J.W. Hightower (Eds.), Catalytic Selective Oxidation, ACS Symposium Series, ACS, Washington, 1993, p. 326.

[37] D.D. Sarma and C.N.R. Rao, J. Electron Spectrosc. Relat. Phenom. 20 (1980) 25 - 45.

[38] H. He, H.X. Dai, K.W. Wong and C.T. Au, Appl. Catal. A-Gen. 251 (2003) 61 - 74.

[39] A. Guzik, E. Talik, A. Pajaczkowska, S. Turczynski and J. Kusz, Mater. Sci.-Poland, 32(4) (2014) 633 - 640.

[40] L. Pei, Z. Jiaqi, Z. Yuankun and H. Jiecai, Nucl. Instrum. Methods Phys. Res. B, 307 (2013) 429 - 433.

[41] Y.M. Shulga, T.C. Tien, C.C. Huang, S.C. Lo, V.E. Muradyan, N.V. Polyakova, Y.C. Ling, R.O. Loutfy and A.P. Moravsky, J. Electron Spectrosc. Relat. Phenom. 160 (2007) 22 - 28.

[42] S. Blomberg, M.J. Hoffmann, J. Gustafson, N. M. Martin, V. R. Fernandes, A. Borg, Z. Liu, R. Chang, S. Matera, K. Reuter and E. Lundgren, Phys. Rev. Lett. 110 (2013) 117601 – 117606.

[43] X. Zhang, S. Cheng, W. Zhang, C. Zhang, N. E. Drewett, X. Wang, D. Wang, S. J. Yoo, J-G. Kim and W. Zheng, Ind. Eng. Chem. Res. 56 (2017) 11042 - 11048.

[44] W. Wen, X. Ya-wen and Y. Jiang-nong, J. Chem. Pharm. Res. 6(11) (2014) 590 - 594.

[45] P. Dorenbos, J. Phys.: Condens. Matter, 15 (2003) 8417 - 8434.

[46] T. Balaji and S. Buddhudu, Mater. Chem. Phys. 34 (1993) 310 - 312.

[47] P. Dorenbos, J. Lumin. 91 (2000) 155 - 176.

[48] P. Dorenbos, Phys. Rev. B, 62 (2000) 15640 - 15649.

[49] S. Shen, Z. Xu, Q. Ma, J. Xia, Y. Shi, J. Xu and F. Ai, Appl. Mech. Mater. 84-85 (2011) 631 - 634.

[50] A. M. Srivastava, J. Lumin. 169 (2015) 445 - 449.

[51] Z.J. Zhang, O.M.t. Kate, A. Delsing, P. Dorenbos, J.T. Zhao and H.T. Hintzen, J. Mater. Chem. C, 2 (2014) 7952 - 7959.

[52] J.P. Zuniga, S.K. Gupta, M. Pokhrel and Y. Mao, New J. Chem. 42 (2018) 9381 - 9392.

[53] G. Zhang, C. Liu, J. Wang, X. Kuang and Q. Su, J. Mater. Chem. 22 (2012) 2226 - 2232.

[54] M.Y.A. Yagoub, H.C. Swart, P. Bergman and E. Coetsee, AIP Adv. 6 (2016) 025204 - 025213.

[55] Q.J. Chen, W.J. Zhang, X.Y. Huang, G.P. Dong, M.Y. Peng and Q.Y. Zhang, J. Alloys Compd. 513 (2012) 139 - 144.

[56] J. Collins, M. Geen, M. Bettinelli and D. Bartolo, J. Lumin. B, 132 **(**2012) 2626 - 2633.

[57] H.R. Shih, L.G. Teoh, H.Z. Lin, Y.J. Chen and Y.S. Chang, J. Electronic Mater. 43(4) (2014) 1091 - 1096.

[58] M.Y.A. Yagoub, H.C. Swart and E. Coetsee, Opt. Mater. 42 (2015) 204 - 209.

[59] Y. Guan, T. Tsuboi, Y. Huang and W. Huang, Dalton Trans. 43 (2014) 3698 - 3703.

[60] V. Naresh and B.S. Ham, J. Alloys Compd. 664 (2016) 321 - 330.

[61] R. Naccache, F. Vetrone, A. Speghini, M. Bettinelli and J. A. Capobianco, J. Phys. Chem. C, 112 (2008) 7750 - 7756.

[62] G. Blasse, Philips Res. Rep. 24 (2) (1969) 131 - 144.

[63] T. Petzel, V. Marx and B. Hormann, J. Alloys Compd. 200 (1993) 27 - 31.

[64] K.H. Lee, S.H. Park, H.S. Yoon, Y.I. Kim, H.G. Jang and W.B. Im, Opt. Express, 20(6) (2012) 6248 - 6257.

[65] G. Blasse, Philips Res. Repts. 23 (1968) 344 - 361.

[66] D.L. Dexter, J. Chem. Phys. 21 (1953) 836 - 850.

[67] L.G. Van Uitert, J. Electrochem. Soc. 114 (1967) 1048 - 1053.

[68] L. Ozawa, Cathodoluminescence: Theory and Applications, (VCH, 1990).

[69] H. Chen, R. Lian, M. Yin, L. Lou, W. Zhang, S. Xia and J. C. Krupa, J. Phys.: Condens. Matter. 13 (2001) 1151 - 1158.

[70] E. Cavalli, L. Esposito, M. Bettinelli, A. Speghini, K.V. Ivanovskikh, R.B. Hughes-Currie and M. de Jong, Mater. Res. Express, 1 (2014) 045903.

[71] J. Cybinska, J. Legendziewicz, G. Boulon, A. Bensalah and G. Meyer, Opt. Mater. 28 (2006) 41 - 52.

[72] R.T. Wegh, H. Donker, K.D. Oskam and A. Meijerink, Science, 283 (1999) 663 - 666.

[73] M. Malinowski, M. Kaczkan, S. Turczyński and D. Pawlak, Opt. Mater. 33 (2011) 1004 - 1007.

Chapter 5

Down-conversion of YOF: Pr^{3+},Yb^{3+} phosphor

This chapter reports on the DC investigations of the YOF:Pr^{3+}-Yb^{3+} co-doped phosphor for SC enhancement as well as the energy transfer mechanism. A new excitation band at 225 nm was ascribed to a CT band of Yb^{3+} that existed due to the transfer of electrons from the O^{2-} $3p^6$ level to the $4f^{13}$ level of Yb^{3+}.

5.1 Introduction

In recent years, the field of SC enhancement drew a lot of attention due to the limited efficiency produced by SC. Low energy photons that are not absorbed by the SC inhibits the generation of e-h pairs and this is known as sub-band gap transparency [1]. On the other side, the absorbed photons with energies much higher than the E_g of the SC result in supra-band gap photons that loses their energy through heat and this is known as thermalization loss [1]. The majority of the loss in solar energy is therefore due to the thermalization process. This can be reduced by using a suitable luminescent converter to convert the absorbed high energy photons, like UV or blue, into two lower energy photons and this is called QC or DC.

The DC process can occur through a PCE process with energy transfer between a pair of lanthanide ions [2, 3]. The first evidence of the QC effect was observed in Pr^{3+} doped YF_3 with a QE of about 140 % under the excitation of 185 nm. QC has since been reported in a variety of Pr^{3+} doped fluorides and several oxides [3]. Highly efficient PCE for Pr^{3+} in the VIS region was reported in YF_3 by Piper et al. [4], Sommerdijk et al. [5] and S. Kuck et al. [6]. They have studied the luminescence of Pr^{3+} in different fluoride hosts including YF_3, $KMgF_3$, LuF_3, $BaMgF_4$ and PrF_3. They've showed internal theoretical quantum efficiency with excitation wavelengths below 200 nm between 1.2 and 1.6 by using the Judd-Ofelt model. In spite of the high quantum efficiencies from a single Pr^{3+} ion it cannot be used as lamp phosphors because the first step of the photon cascade lies at about 400 nm and this is too far in the UV spectral region [6].

A combination of Ln^{3+} ion pairs have been investigated in the form of RE – Yb^{3+} (RE = Pr^{3+}, Tb^{3+}, Tm^{3+}) that showed a QC process with a high efficiency [7, 8]. Since Yb^{3+} ions have a single $^2F_{7/2}$ excited state around 10 000 cm^{-1}, the emission of Yb^{3+} can efficiently

be absorbed by c-Si SC [1]. Absorption of the excitation energy by the sensitizer ions yields emission of two Yb^{3+} activator ions [3]. This process implies that the excited level of the sensitizer must be twice the energy of the Yb^{3+} ions and that there must be an intermediate level with the same energy as for the Yb^{3+} ions. Applying Pr^{3+} ions as sensitizer ions will allow for the transfer of the excitation energy to the activator ions [3]. Pr^{3+} ions have been considered good co-doping ions due to the suitability of the energy levels to the Yb^{3+} ions. The $^3P_0$ level of the Pr^{3+} ions are situated around 20 000 cm^{-1} and the $^1G_4$ level around 10 000 cm^{-1} [1]. After excitation the Pr^{3+} ion can transfer its energy from the $^1G_4 \rightarrow {}^3H_4$ level to the $^2F_{7/2} \rightarrow {}^2F_{5/2}$ Yb^{3+} level. Excitation to the Pr^{3+} ions and population of the ^3P_J manifolds, result in emission of two NIR photons through two Yb^{3+} ions.

This research study is an extension of our previous work done on the luminescence of Pr^{3+} ions in the YOF host. Investigation is therefore done on the suitability of the energy levels between Pr^{3+} and Yb^{3+} ions for possible DC.

5.2 Experimental

Pure YOF and Pr^{3+} doped YOF powder samples were prepared by the pyrolysis method with CF_3COO as precursor from a single source as described in chapter 3, section 3.1. The doped YOF: 0.3 mol % Pr^{3+}, x mol % Yb^{3+} (x = 1, 1.5, 2, 2.5, 3, 4, 5 and 6) samples were prepared by the same method with only introducing ytterbium (III) oxide (Yb_2O_3) in the starting materials.

The structure of the prepared samples was characterized by XRD using a Bruker Advance D8 diffractometer (40 kV, 40 mA) with Cu K_α x-rays (λ = 0.154 nm). SEM images were taken by using the JEOL JSM-7800F SEM. High resolution XPS was obtained with a PHI 5000 Versa-probe system as was described in chapter 3, section 3.4. All measurements were performed at room temperature. PL, NIR emission and decay time measurements were done using the Edinburgh FLS980 instrument.

5.3 Results & Discussion

Figure 1 shows the XRD results of the high concentration YOF: 0.3 mol % Pr^{3+}, 6 mol % Yb^{3+} co-doped sample compared to the YOF: 0.3 mol % Pr^{3+} single doped and the pure host samples. All the patterns showed a pure rhombohedral YOF structure (space group: $R\bar{3}m$ (166)), without

any noticeable impurities, after annealing at around 900 ^{0}C in air atmosphere [9]. The sample doped with 0.3 mol % of Pr^{3+} ions showed a shift in the diffraction peaks towards the lower angles due to the difference in the ionic radii of the Y^{3+} (0.1019 nm) and Pr^{3+} (0.1126 nm) ions as reported in our previous work on YOF:Pr^{3+} [9]. This shift might be a caveat since we have not used a crystal standard during the measurements. Co-doping with Yb^{3+} resulted in a further shifting of the diffraction peaks towards the lower angles, Yb^{3+} (0.114 nm). We have to mention there were no additional peaks even after 6 mol % of Yb^{3+} doping.

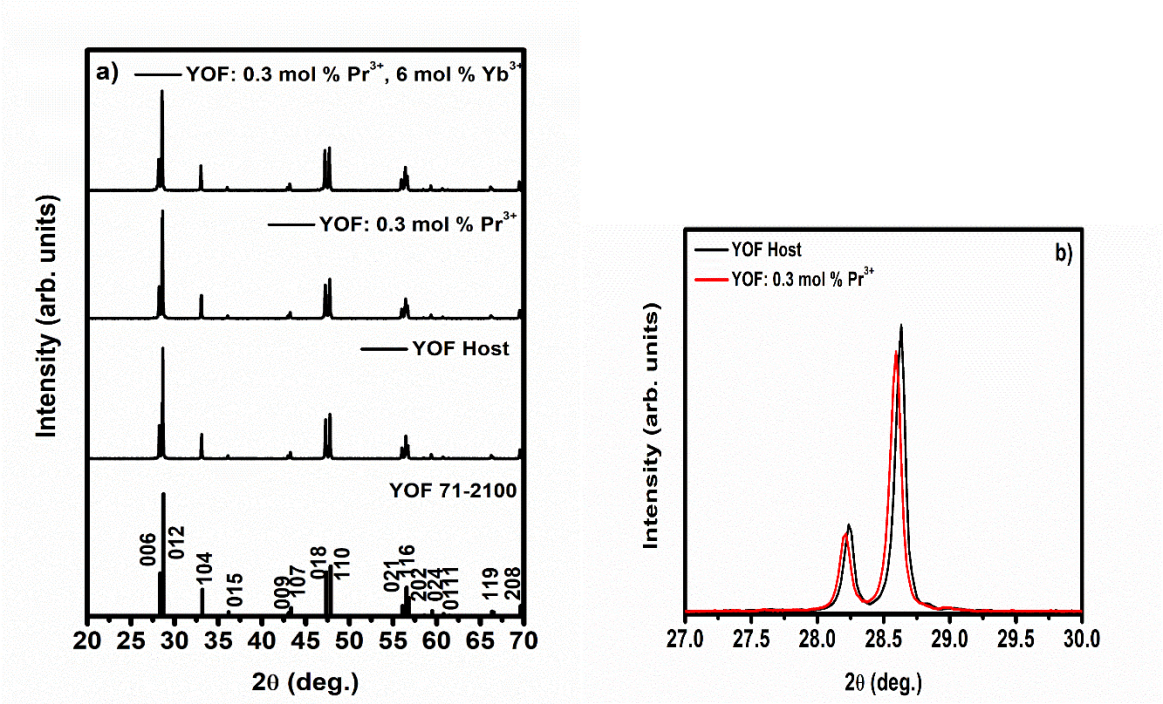

Figure 1: XRD pattern of the host material, of YOF: 0.3 mol % Pr^{3+} and of YOF: 0.3 mol % Pr^{3+}, 6 mol % Yb^{3+} and b) the effect of doping on the diffraction peak of YOF.

The morphology and the effect of different Yb^{3+} ions' concentrations on the morphology were investigated by using SEM. Figure 2 represents the variation of the morphology with different concentrations of Yb^{3+} ions. The morphology of the surface showed a variation of agglomerated, angular, melted particles. The increase in Yb^{3+} concentrations did not affect the morphology. The authors previously reported the agglomeration and melting of the particles during their investigations of the YOF:Pr^{3+} phosphor [9]. This was also reported by Z. Li et al. [10] during their investigations on the pyrolysis method of YOF:Yb^{3+}, Er^{3+} thin films. The same behavior was also reported by Eloussifi et al. [11] upon investigations of the decomposition of YOF into different structures.

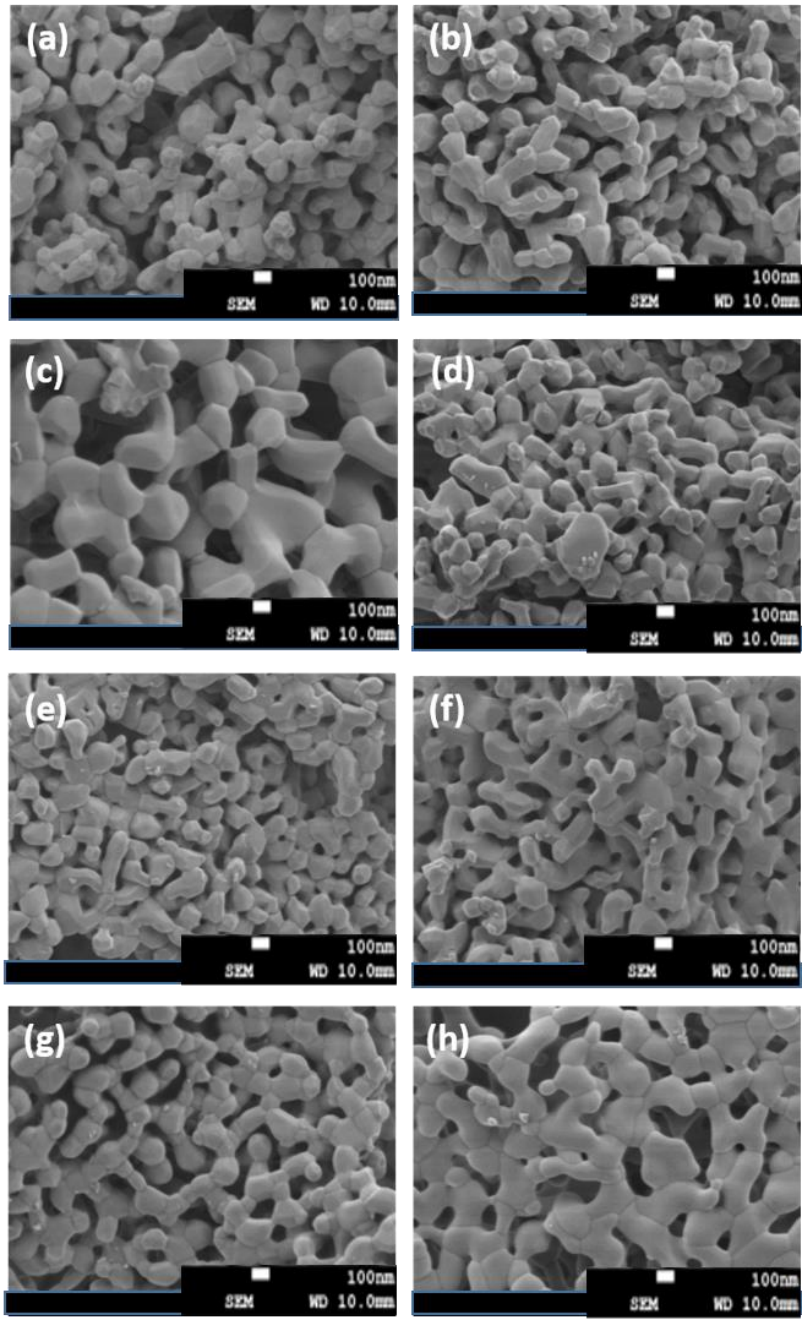

Figure 2: SEM images representing the variation of the morphology of the YOF:Pr^{3+}, x Yb^{3+} samples for x = (a) 1, (b) 1.5, (c) 2, (d) 2.5, (e) 3, (f) 4, (g) 5 and (h) 6 mol % of Yb^{3+}.

XPS was used to investigate the compositional and elemental distribution of the YOF: 0.3 mol % Pr^{3+}, 6 mol % Yb^{3+} sample. All the fitted high-resolution peaks were corrected for charge compensation to the C 1s peak around 284.8 eV. The presence of C contamination was due to adventitious hydrocarbons on the surface [9]. Figure 3 shows the peak deconvolution of the (a) Y 3d, (b) O 1s, (c) F 1s, (d) Pr 3d and (e) & (f) Yb 4d peaks. The Y 3d in fig. 3(a) was

deconvoluted into two binding energy peaks at 157.1 eV and 159.1 eV that were due to the spin orbit splitting into the $3d_{5/2}$ and $3d_{3/2}$ peaks, respectively. The O 1s peak shows two deconvoluted peaks at 529.1 eV and 531.4 eV, see figure 3(b). The F 1s peak shows one peak at 684.9 eV (figure 3(c)) and the Pr 3d peak shows two pairs of peaks for the $3d_{5/2}$ and $3d_{3/2}$ peaks due to the spin orbit splitting (figure 3(d)) at 933.4 eV and 953.8 eV and at 929 eV and 949.4 eV, respectively. In figure 3(e), the deconvolution of the Yb 4d peak was difficult to implement due to the overlapping with two wide peaks related to the Y 3d peak at 172.2 eV and 199 eV. The only detected part of Yb 4d was the spin orbit splitting $4d_{5/2}$ peak at around 185 eV, fitted in figure 3(f). The $4d_{3/2}$ peak was situated inside the wide peak at 199 eV.

The 157.1 eV peak of Y $3d_{5/2}$ corresponded well with other reported values for the Y $3d_{5/2}$ peak in the YOF structure [9, 12, 13]. The peak of O 1s at 529.1 eV was ascribed to the oxygen peak in the YOF structure and this was also reported for the YOF structure [9, 14]. The second peak at 531.4 eV was due to presence of hydroxyl or carbonate groups [15]. The F 1s peak at 684.9 eV correlated well with the reported data for the YOF structure [9, 14]. In our previous study on YOF:Pr^{3+}, we also reported on the presence of two oxidation states for the Pr 3d peak as Pr^{3+} and Pr^{4+}. Figure 3(d) therefore shows the 933.4 eV and 953.8 eV peaks that corresponded to the Pr $3d_{5/2}$ and Pr $3d_{3/2}$ peaks of Pr^{4+} and the other pair at 929 eV and 949.4 eV corresponded to the Pr $3d_{5/2}$ and Pr $3d_{3/2}$ peaks of Pr^{3+} with a separation between each pair of about 20.4 eV. The obtained binding energy values for the Pr 3d peaks were in correlation with results in literature for Pr^{3+} and Pr^{4+} [9, 16-19]. The Pr^{4+} ions might have formed during the synthesis process or annealing where the O^{2-} ions replaced the F^{-} ions to form the YOF structure. The deconvolution of Yb $4d_{5/2}$ was reported in other systems at around 185 eV and this was well in correlation with our obtained value. [20, 21].

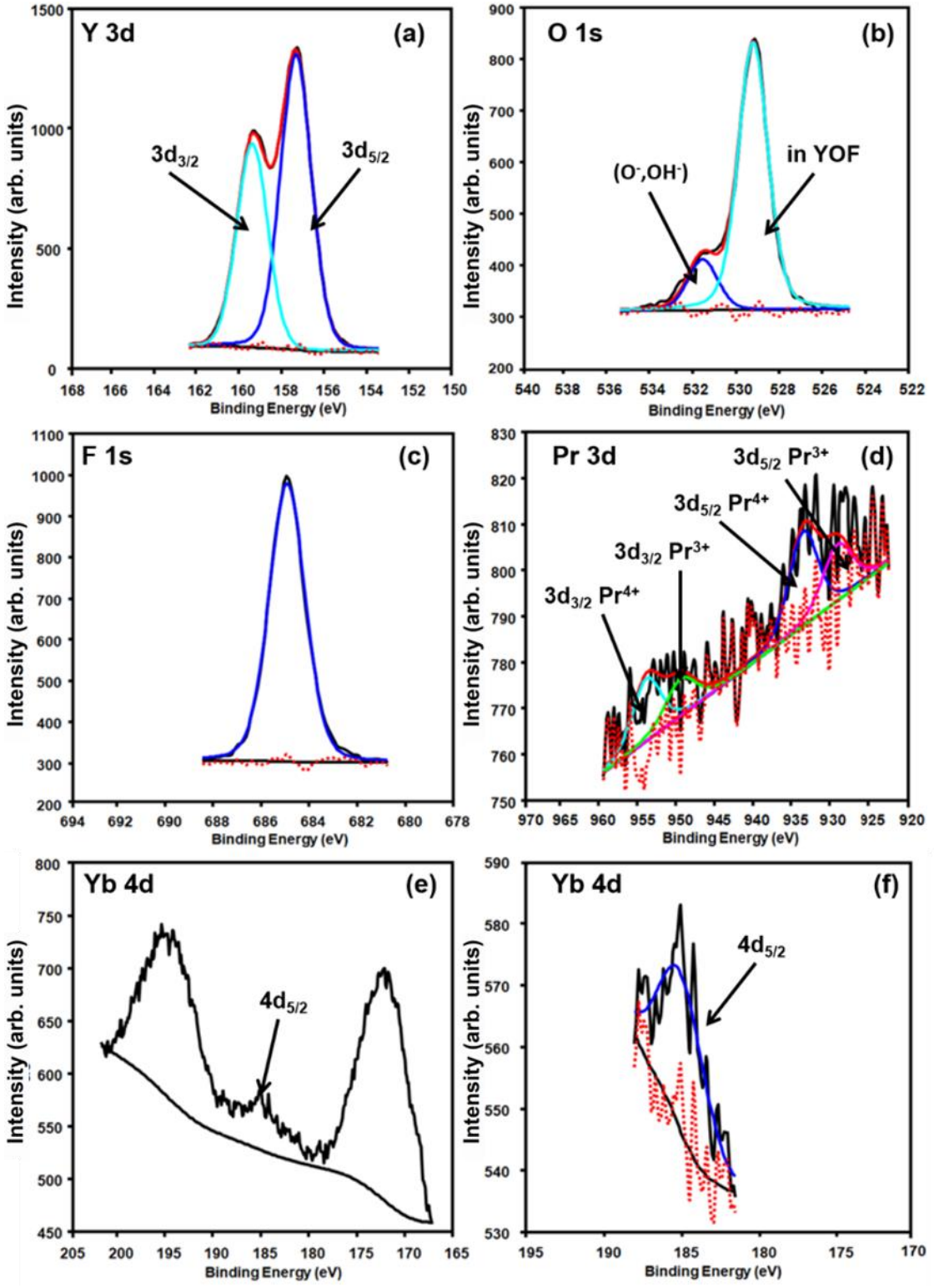

Figure 3: XPS high-resolution peak fits for the (a) Y 3d, (b) O 1s, (c) F 1s, (d) Pr 3d peaks and (e) & (f) Yb 4d full spectrum and its fit, respectively in YOF: 0.3 mol % Pr^{3+}, 6 mol % Yb^{3+}.

The PL studies on the prepared samples were done for the VIS and the IR regions.

5.3.1 Visible (VIS) Emission

Figure 4 shows the VIS excitation spectrum of the prepared YOF: 0.3 mol % Pr^{3+}, x mol % Yb^{3+} samples as a function of the Yb^{3+} ions' concentrations (x = 0, 1, 1.5, 2, 2.5, 3, 4, 5 and 6), obtained for emission at 498 ((a) and (b)) and 659 nm ((c) and (d)). The excitation spectra consisted of two parts. The first part was a broad band centered at 250 nm that was ascribed to the allowed 4f-5d band of Pr^{3+} ions according to Saeed et al. [9], figures 4(a) and (c). The second part was related to the 4f-4f transition of Pr^{3+} ions that peaked around 456 nm, 470 nm and 483 nm. These peaks corresponded to the $^3H_4 \rightarrow {}^3P_2$, $^3H_4 \rightarrow {}^1I_6$, $^3P_1$ and $^3H_4 \rightarrow {}^3P_0$ transitions of the Pr^{3+} ion, respectively [3], figures 4(b) and (d). Co-doping with Yb^{3+} ions gradually resulted in quenching of the Pr^{3+} excitation with an increase in the Yb^{3+} concentration from 1 mol % up to the 6 mol %.

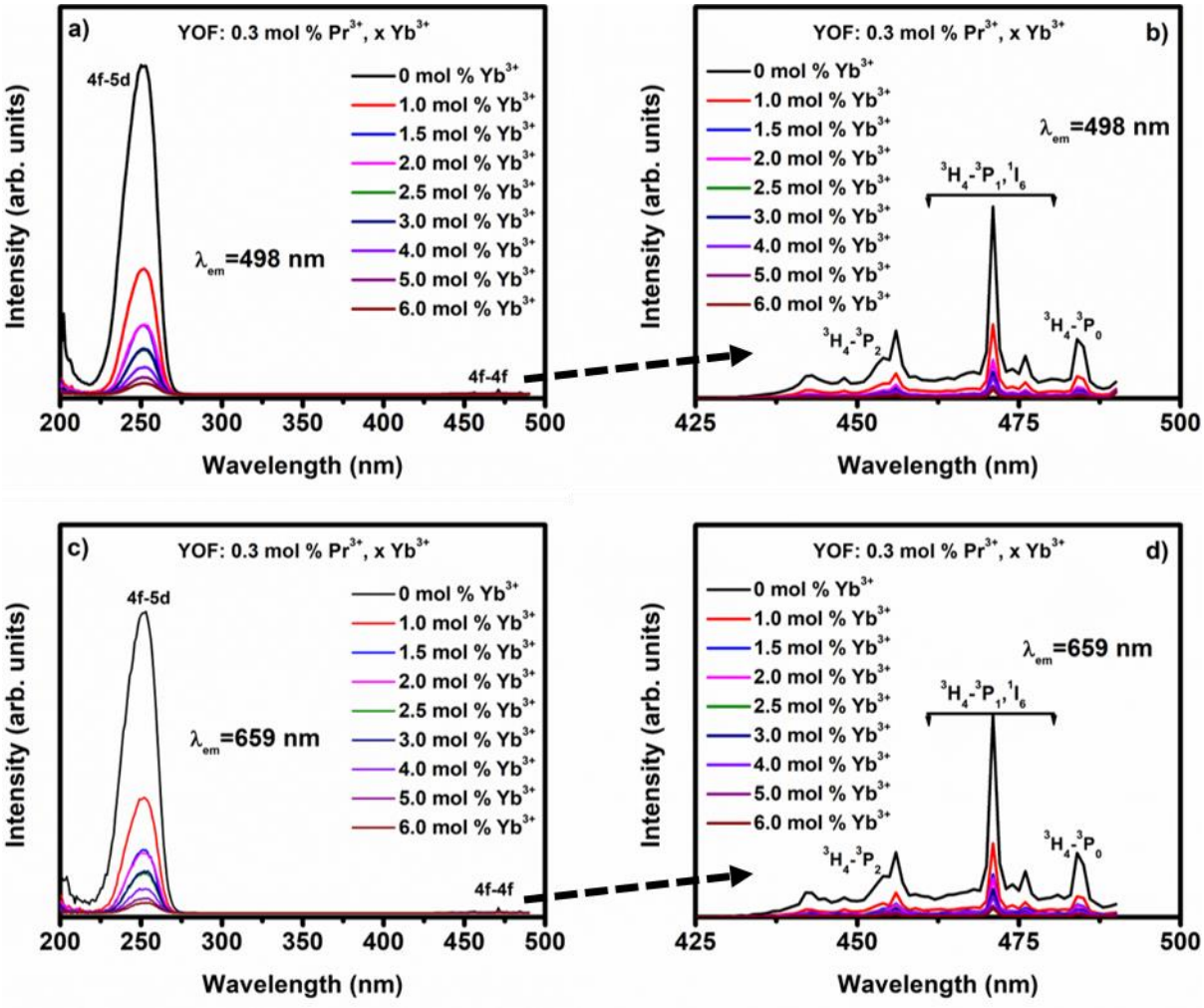

Figure 4: VIS 4f-5d PL excitation of YOF:Pr^{3+}, Yb^3 for different concentrations of Yb^{3+} monitored at a) 498 nm and c) 659 nm emission, b) and d) shows the 4f-4f excitation.

Figure 5(a) shows the VIS emission spectrum at different Yb^{3+} co-doping concentrations. The emission of the samples consisting of multi-narrow emission peaks that originated from different levels of Pr^{3+} ions. The emission spectra were due to the $^3P_0 \rightarrow {}^3H_{4,5,6}$ and $^3P_0 \rightarrow {}^3F_{2,3,4}$ transitions and from the weaker $^1D_2 \rightarrow {}^3H_4$ and $^3P_0 \rightarrow {}^3H_6$ levels of Pr^{3+} [9, 22]. The dominant emission around 498 nm and 659 nm corresponded to the $^3P_0 \rightarrow {}^3H_4$ and $^3P_0 \rightarrow {}^3F_2$ transitions of Pr^{3+}, respectively. The highest emission was recorded for the singly doped sample with 0.3 mol % of Pr^{3+} ions. As was the case for the excitation, an increase in the Yb^{3+} concentrations, up to 6 mol %, also gradually quenched the Pr^{3+} emission. This can be attributed to energy transfer from the Pr^{3+} ions' energy levels to the Yb^{3+} ions' levels. Figure 5(b) shows the variation of the intensity of the dominant $^3P_0 \rightarrow {}^3H_4$ emission as a function of Yb^{3+} concentration.

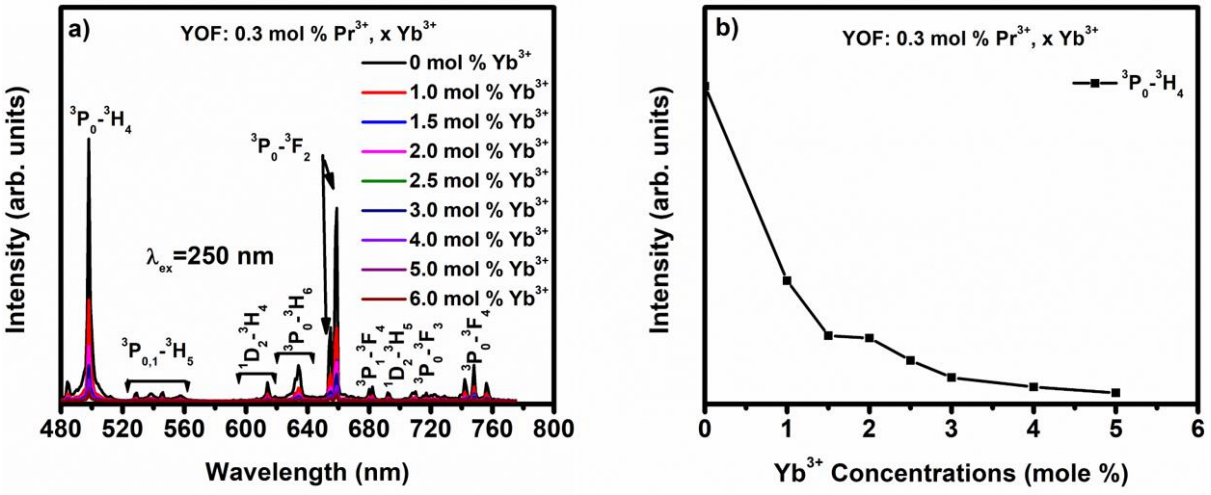

Figure 5: a) VIS PL emission of YOF: 0.3 mol % Pr^{3+}, x mol % Yb^{3+} for different concentrations of Yb^{3+} ions under 250 nm excitation and b) the variation of $^3P_0 \rightarrow {}^3H_4$ emission with Yb^{3+} concentrations.

Investigation on the concentration quenching of the Pr^{3+} emission can be referred to as non-radiative energy transfer from Pr^{3+} to Yb^{3+} in our system. From Dexter's theory for the energy transfer expression of multipolar interactions and Reisfeld's approximation, we can determine the type of the multipolar interaction through the relation [23-26]:

$$\frac{\eta_0}{\eta} \propto C^{\frac{s}{3}} \quad \text{.....1.}$$

Where η_0 and η are the quantum efficiencies of Pr^{3+} in the absence and the presence of Yb^{3+}. C is the total concentrations of Pr^{3+} and Yb^{3+} and s is the type of the multipolar interaction and takes the value 6, 8 and 10 for dipole-dipole, dipole-quadrupole and quadrupole-quadrupole interactions, respectively. The efficiencies' ratio, η_0/η, can also be expressed in terms of the

intensities' ratio, I_{s0}/I_s [25, 26] A plot of the two terms I_{s0}/I_s and $C^{s/3}$ will determine the type of the multipolar interaction as in figure 6. According to our fits done for the different values of s (6, 8 and 10), the best fit was obtained with s = 6, figure 6(a). This allowed us to assign the type of interaction to dipole-dipole interaction. This type of interaction for the Pr^{3+}-Yb^{3+} system has previously been reported by other researchers in various crystal systems [27, 28, 29].

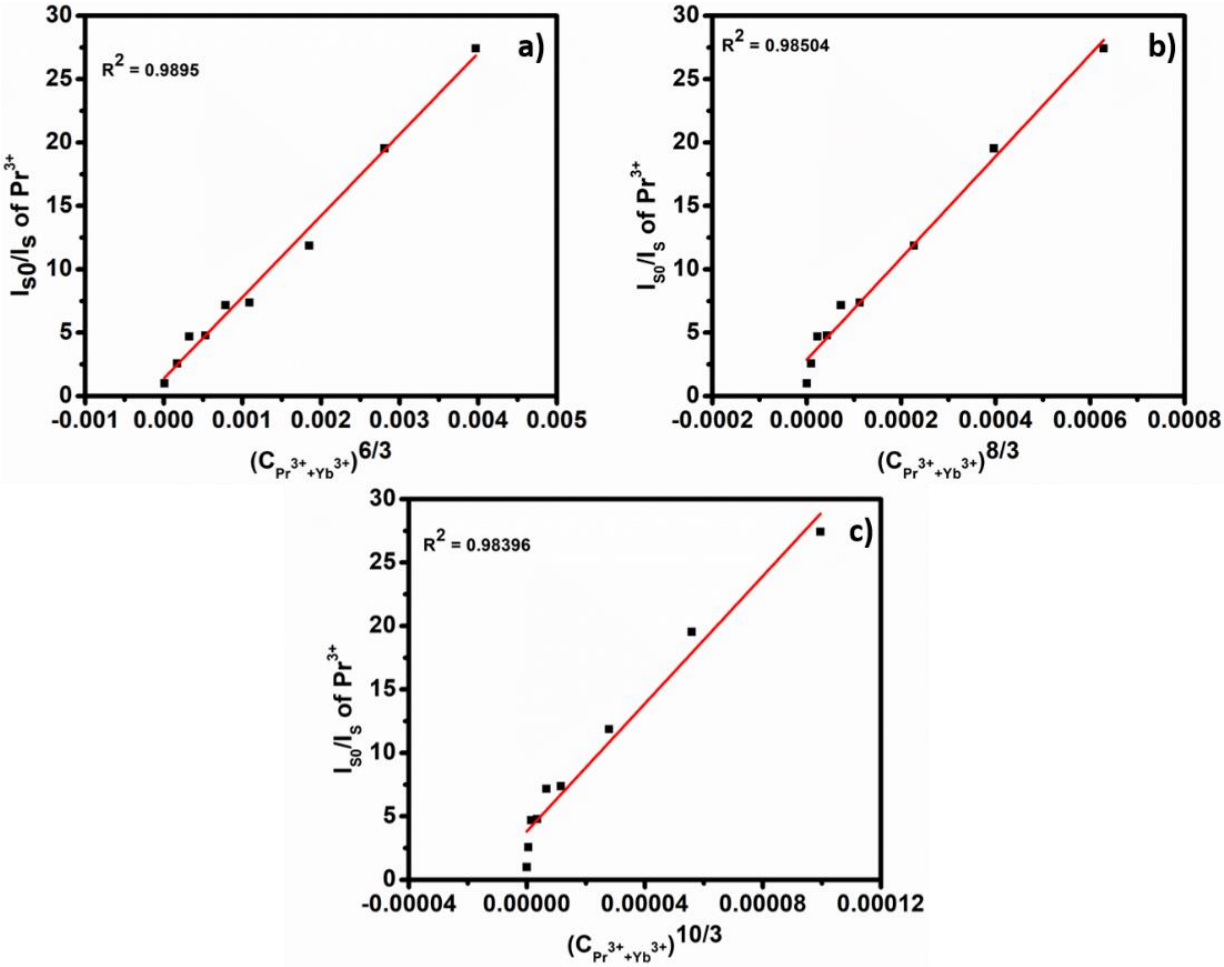

Figure 6: Dependence of Pr^{3+} I_{S0}/I_S on a) $(C_{Pr^{3+}+Yb^{3+}})^{6/3}$, b) $(C_{Pr^{3+}+Yb^{3+}})^{8/3}$ and c) $(C_{Pr^{3+}+Yb^{3+}})^{10/3}$.

5.3.2 Infrared (IR) emission

IR characterization was done on the samples with different Yb^{3+} co-doping concentrations, figure 7. The excitation spectra in figure 7(a) were recorded while monitoring the 907 nm (according to our previous report) main IR Pr^{3+} emission [9]. The excitation spectra in figure 7(b) were recorded for the 971 nm main Yb^{3+} emission. The excitation spectra monitored at 907 nm emission consisted of the characteristic Pr^{3+} excitation bands. It showed a broad 4f-5d band around 250 nm with smaller peaks at 456 nm, 470 nm and 483 nm due to the 4f-4f transitions [9, 22]. The excitation spectra in figure 7(b) also consisted of the Pr^{3+} excitation

bands as well as a new higher intensity band around 225 nm that overlapped with the Pr^{3+} band around 250 nm.

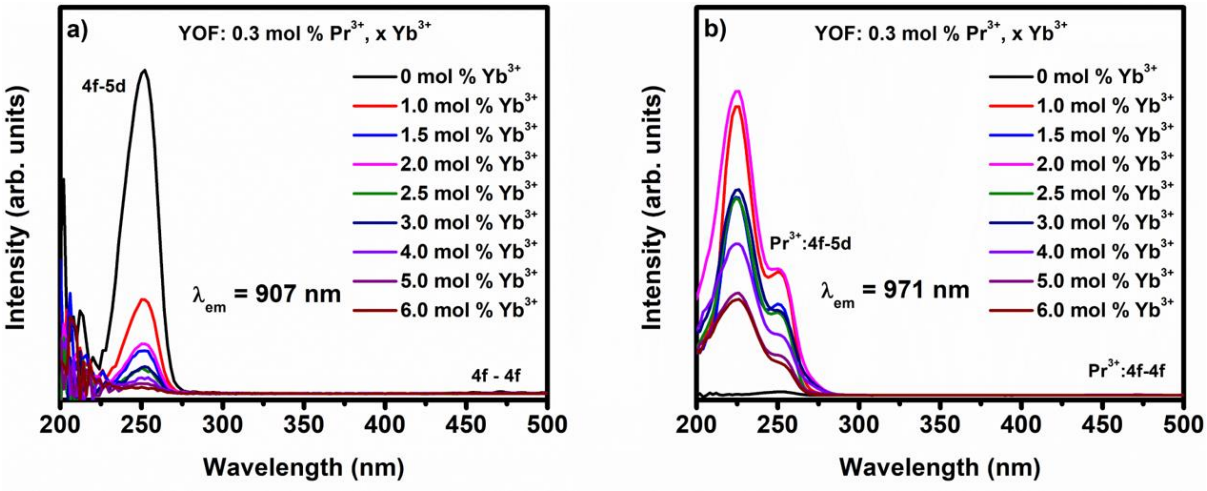

Figure 7: IR excitation of YOF:Pr^{3+}, Yb^3 for different concentrations of Yb^{3+} monitored at a) 907 nm and b) 971 nm emission.

The nature of the 225 nm band can be explained on the basis of 5 hypotheses. This band might be due to (1) some impurity ions such as Eu^{2+}, (2) reduction of Yb^{3+} to Yb^{2+}, (3) the absorption of the YOF host, (4) the 4f-5d band of Yb^{3+} or (5) the presence of a Yb^{3+} - O^{2-} CT band [30]. It is well known that both Eu^{2+} and Yb^{2+} are considered as luminescent centers and have emission characteristics of VIS emission with an excitation due to the 4f-5d transition [31, 32]. To be able to confirm our 1st hypothesis, PL have been done in the 300 – 800 nm VIS range. Figure 8 shows the typical Pr^{3+} visible 4f-4f emission recorded upon 225 nm excitation [30]. No Eu^{2+} or Yb^{2+} emission peaks were observed. This confirmed that Eu^{2+} and Yb^{2+} ions were not present in the system. We therefore excluded the 1st and 2nd possibilities of our hypothesis. In the authors' previous report on YOF:Pr^{3+} [9], there was no emission observed that was related to the YOF host. This excluded the 3rd possibility. Dorenbos et al. [33, 34] have suggested a model to predict the position of the 4f-5d band of Ln^{3+} ions based on experimental studies of 450 different hosts depended on the position of the 4f-5d band of Ce^{3+}. Saeed et al. [9] have done an investigation on the luminescence of YOF:Ce^{3+} to predict the position of the 4f-5d band of Pr^{3+}. The recorded 4f-5d band of Ce^{3+} was found to exist around 362 nm (27 600 cm^{-1}). According to the Dorenbos model the difference between the 4f-5d band of Ce^{3+} and Yb^{3+} remained almost constant (38 000 ± 750 cm^{-1}). The predicted value for the 4f-5d band of Yb^{3+} was therefore calculated to be at around 65 600 ± 750 cm^{-1} (152 ± 6 nm). The nature of

the 225 nm band to be related to the 4f-5d band, the 4th possibility, was then also excluded. The only possibility left was the CT band of Yb^{3+}.

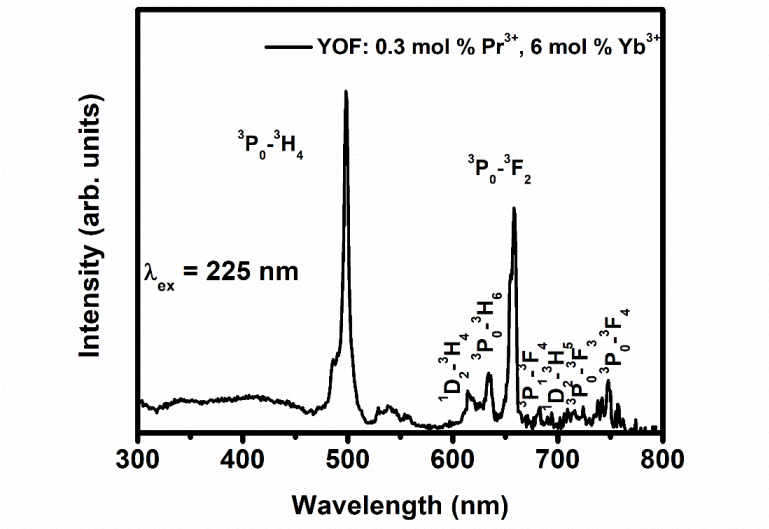

Figure 8: Visible PL emission of YOF: 0.3 mol % Pr^{3+}, Yb^{3+} upon excitation of 225 nm.

The energy of a CT band of a specified ion can be determined on the basis of the value of the electronegativity of the ions. Jörgensen et al. [35] have introduced an empirical formula to predict the position of the CT band as follow:

$$E^{CT} = [\chi_{opt}(m) - \chi_{opt}(x)] \times 30\,000\ cm^{-1} \quad \text{.....2.}$$

E^{CT} is the energy of the CT band, $\chi_{opt}(m)$ is the optical electronegativity of the anion x where the electron is transferred to and $\chi_{opt}(x)$ is the optical electronegativity of the ion metal. The above equation can be rewritten in respect to the position of the CT band of Eu^{3+} in the same host as follow [30]:

$$E_{Yb\text{-}O} = [\chi_{opt}(Eu) - \chi_{opt}(Yb)] \times 30\,000\ cm^{-1} + E_{Eu\text{-}O} \quad \text{.....(3).}$$

$E_{Eu\text{-}O}$ and $E_{Yb\text{-}O}$ are the CT energy of Eu^{3+} and Yb^{3+}, respectively. $\chi_{opt}(Eu)$ and $\chi_{opt}(Yb)$ are the optical electronegativities of Eu^{3+} and Yb^{3+}, respectively. The optical electronegativities were obtained from literature to be Eu^{3+} = 1.377 and Yb^{3+} = 1.415 [36]. The calculated CT band for Yb^{3+} was about 41 200 ± 3000 cm^{-1} (243 ± 25 nm). The estimated value with the given error therefore allowed us to ascribe the band around 225 nm to be the CT band of Yb^{3+}. This result was also confirmed by our XPS results for the highest co-doped YOF: 0.3 mol % Pr^{3+}, 6 mol % Yb^{3+} sample. The XPS results did not show any existence of Yb^{2+}. The CT band at 225 nm therefore exist due to transfer of an electron from the O^{2-} anion's $2p^6$ orbital to the $4f^{13}$ orbital of Yb^{3+}. It can be written as $Yb^{3+} - O^{2-}$ [30]. The presence of the CT band of Yb^{3+} was also reported before by Wang et al. [30].

IR emission was recorded for all the samples upon excitation of 250 nm as well as with 225 nm. Figure 9(a) shows the typical broad $^2F_{7/2} \rightarrow {}^2F_{5/2}$ Yb^{3+} ions' emission of the samples excited with 250 nm with the main emission around 971 nm [37, 38]. The emission also contained sharp emission peaks of Pr^{3+} that corresponded to the $^3P_0 \rightarrow {}^1G_4$ and $^1D_2 \rightarrow {}^3F_4$ transitions at 907 nm and 1074 nm, respectively [9, 39, 40]. During excitation of 225 nm the emission originated only from the $^2F_{5/2} \rightarrow {}^2F_{7/2}$ Yb^{3+} transition, figure 9(b). This confirmed that the band at 225 nm was more related to Yb^{3+} excitation. The optimum co-doping concentration of Yb^{3+} for the IR emission was recorded for both excitations to be 2 mol %, see figure 9(c). The emission drastically decreased beyond the 2 mol % Yb^{3+} concentration and was attributed to concentration quenching for the Yb^{3+} emission [3]. Quenching of Yb^{3+} emission can be explained by interactions that occurred between the neighboring Yb^{3+} ions [41, 42, 43].

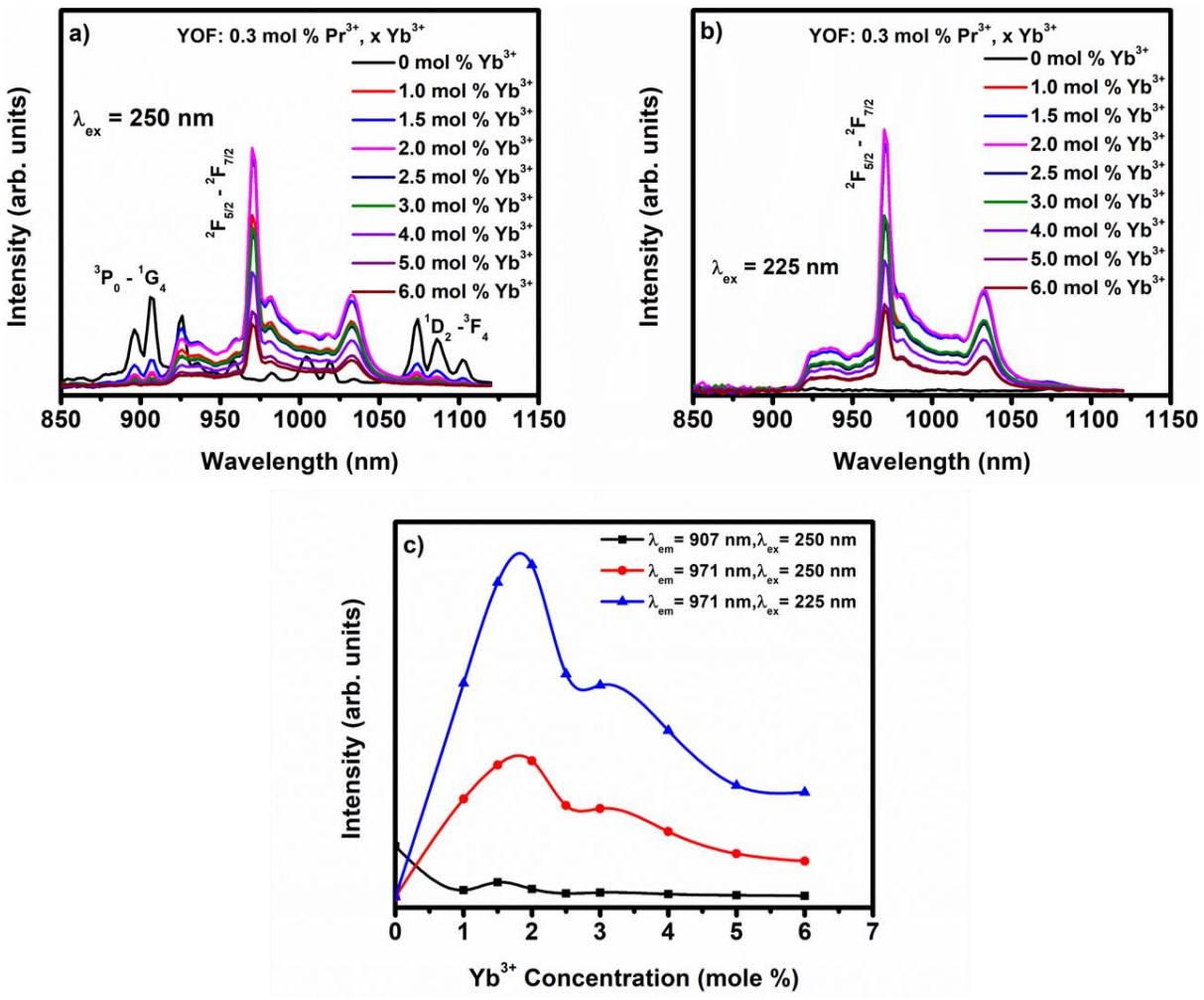

Figure 9: IR emission of YOF:Pr^{3+}, Yb^3 for different concentrations of Yb^{3+} excited at a) 250 nm and b) 225 nm. c) The variation of IR emissions with Yb^{3+} concentration.

The florescence decay curves were recorded to extract more information on the energy transfer process from Pr^{3+} to Yb^{3+} ions for the VIS and the IR emissions. The decay curves of the samples showed double and triple non-exponential decay curves. Figure 10 shows the recorded VIS decay curves of the $^3P_0 \rightarrow {}^3H_4$ (498 nm) transitions of Pr^{3+} ions. The double and triple non-exponential decay curves can be expressed as the following equations [44]:

$$\mathbf{I(t) = A_0 + A_1exp(-t/\tau_1) + A_2exp(-t/\tau_2)}\ldots\ldots\ldots\ldots\ldots\ldots\ldots\ldots\mathbf{4}$$

$$\mathbf{I(t) = A_0 + A_1exp(-t/\tau_1) + A_2exp(-t/\tau_2) + A_3exp(-t/\tau_3)}\ldots\ldots\ldots\ldots\mathbf{5,}$$

where I(t) is the PL intensity, τ_1, τ_2 and τ_3 are the emission decay times, and A_1, A_2 and A_3 are their relative weights [45]. According to literature, the lifetimes of Pr^{3+} doped materials are in the range of nanoseconds up to 50 microseconds (μs) [43]. In the present investigation, the VIS decay times of the $^3P_0 \rightarrow {}^3H_4$ transition were in the 21.4 to 7.5 μs range for the 0.3 mol % single doped Pr^{3+} concentration sample up to the 6 % Yb^{3+} co-doped sample. This is in good agreement with previously reported values for decay lifetimes calculated for the $^3P_0 \rightarrow {}^3H_4$ emission [37, 38, 46, 47].

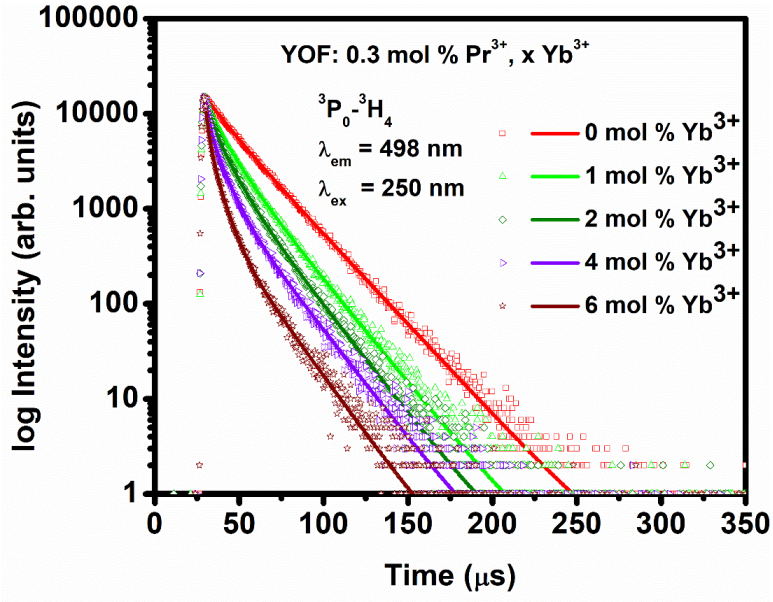

Figure 10: The measured decay times of the Pr^{3+} $^3P_0 \rightarrow {}^3H_4$ transition upon excitation of 250 nm and emission of 498 nm.

The energy transfer efficiency ($\eta_{tr\ x\%Yb}$) and the total efficiency between Pr^{3+} and Yb^{3+} ($\eta_{x\%Yb}$) can be calculated from the theoretical expressions [1, 44]:

$$\eta_{tr\ x\%Yb} = \frac{\tau_{x\%Yb}^{-1} - \tau_{0\%Yb}^{-1}}{\tau_{x\%Yb}^{-1}} = 1 - \frac{\tau_{x\%Yb}^{-1}}{\tau_{x\%Yb}^{-1}} \ldots\ldots\ldots\ldots\ldots\ldots\ldots\ldots\ldots\ldots\mathbf{6}$$

$$\eta_{x\%Yb} = \eta_{Pr}\,(1 - \eta_{tr\ x\%Yb}) + 2\,\eta_{Pr}\,\eta_{tr\ x\%Yb} \ldots\ldots\ldots\ldots\ldots\ldots\ldots\mathbf{7,}$$

where $\tau_{0\%Yb}$ and $\tau_{x\%Yb}$ represents the decay time in absence and in the presence of Yb^{3+}, respectively. η_{Pr} and η_{Yb} are the quantum efficiency of Pr^{3+} and Yb^{3+} and both of them were normalized to unity where the non-radiative relaxation was ignored [44]. The obtained visible decay times in the order of microseconds as well as the corresponding efficiencies are depicted in table 2.

Table 2: The obtained decay time of $^3P_0 \rightarrow {}^3H_4$ and the corresponding efficiencies calculated using equations (6) & (7) as a function of Yb^{3+} concentrations.

YOF: 0.3 mol % Pr^{3+}, x mol % Yb^{3+}	τ_1/ µs	τ_2/ µs	τ_3/ µs	τ/ µs	$\eta_{tr\ x\%Yb}$ %	$\eta_{x\%Yb}$ %
0	10.74	22.87	—	21.4	—	—
1	6.7	19	—	15.87	25.8	125.8
1.5	6.1	18.1	—	14.54	32	132
2	5.73	17.51	—	13.38	37	137
2.5	5	15.66	—	11.72	45	145
3	4.66	16.86	—	11.57	46	146
4	2.1	7.49	19.23	11.1	48	148
5	2.03	7.38	19.76	10.8	50	150
6	1.98	6.25	18.1	7.5	65	165

The decay times of the IR emission were also investigated for both $^3P_0 \rightarrow {}^1G_4$ and $^2F_{5/2} \rightarrow {}^2F_{7/2}$ transitions of Pr^{3+} and Yb^{3+}, respectively. The IR decay times were recorded under excitation of 250 nm for Pr^{3+} and 225 nm for Yb^{3+}. The recorded decay times were depicted in figure 11(a) and (b) for $^3P_0 \rightarrow {}^1G_4$ and $^2F_{5/2} \rightarrow {}^2F_{7/2}$ emissions, respectively. The calculated IR decay times of Pr^{3+} and Yb^{3+} were depicted in table 3 in respect to an increase of Yb^{3+} concentrations from 0 mol % up to 6 mol %. The decrease of the decay time of the 907 nm emission as a function of Yb^{3+} indicated that non-radiative energy transfer occurred from Pr^{3+} to Yb^{3+}. This lead to the quenching of the Pr^{3+} VIS emission. The decrease in the decay time of Yb^{3+} indicated that energy transfer occurred between the Yb^{3+} ions. The recorded decay times for both transitions were also reported for different Pr^{3+}- Yb^{3+} co-doped systems [37, 38, 46, 47].

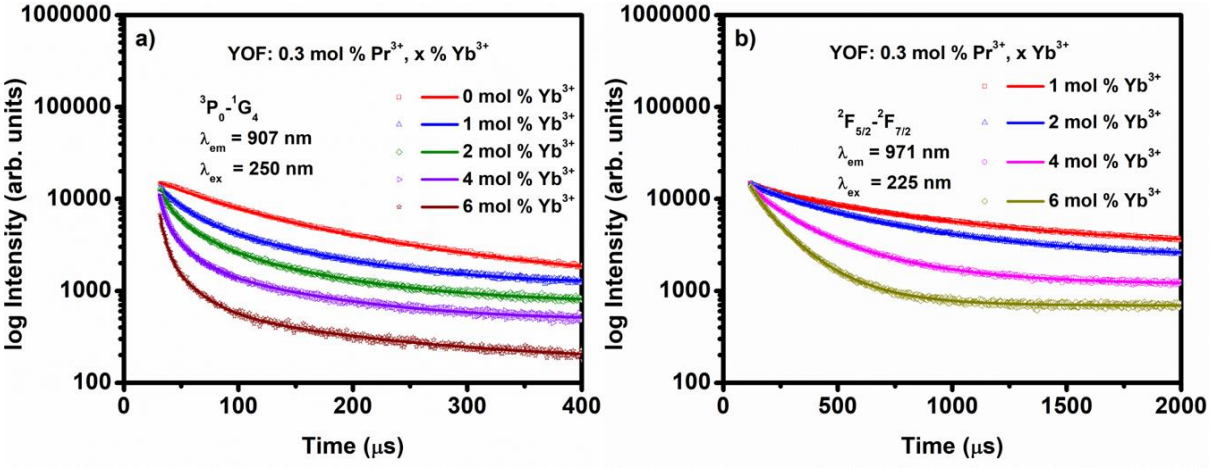

Figure 11: The measured decay times of a) $^3P_0 \rightarrow {}^1G_4$ (907 nm) and b) $^2F_{5/2} \rightarrow {}^2F_{7/2}$ (971 nm) transitions upon excitation of 250 nm and 225 nm, respectively.

Table 3: The obtained decay times of both $^3P_0 \rightarrow {}^3H_4$ and $^2F_{5/2} \rightarrow {}^2F_{7/2}$ transitions as a function of Yb^{3+} concentrations.

YOF: 0.3 mol % Pr^{3+}, x mol % Yb^{3+}	**τ/ μs** $^3P_0 \rightarrow {}^1G_4$	**τ/ μs** $^2F_{5/2} \rightarrow {}^2F_{7/2}$
0	85.1	—
1	80.8	686.4
1.5	79.3	617.5
2	71.6	507.5
2.5	70.5	447.6
3	69.7	388.6
4	66.1	290.6
5	63.8	204.1
6	52.5	161.5

The proposed energy level diagram and luminescent mechanism is therefore illustrated in figure 12. Excitation of 225 nm to the CT band of Yb^{3+} ions relaxed non-radiatively to the 4f-5d band of Pr^{3+} that resulted in a further non-radiative relaxation to the $^3P_0$ level of Pr^{3+}. Excitation of 250 nm to the 4f-5d band Pr^{3+} also relaxed non-radiatively to the $^3P_0$ level. Population of the $^3P_0$ level then resulted in Pr^{3+} emission that corresponded to the $^3P_0 \rightarrow {}^3H_4$ and $^3P_0 \rightarrow {}^3F_2$ transitions. Energy transfer then occurred from the $^3P_0$ level of Pr^{3+} to the Yb^{3+} levels through a two-step resonant energy transfer process that resulted in the $^2F_{5/2} \rightarrow {}^2F_{7/2}$ IR emission. The first step occurred through the cross-relaxation mechanism according to the [$^3P_0$

(Pr^{3+}) + $^2F_{7/2}$ (Yb^{3+}) → $^1G_4$ (Pr^{3+}) + $^2F_{5/2}$ (Yb^{3+})] process. The second step involved the de-excitation of the energy in the $^1G_4$ level to the $^3H_4$ ground state. This resulted in the transfer of energy to a second Yb^{3+} ion and occurred through [$^1G_4$ (Pr^{3+}) + $^2F_{7/2}$ (Yb^{3+}) → $^3H_4$ (Pr^{3+}) + $^2F_{5/2}$ (Yb^{3+})]. This two-step resonant energy transfer process was applicable for both excitations of 225 and 250 nm [45]. Cooperative energy transfer cannot be neglected since the $^3P_0$ level of Pr^{3+} were situated at an energy approximately twice of the $^2F_{5/2}$ Yb^{3+} level. The cooperative process occurred through the [$^3P_0$ (Pr^{3+}) → $^2F_{5/2}$ (Yb^{3+}) + $^2F_{5/2}$ (Yb^{3+})] process that resulted in emission of two IR photons. Quenching of the emission at 1074 nm might have been due to the cross-relaxation process [$^1D_2$ (Pr^{3+}) + $^2F_{7/2}$ (Yb^{3+}) → $^3F_4$ (Pr^{3+}) + $^2F_{5/2}$ (Yb^{3+})], that favored 971 nm emission of Yb^{3+} [48, 49]. Sufficient energy transfers therefore occurred from Pr^{3+} to Yb^{3+} ions.

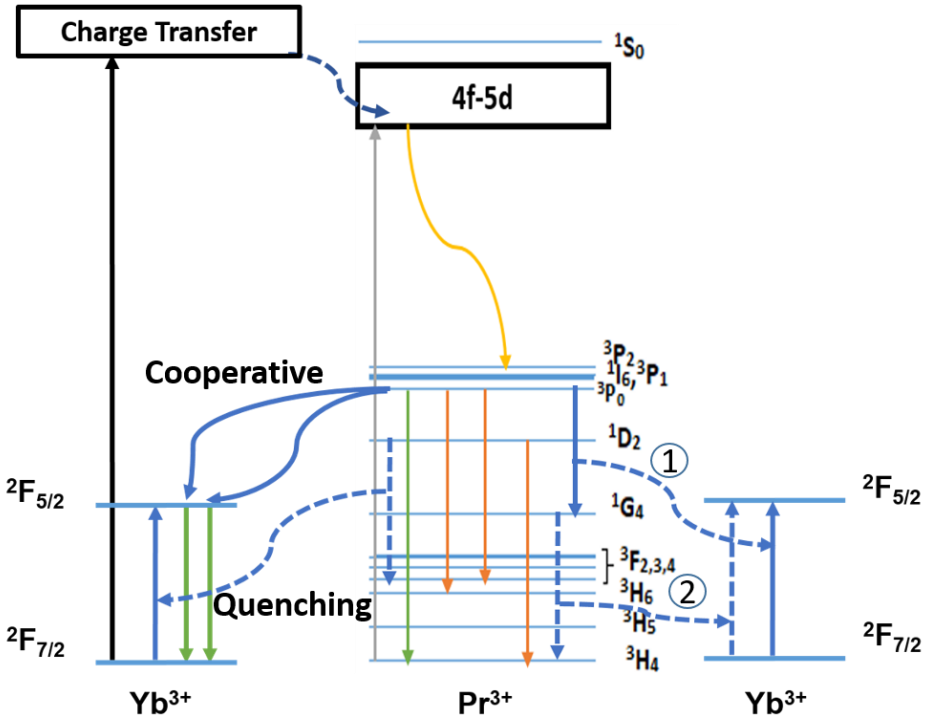

Figure 12: Proposed energy level diagram for the YOF: Pr^{3+}, Yb^{3+} phosphor.

5.4 Conclusion

The YOF:Pr, Yb phosphor was successfully synthesized using the pyrolysis method with CF_3COO as precursor. XRD results showed a rhombohedral YOF structure (space group: $R\bar{3}m$ (166)) after annealing at 900 ^{0}C. XPS peak deconvolutions showed the presence of both Pr^{3+} and Pr^{4+} for the Pr 3d peak. It also showed only the Yb 4d peak of Yb^{3+}. Visible PL results

showed 4f-4f emission of Pr^{3+} upon 250 nm excitation. The IR excitation showed the typical Pr^{3+} 4f-5d band as well as the 4f-4f transitions upon 907 nm emission of Pr^{3+}. The existence of a new band at 225 nm during 971 nm emission of Yb^{3+} was interpreted in respect to YOF:Ce^{3+}. Theoretical investigations were also done in order to determine the nature of the 225 nm band and it was attributed to be a CT band of Yb^{3+}. IR emission was due to Pr^{3+} and Yb^{3+} transitions upon excitation of 250 nm. Only emission due to the Yb^{3+} transitions was detected during excitation of 225 nm. Quenching of the Pr^{3+} IR emission during excitation of 225 nm was due to the cross-relaxation [$^1D_2$ (Pr^{3+}) + $^2F_{7/2}$ (Yb^{3+}) → $^3F_4$ (Pr^{3+}) + $^2F_{5/2}$ (Yb^{3+})] process that favours the 971 nm Yb^{3+} emission. The optimum Yb^{3+} concentration for IR emission was recorded for the sample co-doped with 2 mol % of Yb^{3+} as concentration quenching occurred at higher concentrations through cross relaxation processes. The obtained IR emission of YOF:Pr^{3+},Yb^{3+} was within the effective response range for Si SC. YOF:Pr^{3+},Yb^{3+} is therefore an appropriate candidate for Si SC enhancement. The decay times were in order of μs which is consistent with other reported values of Pr^{3+},Yb^{3+} doped materials.

References

[1] D. Serrano, A. Braud, J.-L. Doualan, P. Camy, A. Benayad, V. Ménard and R. Moncorgé, Opt. Mater. 33 (2011) 1028 - 1031.

[2] B.M. Van der Ende, L. Aarts and A. Meijerink, Phys. Chem. Chem. Phys. 11 (2009) 11081 - 11095.

[3] Q.Y. Zhang and X.Y. Huang, Prog. Mater. Sci. 55 (2010) 353 - 427.

[4] W.W. Piper, J.A. DeLuca, and F. S. Ham, J. Lumin. 8 (1974) 344 - 348.

[5] J.L. Sommerdijk, A. Bril and A.W. de Jager, J. Lumin. 8 (1974) 341 - 343.

[6] S. Kuck, I. Sokolska, M. Henke, M. Doring and T. Scheffler, J. Lumin. 102–103 (2003) 176 - 181.

[7] Y. Xu, X. Zhang, S. Dai, B. Fan, H. Ma, J. Adam, J. Ren and G. Chen, J. Phys. Chem. C, 115 (2011) 13056 - 13062.

[8] Z. Liu, L. Yang, N. Dai, Y. Chu, Q. Chen and J. Li, Opt. Express, 21 (2013) (8 pages).

[9] N.A.M. Saeed, E. Coetsee and H.C. Swart, Opt. Mater. 96 (2019) 109331 (12 pages).

[10] Z. Li, L. Zheng, L. Zhang and L. Xiong, J. Lumin. 126 (2007) 481 - 486.

[11] H. Eloussifi, J. Farjas, P. Roura, J. Camps, M. Dammak, S. Ricart, T. Puig and X. Obradors, J. Therm. Anal. Calorim. 108 (2012) 589 - 596.

[12] L. Sun, J. Pan, X. Zhang, H. Wang, L. Li and Y. Yu, RSC Adv. 5 (2015) 77673 - 77681.

[13] J.H. Su, P.P. Joshi, V. Chintamaneni and S.M. Mukhopadhyay, Appl. Surf. Sci. 253 (2007) 4652 - 4658.

[14] M. Rizhkov, V.A. Gubanov and M.P. Bytzman, J. Electron Spectrosc. Relat. Phenom. 18 (1980) 227 - 233.

[15] J.F. Moulder, W.F. Stickle, P.W. Sobol and K.D. Bomben, Handbook of X-ray Photoelectron Spectroscopy (Perkin-Elmer, Eden Prairie, MN, 1992).

[16] C.K. Narula, L.P. Haack, W. Chun, H.W. Jen and G.W. Graham, J. Phys. Chem. B, 103 (1999) 3634 - 3639.

[17] Y. Matsumura, S. Sugiyama and J.B. Moffat, in: S.T. Oyama and J.W. Hightower (Eds.), Catalytic Selective Oxidation, ACS Symposium Series, ACS, Washington, 1993, p. 326.

[18] D.D. Sarma and C.N.R. Rao, J. Electron Spectrosc. Relat. Phenom. 20 (1980) 25 - 45.

[19] H. He, H.X. Dai, K.W. Wong and C.T. Au, Appl. Catal. A-Gen. 251 (2003) 61 - 74.

[20] F. Rivera-López and M. Pérez, Surf. Interface Anal. 44 (2012) 927 - 930.

[21] L. Pasquali, M. Montecchi, S. Nannarone and F. Boscherini, J. Phys.: Condens. Matter. 23 (2011) 355003 (11 pages).

[22] J. Hölsä, E. Kestilä, P. Ylha, E. Antic-Fidancev, M. Lemaitre-Blaise, P. Porcher, P. Deren and W. Strek, J. App. Spect. 62 (1995) 697 - 705.

[23] R. Reisfeld, E. Greenberg, R. Velapoldi and B. Barnett, J. Chem. Phys. 56 (1972) 1698.

[24] D.L. Dexter, J. Chem. Phys. 21 (1953) 836 - 850.

[25] P.A. Tanner, L. Zhou, C. Duan and K.L. Wong, Chem. Soc. Rev. 47 (2018) 5234 - 5265.

[26] C. Peng, C. Li, G. Li, S. Li and J. Lin, Dalton Trans. 41 (2012) 8660 - 8668.

[27] H. Wen and P.A. Tanner, Opt. Mater. 33 (2011) 1602 - 1606.

[28] D. Serrano, A. Braud, J.L. Doualan, P. Camy, and R. Moncorgé, J. Opt. Soc. Am. B, 29 (2012) 1854 - 1861.

[29] J.T. van Wijngaarden, S. Scheidelaar, T.J.H. Vlugt, M.F. Reid, and A. Meijerink, Phys. Rev. B, 81 (2010) 155112 (6 pages).

[30] Y. Wang, X. Zhou, J. Shen, X. Zhao, B. Wu, S. Jiang and L. Li, J. Am. Ceram. Soc. 99 (2016) 115 - 120.

[31] M. Henke, J. Perßon, and S. Kück, J. Lumin. 87 (2000) 1049 - 1051.

[32] S. Lizzo, E.P. Klein, N. Nagelvoort, R. Erens, A. Meijerink, and G. Blasse, J. Phys. Chem. Solids, 58 (1997) 963 - 968.

[33] P. Dorenbos, J. Lumin. 91 (2000) 155 - 176.

[34] P. Dorenbos, Phys. Rev. B, 62 (2000) 15640 - 15649.

[35] C.K. Jörgensen, Modern Aspects of Ligand Field Theory, North-Holland Publishing Company, Amsterdam, (1971).

[36] K. Li and D. Xue, J. Phys. Chem. A, 110 (2006) 11332 - 11337.

[37] O. Maalej, B. Boulard, B. Dieudonné, M. Ferrari, M. Dammak and M. Dammak, J. Lumin. 161 (2015)198 - 201.

[38] Y. Xu, X. Zhang, S. Dai, Bo Fan, H. Ma, J.L. Adam, J. Ren and G. Chen, J. Phys. Chem. C, (2011) 115 13056 - 13062.

[39] E. Cavalli, L. Esposito, M. Bettinelli, A. Speghini, K.V. Ivanovskikh, R.B. Hughes-Currie and M. de Jong, Mater. Res. Express, 1 (2014) 045903.

[40] J. Cybinska, J. Legendziewicz, G. Boulon, A. Bensalah and G. Meyer, Opt. Mater. 28 (2006) 41 - 52.

[41] B.M. van der Ende, L. Aartes and A. Meijerink, Adv. Mater. 21 (2009) 3073 - 3077.

[42] Q.Y. Zhang, C.H. Yang, Z.H. Jiang and X.H. Ji, Appl. Phys. Lett. 90 (2007) 061914.

[43] K. Deng, X. Wei, X. Wang, Y. Chen and M. Yin, Appl. Phys. B, 102 (2011) 556.

[44] X. Zhou, Y. Wang, X. Zhao, L. Li, Z. Wang, and Q. Li, J. Am. Ceram. Soc. 97 (2014) 179 - 184.

[45] M.Y.A. Yagoub, H.C. Swart, P. Bergman and E. Coetsee, AIP Adv. 6 (2016) 025204 - 025213.

[46] D.H. Li, Y.J. Chen, J.H. Huang, X.H. Gong, Y.F. Lin, Z.D. Luo and Y.D. Huang, Physica B, 446 (2014) 12 - 16.

[47] L.J. Borrero-González, G. Galleani, D. Manzani, L.A.O. Nunes and S.J.L. Ribeiro, Opt. Mater. 35 (2013) 2085 - 2089.

[48] Y. Katayama and S. Tanabe, J. Lumin. 134 (2013) 825 - 829.

[49] Q.J. Chen, W.J. Zhang, X.Y. Huang, G.P. Dong, M.Y. Peng and Q.Y. Zhang, J. Alloy Compd. 513 (2012) 139 - 144.

Chapter 6

Photoluminescence Studies of Bi^{3+} Doped YOF Phosphor

PL investigations on Bi^{3+} doped YOF was done in this chapter. Bi^{3+} is considered to be the most promising ion for a variety of applications such as FEDs, white light emitting diodes and NIR QC. Results obtained in this chapter showed that the YOF:Bi^{3+} phosphor is therefore an appropriate candidate for optoelectronic applications such as for UV-LED, SC and scintillators and that it can be applied as a sensitizer with other Ln^{3+} ions.

6.1 Introduction

YOF is considered to be a promising host for many lighting applications since it combines the benefits of both Y_2O_3 and YF_3. Some of these benefits are its low phonon energy of ~400 cm^{-1} (compared to YF_3 (350 cm^{-1}) and Y_2O_3 (>500 cm^{-1})), good optical transparency and high chemical and thermal stability [1, 2]. YOF is also considered an excellent host for DC and UC applications and has already been used in optoelectronic devices, SC, bioimaging, biodetection and photocatalysis [3, 4]. YOF doped with Ln^{3+} ions emits in various wavelength ranges e.g. the blue region if it is doped with thulium ions, the yellow region if doped with Dy^{3+} ions, the green region if doped with Tb^{3+} ions or the red region if doped with Eu^{3+} ions [5].

The electronic configuration of Bi ($[Xe]4f^{14}5d^{10}6s^{26}p^3$) allows it to exist in different oxidation states such as 0, 1+, 2+, 3+ and 5+ [6, 7]. Bi^{3+} is considered to be the most promising ion for a variety of applications due to the high stability if compared to the other oxidation states [8]. These applications include FEDs, white light emitting diodes and NIR QC if co-doped with Ln^{3+} ions [9, 10]. Bi^{3+} doping in inorganic materials has significant applications as luminescent materials. This is due to the unique optical properties that allow Bi^{3+} to emit in different wavelength ranges such as in the blue, yellow and UV ranges as in $Ca_4ZrGe_3O_{12}$:Bi^{3+}, La_3SbO_7:Bi^{3+} and YBO_3:Bi^{3+}, respectively [11, 12, 13]. Bi^{3+} emission is highly dependent on the host lattice [14]. The electronic structure of the free Bi^{3+} ion consists of different energy levels with a ground state $^1S_0$ and different excited states due to the triplet ($^3P_0$, $^3P_1$ and $^3P_2$) of the excited configuration 6s6p together with one singlet higher energy $^1P_1$ state [15, 16]. The lowest excitation transition $^1S_0 \rightarrow {}^3P_0$ is strongly forbidden. The $^1S_0 \rightarrow {}^3P_1$ (A band) transition becomes allowed due to the spin orbit coupling. The $^1S_0 \rightarrow {}^3P_2$ (B band) transition is also

allowed due to the induced coupling with unsymmetrical lattice vibration modes. The high energy $^1S_0 \rightarrow {}^1P_1$ (C band) transition is an allowed electric dipole transition [17, 18, 19]. Bi^{3+} can easily be doped into the YOF host to replace the Y^{3+} ion, due to the close ionic radius (Bi^{3+} = 0.117 nm, Y^{3+} = 0.1019 nm, for coordination number 8) [20]. If Bi^{3+} is doped in yttrium compounds it replaces the Y^{3+} ions and can yield multiple emissions. Cavalli et al. [21] investigated the utilization of the host material $Y(P_xV_{1-x})O_4:Bi^{3+}$ with tuning emission ranges from blue to yellow. They ascribed the ability to tune the emission to be dependent on the composition and the excitation wavelengths. UV emission has been investigated in 8-coordinated garnet hosts by Setlur and Srivastava [18]. They found UV emission bands that originated from the $^3P_1$ and $^3P_0$ levels to the $^1S_0$ ground state upon excitation to the $^1S_0 \rightarrow {}^3P_1$ level. Chen Lei et al. [13] ascribed a UV emission to occur from either the excitation to the $^1P_1$ or $^3P_1$ levels, from the $^1S_0$ ground state with a strong emission when excitation occurred to the $^3P_1$ level comparing to emission due to excitation to $^1P_1$. They've also explained the presence of two Y^{3+} sites for Bi^{3+} to occupy.

Previous studies on the luminescence of Bi^{3+} ion doped in oxyhalide materials like $YOF:Bi^{3+}$ and $YOCl:Bi^{3+}$ were done by Blasse and Brill in 1968 [14]. They ascribed the nature of the luminescence of these oxyhalides to emission that originated from the $^3P_1$ level to the $^1S_0$ ground state level for both hosts around 330 nm and 400 nm, respectively. They also reported the absence of the $^1S_0 \rightarrow {}^1P_1$ excitation band due to the limitation of the instruments.

To the best of the authors' knowledge, no systematic studies on the luminescence of $YOF:Bi^{3+}$ and specifically on Bi^{3+} as a activator in the YOF system has been done. This work therefore investigated the luminescence of the $YOF:Bi^{3+}$ phosphor with excitation to the $^3P_1$ level. Clarification was also obtained on the existence of a MMCT band as it seems to be present in most of the inorganic hosts doped with Bi^{3+} ions [22, 23].

6.2 Experimental

Pure YOF and Bi^{3+} doped YOF powder samples were prepared by the pyrolysis method with trifluoroacetate as precursor from a single source as described in chapter 3, section 3.1. The doped YOF: x mol % Bi^{3+} (x = 0.2, 0.3, 0.4, 0.5, 0.6 and 0.8) samples were prepared by the same method with bismuth (III) oxide added to the starting materials.

The structure of the prepared samples was characterized by XRD using a Bruker Advance D8 diffractometer (40 kV, 40 mA) with Cu K_α x-rays (λ = 0.154 nm). SEM images were taken by using the JEOL JSM-7800F SEM. High resolution XPS was obtained with a PHI 5000 Versa-probe system as was described in chapter 3, section 3.4. All measurements were performed at room temperature. PL, NIR emission and decay time measurements were done using the Edinburgh FLS980 instrument. The quantum yield measurements were done by using the same instrument equipped with an integrating sphere.

6.3 Results & Discussion

The XRD patterns of the prepared phosphors showed the crystalline phase of YOF, see figure 1(a), with a rhombohedral structure (space group: $R\bar{3}m$ (166)) [A. W. Mann, D. J. M. Bevan, Acta Cryst. B26 (1970) 2129] as confirmed by a standard card file (ICSD No. 71-2100). The difference in the ionic radius of Y^{3+} for coordination number 8 (0.1019 nm) and Bi^{3+} (0.117 nm) [20] caused a slight shift in the peaks towards lower angles with increased doping concentrations. This kind of behaviour was also reported during investigations done on zinc oxide doped with manganese for which it was reported that the shifting of the diffraction peaks towards lower angles was attributed to compressive stress and expansion of the lattice parameters [24]. The schematic illustration for the crystal structure of the YOF host is shown in figure 1(b). Each Y^{3+} ion is surrounded with four F^- and four O^{2-} ions that yields the 8 coordination for Y^{3+} ions. The Y^{3+}, O^{2-} and F^- ions are coordinated in the structure in an arrangement of a bi-capped trigonal antiprism with 6c Wyckoff positions with the symmetry for the Y^{3+} cation as C_{3v} site symmetry. The crystal structure of YOF can be derived from the fluorite cubic structure with a slight trigonal distortion [25, 26].

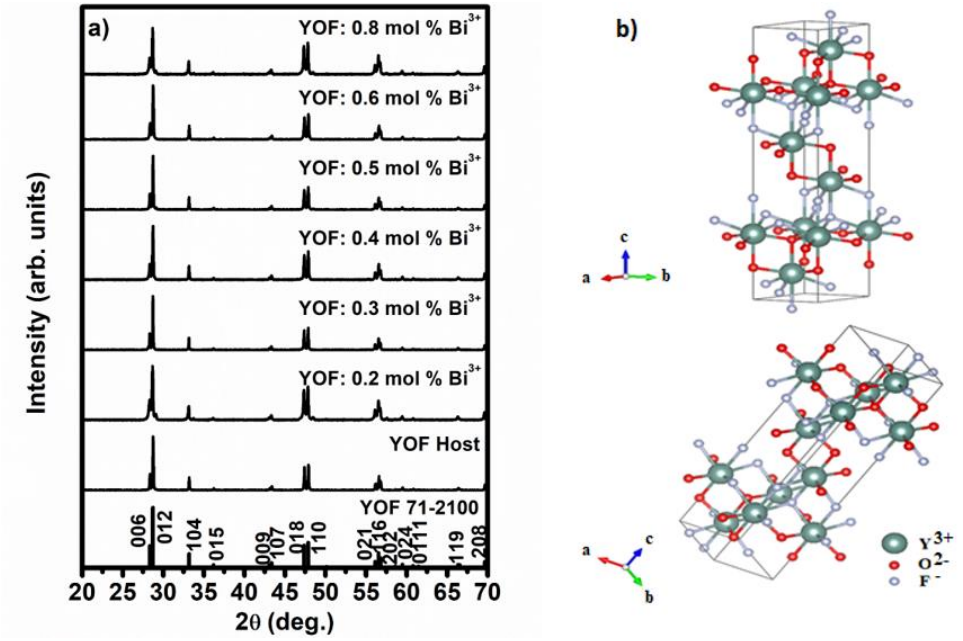

Figure 1(a): XRD patterns for the YOF: x Bi^{3+} phosphors annealed at 900 °C and (b) the schematic illustration for the crystal structure of the YOF host. The crystal structure was drawn by using Vesta software [27].

The estimation of the crystallite sizes of the prepared powders was done by using the Scherrer equation for the broadening of the diffraction peaks [28]. The broadening of the diffraction peaks can result from both instrumental broadening as well as sample broadening. Instrumental broadening can be obtained by collecting the diffraction pattern and the line broadening of a standard material (e.g. Si single crystal). The corrected broadening (β_{hkl}) corresponding to the diffraction peak at a specified hkl index of the material can then be calculated using

$$(\beta_{hkl})^2 = (\beta_{hkl})^2_{measured} - (\beta_{hkl})^2_{instrumental} \text{.....1.}$$

This is related to the crystallite size according to the Scherrer equation

$$\beta_{hkl} = \frac{k\lambda}{D\cos\theta} \text{ .....2,}$$

where, β_{hkl} represents the peak broadening or FWHM corresponding to the diffraction angle θ and Miller indices hkl, λ represents the wavelength of Cu K_α X-ray radiation (0.154 nm), D is the crystallite size in nanometers and k represents the shape factor and is approximately 0.9 for spherical shapes [29, 30].

The crystallite sizes of the prepared phosphors were calculated by using Scherrer equation (2) with the diffraction peaks and corresponding Miller indices and are given in table 1. The

variation of the crystallite sizes is depicted in figure 2 and decreased from 81 nm for the host down to 41 nm for the samples doped with 0.8 mol % of Bi^{3+}. An increase in the doping concentration resulted in the broadening of the FWHM of the XRD peaks, therefore the result is a decrease in the crystallite size. This behaviour might be due to the increase in the lattice strain caused by an increase in the dopant concentration.

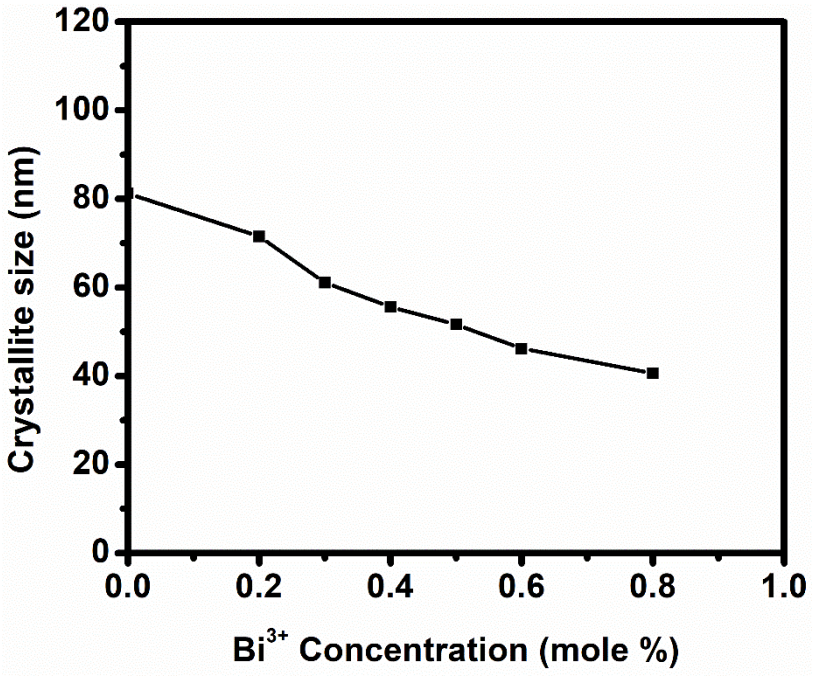

Figure 2: The variation of the crystallite size with Bi^{3+} concentrations.

Table 1: The crystallite sizes of the prepared samples obtained by using the Scherrer equation.

Sample	Crystallite size (nm) (± 1)
YOF: 0 mol % Bi^{3+}	81
YOF: 0.2 mol % Bi^{3+}	72
YOF: 0.3 mol % Bi^{3+}	61
YOF: 0.4 mol % Bi^{3+}	56
YOF: 0.5 mol % Bi^{3+}	52
YOF: 0.6 mol % Bi^{3+}	46
YOF: 0.8 mol % Bi^{3+}	41

The morphology of the prepared samples was investigated by using SEM and is shown in figure 3. The host sample showed an agglomeration of spherical small particles into bigger particles, see figure 3(a). Li et al. [31] reported the same morphology during investigations done on samples prepared using the pyrolysis method of YOF:Yb^{3+}, Er^{3+} thin films. Eloussifi et al. [32] investigated thermal decomposition of the $Y(CF_3COO)_3$) precursor and the same kind of morphology was reported. Figures 3(b) to 3(g) show an increase in agglomeration of the spherically shaped particles with an increase in the dopant concentration.

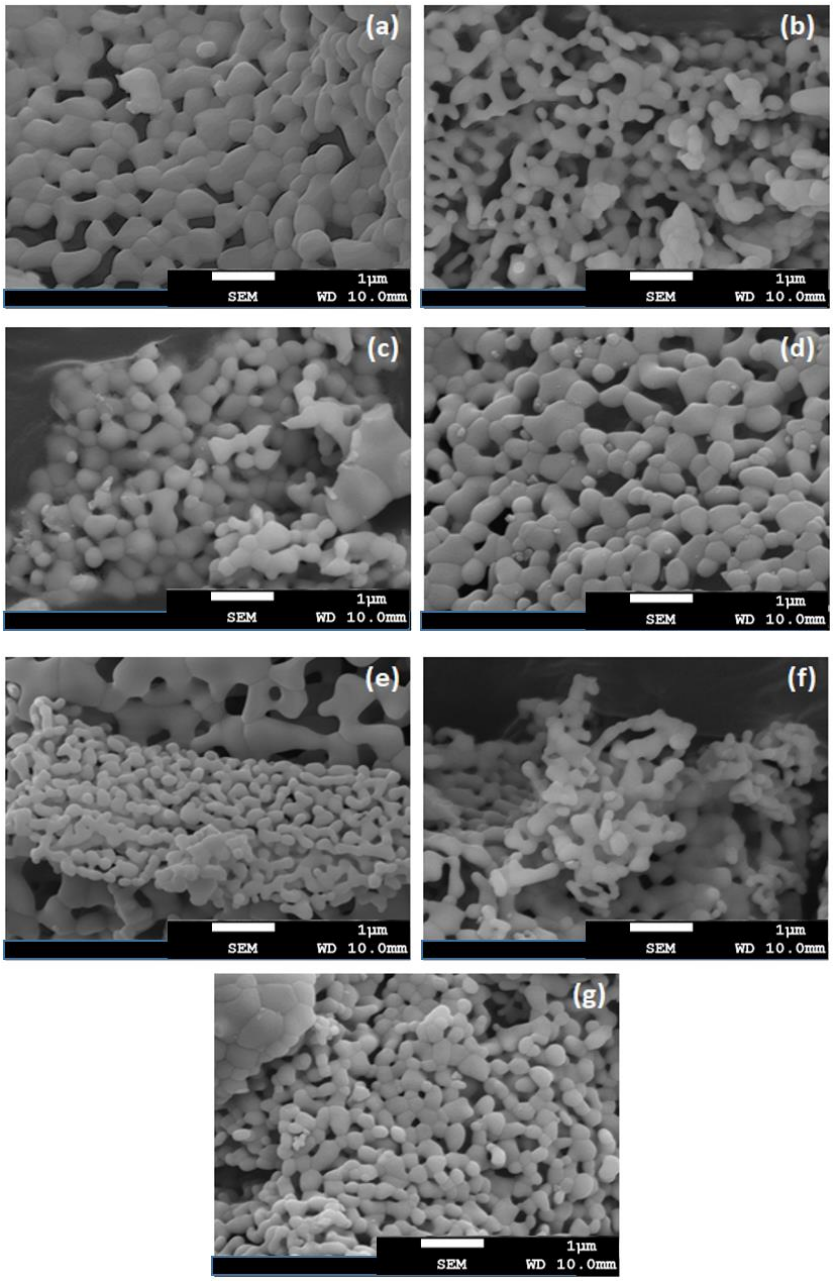

Figure 3: SEM images of the YOF:Bi^{3+} phosphors prepared by the pyrolysis method, (a) 0, (b) 0.2, (c) 0.3, (d) 0.4, (e) 0.5, (f) 0.6 and (g) 0.8 mol %.

AES studies and SEM images were also done on five different areas on the YOF: 5 mol % Bi^{3+} high concentration sample in order to clarify the identity of the smaller particles and bigger agglomerations. Figure 4(a) shows the SEM image with five different areas marked with a blue pointer and figure 4(b) shows the corresponding AES spectra. All the areas clearly showed AES peaks for Y, O, F and Bi. The AES peaks around 82 eV, 134 eV, 1606 eV, 1750 eV and 1827 eV were ascribed to Y. The C, O and F peaks were situated at 277 eV, 514 eV and 658 eV, respectively [33]. The Bi peaks were located at 105 eV and 1894 eV. The presence of C was attributed to contamination due to adventitious hydrocarbons and is considered to be a common impurity in fluoride compounds [33]. With the AES results it was concluded that Bi was homogeneously distributed on the surface of the sample.

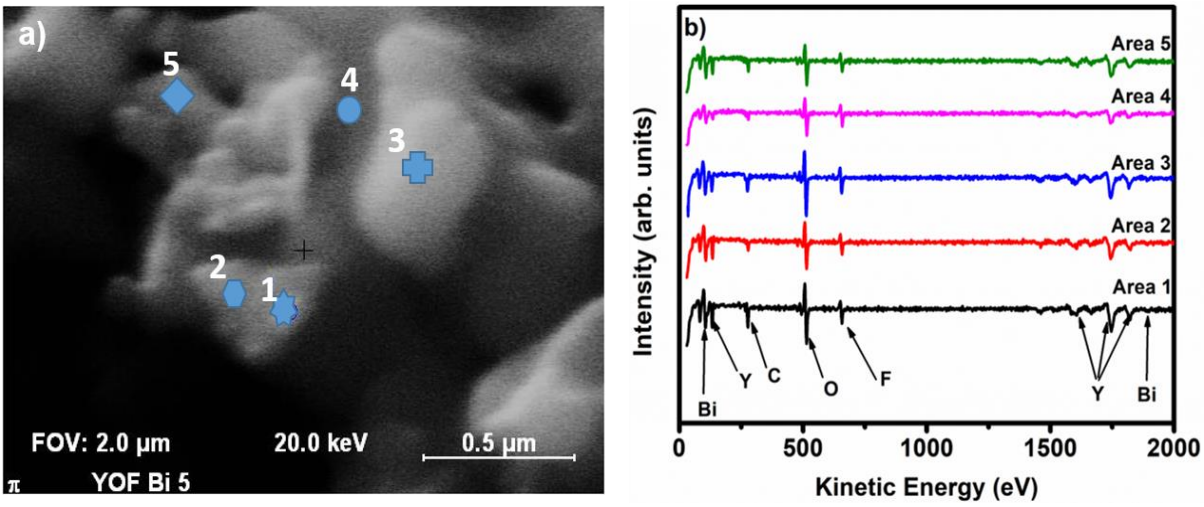

Figure 4 (a): SEM image of the YOF: 5 mol % Bi^{3+} phosphor prepared by the pyrolysis method indicating the different AES analysis areas (1), (2), (3), (4) and (5) and (b) the corresponding AES spectra for each area.

XPS has been used to study the surface composition of a YOF: 5 mol % Bi^{3+} high concentration sample due to the difficulties of detecting Bi^{3+} at low concentrations. All the XPS high-resolution peaks were corrected for charge compensation in respect to the C 1s peak at 284.8 eV. The C contamination was ascribed to adventitious hydrocarbons on the surface [34]. The high-resolution peaks were deconvoluted and analyzed with Multipak software v. 8.2. Figure 5 shows the peak deconvolution of the (a) Y 3d, (b) O 1s and (c) F 1s peaks. The Y 3d peak, figure 5(a), can be deconvoluted into two main binding energy peaks of Y 3d at 157.1 eV and 159.1 eV that were due to the spin orbit splitting into the $3d_{5/2}$ and $3d_{3/2}$ peaks, respectively. The energy ranges of the Y 3d and Bi 4f peaks overlap. Therefore, two additional pairs of peaks were also fitted in the Y 3d peak range that corresponded to Bi 4f peaks. The Bi 4f peaks were

situated at 158.7 eV and 164 eV for the first pair and at 156.5 eV and 161.8 eV for the second pair. The lowest binding energy peak in each pair was related to the $4f_{7/2}$ spin orbit splitting peak and the highest binding energy peak to the $4f_{5/2}$ peak. The O 1s peak, figure 5(b), shows two peaks at 529.1 eV and 531.4 eV. The F 1s peak shows one peak at 685 eV (figure 5(c)).

The Y $3d_{5/2}$ peak at 157.1 eV correlated well with other reported values for the Y $3d_{5/2}$ peak in the YOF structure [35, 36]. The O 1s peak at 529.1 eV corresponded to the oxygen peak in the YOF structure and this was also reported by Rizhkof et al. [37]. The second O 1s peak at 531.4 eV can be ascribed to hydroxyl or carbonate groups [38]. The F 1s peak at 685 eV was also in correlation with reported F 1s XPS data for the YOF structure [37]. The two pairs of fitted peaks for the Bi 4f peak corresponded to the Bi^{3+} and Bi metal oxidation states. The 158.7 eV and 164 eV peaks corresponded to the Bi $4f_{7/2}$ and Bi $4f_{5/2}$ peaks of Bi^{3+}, respectively and the other pair at 156.5 eV and 161.8 eV corresponded to the Bi $4f_{7/2}$ and Bi $4f_{5/2}$ peaks of Bi metal [39, 40]. The separation between the spin orbit splitting peaks was 5.31 eV. The presence of the Bi metal therefore is due to the segregation of Bi^{3+} on the surface of the material and its reduction to Bi [39].

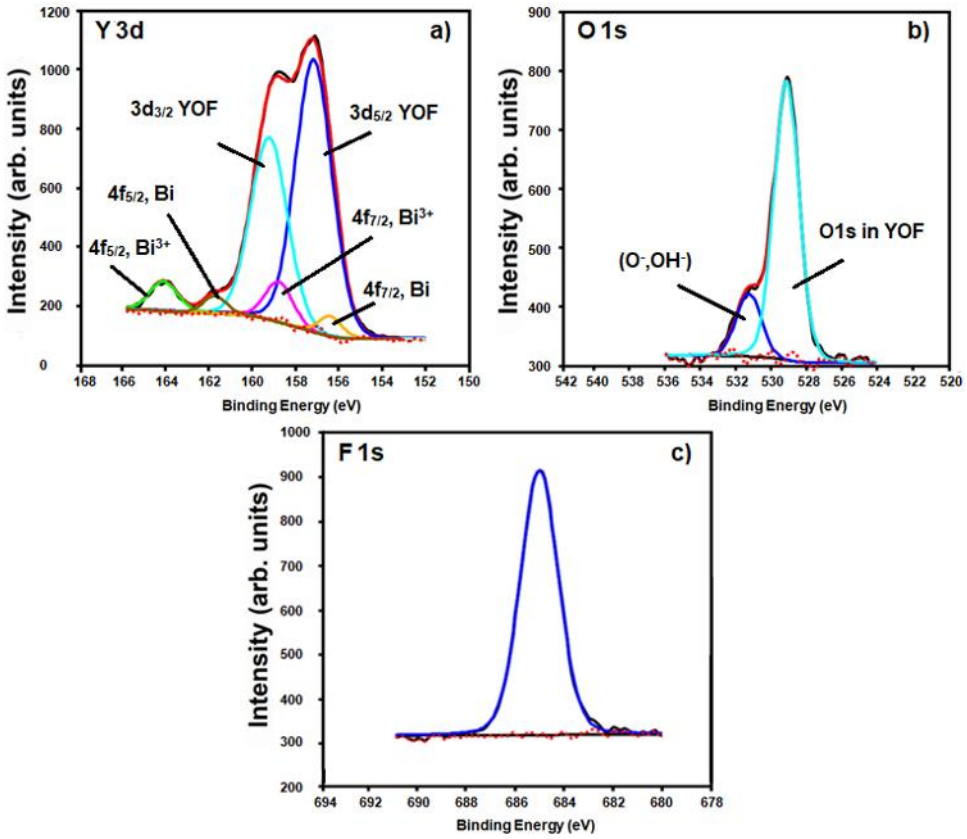

Figure 5: High resolution XPS peaks of YOF:5 mol % Bi^{3+} for the (a) Y 3d, (b) O 1s and (c) F 1s peaks.

The PL excitation and emission spectra were systematically studied for the prepared YOF:Bi^{3+} phosphors in order to determine the luminescent nature of Bi^{3+} in the YOF host. The transition bands $^1S_0 \rightarrow {}^3P_1$, $^1S_0 \rightarrow {}^3P_2$ and $^1S_0 \rightarrow {}^1P_1$ are known as the A, B and C bands. Excitation in the Bi^{3+} ion depends on the positions of the energy levels. In general, excitation can either be to the $^3P_1$ (A band) or to the $^1P_1$ (C band). The $^1S_0 \rightarrow {}^3P_2$ (B band) is not allowed due to the absence of coupling with unsymmetrical lattice vibration modes [17, 18, 19].

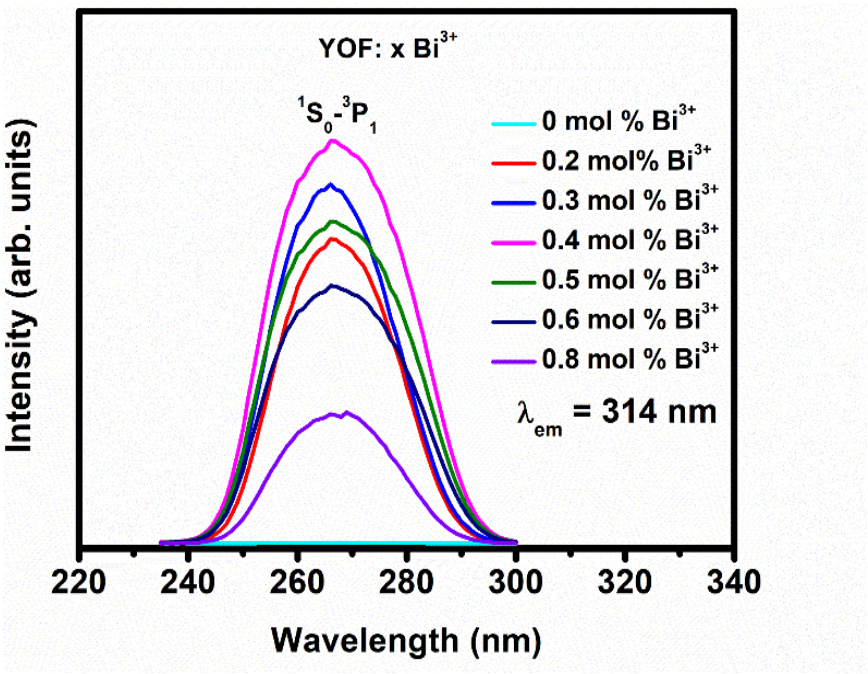

Figure 6: PL excitation of YOF: x Bi^{3+} (x = 0.2, 0.3, 0.4, 0.5, 0.6 and 0.8 mol %) at λ_{em} = 314 nm emission.

The excitation spectrum consisted of one broad band centered at 267 nm that ranged from 240 – 300 nm, see figure 6. Blasse and Brill [14] have studied the luminescence of YOF:Bi^{3+} with an excitation band at 265 nm and they ascribed it to the A band of Bi^{3+}. The positions of the A band in the UV range have also been investigated in other hosts [13, 18]. Chen Lei et al. [13] studied YBO_3:Bi^{3+} and reported on the A band situated at 265 nm. The broad peak at 267 nm in figure 7 can therefore be ascribed to the A band transition.

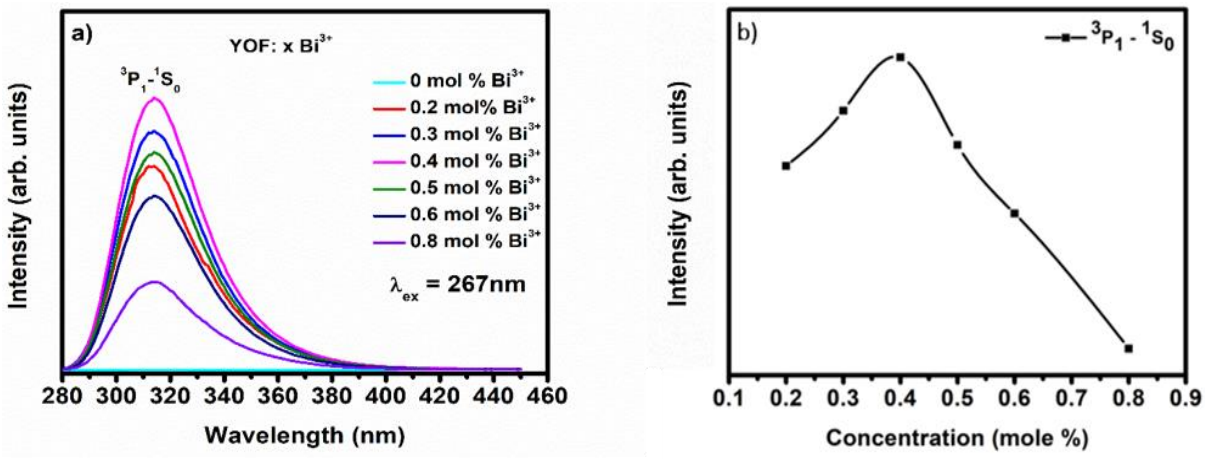

Figure 7: (a) PL emission of YOF: x Bi^{3+} (x = 0.2, 0.3, 0.4, 0.5, 0.6 and 0.8 mol %), λ_{ex} = 267 nm and (b) the variation of the $^3P_1 \rightarrow {}^1S_0$ emission as function of the Bi^{3+} concentration.

The emission spectra under 267 nm excitation is shown in figure 7(a). A broad band in the 280 – 410 nm region centered at 314 nm was observed. Blasse and Brill [41] also studied the luminescence of Bi^{3+} in Y_2SO_4 with the presence of two excitation bands. They ascribed the first excitation band to the edge of the excitation due to the $^1S_0 \rightarrow {}^1P_1$ transition and the second band due to the $^1S_0 \rightarrow {}^3P_1$ transition at 264 nm of Bi^{3+}. They also reported a broad emission band centered at 310 nm with a Stoke shift of about 47 nm. These results correlate well with the emission band obtained in figure 7(a) and therefore the emission band centered at 314 nm can then also be attributed to the $^3P_1 \rightarrow {}^1S_0$ transition, with a Stokes shift of about 47 nm. This transition was also reported in other systems such as YBO_3:Bi^{3+} [13] and $Y_2Sn_2O_7$:Bi^{3+} [42].

The emission intensity increased gradually with increasing Bi^{3+} content from 0.2 mol % up to the optimum concentration of 0.4 mol %, then decreased as depicted in figure 7(b). This behaviour is a well-known phenomenon in Bi^{3+} doped inorganic hosts and is called concentration quenching [43], due to the excitation being transferred in the crystal to non-emitting defects (killer centres). The concentration quenching of Bi^{3+} emission varied in different hosts, e.g. in $Ba_2Mg(BO_3)_2$:Bi^{3+} it occurred for the 0.1 mol % concentration sample [44], for $CaSb_2O_6$:Bi^{3+} at 0.75 mol % [45] and for $Ca_{14}Al_{10}Zn_6O_{35}$:Bi^{3+} at 1 mol % [46]. The critical distance, R_c, can be estimated in order to confirm the type of interaction responsible for concentration quenching. The critical distance is the distance where the transfer probability is equal to the inverse of the intrinsic lifetime [47]. Blasse et al. [48] explained the behaviour of the concentration quenching as a non-radiative transfer of energy between two activator ions

and that the critical distance can be obtained through the transfer probability. They also reported that the critical distance can be obtained as a function of the critical concentration, X_c, by using the following equation [48]:

$$R_c = 2\left[\frac{3V}{4\pi X_C N}\right]^{\frac{1}{3}} \text{.....3,}$$

where V is the volume of the host lattice unit cell and equal to 235.85 $Å^3$ [49] and N is the number of ions in the host unit cell that can be replaced by the dopant and it is equal to 6 [50]. In this procedure, it is assumed that the critical concentration equals the optimum concentration corresponding to the maximum emission intensity. This is a rough approximation allowing to get limited quantitative information. With the experimental value of X_c, the critical distance was then calculated to be 2.7 nm. This calculated value for the critical distance of Bi^{3+} was in good agreement with other reported values such as 3.1 nm for the $Ca_{14}Al_{10}Zn_6O_{35}:Bi^{3+}$ system [44], 2.7 nm for the $Ca_3(BO_3)_2:Bi^{3+}$ system [51] and 2.1 nm for $Ca_5(BO_3)_3F:Bi^{3+}$ [52]. It can be concluded that the critical distance is affected by the crystal structure and different sites. The existence of the migration of energy from one activator to another and eventually to killer centres (eg. Impurity ion or defect) usually occurs at small distances between the dopant ions [53]. Since the exchange interaction is active only for short interionic distances, it can be proposed that the multipolar interaction is the dominant quenching mechanism in the $YOF:Bi^{3+}$ system.

Further investigations can also be done on the type of multipolar interaction responsible for the emission quenching based on a report of Van Uitert that was modified by Ozawa [54, 55]. The suggested equation was first modified to analyse rare earth ions and then it was extended for other types of ions. The equation can be used to determine the strength of the multipolar interaction from the change in the emission intensity with concentration [55]. The strength of the multipolar interaction (s) can be expressed as follows:

$$\frac{I}{C} = k\left(1 + \beta(C)^{\frac{s}{3}}\right)^{-1} \text{.....4.}$$

C is the activator concentration, I/C is the intensity per activator concentration, s = 6, 8 or 10 for dipole-dipole (d-d), dipole-quadrupole (d-q) and quadrupole-quadrupole (q-q) interactions respectively, k and β are constants for the same excitation conditions for a given host material. When the condition $\beta C^{\frac{s}{3}} \gg 1$ is satisfied (which will occur at high concentration), equation (4) reduces to:

$$\frac{I}{C} = \frac{k}{\beta C^{\frac{s}{3}}} \quad \text{.....5,}$$

where k is a constant [54, 56] and C is the dopant concentration greater than the critical concentration. A plot of log(I/C) versus log(C) was obtained with a linear fit and is shown in figure 8. The value of the slope (-2.6) corresponds to –s/3 and was used to obtain the value for s as 7.8 (close to 8) and the type of the multipolar interaction was then identified as the d-q interaction. According to Dexter's theory the non-radiative energy migration will be enhanced with increasing concentration and lead to emission quenching [43]. We suggest the same assumption to occur in our system with mixing of the orbitals which might be 6s+6p of Bi^{3+}. The d-q interaction was also identified during investigations in other systems doped with Bi^{3+} such as the vanadate compounds (Y,Lu,Sc)VO_4:Bi^{3+} [57].

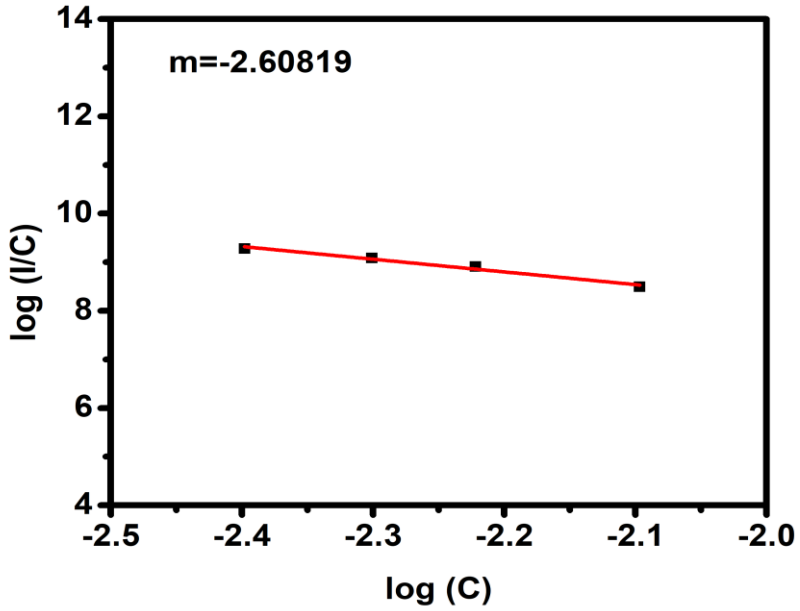

Figure 8: The plot of log(I/C) versus log(C) for the YOF:Bi^{3+} phosphor.

Depiction of excitation and emission peaks was done in figure 9 in order to extract more information on the nature of the emission band. The depiction of the two bands was done in the energy scale. In figure 9(a) the excitation peaked as a single broad peak at 267 nm with FWHM around 31 nm. The FWHM value was reported to be as large as 32 nm for the excitation of Bi^{3+} [8]. Figure 9(b) shows the UV asymmetric emission band that peaked at 314 nm with FWHM around 36 nm.

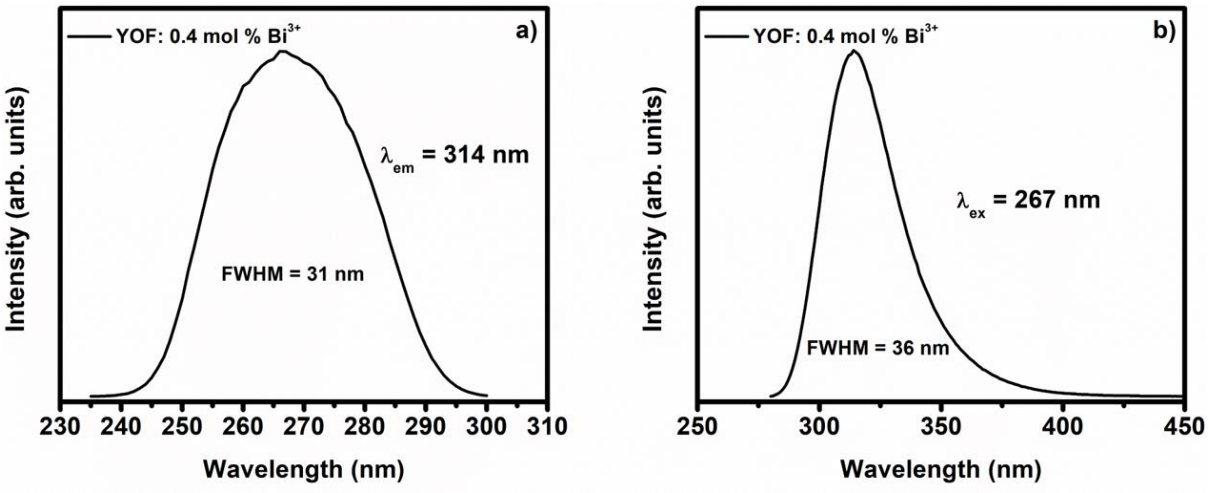

Figure 9: (a) The excitation band of YOF: 0.4 mol % Bi^{3+} monitoring the emission at 314 nm and (b) the emission band excited with 267 nm.

The mechanism of the excitation of YOF:Bi^{3+} can be explained by estimating the position of the MMCT band in respect to the $^1S_0 \rightarrow {}^3P_1$ A band transition. Systematic studies of the existence of the MMCT band in the excitation spectrum of Bi^{3+} was first done by Boutinaud [58]. He proposed an empirical model to predict the position of the MMCT band in any host doped with Bi^{3+} based on experimental data of numerous hosts doped with Bi^{3+} ions. He collected structural properties from the Inorganic Crystal Structure Database and compiled the shortest distances (d_{host}) between the metal (M^{n+} = Y^{3+} ion) site and the cation site for Bi^{3+}. The position of the MMCT band considering the metal Y^{3+} can be predicted by the following expression with an accuracy of 3000 cm^{-1} (26 nm) [58]:

$$\mathbf{MMCT\ (cm^{-1}) = } k_{CN'} \left[\chi_{CN}\ (Bi^{3+}) - \alpha_{CN'}^{CN} \frac{\chi_{CN'}\ (Y^{3+})}{d_{corr}} \right] \text{.....6.}$$

CN = 8 is the coordination number of the Bi^{3+} ion. CN′ = 8 is the coordination number of the metal ion to which CT occurred. $k_{CN'}$ = 41 044 cm^{-1} [58] was a constant depending on the value of CN′. The χ_{CN} = 1.29 and $\chi_{CN'}$ = 1.34 values are the optical electronegativity for both the Y^{3+} and the Bi^{3+} ions respectively [57]. The constant $\alpha_{CN'}^{CN}$ is an adjustable parameter dependent on CN and CN′ and reported by Boutinaud to be 1.11 [58]. The value of d_{corr} is the corrected value that accounted for the effect of anion relaxation subsequent to Bi^{3+} doping. The distance between Bi^{3+} and the M^{n+} ions given by the separation of their sites in the host lattice is therefore corrected by the difference of the Bi^{3+} and M^{n+} crystal ionic radii (r). The expression to obtain d_{corr}, for the crystal radii, r (Bi^{3+}) = 0.131 nm and for r (Y^{3+}) = 0.1159 nm, was d_{corr} =

$d_{Host} + \frac{1}{2}[r(Bi^{3+}) - r(Y^{3+})]$. The value for d_{Host} was obtained from literature to be 0.3102 nm and corresponds to the experimental value [59] and d_{corr} was then calculated to be 0.318 nm. The MMCT band was then finally calculated to be situated at approximately 36 500 ± 3000 cm^{-1} (274 ± 26 nm).

According to Amer and Boutinaud [60], we can differentiate between the A band and the MMCT band by predicting the position of the A band as well. Prediction of the A band is dependent on the nephelauxetic ratio factor (h_e) and the position is given through the relation [60]:

$$\mathbf{E_A\,(X, cm^{-1}) = 23970 + 50051\ exp\left(\frac{-h_e}{0.551}\right)} \text{ ……..7,}$$

h_e is the nephelauxetic ratio factor and for our system we estimated it as 0.819 based on the experimental data for the yttrium oxyhalides [61]. Estimation of the h_e value was determined with the constraints of the ligand type of the host; according to Jorgenson [62, 63] the h_e increases in the sequence of the ligand type (nephelauxetic series) as $F^- > Cl^- > Br^- > I^- > O^{2-} > S^{2-}$. As an example, the h_e value for KaF, KCl, KBr and KI is 0.249, 0.456, 0.494 and 0.629, respectively. The ratio of the h_e value between each consecutive ligand in the nephelauxetic series of the same metal in one group is almost comparable to the ratio of a metal in different groups to the other metals with a slight variation (e.g. ratio of h_e^{KCl}/h_e^{KF} = 1.54 and h_e^{KBr}/h_e^{KCl} = 1.1). Applying this argument, allow us to estimate h_e value for YOF. The obtained h_e value for YOF was based on this constrains and the difference for different ligand types as well as the values of YOBr (h_e = 1.349) and YOCl (h_e = 1.229) with an estimated ratio of $\frac{he^{Cl^-}}{he^{F^-}}$ = 1.5, since the ratio h_e^{YOBr}/h_e^{YOCl} = 1.1 [61]. The estimated value for h_e was difficult to calculate since some required parameters were not presented (e.g. refractive index, dielectric coefficient and average energy gap). The predicted value for the A band is about 35 300 ± 3000 cm^{-1} (283 ± 26 nm) with a difference $|E_{exp}(Bi^{3+})\text{-}E_A(X)|$ of about 2200 cm^{-1} (17 nm). The energy difference $|E_{exp}(Bi^{3+})\text{-MMCT}(Bi^{3+})|$ is about 1000 cm^{-1} (7 nm) where E_{exp} represents the experimental excitation value. According to the energy difference between the experimental excitation value and the roughly calculated values for both the A and MMCT bands, we can therefore consider that the excitation is more likely to be due to the MMCT band. This estimation is within the terms of the given error where MMCT = 36 500 ± 3000 cm^{-1} (274 ± 26 nm) and E_A = 35 300 ± 3000 cm^{-1} (283 ± 26 nm). This suggests that the MMCT band is slightly laying above the A band. We could not detect another band in the excitation spectrum

that might be ascribed to the A band. This motivated us to investigate more in depth the nature of the emission. Considering the Stokes shift of the emission and the fact that MMCT emitters have large stoke shifts [60], we were able to resolve this by looking to the energy difference $|MMCT(Bi^{3+})-E_A(X)-\Delta Stokes|$ which has been suggested by Amer and Boutinaud [60]. According to this model, the maximum energy difference of about 4000 cm^{-1} (32 nm) is related to the A band emitter whereas, the minimum energy difference for MMCT is about 7500 cm^{-1} (52 nm). The calculated energy difference according to the previous equation is about 4400 cm^{-1} (35 nm) and this value is slightly above the 4000 cm^{-1} (32 nm) limit and allows us to consider that our system is intermediate between the A band emitters and the MMCT emitters. On the basis of the Stokes shift value which is a characteristic of A band emitters, we can consider our emission to originate from the A band. This corresponded well with the model suggested by Amer and Boutinaud. According to the two models of the excitation energy differences $|E_{exp}(Bi^{3+})-E_A(X)|$ and $|E_{exp}(Bi^{3+})-MMCT(Bi^{3+})|$ and the Stokes shift expression $|MMCT(Bi^{3+})-E_A(X)-\Delta Stokes|$, a final suggestion can therefore be made that the MMCT band is slightly lying above A band. During the excitation process to both the MMCT and the A band, the energy transferred non-radiatively from the MMCT to the A band and consequently the emission is only due to the A band. See figure 10 for the proposed energy level and mechanism controlled the luminescence of $YOF:Bi^{3+}$.

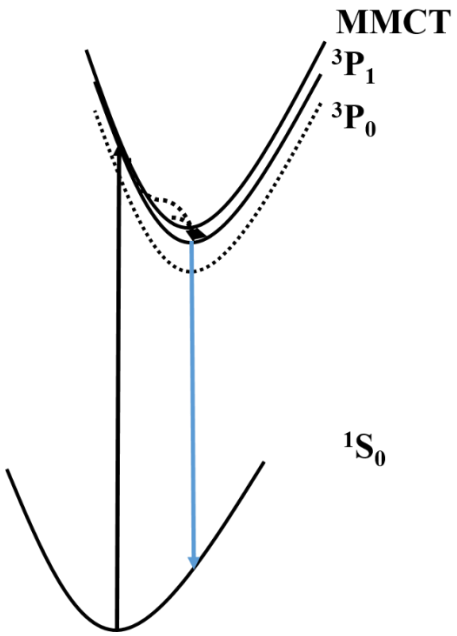

Figure 10: Proposed energy level diagram and luminescent mechanism of Bi^{3+} doped in YOF.

The fluorescence decay curves for the prepared YOF:Bi^{3+} samples are depicted in figure 11. The decay curves showed a clear non-exponential profile. This behaviour is consistent with the multi-component of the Bi^{3+} emission. The non-exponential decay curves were fitted using a bi-exponential equation [64, 65]:

$$\mathbf{I(t) = A_0 + A_1 exp(-t/\tau_1) + A_2 exp(-t/\tau_2) \ldots\ldots\ldots\ldots\ldots\ldots 8}$$

$$\mathbf{< \tau > = (A_1 \tau_1^2 + A_2 \tau_2^2)/(A_1 \tau_1 + A_2 \tau_2) \ldots\ldots\ldots\ldots\ldots\ldots 9,}$$

where I(t) is the PL intensity, $< \tau >$ is the average decay time, τ_1 and τ_2 the emission decay times and A_1 and A_2 are their relative weights [64]. The calculated lifetimes τ_1 and τ_2 were in the order of microseconds and depicted in table 2. This is in good agreement with previously reported values for decay lifetimes calculated for $Ca_3Al_2O_6:Bi^{3+}$, Sm^{3+} [66] and $Sr_2Y_8(SiO_4)_6O_2:Bi^{3+}$, Eu^{3+} [67]. The lifetimes of Bi^{3+} doped materials were reported to be in the range of nanoseconds up to microseconds [59]. The ns^2 ions is sensitive to the surrounding ligands [14] and any presence of defects in the host will affect the position of both the ground-excited levels [68]. Thus, we might suggest that the shortest decay time was related to the Bi^{3+} ions locally perturbed by defects.

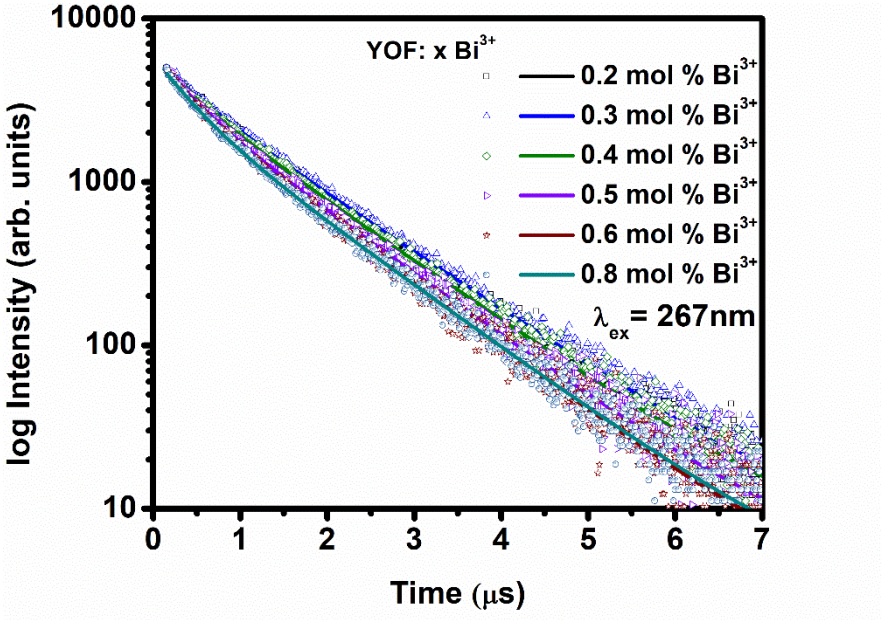

Figure 11: Decay curves of the $^3P_1 \rightarrow {}^1S_0$ transition for the YOF:Bi^{3+} doped samples (λ_{ex} = 267 nm, λ_{em} = 314 nm).

Table 2: The calculated decay times for the prepared YOF:Bi^{3+} samples.

Sample	τ_1/ µs	τ_2/ µs	$< \tau >$ / µs
YOF: 0.2 mol % Bi^{3+}	0.40	1.18	1.11
YOF: 0.3 mol % Bi^{3+}	0.37	1.21	1.14
YOF: 0.4 mol % Bi^{3+}	0.34	1.17	1.09
YOF: 0.5 mol % Bi^{3+}	0.27	1.1	1
YOF: 0.6 mol % Bi^{3+}	0.26	1.1	0.97
YOF: 0.8 mol % Bi^{3+}	0.3	1.1	0.98

The fluorescence quantum yield (η) of the YOF:Bi^{3+} (0.4 mol %) prepared sample was measured using the FLS980 system equipped with the integrating sphere and is shown in figure 12. The absolute quantum yield (η) is the number of the emitted photons (N^{em}) to the number of the absorbed photons (N^{ab}) and can be expressed as:

$$\eta = \frac{N^{em}}{N^{ab}} \quad \text{.....10.}$$

The scatter and emission of the sample was recorded for the direct excitation method [69] and the absolute quantum yield (η_{DExc}) can be written as:

$$\eta_{DExc} = \frac{E_B - E_A}{S_A - S_B} \quad \text{.....11,}$$

with $E_B(\lambda)$ the emission record of the sample, $E_A(\lambda)$ the emission record of the reference, $S_A(\lambda)$ is the scatter record of the reference and $S_B(\lambda)$ the scatter record of the sample. This data is depicted in figure 12 and the quantum yield was found to be 60 %. This quantum yield value is very suitable for sensitizer application with other luminescent ions through energy transfer mechanisms.

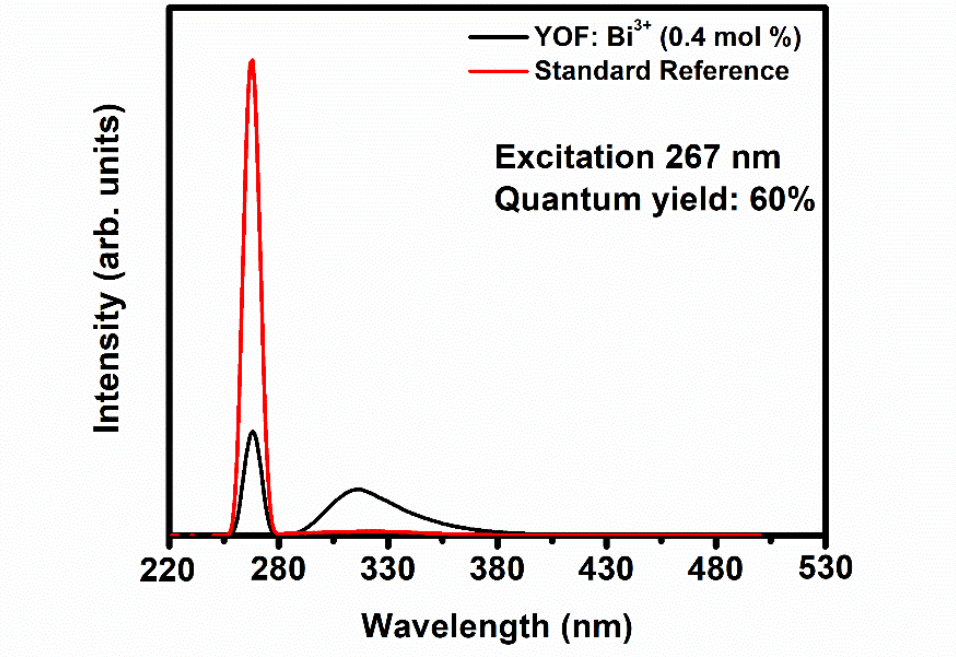

Figure 12: The measured quantum yield using the integrated sphere for the YOF: 0.4 mol % Bi^{3+} sample with λ_{ex} = 267 nm.

6.4 Conclusions

The YOF:Bi^{3+} phosphor was successfully synthesized by using the pyrolysis method. XRD results showed a high crystallinity of the powder, with a rhombohedral YOF structure (space group: $R\bar{3}m$ (166)), after annealing at 900 ^{0}C. The crystallite sizes as calculated by the Scherrer equation decreased from 81 to 41 nm with increasing doping concentration. SEM images showed an agglomeration of spherically shaped small particles into bigger particles for the host sample. The particles started to form bigger agglomerated particles with an increase in the dopant concentration. AES results confirmed that Bi was homogeneously distributed on the surface of the sample. Two pairs of peaks could be fitted to the XPS data for the Bi 4f peak. The peaks were attributed to Bi^{3+} and Bi metal. PL studies revealed a broad UV emission band centered at 314 nm that originated from the $^3P_1 \rightarrow {}^1S_0$ A band with a symmetric excitation of 267 nm that corresponded to the $^1S_0 \rightarrow {}^3P_1$ A band of Bi^{3+}. In order to explain the excitation and emission mechanism, investigations and theoretical calculations were done to predict the MMCT band. The MMCT excitation band was calculated to be situated at approximately 36 500 ± 3000 cm^{-1} (274 ± 26 nm) that was in the same range than the A band. The emission peak at 314 nm was attributed to the $^3P_1 \rightarrow {}^1S_0$ A band transition. During excitation to the MMCT band and to both the A band levels, non-radiative decay occurs from the MMCT to the emitting $^3P_1$ level. The interconfigurational nature of the transition and the presence of defects could

result in the broadening of the excitation and emission peaks. The decay times obtained were in the microsecond range and showed the presence of Bi^{3+} centres perturbed by nearby defects. The measured quantum yield was measured to be 60 % by using the integrating sphere. According to the PL investigations the YOF:Bi^{3+} phosphor is therefore an appropriate candidate for optoelectronic applications such as for UV-LED, SC and scintillators, or to be applied as a sensitizer with other Ln^{3+} ions.

References

[1] G. Chai, G. Dong, J. Qiu, Q. Zhang and Z. Yang, Sci. Rep. 3 (2013) 1 - 10.

[2] H. He, Q. Liu, D. Yang, Q. Pan, J. Qiu and G. Dong, Sci. Rep. 6 (2016) 1 - 11.

[3] Y. Zhang, D. Geng, X. Kang, M. Shang, Y. Wu, X. Li, H. Lian, Z. Cheng and J. Lin, Inorg. Chem. 52 (2013) 12986 - 12994.

[4] Y. Zhang, X. Li, Z. Hou and J. Lin, Nanoscale, 6 (2014) 6763 - 6771.

[5] R. Li, L. Li, W. Zi, J. Zhang, L. Liu, L. Zou and S. Gan, New J. Chem. 39 (2015) 115 - 121.

[6] H. Ju, J. Liu, B. Wang, X. Tao, Y. Ma, S. Xu, Ceram. Int. 39 (2013) 857 - 860.

[7] R. Cao, Y. Cao, T. Fu, S. Jiang, W. Li, Z. Luo, J. Fu, J. Alloys Compd. 661 (2016) 77 - 81.

[8] H.T. Sun, J. Zhou and J. Qiu, Prog. Mater. Sci. 64 (2014) 1 - 72.

[9] B. Han, J. Zhang, P. Li, J. Li, Y. Bian, H. Shi, Opt. Mater. 37 (2014) 241 - 244.

[10] A. Huang, Z. Yang, C. Yu, Z. Chai, Ji. Qiu, and Z. Song, IEEE Photonic J. 10 (2018) 1 - 7.

[11] Z. Jiang, J. Gou, Y. Min, C. Huang, W. Lv, X. Yu, X. Su and L. Duan, J. Alloys Compds. 727 (2017) 63 - 68.

[12] V.G. Suchithra, P.P. Rao and B.A. Aswathy, Chemistry Select, 2 (2017) 7602 - 7611.

[13] L. Chen, H. Zheng, J. Cheng, P. Song, G. Yang, G. Zhang and C. Wu, J. Lumin. 128 (2008) 2027 - 2030.

[14] G. Blasse and A. Bril, J. Chem. Phys. 47 1920 (1967) 217 - 222.

[15] A.M. Srivastava and A. Szarowski, J. Solid State Chem. 146 (1999) 494 - 498.

[16] L. Wang, Q. Sun, Q. Liu, J. Shi, J. Solid State Chem. 191 (2012) 142 - 146.

[17] A.M. Srivastava, Mater. Res. Bull. 37 (2002) 745 - 751.

[18] A.A. Setlur and A.M. Srivastava, Opt. Mater. 29 (2006) 410 - 415.

[19] H.C. Swart and R.E. Kroon, Opt. Mater. X, 2 (2019) 100025 (22 pages).

[20] R.D. Shannon, Acta Cryst. A32 (1976) 751 - 767.

[21] E. Cavalli, F. Angiuli, F. Mezzadri, M. Trevisani, M. Bettinelli, P. Boutinaud and M. G. Brik, J. Phys.: Condens. Matter. 26 (2014) 1 - 13.

[22] M. Ilmer, B.C. Grabmaier and G. Blasse, Chem. Mater. 6 (1994) 204 - 206.

[23] P. Boutinaud, E. Cavalli, Chem. Phys. Lett. 503 (2011) 239 - 243.

[24] R. Karmakar, S.K. Neogi, A. Banerjee, S. Bandyopadhyay, Appl. Surf. Sci. 263 (2012) 671 - 677.

[25] Y. Zhang, X. Li, D. Geng, M. Shang, H. Lian, Z. Cheng and J. Lin, Cryst. Eng. Comm. 16 (2014) 2196 - 2204.

[26] J. Hölsä, E. Kestilä, P. Ylha, E. Antic-Fidancev, M. Lemaitre-Blaise, P. Porcher, P. Deren and W. Strek, J. App. Spect. 62 (1995) 697 - 705.

[27] K. Momma and F. Izumi, J. Appl. Crystallogr. 44 (2011) 1272 - 1276.

[28] V.D. Mote, J.S. Dargad, B.N. Dole, J. Nanosci. Nanotechnol. 1 (2013) 116 - 122.

[29] Y.T. Prabhu, K.V. Rao, V.S.S. Kumar, and B.S. Kumari, World Journal of Nano Science and Engineering, 4 (2014) 21 - 28.

[30] T. Many, K. Thandavan, S.M. Abdul Gani, C.S. Wong and R.M. Nor, J Nondestruct. Eval. 34 (2015) 1 - 14.

[31] Z. Li, L. Zheng, L. Zhang and L. Xiong, J. Lumin. 126 (2007) 481 - 486.

[32] H. Eloussifi, J. Farjas, P. Roura, J. Camps, M. Dammak, S. Ricart, T. Puig, X. Obradors, J. Therm. Anal. Calorim. 108 (2012) 589 - 596.

[33] R.E. Kroon, H.C. Swart, O.M. Ntwaeaborwa and H.A.A. Seed Ahmed, Physica B, 439 (2014) 83 - 87.

[34] G.C. Smith, J. Electron Spectrosc. Relat. Phenom. 148 (2005) 21 - 28.

[35] L. Sun, J. Pan, X. Zhang, H. Wang, L. Li and Y. Yu, RSC Adv. 5 (2015) 77673 - 77681.

[36] J.H. Su, P.P. Joshi, V. Chintamaneni and S. M. Mukhopadhyay, Appl. Surf. Sci. 253 (2007) 4652 - 4658.

[37] M. Rizhkov, V.A. Gubanov and M.P. Bytzman, J. Electron Spectrosc. Relat. Phenom. 18 (1980) 227 - 233.

[38] J.F. Moulder, W.F. Stickle, P.W. Sobol and K.D. Bomben, Handbook of X-ray Photoelectron Spectroscopy (Perkin-Elmer, Eden Prairie, MN, 1992).

[39] F.J. Palomares, E. Paz, F. Soria, and J.S. Moya, J. Am. Ceram. Soc. 92 (2009) 2993 – 2998.

[40] E. Bennett, J. Monzo, J. Humphrey, D. Plana, M. Walker, C. McConville, D. Fermin, A. Yanson and P. Rodriguez, ACS Catal. 6 (2016) 1533 - 1539.

[41] G. Blasse and A. Brill, Philips Res. Repts. 23 (1968) 461 - 468.
[42] A.M. Srivastava, Mater. Res. Bull. 37 (2002) 745 - 751.
[43] D.L. Dexter, J. Chem. Phys. 22 (1954) 1063 - 1070.
[44] N. Lakshminarasimhan, S. Jayakiruba and K. Prabhavathi, Solid State Sci. 72 (2017) 1 - 4.
[45] L. Chen, Y. Long, Y. Qin and W. Li, Mater. Lett. 102 - 103 (2013) 59 - 61.
[46] L. Li, Y. Pan, Z. Chen, S. Huang and M. Wu, RSC Adv. 7 (2017) 14868 - 14875.
[47] S. Shen, A. Jha, E. Zhang and Steve Wilson, J. Lumin. 126 (2007) 434 - 440.
[48] G. Blasse, Philips Res. Rep. 24 (2) (1969) 131 - 144.
[49] T. Petzel, V. Marx and B. Hormann, J. Alloys Compd. 200 (1993) 27 - 31.
[50] S. Fujihara, S. Koji, Y. Kadota and T. Kimura, J. Am. Ceram. Soc. 87 (2004) 1659 - 1662.
[51] A.B. Gawande, R.P. Sonekar and S.K. Omanwar, Int. J. Opt. 2014 (2014) 1 - 6.
[52] X. Li, P. Li, Z. Wang, S. Liu, Q. Bao, X. Meng, K. Qiu, Y. Li, Z. Li and Z. Yang, Chem. Mater. 29 (2017) 8792 - 8803.
[53] G. Blasse, Philips Res. Repts. 23 (1968) 344 - 361.
[54] L.G. Van Uitert, J. Electrochem. Soc. 114 (1967) 1048 - 1053.
[55] L. Ozawa, and P.M. Jaffe, J. Electrochem. Soc. 118 (1971) 1678 - 1679.
[56] L. Ozawa, Cathodoluminescence: Theory and Applications, (VCH, 1990).
[57] F. Kang, M. Peng, X. Yang, G. Dong, G. Nie, W. Liang, S. Xu and J. Qiu, J. Mater. Chem. C, 2 (2014) 6068 - 6076.
[58] P. Boutinaud, Inorg. Chem. 52 (2013) 6028 - 6038.
[59] A.W. Mann and D.J.M. Bevan, Acta Cryst. B26 (1970) 2129 - 2131.
[60] M. Amer, P. Boutinaud, Phys. Chem. Chem. Phys. 19 (2017) 2591 - 2596.
[61] L. Li and S. Zhang, J. Phys. Chem. B, 110 (2006) 21438 - 21443.
[62] C.K. Jorgenson, Prog. Inorg. Chem. 4 (1962) 73.
[63] J.S. Shi and S.Y. Zhang, J. Phys. Chem. B, 108 (2004) 18845 - 18849.
[64] J.P. Zuniga, S.K. Gupta, M. Pokhrel and Y. Mao, New J. Chem. 42 (2018) 9381 - 9392.
[65] J. Zhang, Y. Wang, L. Guoa, and P. Dong, Dalton Trans. 42 (2013) 3542 - 3551.
[66] L. Wang, H. Guo, Y. Wei, H.M. Noh and J.H. Jeong, Opt. Mater. 42 (2015) 233 - 236.
[67] K. Li, J. Fan, M. Shang, H. Lian and J. Lin, J. Mater. Chem. C, 3 (2015) 9989 - 9998.
[68] M. Nikl, A. Novoselov, E. Mihoková, K. Polák1, M. Dusek, B. McClune, A. Yoshikawa and T. Fukuda, J. Phys.: Condens. Matter. 17 (2005) 3367 - 3375.
[69] J.C. De Melo, H.F. Wittmann and R. H. Friend, Adv. Mater. 9 (1997) 230 - 232.

Chapter 7

Infrared emission enhancement through Ho^{3+} co-doped YOF:Bi^{3+} Phosphor

In this chapter IR emission were enhanced through Ho^{3+} co-doped Bi^{3+} doped YOF for SC applications. PL studies were investigated for energy transfer possibilities for IR emission.
It was shown that the Bi^{3+}-Ho^{3+} co-doped YOF phosphor is an appropriate candidate to enhance the spectral response of Si SC.

7.1 Introduction

Bi^{3+} has a $[Xe]4f^{14}5d^{10}6s^2$ electronic configuration that ensure it to be considered as one of the most important luminescent ions due to the wide range of emission in the UV and VIS regions [1, 2, 3, 4]. Bi^{3+} is well known to have excited electronic levels responsible for different emissions. It is characterized with three triplet energy levels known as $^3P_2$, $^3P_1$ and $^3P_0$ and one high energy level known as $^1P_1$ with a $^1S_0$ ground state [5]. Transitions from the $^1S_0$ ground state to the $^3P_1$ and $^3P_2$ excited states are forbidden but can become allowed due to spin orbit coupling and to coupling with unsymmetrical lattice vibrational modes [5]. Transitions to the $^3P_0$ excited level is strongly forbidden and the $^1P_1$ level is a spin allowed transition [5]. Various energy transfer investigations where the energy is transferred from Bi^{3+} to different luminescent ions (Bi^{3+} is utilized as a sensitizer for the emission) have already been done by other authors [4-8]. There are also various reports where Bi^{3+} sensitize other RE ions in different systems such as oxides, phosphates, molybdates, vanadates, tungstates and nibobates [9-19].

Ho^{3+} is considered as one of the best co-doping ions due to its wide spectral absorption [6, 20]. Ho^{3+} is characterized with a wealth of energy levels leading to many luminescent states due to the complexity of the $4f^{10}$ energy level system [6]. Malinowski et al. [21] explained that Ho^{3+} can be utilized for different applications such as infrared lasers, medical applications and remote sensing. Periša et al. [22] studied Ho^{3+} as a DS, co-doped in Yb^{3+} doped YOF. The system showed strong green emission around 540 nm and two weak emissions in the red region around 663 nm and 754 nm that were ascribed to the $^5F_4$, $^5S_2 \rightarrow {}^5I_8$, $^5F_5 \rightarrow {}^5I_8$ and $^5F_4$, $^5S_2 \rightarrow {}^5I_7$ electronic transitions, respectively. Yang Zhang and his group have also studied the luminescence of YOF:Ho^{3+} and they showed that the dominate green emission around 545 nm

for the $^5S_2 \rightarrow {}^5I_8$ transition was due to the 450 nm excitation that was ascribed to the $^5I_8 \rightarrow {}^5F_1$, $^5G_6$ transition [23].

This research study is an extension of our previous work done on the luminescence of YOF:Bi^{3+}. Investigation is therefore done on the suitability of the energy levels between Bi^{3+} and Ho^{3+} ions for possible energy transfer and sensitization of the VIS and NIR emissions.

7.2 Experimental

Pure YOF and Bi^{3+}, Ho^{3+} co-doped YOF powder samples were prepared by the pyrolysis method with CF_3COO as precursor from a single source. The pyrolysis method used was reported in our reported work on Pr^{3+} doped YOF [24]. The doped YOF: 0.4 mol % Bi^{3+}, x Ho^{3+} (x = 0.8, 1.4, 2, 3, 4 and 5 mol %) samples were prepared by the same method with only introducing holmium (III) oxide (Ho_2O_3) in the starting materials, see chapter 3, section 3.1.

The structure of the prepared samples was characterized by XRD using a Bruker Advance D8 diffractometer (40 kV, 40 mA) with Cu K_α x-rays (λ = 0.154 nm). SEM images were taken by using the JEOL JSM-7800F SEM. High resolution XPS was obtained with a PHI 5000 Versaprobe system as was described in chapter 3, section 3.4. All measurements were performed at room temperature. PL, NIR emission and decay time measurements were done by using the Edinburgh FLS980 instrument.

7.3 Results & discussion

Figure 1 shows the XRD results of the high concentration YOF: 0.4 mol % Bi^{3+}, 5 mol % Ho^{3+} co-doped sample compared to the YOF: 0.4 mol % Bi^{3+} single doped and the pure host samples. All the patterns showed a pure rhombohedral YOF structure (space group: $R\bar{3}m$ (166)), without any noticeable impurities, after annealing at around 900 ^{0}C in air atmosphere [24]. The sample doped with 0.4 mol % of Bi^+ ions showed a shift in the diffraction peaks towards the lower angles due to the difference in the ionic radii of the Y^{3+} (0.1019 nm) and Bi^{3+} (0.117 nm) ions, as reported in our previous work on YOF:Pr^{3+}. It was reported that the difference in the ionic radii between Pr^{3+} (0.1126 nm) and Y^{3+} (0.1019 nm) resulted in a slight shift towards the lower angles [24]. Co-doping with Ho^{3+} resulted in no further shifting of the diffraction peaks, Ho^{3+}

(0.1015 nm). We have to mention there was no additional peaks even after 5 mol % of Ho^{3+} doping.

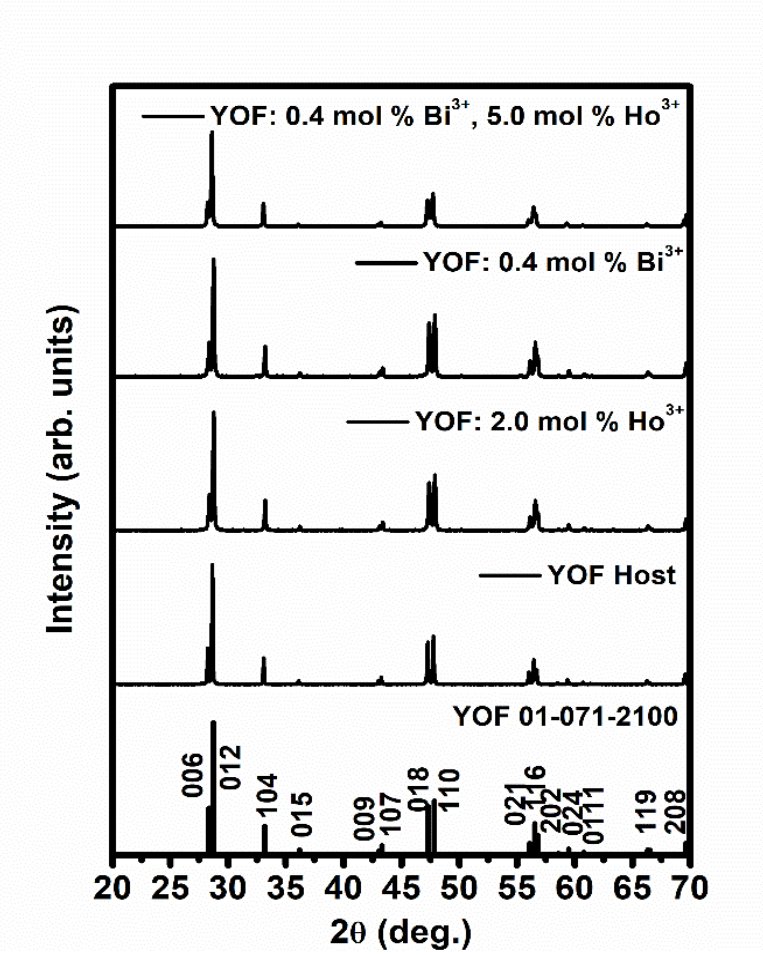

Figure 1: XRD pattern of the host material, of YOF: 0.4 mol % Bi^{3+} and of YOF: 0.4 mol % Bi^{3+}, 5 mol % Ho^{3+}.

Morphology investigations on the prepared samples with different Ho^{3+} ions' concentrations were done by using SEM. The variation of the morphology is depicted in figure 2. The morphology of the surface showed a variation of agglomerated melted particles. The increase in Ho^{3+} concentrations did not affect the morphology. The authors previously reported the agglomeration and melting of the particles during their investigations of the YOF:Pr^{3+} phosphor [24]. This was also reported by Z. Li et al. [25] during their investigations on the pyrolysis method of YOF:Yb^{3+}, Er^{3+} thin films. The same behavior was also reported by Eloussifi et al. [26] upon investigations of the decomposition of YOF into different structures.

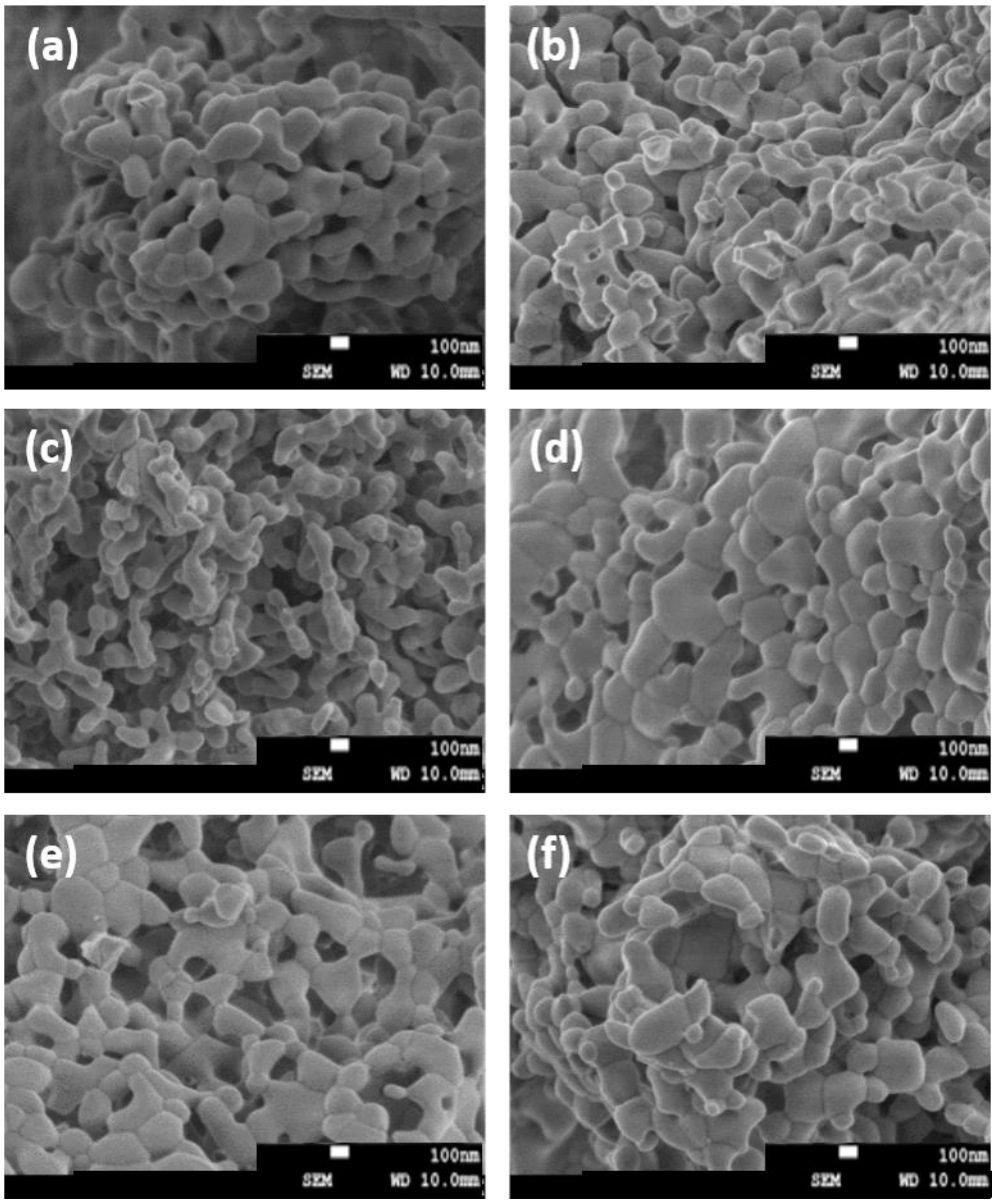

Figure 2: SEM images representing the variation of the morphology of the YOF: Bi^{3+}, Ho^{3+} samples for (a) 0.8, (b) 1.4, (c) 2, (d) 3, (e) 4 and (f) 5 mol % of Ho^{3+}.

Investigations on the surface elemental composition were done on the high co-doped sample YOF: 0.4 mol % Bi^{3+}, 5 mol % Ho^{3+} by using XPS. A correction for charge compensation of the high-resolution peaks was done in respect to the C 1s peak at 284.8 eV. The contaminated C on the surface was due to the adventitious hydrocarbons [24]. Figure 3 shows the deconvoluted peaks for (a) Y 3d, (b) O 1s and (c) F 1s. Deconvolution of the Y 3d peak in figure 3(a) yielded two peaks due to the spin orbit splitting at 157.1 eV and 159.1 eV that corresponded to the $3d_{5/2}$ and $3d_{3/2}$ peaks, respectively. The energy ranges of Y 3d, Bi 4f and Ho 4d peaks overlap. The Y 3d peak therefore also contained the peaks ascribed to the spin

orbit splitting of Bi 4f at 156 eV and 161.31 eV, $4f_{7/2}$ and $4f_{5/2}$, respectively and it contained the Ho 4d peak at 159.3 eV. In figure 3(b) the O 1s peak showed two components at 529 eV and 531.3 eV. Figure 3(c) shows the F 1s peak situated at 685 eV.

The obtained values for the Y 3d peak correlated well with previous reported values and in our previous work on YOF: Pr^{3+} [24, 27, 28]. The O 1s peak at 531 eV was ascribed to the O peak related to the YOF structure whereas the peak at 529 eV was ascribed to the presence of hydroxyl or carbonate groups [24, 29]. The obtained F 1s peak was also in correlation with reported values for YOF [24, 29]. The fitted peaks for Bi 4f were well in correlation with other reported values for YOF: Bi^{3+} [30, 31, 32]. The Bi 4f peaks were ascribed to Bi metal on the surface of the sample. The presence of Bi metal was due to the segregation of Bi^{3+} to the surface of the material and its reduction to Bi [32]. Bi 4f peaks of Bi metal were detected even at low concentrations of Bi^{3+} whereas, Bi 4f peaks of Bi^{3+} were started to appear at high concentrations of Bi^{3+}, this was also confirmed for other samples (data not shown). The fitted Ho 4d peak was in correlation with the reported value [33, 34].

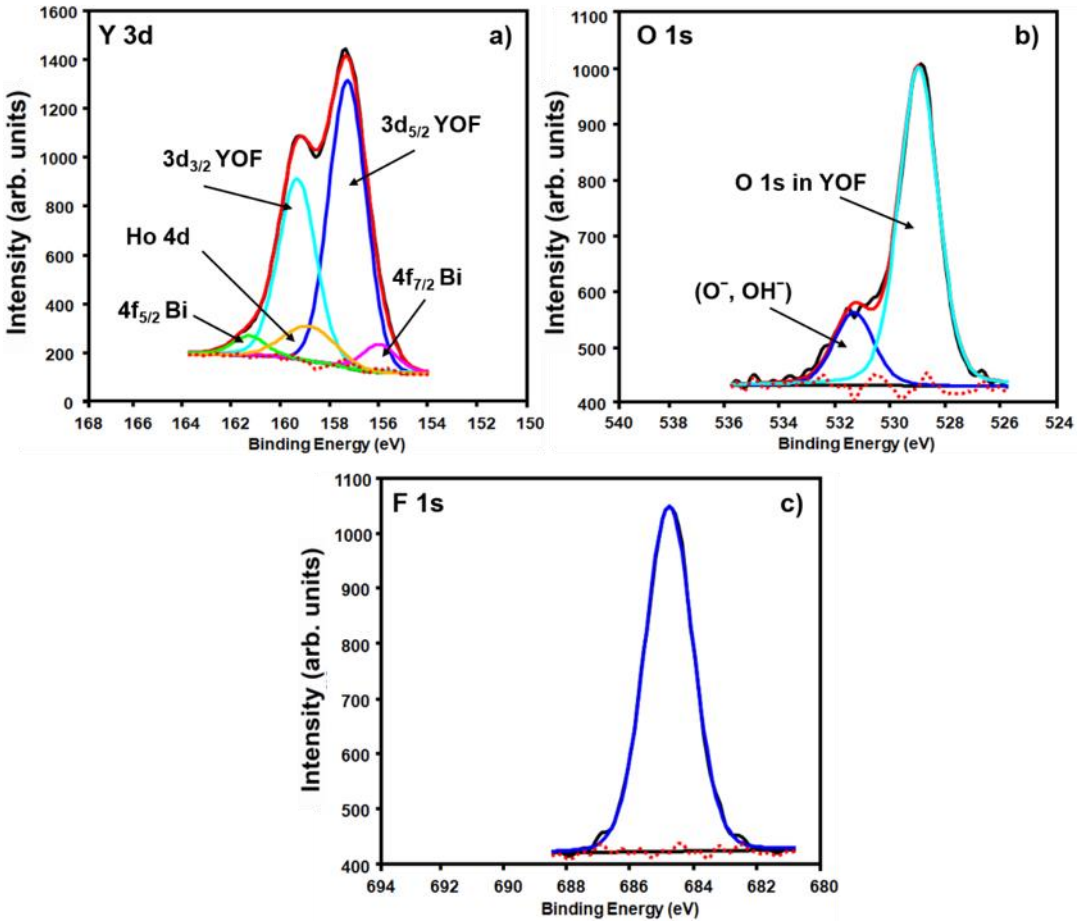

Figure 3: XPS high-resolution peak fits for (a) Y 3d with Bi 4f and Ho 4d, (b) O 1s and (c) F 1s in YOF: 0.4 mol % Bi^{3+}, 5 mol % Ho^{3+}.

PL studies on the prepared samples were done for the VIS and the IR regions.

7.3.1 Visible (VIS) Emission

The 0.4 mol % Bi^{3+} concentrated doped sample was previously shown by the authors to be the optimum sample for PL, article in preparation. Figure 4 shows the VIS excitation spectra of the prepared YOF: 0.4 mol % Bi^{3+}, x Ho^{3+} samples as a function of Ho^{3+} ions' concentrations (x = 0, 0.8, 1.4, 2, 3, 4, 5 mol %). Figure 4(a) shows the Bi^{3+} excitation spectra with increasing Ho^{3+} co-doped concentrations. The Bi^{3+} spectra showed a broad band centered at 265 nm that was characteristic to the $^1S_0 \rightarrow {}^3P_1$ transition of Bi^{3+} according to our previous work on YOF:Bi^{3+}. Figure 4(b) shows the Bi^{3+} and the Ho^{3+} excitation spectra with increasing Ho^{3+} co-doped concentrations. The 4f-4f transitions of Ho^{3+} peaked around 348 nm, 360 nm, 383 nm, 419 nm, 449 nm and 483 nm. These peaks corresponded to the $^5I_8 \rightarrow {}^5G_2, {}^5G_3$, $^5I_8 \rightarrow {}^5G_5, {}^3H_6$, $^5I_8 \rightarrow {}^5G_4$, $^5I_8 \rightarrow {}^5G_5$, $^5I_8 \rightarrow {}^5F_1, {}^5G_6$ and $^5I_8 \rightarrow {}^5F_2, {}^5F_3$ transitions of the Ho^{3+} ion, respectively [35] The Bi^{3+} excitation first decreased with 0.8 mol % Ho^{3+} then it increased from 0.8 mol % to 2 mol % and then it decreased again to 5 mol %. The Ho^{3+} excitation increased to 2 mol % and then it decreased to 5 mol %. This indicated that energy was transferred from Bi^{3+} to Ho^{3+} and that the 2 mol % Ho^{3+} co-doped sample was the optimum concentrated sample. The overlap between the emission of the YOF: 0.4 mol % Bi^{3+} and the excitation of the YOF: 2 mol % Ho^{3+} sample is shown in figure 4(c). This clearly showed that energy transfer can occur from Bi^{3+} to Ho^{3+}.

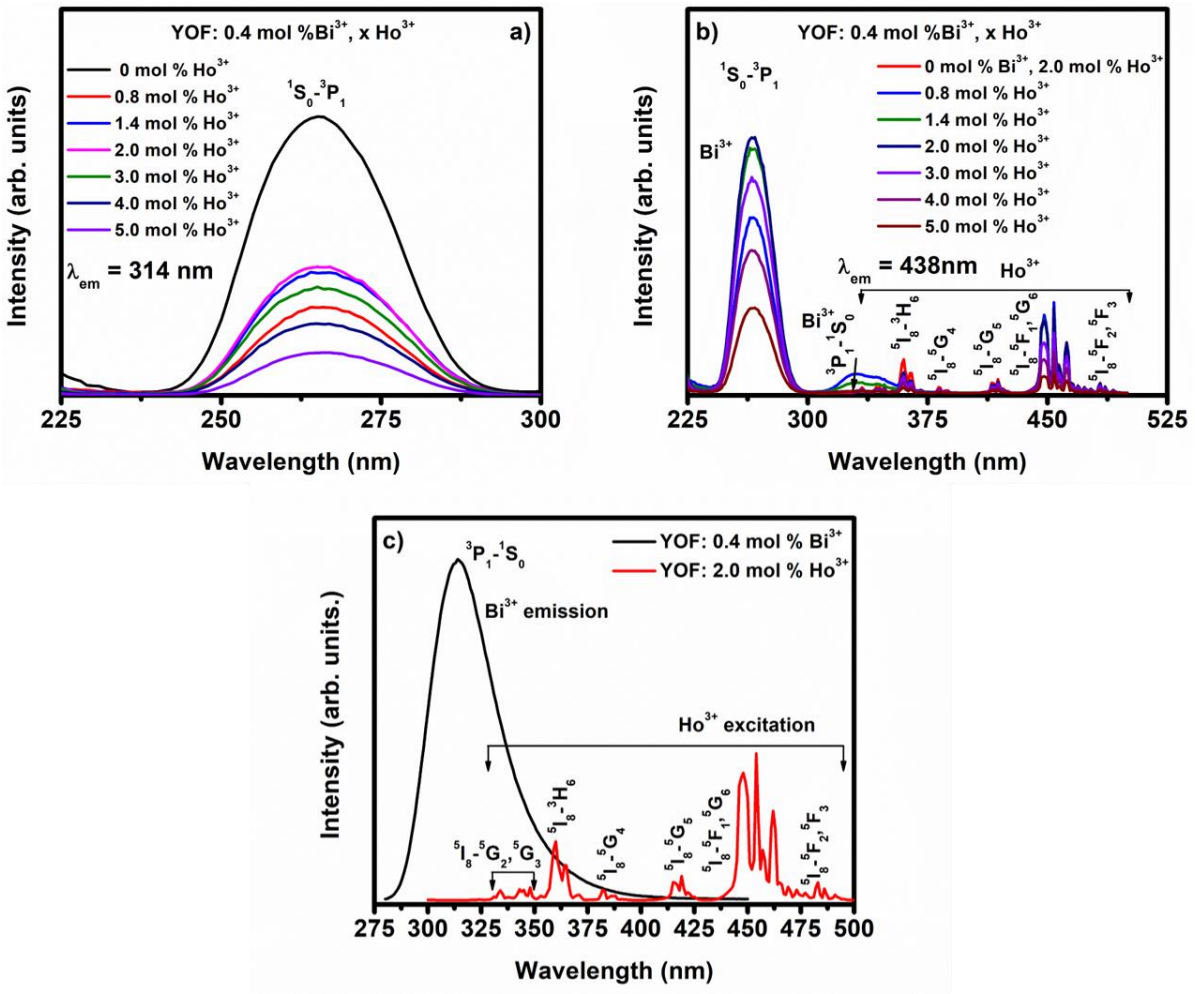

Figure 4: (a) and (b) show the effect of Ho^{3+} on the excitation parts of Bi^{3+} and Ho^{3+} monitoring 314 nm and 538 nm emissions, respectively and c) the overlap of the emission and excitation of Bi^{3+} and Ho^{3+}, respectively.

Figure 5 shows the VIS emission spectra of Bi^{3+} and Ho^{3+} at different Ho^{3+} co-doping concentrations and excitation. The Bi^{3+} emission, figure 5(a), consisted of a broad band that peaked around 314 nm and this was consistent with our previous work on YOF:Bi^{3+}. This broad band corresponded to the $^3P_1 \rightarrow {}^1S_0$ transition. The Bi^{3+} emission increased up to 2 mol % Ho co-doped and then it decreased again. The emission of Ho^{3+}, figure 5(b) and (c), with both the 265 nm and 449 nm excitations consisted of multi-narrow emission peaks that originated from different levels of Ho^{3+} ions. The emission spectra were due to the $^5F_4,{}^5S_2 \rightarrow {}^5I_8$ and $^5F_4,{}^5S_2 \rightarrow {}^5I_7$ transitions with weaker emissions from the $^5F_5 \rightarrow {}^5I_8$ levels of Ho^{3+} [35 , 36]. The dominant emission around 538 nm and 754 nm corresponded to the $^5F_4,{}^5S_2 \rightarrow {}^5I_8$ and $^5F_4,{}^5S_2 \rightarrow {}^5I_7$ transitions of Ho^{3+}, respectively. The weaker emission at 663 nm were attributed to the $^5F_5 \rightarrow {}^5I_8$ transition [35, 36]. The emission of Ho^{3+} during both the 265 nm and 449 nm excitation

showed an increase in the emission up to 2 mol % of Ho^{3+} and then it decreased gradually with increasing concentration. The decrease after 2 mol % was due to concentration quenching behavior [21]. The increase in the Ho^{3+} up to 2 mol % can be attributed to energy transfer from the Bi^{3+} ions' energy levels to the Ho^{3+} ions' as in figure 4(b). Figure 5(d) shows the variation of the intensity of different emission transitions as a function of Ho^{3+} concentration. Despite the presence of Bi metal which was confirmed by XPS investigation, it is well known Bi metal has no emission [37].

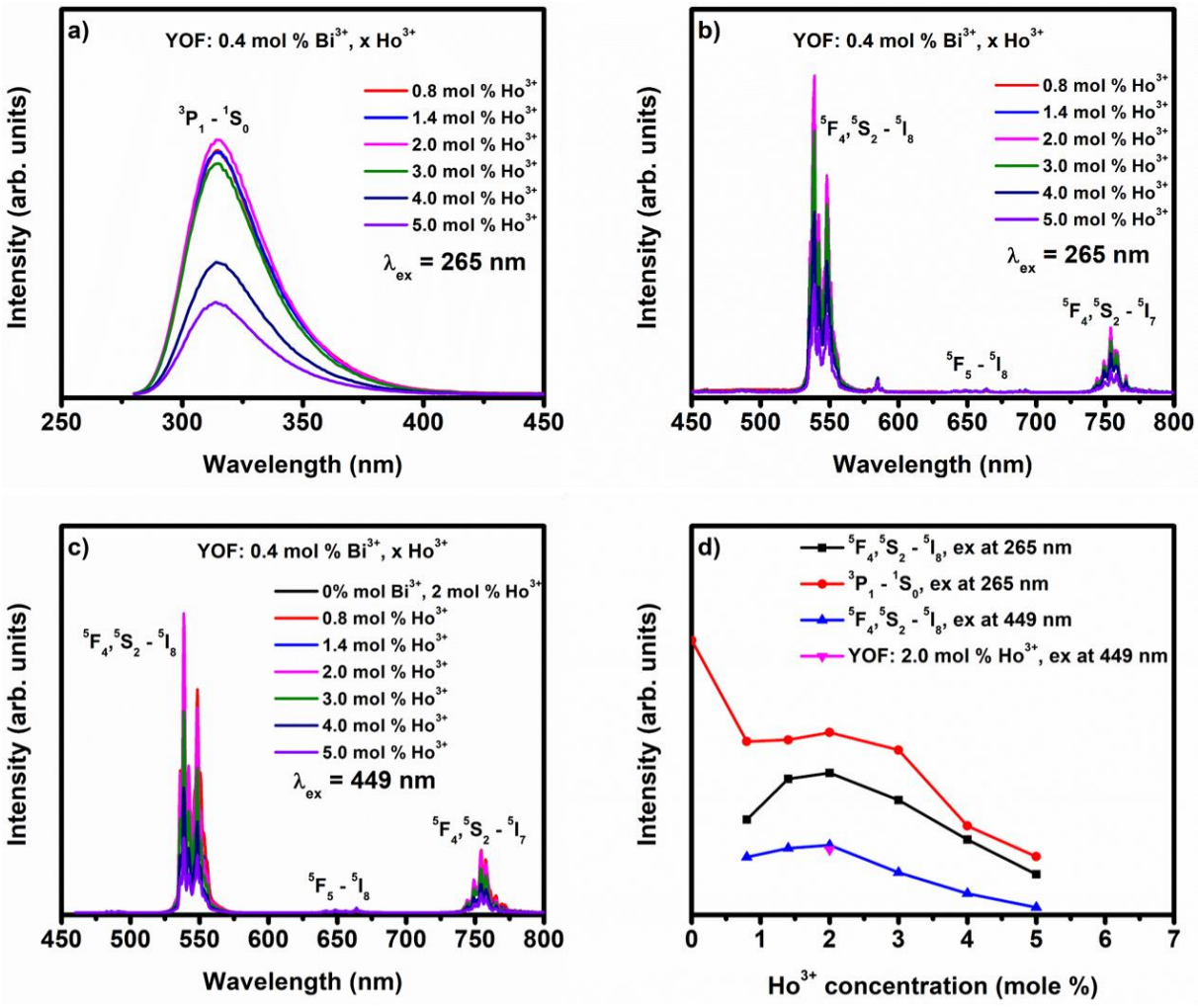

Figure 5: (a) PL emission of Bi^{3+} for different concentrations of Ho^{3+} ions under 265 nm excitation, (b) & (c) the Ho^{3+} emission for 265 nm and 449 nm excitations, respectively and d) the variation of different emissions for different excitations.

Investigation of the energy transfer between Bi^{3+} and Ho^{3+} was done based on the theory of energy transfer between sensitizer and activator. If we neglect the energy transfer through the movement of the charge carriers, the energy transfer occurred through either radiative transfer

through emission of the sensitizer (Bi^{3+}) and reabsorption of the activator (Ho^{3+}) or through non-radiative transfer followed by resonance between emitter and absorber. Efficiency of energy transfer is related to the spectral overlap between sensitizer and activator. Significant overlap between the sensitizer and the activator result in magnification of the activator emission [38]. The major participants in non-radiative transfer are multiple interactions and exchange interaction [38]. The probability of non-radiative transfer by multiple interaction can be represented by [38]:

$$\mathbf{P_{SA1} \propto Q_A E_{SA} / \tau_s R_{SA}^n = g_{SA} E_{SA} \ldots\ldots\ldots\ldots\ldots\ldots\ldots\ldots 1.}$$

Q_A is the absorption region of the activator, E_{SA} is the energy overlap of the activator absorption and sensitizer emission, τ_s is the radiative decay time and R_{SA}^n is the critical distance between sensitizer and activator.

In the case of YOF:Bi^{3+}, Ho^{3+}, the overlap area between the Bi^{3+} emission and Ho^{3+} excitation is not significant. This resulted in pumping into the $^3H_6$ level instead of the main $^5F_1$ and $^5G_6$ excitation levels of Ho^{3+}. This might be the reason for the decrease in the Bi^{3+} emission from the single doped sample to the introduction of the 0.8 mol % Ho^{3+} doped sample and for the increase in the Bi^{3+} emission with increased Ho^{3+} ions concentration up to 2 mol %. The plausible explanation is therefore that at low concentrations of Ho^{3+}, the radiative energy transfers between Bi^{3+} ions competed with the non-radiative energy transfer to Ho^{3+}. The result was then that a small amount of energy was transferred to Ho^{3+} and this lead to the increase in the Bi^{3+} emission up to 2 mol %. In any sensitizer-activator system, the energy transfer depends on the probability of transfer but also on the back energy transfer from activator to sensitizer or/and the probability of energy transfer amongst the sensitizers [39].

To explain the possibility of back energy transfer from Ho^{3+} to Bi^{3+}, we looked into the Bi^{3+} excitation spectra recorded in figure 4(a), while monitoring the Bi^{3+} emission at 314 nm. Ho^{3+} excitation was not detected in the Bi^{3+} excitation region. This did not eliminate the possibility of back energy transfer from Ho^{3+} to Bi^{3+}. If the probability of energy transfer amongst the sensitizers increased, excitation of sensitizers, followed by one or several other sensitizers, occurred before energy was transferred to the activator [39]. These transfers between sensitizers were followed by a small amount of absorption energy as a result of relaxation of lattice and quenching sites [39]. Therefore, the reduction of the energy transferred from sensitizer to activator is a result of energy transferred between sensitizers [39]. At high Ho^{3+} concentrations,

the probability of transferring between sensitizers was reduced and as a result the Ho^{3+} emission was enhanced. This was also confirmed by the coexistence of the $^3P_1 \rightarrow {}^1S_0$ emission in the excitation spectra when the $^5F_4,^5S_2 \rightarrow {}^5I_8$ emission of Ho^{3+} where monitored. The energy was therefore partially transferred from Bi^{3+} to Ho^{3+}.

7.3.2 Infrared (IR) emission

An investigation on the IR emission for the YOF: 0.4 mol % Bi^{3+},Ho^{3+} system was done with different Ho^{3+} co-doping concentrations. Figure 6 shows the excitation spectra for the IR emission monitored around 1200 nm of Ho^{3+} emission [36]. The excitation spectra showed the same excitation for the visible emission that consisted of 4f-4f transitions of Ho^{3+} and a broad band ascribed to Bi^{3+} excitation with optimum concentration of Ho^{3+} about 3 mol %. The excitation broad band around 265 nm was ascribed to the $^1S_0 \rightarrow {}^3P_1$ transition of Bi^{3+}. The 4f-4f excitation transitions of Ho^{3+} peaked at 334 nm, 348 nm, 360 nm, 383 nm, 419 nm, 449 nm and 483 nm. These peaks corresponded to the $^5I_8 \rightarrow {}^5G_2$, $^5I_8 \rightarrow {}^5G_3$, $^5I_8 \rightarrow {}^3H_6$, $^5I_8 \rightarrow {}^5G_4$, $^5I_8 \rightarrow {}^5G_5$, $^5I_8 \rightarrow {}^5F_1$, $^5G_6$ and $^5I_8 \rightarrow {}^5F_2$, $^5F_3$ transitions of the Ho^{3+} ion, respectively [35].

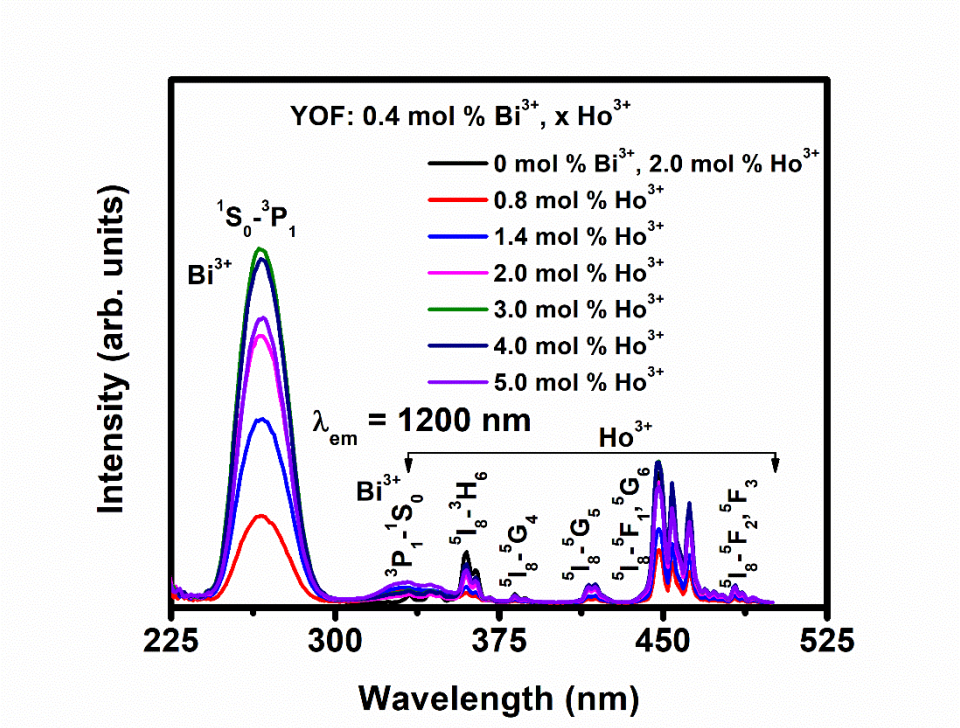

Figure 6: Infrared excitation of YOF: 0.4 mol % Bi^{3+}, x mol % Ho^3 for different concentrations of Ho^{3+} monitored at 1200 nm.

The IR emission spectra were recorded upon 265 nm and 449 nm excitation wavelengths into Bi^{3+} and Ho^{3+} levels, respectively, see figure 7(a) and (b) [36, 40]. The emission consisted of a range of characteristic Ho^{3+} peaks centered at 753 nm, 1014 nm, a broad sharp peak centered at 1200 nm and lastly a weak peak around 1400 nm. These emission peaks were ascribed to the $^5F_4,^5S_2 \rightarrow {}^5I_7$, $^5F_4,^5S_2 \rightarrow {}^5I_6$, $^5I_6 \rightarrow {}^5I_8$ and $^5F_4$, $^5S_2 \rightarrow {}^5I_5$ transitions of Ho^{3+}, respectively [36, 39, 40]. A comparison of the IR emission between the two different excitations of 449 nm and 265 nm, for the sample doped with 3 mol % of Ho^{3+}, was depicted in figure 7(c). Figure 7(d) shows the variation of the intensity of the IR emission for both the 449 and 265 nm excitations as a function of Ho^{3+} concentrations. A significant enhancement in the Ho^{3+} emission occurred upon 265 nm excitation compared to the 449 nm excitation. This confirmed that energy transfer occurred from the Bi^{3+} to the Ho^{3+} energy levels. We have to mention that we did not detect any emission ascribed to Bi^{3+} since it is not an IR emitter [37].

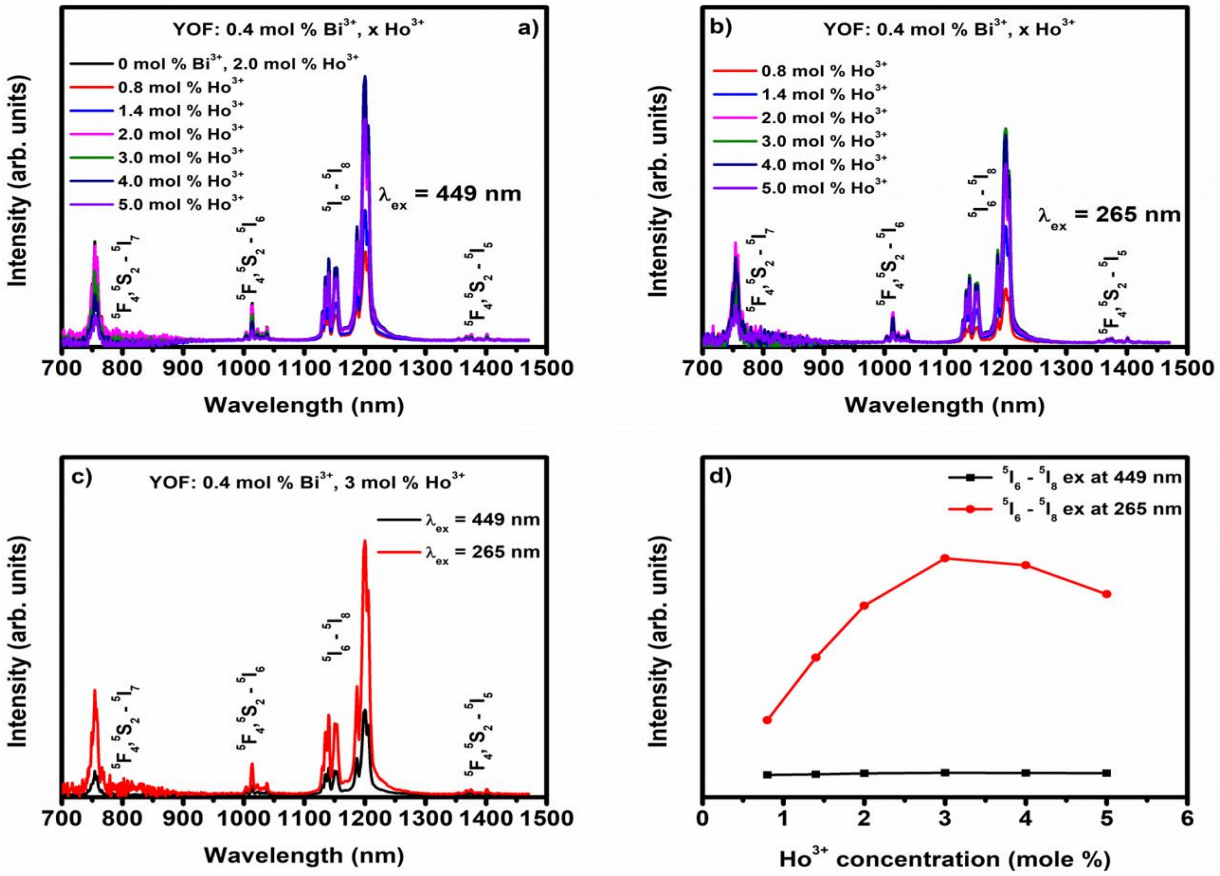

Figure 7: IR emission of YOF: 0.4 mol % Bi^{3+}, x mol % Ho^3 for different concentrations of Ho^{3+} excited at (a) 449 nm, (b) 265 nm, (c) a comparison between the YOF: 0.4 mol % Bi^{3+}, 3 mol % Ho^{3+} sample's $^5I_6 \rightarrow {}^5I_8$ emission at 449 nm and 265 nm excitation and (d) the variation of the $^5I_6 \rightarrow {}^5I_8$ emission as function of different Ho^{3+} ions concentration.

The decay time for the prepared samples were recorded to extract more information on the energy transfer between Bi^{3+} and Ho^{3+}. The decay times were recorded in the VIS as well as in the IR region. All samples showed doublet and triplet components of decay. Figure 8(a) and (b) show the VIS decay times of Bi^{3+} and Ho^{3+} for the $^3P_1 \rightarrow {}^1S_0$ and $^5F_4,{}^5S_2 \rightarrow {}^5I_8$ transitions that peaked around 314 nm and 538 nm, respectively. Generally, the doublet and triplet decay components can be expressed as [41, 42]:

$$\mathbf{I(t) = A_0 + A_1exp(-t/\tau_1) + A_2exp(-t/\tau_2)}\text{.....2}$$

$$\mathbf{I(t) = A_0 + A_1exp(-t/\tau_1) + A_2exp(-t/\tau_2) + A_3exp(-t/\tau_3)}\text{.....3,}$$

and the average decay time for doublet and triplet components can be expressed as:

$$\mathbf{< \tau > = (A_1 \tau_1^2 + A_2 \tau_2^2)/(A_1 \tau_1 + A_2 \tau_2)}\text{ .....4}$$

$$\mathbf{< \tau > = (A_1 \tau_1^2 + A_2 \tau_2^2 + A_3 \tau_3^2)/(A_1 \tau_1 + A_2 \tau_2 + A_3 \tau_3)}\text{ .....5.}$$

I(t) is the PL intensity, $< \tau >$ is the average decay time, τ_1, τ_2 and τ_3 are the emission decay times, and A_1, A_2 and A_3 are their relative weightages [43]. According to our previous report on YOF:Bi^{3+} the decay time of $^3P_1 \rightarrow {}^1S_0$ transition was in the order of a few μs. The measured decay time for all the samples were in range of μs. This is in good agreement with previously reported values for decay times calculated for the $^3P_1 \rightarrow {}^1S_0$ and $^5F_4,{}^5S_2 \rightarrow {}^5I_8$ emissions [1-4, 20, 21]. A decrease in the $^3P_1 \rightarrow {}^1S_0$ transition indicated that energy transfer occurred from Bi^{3+} to Ho^{3+} whereas, the decrease in the $^5F_4,{}^5S_2 \rightarrow {}^5I_8$ indicated that energy transfer occurred between the Ho^{3+} ions.

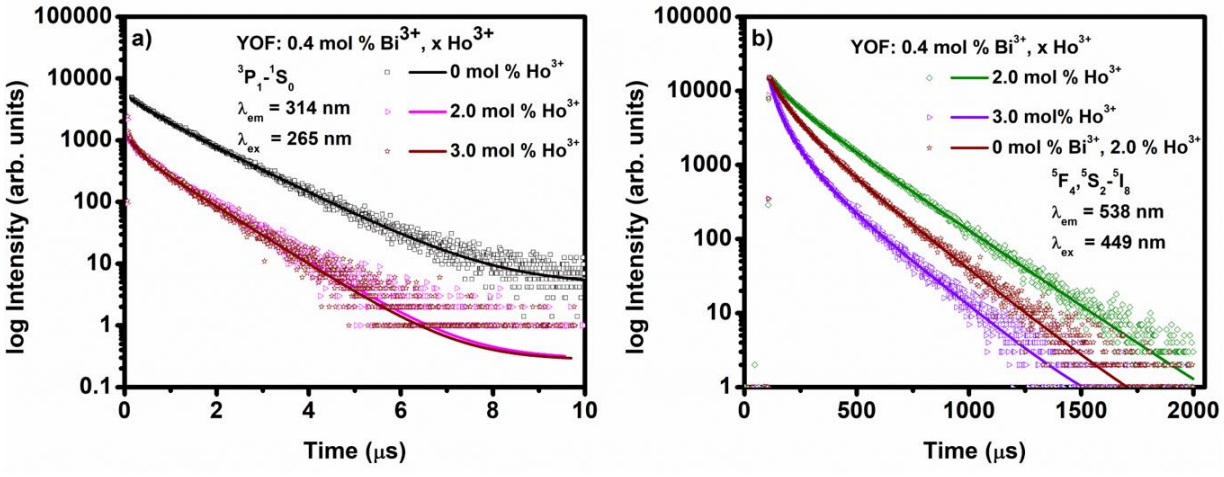

Figure 8: (a) The measured decay times of the Bi^{3+} $^3P_1 \rightarrow {}^1S_0$ transition upon excitation of 265 nm and emission of 314 nm and (b) decay times of Ho^{3+} $^5F_4,{}^5S_2 \rightarrow {}^5I_8$ transition upon excitation of 449 nm and emission of 538 nm.

Table 1: The obtained decay time of the $^3P_0 \rightarrow {}^1S_0$ level of Bi^{3+} and of the $^5F_4,{}^5S_2 \rightarrow {}^5I_8$ level of Ho^{3+} calculated by using equations (4) & (5) and their corresponding average as a function of Ho^{3+} concentrations in YOF.

0.4 mol % Bi^{3+}, x mol % Ho^{3+}	$^3P_1 \rightarrow {}^1S_0$				$^5F_4,{}^5S_2 \rightarrow {}^5I_8$			
	τ_1/ µs	τ_2/ µs	τ_3/ µs	< τ >/ µs	τ_1/ µs	τ_2/ µs	τ_3/ µs	< τ >/ µs
0	0.428	1.183	—	1.102	—	—	—	—
0.8	0.276	1.038	—	0.976	39.6	117.9	223.8	195.2
1.4	0.261	0.994	—	0.907	38.0	103.8	200.6	162.6
2.0	0.226	0.948	—	0.873	36.7	91.9	183.8	140.0
3.0	0.227	0.927	—	0.840	30.6	83.0	182.7	119.0
4.0	0.222	0.910	—	0.804	25.3	72.3	180.9	101.5
5.0	0.222	0.900	—	0.786	21.2	59.1	170.8	78.2
0 mol % Bi^{3+}, 2.0 mol % Ho^{3+}	—	—	—	—	38.5	94.1	185.5	136.4

The decay times of the IR emission were also investigated for both the $^5F_4,{}^5S_2 \rightarrow {}^5I_6$ and $^5I_6 \rightarrow {}^5I_8$ transitions of Ho^{3+}. The IR decay times were recorded under excitation of 449 nm. The recorded decay times were depicted in figure 9(a) and (b) for $^5F_4,{}^5S_2 \rightarrow {}^5I_6$ and $^5I_6 \rightarrow {}^5I_8$ transitions of Ho^{3+} emissions, respectively. The calculated IR decay times for both transitions were depicted in table 2 in respect to an increase of Ho^{3+} concentrations from 0.8 mol % up to 5 mol % and for the individual sample doped with only 2 mol % of Ho^{3+}. The decrease in the decay time of the 1014 nm emission as a function of Ho^{3+} indicated that energy transfer occurred between the Ho^{3+} ions. This led to quenching of the Bi^{3+} UV emission. The decay time of $^5I_6 \rightarrow {}^5I_8$ at 1200 nm increased for low Ho^{3+} concentrations up to 2 mol % and then it decreased again up to 4 mol % after which it then increased again at 5 mol %. The decay curve of the $^5F_4,{}^5S_2 \rightarrow {}^5I_6$ transition indicated a short rising time that indicated that some processes were responsible for the population of this level [44]. Population of the $^5I_6$ level can occurred through a $^5S_2$, $^5I_8 \rightarrow {}^5I_7$, $^5I_7$, $^5I_6$ cross relaxation process [45]. The recorded decay times for both transitions were in µs and this was also reported for different Ho^{3+} doped and co-doped systems [44, 46, 47].

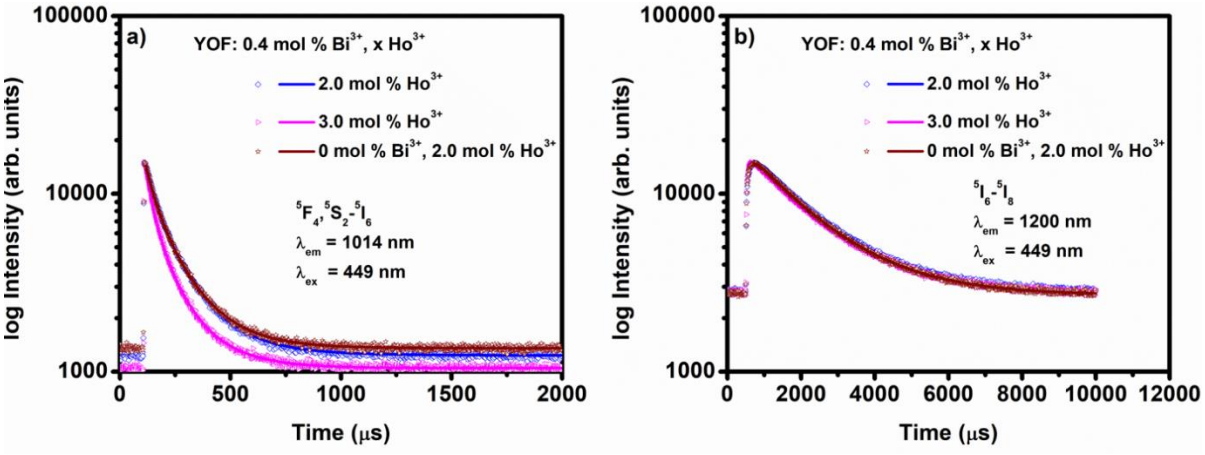

Figure 9: The measured decay times of a) $^5F_4$,$^5S_2$ → $^5I_6$ (1014 nm) and b) $^5I_6$ → $^5I_8$ (1200 nm) transitions upon excitation of 449 nm.

Table 2: The obtained decay times of both the $^5F_4$,$^5S_2$ → $^5I_6$ and $^5I_6$ → $^5I_8$ transitions as a function of Ho^{3+} concentrations in YOF.

0.4 mol % Bi^{3+}, x mol % Ho^{3+}	**$^5F_4$,$^5S_2$ → $^5I_6$**				**$^5I_6$ → $^5I_8$**			
	τ_1/ μs	**τ_2/ μs**	**τ_3/ μs**	**< τ >/ μs**	**τ_1/ μs**	**τ_2/ μs**	**τ_3/ μs**	**< τ >/ μs**
0.8	79.1	198.6	243.1	196.1	166.3	1268.2	1920.7	1734.5
1.4	53.3	144.1	205.6	161.5	137.5	1396.2	2014.5	1769
2.0	40.2	125.1	251.9	143.5	209.4	374.1	1724.6	1727
3.0	31.5	85.3	183.6	116.4	197.5	204.3	1698.5	1698.2
4.0	26.1	77.7	193.4	102	80.2	746	1699.3	1678.1
5.0	20.3	52.9	158.4	79.8	91.1	777.8	1754.5	1692
0 mol % Bi^{3+}, 2.0 mol % Ho^{3+}	40.1	110.9	192.7	136.2	127.9	1458.3	1840.9	1714

The proposed energy transfers and luminescent mechanism from Bi^{3+} to Ho^{3+} can be explained based on both the VIS and IR emissions, see figure 10. During excitation into the $^3P_1$ level of Bi^{3+} a fast radiative emission occurred leading to UV emission of Bi^{3+} ions. Partial energy was transferred to Ho^{3+} $^3H_6$ and $^5G_5$ energy levels and this was followed by multiple non-radiative transitions that populated the $^5F_4$ and $^5S_2$ levels of Ho^{3+}. Population of the $^5F_4$ and $^5S_2$ levels lead to VIS radiative emissions from the $^5F_4$,$^5S_2$ → $^5I_8$ and $^5F_4$,$^5S_2$ → $^5I_7$ transitions. Population of the $^5F_5$ level was achieved through non-radiative relaxation from the excited $^5F_4$ and $^5S_2$

levels where radiative emission occurred to the $^5I_8$ ground level at 663 nm. Emission also occurred in the IR region through the $^5F_4$,$^5S_2 \rightarrow {}^5I_6$ and $^5I_6 \rightarrow {}^5I_8$ transitions at 1014 nm and 1200 nm, respectively. Population of the $^5I_6$ level occurred through the $^5S_2$, $^5I_8 \rightarrow {}^5I_7$, $^5I_6$ cross-relaxation process that was responsible for the long decay time of the $^5I_6 \rightarrow {}^5I_8$ emission. The same energy transfer mechanism occurred during excitation of 449 nm except that pumping occurred to the $^5G_6$ and $^5F_1$ levels in which non-radiative transition occurred to the $^5F_4$ and $^5S_2$ levels. Characteristic Ho^{3+} emission therefore occurred to different levels in the VIS and IR regions.

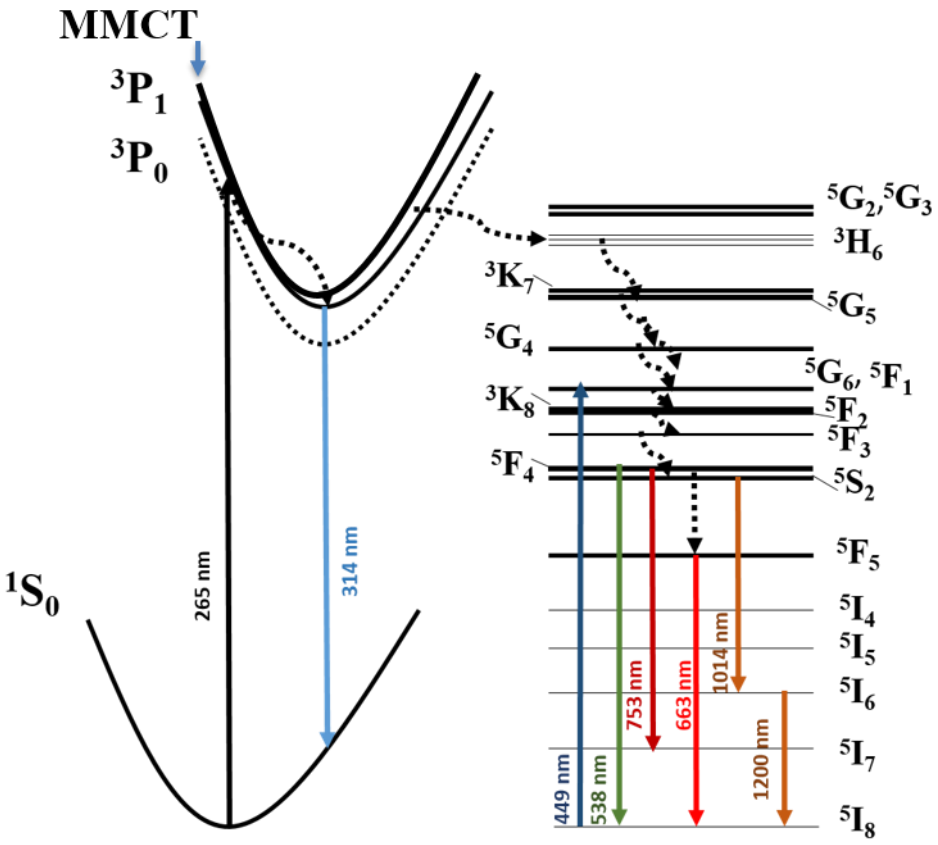

Figure 10: Proposed energy level diagram for the YOF: 0.4 mol % Bi^{3+}, x mol % Ho^{3+} phosphor.

7.4 Conclusion

The YOF: 0.4 mol % Bi^{3+}, x mol % Ho^{3+} phosphor was successfully synthesized using the pyrolysis method with CF_3COO as precursor. XRD results showed a high crystallinity of the powder as rhombohedral YOF (space group: $R\bar{3}m$ (166)) after annealing at 900 ^{0}C. XPS investigations showed an overlap of Bi 4f and Ho 4d peaks in the Y 3d peak. Visible PL results showed both the $^3P_1 \rightarrow {}^1S_0$ emission of Bi^{3+} and the 4f-4f transitions of Ho^{3+} under excitation

of 265 nm and 449 nm. The broad excitation band that peaked at 265 nm was ascribed to the $^1S_0 \rightarrow {}^3P_1$ transition of Bi^{3+} whereas, the excitation peak at 449 nm was ascribed to the $^5I_8 \rightarrow {}^5F_1$, $^5G_6$ transition of Ho^{3+}. The UV (250 – 450) emission part at 314 nm originated from the $^3P_1 \rightarrow {}^1S_0$ transition of Bi^{3+}. The green (450 – 800 nm) emission part that peaked at 538 nm and 753 nm originated from Ho^{3+} and were ascribed to the $^5F_4$,$^5S_2 \rightarrow {}^5I_8$ and $^5F_4$,$^5S_2 \rightarrow {}^5I_7$ transitions of Ho^{3+}. The optimum Ho^{3+} concentration for visible PL emission was recorded for the sample co-doped with 2 mol % of Ho^{3+}. The IR emission was recorded for both 449 nm and 265 nm excitations with optimum concentration of about 3 mol % of Ho^{3+}. The IR emission that peaked at 1014 nm and 1200 nm were ascribed to the $^5F_4$,$^5S_2 \rightarrow {}^5I_6$ and $^5I_6 \rightarrow {}^5I_8$ transitions of Ho^{3+}. Population of the $^5I_6$ level might occur through the $^5S_2$, $^5I_8 \rightarrow {}^5I_7$, $^5I_7$, $^5I_6$ cross-relaxation process. The decay times for all emissions were in order of μs. The Bi^{3+}-Ho^{3+} co-doped YOF phosphor is therefore an appropriate candidate to enhance the spectral response of Si SC. Despite the efficient energy conversion in the Bi^{3+}, Ho^{3+} system, enhancement of the energy flow from Bi^{3+} to Ho^{3+} needs to be considered. This will reduce the dissipated energy into many unnecessary manifolds of Ho^{3+} and direct it to the range of spectral absorption of Si-SC.

References

[1] F. Kang and M. Peng, Dalton Trans. 43 (2014) 277 - 284.

[2] L. Chen, H. Zheng, J. Cheng, P. Song, G. Yang, G. Zhang and C. Wu, J. Lumin. 128 (2008) 2027 - 2030.

[3] Z. Jiang, J. Gou, Y. Min, C. Huang, W. Lv, X. Yu, X. Su and L. Duan, J. Alloys Compds. 727 (2017) 63 - 68.

[4] V.G. Suchithra, P.P. Rao and B.A. Aswathy, Chemistry Select, 2 (2017) 7602 - 7611.

[5] A.M. Srivastava and A. Szarowski, J. Solid State Chem. 146 (1999) 494 - 498.

[6] X. Zhang, G. Zhou, J. Zhou, H. Zhou, P. Kong, Z. Yu and J. Zhan, RSC Adv. 4 (2014) 13680 - 13686.

[7] X.Y. Liu, H. Guo, S.X. Dai, M.Y. Peng and Q.Y. Zhang, Opt. Mater. Express, 6 (2016) 3574 - 3585.

[8] J. Xue, X. Wang, J.H. Jeong and X. Yan, Phys. Chem. Chem. Phys. 20 (2018) 11516 - 11541.

[9] G. Ju, Y. Hu, L. Chen, X. Wang, Z. Mu, H. Wu and F. Kang, J. Lumin. 132 (2012) 1853 - 1859.

[10] M.N. Luwang, R.S. Ningthoujam, S.K. Srivastava and R.K. Vatsa, J. Am. Chem. Soc. 133 (2011) 2998 - 3004.

[11] S. Yan, J. Zhang, X. Zhang, S. Lu, X. Ren, Z. Nie and X. Wang, J. Phys. Chem. C, 111 (2007) 13256 - 13260.

[12] Y. Chen, Y. Wu, D. Wang and T. Chen, J. Mater. Chem. 22 (2012) 7961 - 7969.

[13] D. Chen, Y. Yu, P. Huang, H. Lin, Z. Shan, L. Zeng, A. Yang and Y. Wang, Phys. Chem. Chem. Phys. 12 (2010) 7775 - 7778.

[14] U. Rambabu and S. Han, Ceram. Int. 39 (2013) 1603 - 1612.

[15] U. Rambabu, N. R. Munirathnam, S. Chatterjee, B. Sudhakar Reddy and S. Han, Ceram. Int. 39 (2013) 4801- 4811.

[16] C.V. Devi, G. Phaomei, N. Yaiphaba and N.R. Singh, J. Alloys Compd. 583 (2014) 259 - 266.

[17] L. Wang, Q. Wang, X. Xu, J. Li, L. Gao, W. Kang, J. Shi and J. Wang, J. Mater. Chem. C, 1 (2013) 8033 - 8040.

[18] L. Wang, Z. Lv, W. Kang, X. Shangguan, J. Shi and Z. Hao, Appl. Phys. Lett. 102 (2013) 151909 (4 pages).

[19] X. Xiao and B. Yan, J. Alloys Compd. 421 (2006) 252 - 257.

[20] X.P. Chen, W.J. Zhang and Q.Y. Zhang, Physica B, 406 (2011) 1248 - 1252.

[21] M. Malinowski, M. Kaczkan, A. Wnuk, M. Szufliñska, J. Lumin. 106 (2004) 269 - 279.

[22] J. Periša, J. Papan, S.D. Dolić, D.J. Jovanović and M.D. Dramićanin, Dyes and Pigments 155 (2018) 233 - 240.

[23] Y. Zhang, D. Geng, X. Kang, M. Shang, Y. Wu, X. Li, H. Lian, Z. Cheng and J. Lin, Inorg. Chem. 52 (2013) 12986 - 12994.

[24] N.A.M. Saeed, E. Coetsee and H.C. Swart, Opt. Mater. 96 (2019) 109331 (12 pages).

[25] Z. Li, L. Zheng, L. Zhang and L. Xiong, J. Lumin. 126 (2007) 481 - 486.

[26] H. Eloussifi, J. Farjas, P. Roura, J. Camps, M. Dammak, S. Ricart, T. Puig and X. Obradors, J. Therm. Anal. Calorim. 108 (2012) 589 - 596.

[27] L. Sun, J. Pan, X. Zhang, H. Wang, L. Li and Y. Yu, RSC Adv. 5 (2015) 77673 - 77681.

[28] J.H. Su, P.P. Joshi, V. Chintamaneni and S.M. Mukhopadhyay, Appl. Surf. Sci. 253 (2007) 4652 - 4658.

[29] M. Rizhkov, V.A. Gubanov and M.P. Bytzman, J. Electron Spectrosc. Relat. Phenom. 18 (1980) 227 - 233.

[30] E. Bennett, J. Monzo, J. Humphrey, D. Plana, M. Walker, C. McConville, D. Fermin, A. Yanson and P. Rodriguez, ACS Catal. 6 (2016) 1533 - 1539.

[31] K.L. Li, W.W. Lee, C.S. Lu, Y.M. Dai, S.Y. Chou, H.L. Chen, H.P. Lin and C.C. Chen, J. Taiwan Inst. Chem. E, 45 (2014) 2688 - 2697.

[32] F.J. Palomares, E. Paz, F. Soria, and J.S. Moya, J. Am. Ceram. Soc. 92 (2009) 2993 - 2998.

[33] J.F. Moulder, W.F. Stickle, P.W. Sobol and K.D. Bomben, Handbook of X-ray Photoelectron Spectroscopy (Perkin-Elmer, Eden Prairie, MN, 1992).

[34] X. Xu, S. Zhou, J. Long, T. Wu and Z. Fan, Mater. 10 (2017) 302 (15 pages).

[35] X. Zhou, Y. Wang, X. Zhao, L. Li, Z. Wang and Q. Li, J. Am. Ceram. Soc. 97 (2014) 179 - 184.

[36] J. Xu, D. Murata, B. So, K. Asami, J. Ueda, J. Heo and S. Tanabe, J. Mater. Chem. C, 6 (2018) 11374 - 11383.

[37] H.T. Sun, J. Zhou and J. Qiu, Prog. Mater. Sci. 64 (2014) 1 - 72.

[38] M. Wang, X. Fan and G. Xiong, J. Phys. Chem. Solids, 56 (1995) 859 - 862.

[39] A.D. Sontakke, A. Tarafder, K. Biswas and K. Annapurna, Physica B, 404 (2009) 3525 - 3529.

[40] L. Guo, Y. Wang, J. Zhang, Y. Wang and P. Dong, Nanoscale Res. Lett. 7 (2012) 636 (7 pages).

[41] X. Zhou, Y. Wang, X. Zhao, L. Li, Z. Wang, and Q. Li, J. Am. Ceram. Soc. 97 (2014) 179 - 184.

[42] J. Zhang, Y. Wang, L. Guoa, and P. Dong, Dalton Trans. 42 (2013) 3542 - 3551.

[43] M.Y.A. Yagoub, H.C. Swart, P. Bergman and E. Coetsee, AIP Adv. 6 (2016) 025204 - 025213.

[44] A.A. Lyapin, P.A. Ryabochkina, A.N. Chabushkin, S.N. Ushakov and P.P. Fedorov, J. Lumin. 167 (2015) 120 - 125.

[45] P.J. Dereń and K. Lemański, J. Lumin. 154 (2014) 62 - 67.

[46] A.F.H. Librantz, S.D. Jackson, F.H. Jagosich, L. Gomes, G. Poirier, S.J.L. Ribeiro, and Y. Messaddeq, J. APPL. Phys. 101 (2007) 123111 (9 pages).

[47] A. Méndez-Blas, M. Rico, V. Volkov, C. Zaldo, and C. Cascales, Phys. Rev. B, 75 (2007) 174208 (14 pages).

Chapter 8

Tunable Ho^{3+} co-doped YOF:Bi^{3+} emission through cathodoluminescence

In this chapter results were obtained that can be used to tune the YOF:Bi^{3+}, Ho^{3+} phosphor's emission. CL studies were done under electron beam irradiation (5 keV) for both YOF: x mol % Bi^{3+} (x = 0.3, 0.4, 0.5, 0.6 and 0.8) and YOF: 0.4 mol % Bi^{3+}, x mol % Ho^{3+} (x = 0.8, 1.4, 2, 3, 4 and 5) samples. The Bi^{3+} single doped and Bi^{3+}-Ho^{3+} co-doped YOF phosphor is therefore an appropriate candidate for optoelectronic applications such as for UV-LEDs and scintillators.

8.1 Introduction

Phosphor materials can be used for flat panel displays such as FEDs, plasma display panels, vacuum fluorescent displays and electroluminescent displays [1]. Other optical applications that involve semiconductors and/or phosphor materials, such as light-emitting diodes (LEDs), have lately gained a lot of research attention due to low energy consumption, long lifetimes and ecofriendly characteristics [2, 3]. Phosphor materials must have good energy efficiencies in order to reduce power consumption for flat panel displays or LEDs applications, for example [4]. Recently, several researchers investigated rare earth materials as potential candidates for various optical applications [5-8]. Investigations on the ns^2- ions, like Bi^{3+} have also been done for optical applications for many years [9-11].

Bi^{3+} is one of the ns^2-sp ions, such as Pb^{2+}, Sn^{2+} and Sb^{3+} [9]. Bi^{3+} has an $[Xe]4f^{14}5d^{10}6s^2$ electronic configuration due to the loss of electrons in p shell of elemental Bi [12]. This allows Bi^{3+} to be applied in a variety of applications due to its intrinsic energy levels. The energy levels are characterized with a single $^1S_0$ ground state and multiple excited levels [9]. The excited levels consist of one excited $^1P_1$ state and a triplet excited state known as $^3P_2$, $^3P_1$ and $^3P_0$. The $^1S_0 \rightarrow {}^1P_1$ transition is a spin allowed transition. The transitions $^1S_0 \rightarrow {}^3P_2$ and $^1S_0 \rightarrow {}^3P_1$ are forbidden but can become allowed due to induced coupling with unsymmetrical lattice vibration modes and spin orbit coupling, respectively [9]. The $^1S_0 \rightarrow {}^3P_0$ transition is strongly forbidden. Ho^{3+} is considered as one of the best choices for a co-doping ion for luminescent applications because of its wide spectral absorption [13, 14]. Ho^{3+} is characterized with numerous energy levels that result in various luminescent states due to the complexity of the $4f^{10}$ energy level system [13].

CL studies of YOF doped with various rare earth ions have been carried out for many years [15, 16]. YOF has a large band gap (~ 7.2 eV) and a low phonon energy (~ 400 cm^{-1}) that makes it a suitable host for different types of ions [17]. Zhang and his group have done various studies on the CL of different lanthanide ions (Tb^{3+}, Eu^{3+}, Tm^{3+}, Dy^{3+}, Ho^{3+}, Sm^{3+}), single or co-doped, in YOF with different morphologies that showed promising behavior for FEDs, fields of solid state light, color displays, anti-counterfeit and luminescent labels [15, 16]. CL of Bi^{3+} has been investigated in different hosts as a single doping or co-doped with lanthanide ions that showed promising performances for different applications such as fabrication of near-ultraviolet/blue InGaN-based LEDs and FEDs [10, 11, 18].

Our previous PL studies on YOF:Bi^{3+} and YOF:Bi^{3+}, Ho^{3+} (chapter 7) revealed an intense ultraviolet and green emission for both phosphors and an enhancement of the NIR emission for the co-doped sample. The present research is an extension of the work done on the PL of YOF:Bi^{3+} and YOF: Bi^{3+}, Ho^{3+}. It involves the CL investigations of YOF:Bi^{3+} and YOF:Bi^{3+}, Ho^{3+} for possible application for FEDs, LEDs and other optical applications.

8.2. Experimental

Pure YOF and Bi^{3+} and Ho^{3+} co-doped YOF powder samples were prepared by the pyrolysis method with trifluoroacetate as precursor from a single source. The pyrolysis method used was previously reported in our research done on YOF:Pr^{3+} [17]. The doped YOF: 0.4 mol % Bi^{3+}, x mol % Ho^{3+} (x = 0.8, 1.4, 2, 3, 4 and 5) samples were prepared by the same method with only introducing Ho_2O_3 in the starting materials.

The structure of the prepared samples was characterized by XRD using a Bruker Advance D8 diffractometer (40 kV, 40 mA) with Cu K_α x-rays (λ = 0.154 nm). SEM images were taken by using the JEOL JSM-7800F SEM. High resolution XPS was obtained with a PHI 5000 Versa-probe system as was described in chapter 3, section 3.4. All measurements were performed at room temperature. The CL emission spectra were measured using a Gatan MonoCL4 equipped to the JEOL JSM-7800F system in a vacuum of the order of 10^{-5}–10^{-6} Torr and with an electron beam energy of 5 keV.

8.3. Results & discussion

Figure 1 shows the XRD results of the high Ho^{3+} concentration (YOF: 0.4 mol % Bi^{3+}, 5 mol % Ho^{3+}) co-doped sample, the YOF: 0.4 mol % Bi^{3+} and YOF: 2 mol % Ho^{3+} single doped samples compared to the pure host sample. Both the 0.4 mol % Bi^{3+} and the 2 mol % Ho^{3+} doped samples were previously determined by the authors to be the optimum singly doped concentrations [articles in preparation]. All the patterns showed a pure rhombohedral YOF structure (space group: $R\bar{3}m$ (166)), without any noticeable impurities, after annealing at around 900 ^{0}C in air atmosphere [17]. A small shift towards the lower angles of the diffraction peaks was a resulted from doping with 0.4 mol % of Bi^{3+}. This shift might be due to the difference in the ionic radii of the Y^{3+} (0.1019 nm) and Bi^{3+} (0.117 nm) ions and this also occurred after doping with Pr^{3+} ions as was reported in our previous research done on YOF:Pr^{3+} [17]. There was no extra shift observed in the diffraction peaks after doping and co-doping with Ho^{3+} as the ionic radii of Ho^{3+} was 0.1015 nm. We have to mention that wasn't any additional peaks even after doping with 5 mol % of Ho^{3+}.

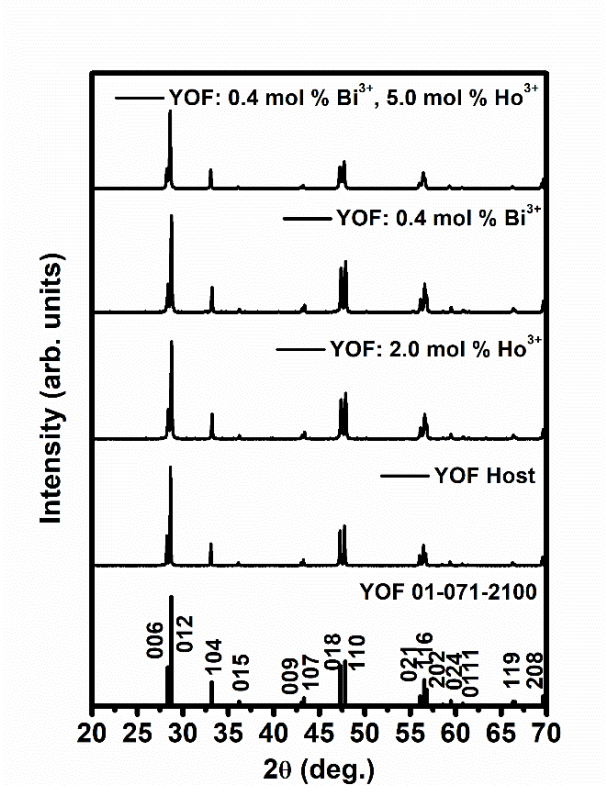

Figure 1: XRD pattern of the host material, of YOF: 2 mol % Ho^{3+}, of YOF: 0.4 mol % Bi^{3+} and of YOF: 0.4 mol % Bi^{3+}, 5 mol % Ho^{3+}.

SEM was used to investigate the prepared samples' morphology. The variation of the morphology is shown in figure 2. The morphology of the surface showed a variation of agglomerated melted particles for the host as well as for the Ho^{3+} and Bi^{3+} doped and co-doped samples. The Ho^{3+} single doped sample, figure 2(b), shows big agglomerated particles and the Bi^{3+} single doped sample, figure 2(c), shows smaller agglomerated particles. The Ho^{3+} and Bi^{3+} co-doped sample, figure 2(d), shows the same morphology as for the Bi^{3+} single doped sample, figure 2(c). Co-doping with Ho^{3+} and the increase in the Ho^{3+} concentrations did not affect the morphology. The authors previously reported on the agglomeration and melting of the particles during their investigations of the YOF:Pr^{3+} phosphor [17]. This kind of morphology was also reported by Z. Li et al. [19] and Eloussifi et al. [20] during their investigations on the pyrolysis method of YOF:Yb^{3+}, Er^{3+} thin films and of the thermal decomposition of YOF, respectively.

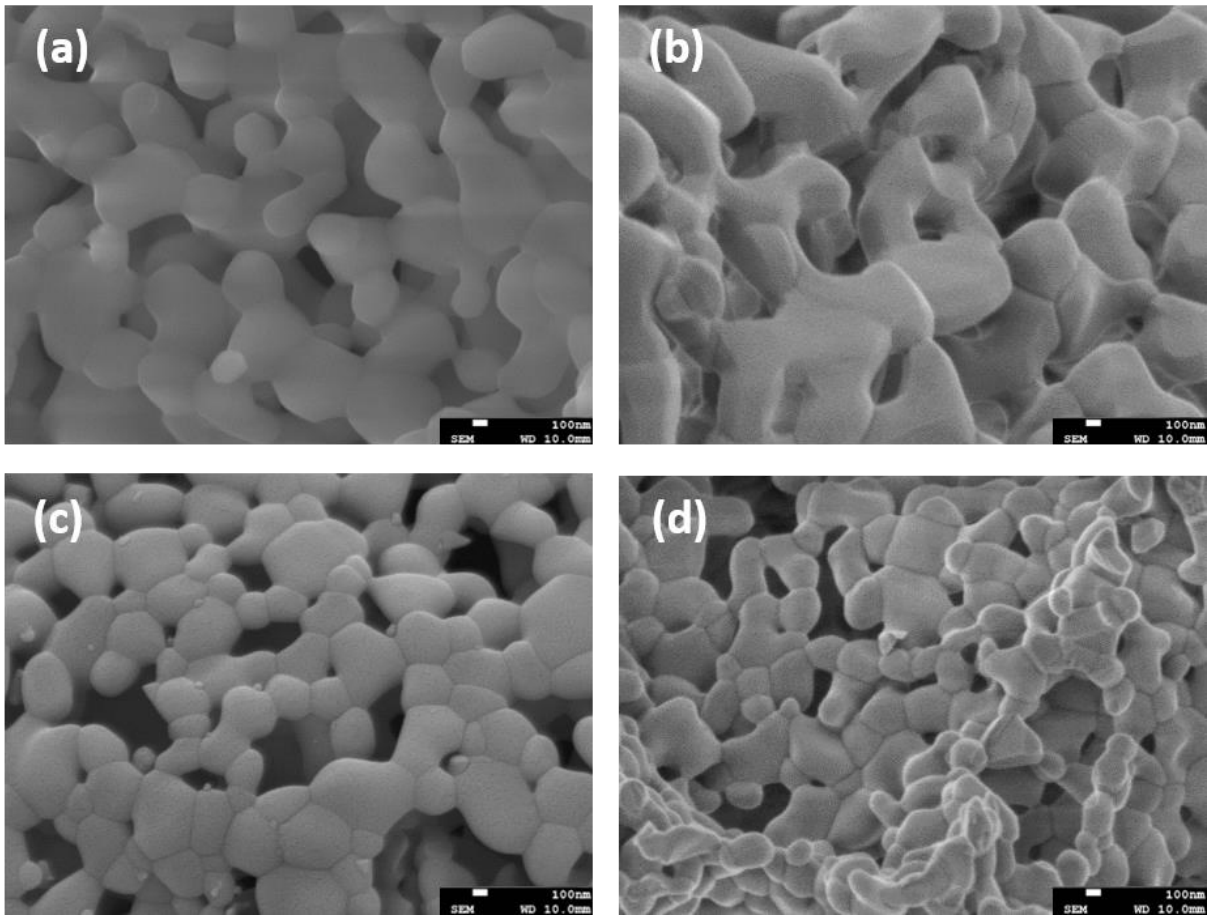

Figure 2: SEM images representing the variation of the morphology of the (a) YOF host, (b) YOF: 2 mol % Ho^{3+}, (c) YOF: 0.4 mol % Bi^{3+} and (d) YOF: 0.4 mol % Bi^{3+}, 5 mol % Ho^{3+}.

Surface elemental composition was done by XPS on the high co-doped YOF: 0.4 mol % Bi^{3+}, 5 mol % Ho^{3+} sample as well as for an additional YOF: 5 mol % Bi^{3+} sample. Figures 3(a) and

(b) show the survey scan for both the YOF: 5 mol % Bi^{3+} and YOF: 0.4 mol % Bi^{3+}, 5 mol % Ho^{3+} samples, respectively. Both samples showed the Y 3d, O 1s, F 1s and Bi 4d peaks. Bi 4f and Ho 4d peaks overlap with Y 3d peaks. The XPS high-resolution Y 3d peak fits were done by the authors with the previous PL investigations of YOF: 0.4 mol % Bi^{3+}, 5 mol % Ho^{3+} and it showed that the obtained Bi 4f and Ho 4d peak positions' correlated well with other reported values [21-24]. The presence of only Bi metal was due to the segregation of Bi^{3+} to the surface during annealing and its reduction to Bi metal [22]. Bi 4f peaks of Bi metal were detected even at low concentrations of Bi^{3+} whereas, Bi 4f peaks of Bi^{3+} were started to appear at high concentrations of Bi^{3+}, this was also confirmed for other samples (data not shown). The presence of the C 1s peak was due to the presence of C contamination on the surface due to adventitious hydrocarbons [17].

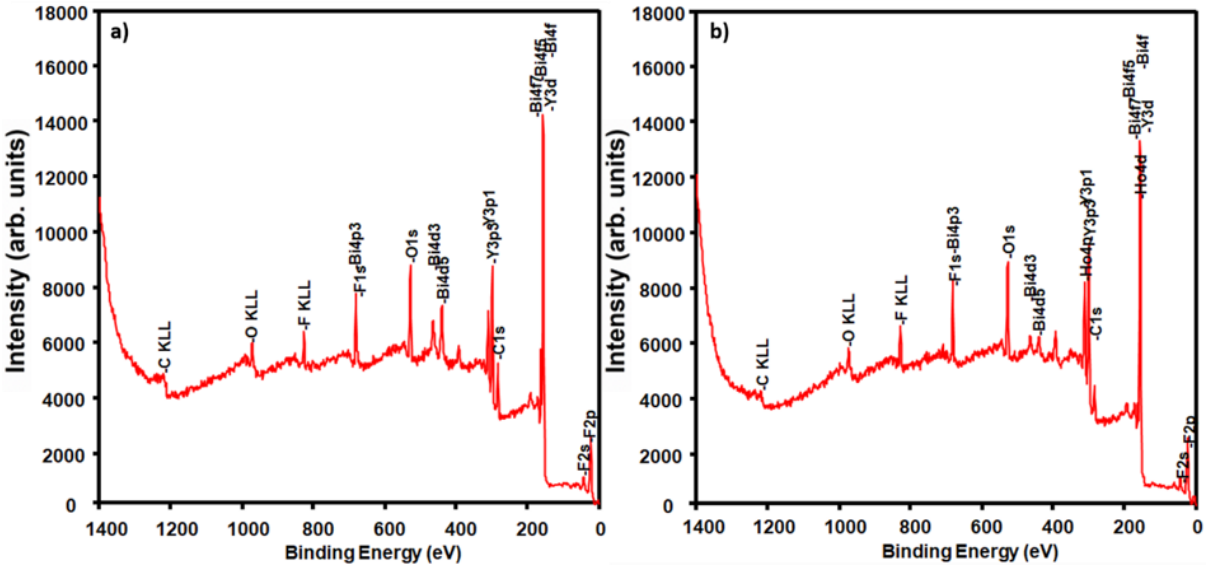

Figure 3: XPS survey scans showing the Y 3d, O 1s, F 1s, Bi 4f and Ho 4d peaks in the (a) YOF: 5 mol % Bi^{3+} and in the (b) YOF: 0.4 mol % Bi^{3+}, 5 mol % Ho^{3+} sample.

The prepared YOF:Bi^{3+} and YOF:Bi^{3+}, Ho^{3+}samples' emission were investigated by CL. Figure 4(a) shows the normalized CL spectra for the YOF: x mol % Bi^{3+} (x = 0.3, 0.4, 0.5, 0.6, 0.8) sample. The CL spectra consisted of the characteristic Bi^{3+} broad band emission ascribed to the $^3P_1 \rightarrow {}^1S_0$ transition at around 316 nm [25]. This emission also correlated well with the PL emission results from the authors' previous investigation of YOF:Bi^{3+}, that peaked at 314 nm. An additional broad emission was detected around 624 nm. Bi^{2+} usually emits in the red region due to the $^2P_{3/2}$ (1) $\rightarrow {}^2P_{1/2}$ transition [26, 27]. Bi^{2+} has an electronic configuration of $[Xe]4f^{14}5d^{10}6s^2p^1$ with a $^2P_{1/2}$ ground state and a $^2P_{3/2}$ first (1) excited state derived from $6s^26p^1$

[26, 27]. The $^3P_{3/2}$ level can split into $^3P_{3/2}$ (1) and $^3P_{3/2}$ (2) levels due to the crystal field splitting effect [26]. The intensity ratio of Bi^{2+} to Bi^{3+} emission is shown in figure 4(b). The intensity ratio increased gradually from 0.3 mol % concentration up to the optimum concentration of 0.5 mol % and then it decreased for the highest 0.6 and 0.8 mol % concentrations. In figure 4(c) a comparison of the normalized PL and CL emissions of the YOF: 0.4 mol % Bi^{3+} sample is shown in the 200 – 800 nm range that confirmed that Bi^{2+} emission only existed for the CL irradiation due to the crystal disturbance [28]. Despite the presence of Bi metal that was confirmed by XPS investigation, it is well known that Bi metal has no emission [9]. Further XPS investigations will be done after CL irradiation in order to show the Bi^{2+} binding energy peaks.

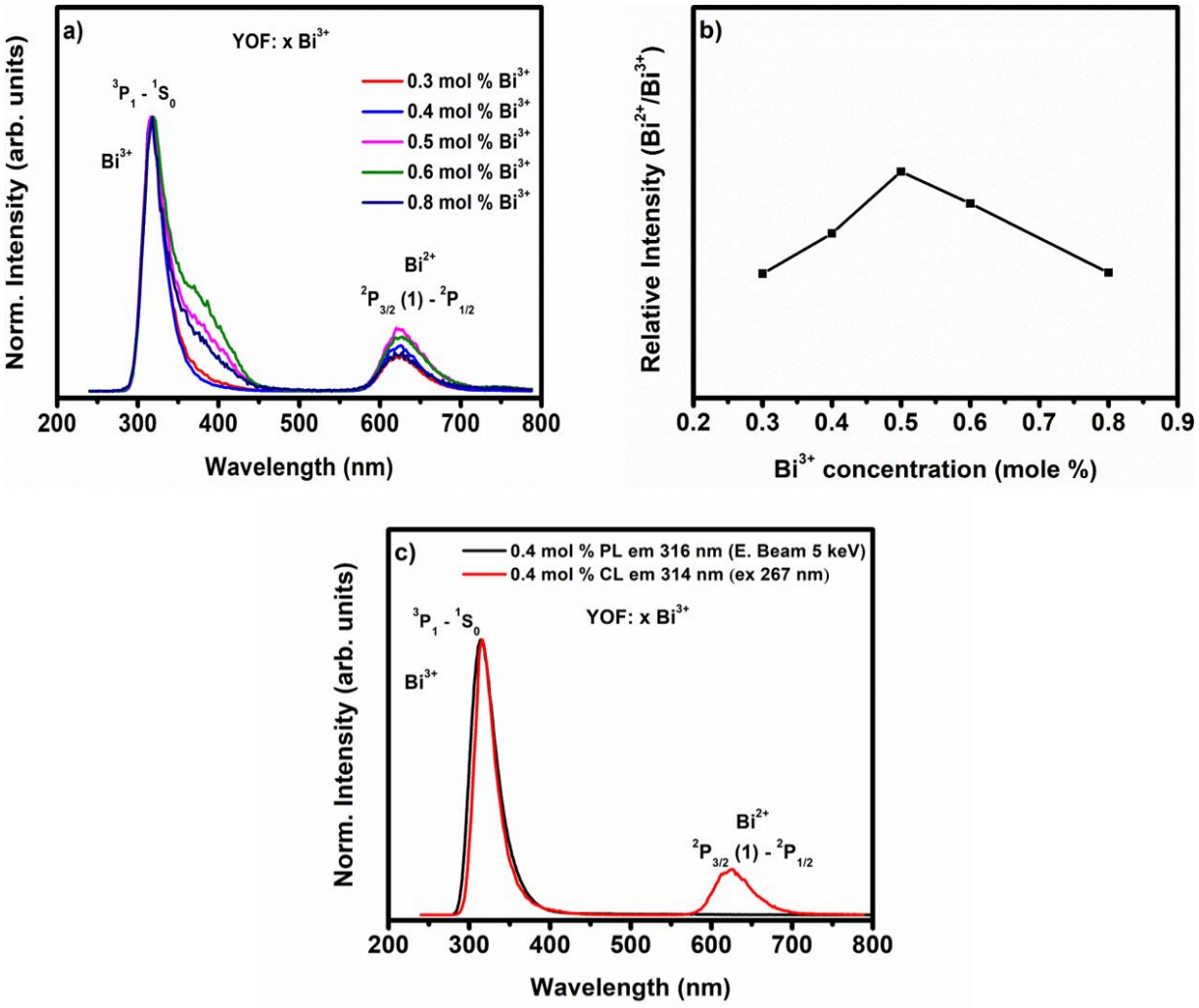

Figure 4: (a) CL emission of Bi^{3+} for different concentrations of Bi^{3+} ions under 5 keV electron beam irradiation, (b) the intensity ratio of the relative Bi^{2+}/Bi^{3+} emission for different Bi^{3+} concentrations and (c) the normalized PL and CL emission of the YOF: 0.4 mol % Bi^{3+} sample.

The broadening of the CL spectra for some of the samples in figure 4(a) might be due to defects that were created inside the structure. A distortion in the crystal lattice can appear as a peak shift or as a broadening in the CL emission peaks [28]. This will then result in changes in the crystal field's parameters that causes a variation in the excited state energy or it can create non-radiative electron transitions [28]. The presence of the Bi^{2+} emission might therefore be due to the disturbance in the host lattice that resulted from the high electron energy excitation of the excitation source. The photon energy of PL excitation sources are usually in the order of eV while CL excitation sources (electron beam) is in the order of keV [29]. PL excitation sources usually only excites the dopant ion while CL excitations might excite the band gap of the host material as well as the dopant ion. In CL excitation, the primary electrons will cause ionization and creates many secondary electrons. The secondary electrons will create more electron – hole pairs [29]. It is known that Bi^{3+} segregate to the surface during annealing [30, 31]. During electron beam irradiation the Bi^{3+} on the surface, will therefore be ionized and give rise to Bi^{2+}. The high excitation energy caused the electrons to be excited to the $^1S_{1/2}$ level that will relax to the $^3P_{3/2}$ (1) level through multi-relaxation and cause the red emission in the CL spectra. The presence of Bi^{2+} during CL investigation is well known for Bi^{3+} doped in different hosts and was also investigated by other researchers in other systems such as $CaO:Bi^{3+}$ [26] and with X-Ray excitation as in $YPO_4:Bi^{3+}$ [27].

Further CL investigations were done on a single doped YOF: 2 mol % Ho^{3+} and a co-doped YOF: 0.4 mol % Bi^{3+}, x mol % Ho^{3+} (x = 0.8, 1.4, 2, 3, 4 and 5) sample. Figure 5(a) shows the normalized CL and PL spectra of the YOF: 2 mol % Ho^{3+} sample. It shows the main emission peak around 540 nm that were ascribed to the $^5F_4,^5S_2 \rightarrow {}^5I_8$ transition of Ho^{3+} for CL [32 , 33]. It was noticed that the CL emission did not show the red emission of Ho^{3+} if compared to the PL emission. This might be due to the CL excitation mechanism as described above. The obtained CL spectra for all YOF: 0.4 mol % Bi^{3+}, x mol % Ho^{3+} co-doped samples showed the same typical emissions of Bi^{3+} and Bi^{2+} at 316 nm and 624 nm, respectively, see figure 5(b) [32, 33]. The existence of the Ho^{3+} emission was due to the $^5F_4,^5S_2 \rightarrow {}^5I_8$ transition at 540 nm and this indicated a possible energy transfer between Bi^{3+} and Ho^{3+}. Figure 5(c) shows the intensity ratios of the relative Bi^{2+}/Bi^{3+} and Ho^{3+}/Bi^{3+} intensities as a function of Ho^{3+} co-doping concentrations. The intensity ratio of Ho^{3+}/Bi^{3+} indicated that an energy transfer occurred from Bi^{3+} to Ho^{3+} as was shown with the decrease in the Bi^{3+} intensity in respect to increase in Ho^{3+} emission. The optimum Ho^{3+} concentration for the YOF: 0.4 mol % Bi^{3+}, x mol % Ho^{3+} sample was obtained for the 4 mol % Ho^{3+} co-doped sample. The decrease to 5

mol % of Ho^{3+} concentration was due to concentration quenching [26, 27]. In contrast to the Ho^{3+}/Bi^{3+} intensity ratio, the Bi^{2+}/Bi^{3+} ratio showed a fluctuation in the ratio and this can be explained based on the nature of Bi^{3+} emission in different systems where Bi^{3+} is highly influenced with the surrounding ligands and the effects of co-doping [34, 35]. This also explains that the Bi^{2+} emission was less influenced by the presence of Ho^{3+} and also confirmed the presence of Bi^{2+} on the surface. In the present YOF:Bi^{3+}, Ho^{3+} system, a plausible reason for the slight fluctuation might therefore be due to presence of Ho^{3+} and that some defects were created during co-doping and electron beam irradiation.

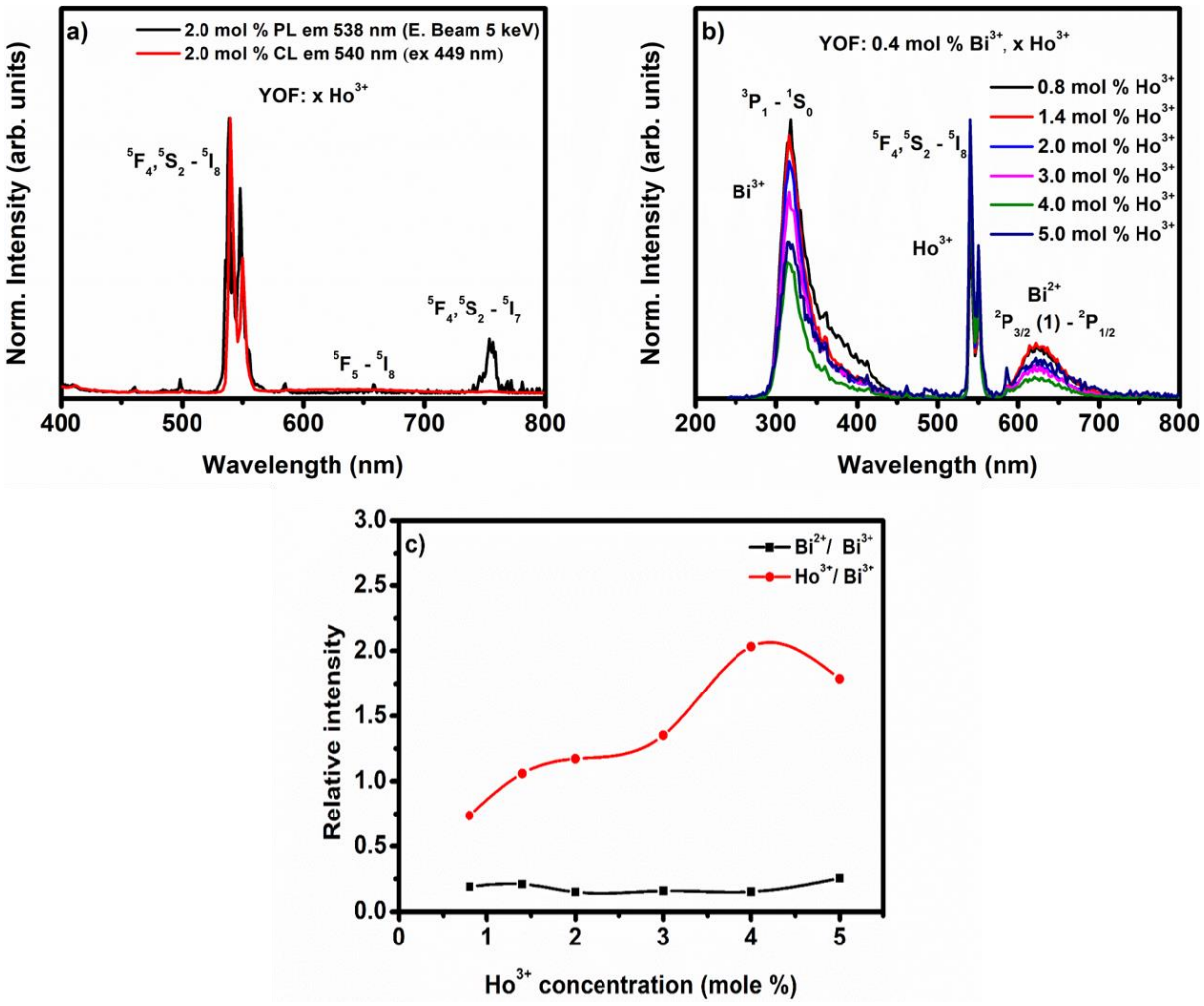

Figure 5: (a) The normalized CL and PL emissions of YOF: 2 mol % Ho^{3+}, (b) CL emission of YOF: 0.4 mol % Bi^{3+}, x mol % Ho^{3+} (x = 0.8, 1.4, 2, 3, 4, 5) under 5 keV electron beam irradiation and (c) the variation of the relative Bi^{2+}/Bi^{3+} and Ho^{2+}/Bi^{3+} intensity ratios for different Ho^{3+} concentrations.

The Commission Internationale de l'Eclairage (CIE) color coordinates for the YOF: 2 mol % Ho^{3+} and YOF: 0.4 mol % Bi^{3+}, x mol % Ho^{3+} (x = 0.8, 1.4, 2, 3, 4 and 5) phosphors under

electron beam irradiation at 5 keV are shown in figure 6 and tabulated in table 1. The CIE coordinates was obtained by using the Edinburgh FS5 fluorometer. The CL emission of the phosphors showed tunable emission from green to yellow and orange.

Table 1: CIE X and Y coordinates of the YOF: 2 mol % Ho^{3+} and the YOF: 0.4 mol % Bi^{3+}, x mol % Ho^{3+} samples (x = 0.8, 1.4, 2, 3, 4 and 5).

No.	Sample	X	Y
1	YOF: 2 mol % Ho^{3+}	0.29	0.64
2	0.8	0.43	0.43
3	1.4	0.45	0.47
4	2	0.40	0.52
5	3	0.39	0.52
6	4	0.37	0.56
7	5	0.39	0.50

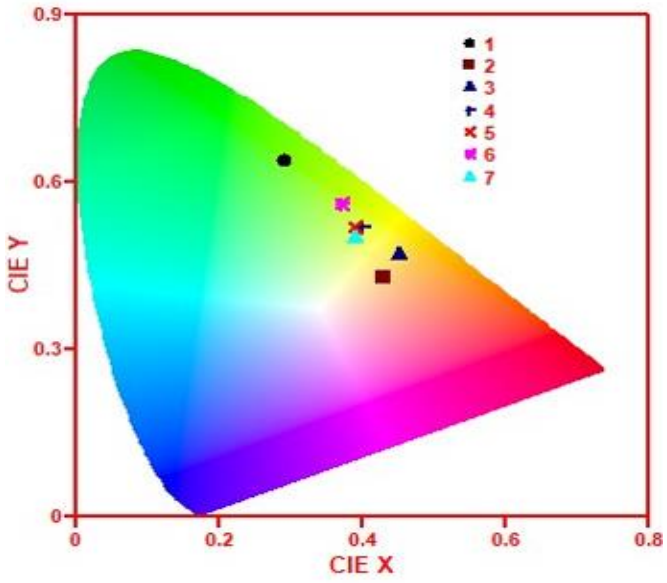

Figure 6: The plotted chromaticity coordinates for the YOF: 2 mol % Ho^{3+} and YOF: 0.4 mol % Bi^{3+}, x mol % Ho^{3+} (x = 0.8, 1.4, 2, 3, 4 and 5) samples under 5 keV electron beam irradiation.

Based on the obtained emissions for both the YOF:Bi^{3+} and YOF:Bi^{3+}, Ho^{3+} samples we can propose a possible mechanism for the energy transfer between Bi^{3+} and Ho^{3+}. Figure 12 shows

the proposed energy levels for Bi^{2+}, Bi^{3+} and co-doped with Ho^{3+} and the possible energy paths for both YOF:Bi^{3+} and YOF:Bi^{3+}, Ho^{3+}. During electron beam irradiation at 5 keV, in the YOF:Bi^{3+} system, the high excitation energy will result in an excitation of the host itself. Relaxation of the energy will result in excitation of Bi^{3+} and then emission through the $^3P_1 \rightarrow {}^1S_0$ transition, see figure 12. Some of the energy will then relax to some defect levels created within the band gap that caused the broadening in the Bi^{3+} CL emission. The presence of the Bi^{2+} emission was a result of high energy electron irradiation. Excitation to the $^1S_{1/2}$ excited level of Bi^{2+} caused a multi-relaxation to the splitted $^3P_{3/2}$ (1) level and finally resulted in $^2P_{3/2}$ (1) $\rightarrow {}^2P_{1/2}$ emission at 624 nm. In the YOF:Bi^{3+}, Ho^{3+} sample the same process occurred in the system for Bi^{3+} and Bi^{2+} emissions. The excitation energy will excite both Bi^{3+} and Ho^{3+}. Energy will be transferred from Bi^{3+} to Ho^{3+} that was explained by the decrease of Bi^{3+} emission while Ho^{3+} emission increased with increasing Ho^{3+} ions concentration. The significant decrease (quenching) of the Bi^{3+} UV emission and the increase in the Ho^{3+} green emission at high Ho^{3+} concentrations resulted in tuning of the emission from UV to orange, to yellow to green. According to the author's previous YOF:Bi^{3+}, Ho^{3+} PL investigations, the energy is transferred from Bi^{3+} to the $^3H_6$ level of Ho^{3+} in which multi-relaxation occurred to populate the $^5F_4$ and $^5S_2$ levels. Population of both the $^5F_4$ and $^5S_2$ levels was followed by radiative emission to the $^5I_8$ ground level that is represented by $^5F_4$,$^5S_2 \rightarrow {}^5I_8$ emission [13].

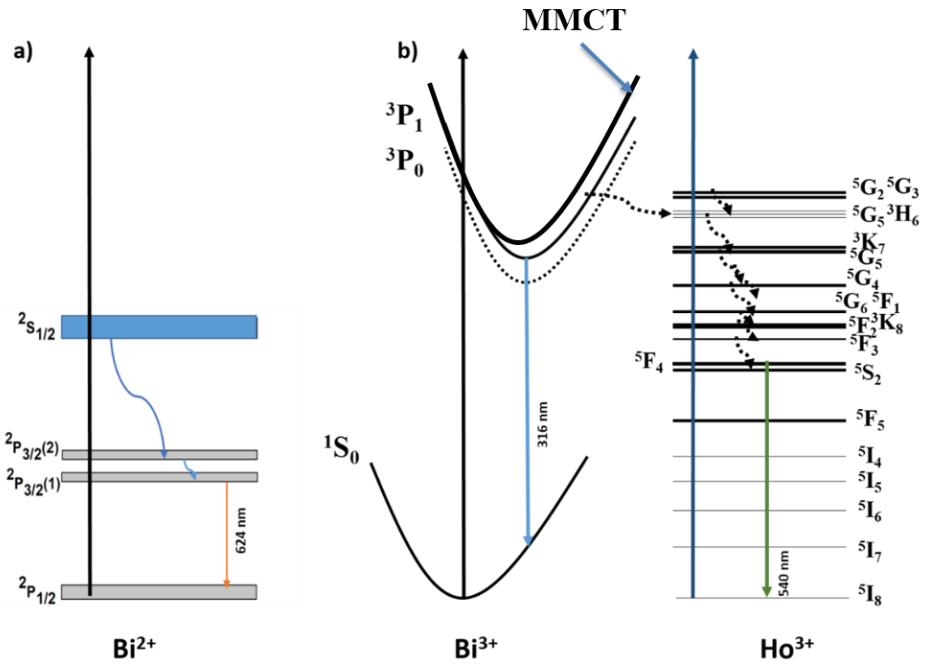

Figure 12: Proposed energy level diagram of the YOF: x mol % Bi^{3+} (x = 0.3, 0.4, 0.5, 0.6 and 0.8) and YOF: 0.4 mol % Bi^{3+}, x mol % Ho^{3+} (x = 0.8, 1.4, 2, 3, 4 and 5) phosphors for (a) Bi^{2+} and (b) Bi^{3+} and Ho^{3+}.

8.4. Conclusion

The YOF: x mol % Bi^{3+} (x = 0.3, 0.4, 0.5, 0.6 and 0.8) and YOF: 0.4 mol % Bi^{3+}, x mol % Ho^{3+} (x = 0.8, 1.4, 2, 3, 4 and 5) phosphors were successfully synthesized using the pyrolysis method with trifluoroactate as precursor. XRD results showed a high crystallinity of the powder as rhombohedral YOF (space group: $R\bar{3}m$ (166)) after annealing at 900 ^{0}C. XPS survey investigation for both YOF: 5 mol % Bi^{3+} and YOF: 0.4 mol % Bi^{3+}, 5 mol % Ho^{3+} samples showed the C 1s, Y 3d, O 1s, F 1s and Bi 4d binding energy peaks with Bi 4f and Ho 4d in the same energy range as Y 3d. CL results for the YOF: x mol % Bi^{3+} samples showed both the $^3P_1 \rightarrow {}^1S_0$ emission of Bi^{3+} at 316 nm and the $^2P_{3/2}$ (1) $\rightarrow {}^2P_{1/2}$ transition of Bi^{2+} emission at 624 nm. Bi^{2+} was a result from ionization due to the high electron energy radiation. The YOF: 0.4 mol % Bi^{3+}, x mol % Ho^{3+} co-doped samples showed ultraviolet (UV) (250 – 450 nm) CL emission at 316 nm that originated from the $^3P_1 \rightarrow {}^1S_0$ transition of Bi^{3+}. The green (450 – 580 nm) CL emission that peaked at 540 nm originated from the $^5F_4$,$^5S_2 \rightarrow {}^5I_8$ transition of Ho^{3+}. The red (580 – 800 nm) CL emission that peaked at 624 nm was ascribed to the $^2P_{3/2}$ (1) $\rightarrow {}^2P_{1/2}$ transition of Bi^{2+}. The optimum Ho^{3+} concentration for visible CL emission was recorded for the sample co-doped with 4 mol % of Ho^{3+}. The fitted CIE coordinates showed tunable emission for different YOF: 0.4 mol % Bi^{3+}, x mol % Ho^{3+} co-doped samples from green to yellow and orange. The Bi^{3+} single doped and Bi^{3+}-Ho^{3+} co-doped YOF phosphor is therefore an appropriate candidate for optoelectronic applications such as for UV-LEDs and scintillators.

References

[1] G. Li and J. Lin, Chem. Soc. Rev. 43 (2014) 7099 - 7131.

[2] L.L. Wang, Q.L. Wang, X.Y. Xu, J.Z. Li, L.B. Gao, W.K. Kang, J.S. Shi and J. Wang, J. Mater. Chem. C, 1 (2013) 8033 - 8040.

[3] W.R. Liu, C.H. Huang, C.W. Yeh, J.C. Tsai, Y.C. Chiu, Y.T. Yeh and R.S. Liu, Inorg. Chem. 51 (2012) 9636 - 9641.

[4] M.K. Mahata, T. Koppe, H. Hofsäss, K. Kumar and U. Vetter, Phys. Procedia, 76 (2015) 125 - 131.

[5] M.K. Mahata, K. Kumar and V.Kr. Rai, Sensors and Actuators B, 209 (2015) 775 - 780.

[6] Z. Gu, L. Yan, G. Tian, S. Li, Z. Chai, and Y. Zhao, Adv. Mater. 25 (2013) 3758 - 3779.

[7] X. Huang, S. Han, W. Huang and X. Liu, Chem. Soc. Rev. 42 (2013) 173 - 201.

[8] A.K. Singh, S. Singh, D. Kumar, D.K. Rai, S.B. Rai and K. Kumar, Opt. Lett. 37 (2012) 776 - 778.

[9] H.T. Sun, J. Zhou and J. Qiu, Prog. Mater. Sci. 64 (2014) 1 - 72.

[10] P. Du, L.K. Bharat and J. S. Yu, J. Alloys Compds. 633 (2015) 37 - 41.

[11] D. Huang, Y. Zhou, W. Xu, Z. Yang, Z. Liu, M. Hong, Y. Lin and J. Yu, J. Alloys Compds. 554 (2013) 312 - 318.

[12] F. Kang and M. Peng, Dalton Trans. 43 (2014) 277 - 284.

[13] X. Zhang, G. Zhou, J. Zhou, H. Zhou, P. Kong, Z. Yu and J. Zhan, RSC Adv. 4 (2014) 13680 - 13686.

[14] X.P. Chen, W.J. Zhang and Q.Y. Zhang, Physica B, 406 (2011) 1248 - 1252.

[15] Y. Zhang, D. Geng, X. Kang, M. Shang, Y. Wu, X. Li, H. Lian, Z. Cheng and J. Lin, Inorg. Chem. 52 (2013) 12986 - 12994.

[16] Y. Zhang, X. Li, D. Geng, M. Shang, H. Lian, Z. Cheng and J. Lin, Cryst. Eng. Comm. 16 (2014) 2196 - 2204.

[17] N.A.M. Saeed, E. Coetsee and H.C. Swart, Opt. Mater. 96 (2019) 109331 (12 pages).

[18] J.H. Bahng, E.S. Oh, S.H. Seo, J.S. Kim, M. Lee, H.L. Park, C. Lee, G.C. Kim and K.J. Kim, phys. stat. sol. 191 (2002) 291 - 295.

[19] Z. Li, L. Zheng, L. Zhang and L. Xiong, J. Lumin. 126 (2007) 481 - 486.

[20] H. Eloussifi, J. Farjas, P. Roura, J. Camps, M. Dammak, S. Ricart, T. Puig and X. Obradors, J. Therm. Anal. Calorim. 108 (2012) 589 - 596.

[21] K.L. Li, W.W. Lee, C.S. Lu, Y.M. Dai, S.Y. Chou, H.L. Chen, H.P. Lin and C.C. Chen, J. Taiwan Inst. Chem. E, 45 (2014) 2688 - 2697.

[22] F.J. Palomares, E. Paz, F. Soria, and J.S. Moya, J. Am. Ceram. Soc. 92 (2009) 2993 - 2998.

[23] J.F. Moulder, W.F. Stickle, P.W. Sobol and K.D. Bomben, Handbook of X-ray Photoelectron Spectroscopy (Perkin-Elmer, Eden Prairie, MN, 1992).

[24] X. Xu, S. Zhou, J. Long, T. Wu and Z. Fan, Mater. 10 (2017) 302 (15 pages).

[25] A.A. Setlur and A.M. Srivastava, Opt. Mater. 29 (2006) 410 - 415.

[26] Yousif, R.M. Jafer, S. Som, M.M. Duvenhage, E. Coetsee and H.C. Swart, RSC Adv. 5 (2015) 54115 - 54122.

[27] R.H.P. Awater, L.C.N. Berghuijs and P. Dorenbos, Opt. Mater. 66 (2017) 351 - 355.

[28] A. Guscik, Cathodoluminescence and its Application in the Planetary Sciences, Springer-Verlag Berlin Heidelberg, (2009).

[29] G.S.R. Raju, E. Pavitra, Y.H. Ko and J.S. Yu, J. Mater. Chem. 22 (2012) 15562 - 15569.

[30] Y. Zorenko, V. Gorbenko, T. Voznyak, V. Vistovsky, S. Nedilko and M. Nikl, Radiat. Meas. 42 (2007) 882 - 886.

[31] X. Wu, Y. Liang, R. Chen, M. Liu and Y. Li, J. Mater. Sci. 46 (2011) 5581 -5586.

[32] Y. Zhang, D. Geng, X. Kang, M. Shang, Y. Wu, X. Li, H. Lian, Z. Cheng and J. Lin, Inorg. Chem. 52 (2013) 12986 - 12994.

[33] Y. Zhang, X. Li, D. Geng, M. Shang, H. Lian, Z. Cheng and J. Lin, Cryst. Eng. Comm. 16 (2014) 2196 - 2204.

[34] G. Blasse and A. Bril, J. Chem. Phys. 47 1920 (1967) 217 - 222.

[35] P. Boutinaud, Inorg. Chem. 52 (2013) 6028 - 6038.

Chapter 9

Conclusions and future work

This chapter contains the general conclusion of the results obtained as well as future work for the current research study.

9.1 Conclusion

The research presented in this thesis described the synthesis of the phosphor powders and the related structural, elemental and optical investigations for a set of luminescent ions doped in the YOF host. The obtained phosphors showed good optical behavior and the Pr^{3+}-Yb^{3+} and Bi^{3+}-Ho^{3+} couples are definitely possible candidates for c-Si SC enhancement.

YOF doped with different lanthanide ions (Pr^{3+}, Ce^{3+}, Yb^{3+}, Bi^{3+} and Ho^{3+}) were successfully synthesized by using the pyrolysis method with CF_3COO as precursor. XRD results showed a high crystallinity of the samples as stoichiometric rhombohedral YOF (space group: $R\bar{3}m$ (166)) after annealing in air at 900 ^{0}C for 2 hours. The crystallite sizes decreased with increasing doping concentrations. During the thermal decomposition to form YOF (600 ^{0}C to 900 ^{0}C), the SEM image showed an agglomeration of small particles (< 100 nm) that started to melt and agglomerate to form bigger particles with sizes > 500 nm.

XPS investigations showed two sets of fitted peaks for the Pr 3d peak that correspond to two different oxidation states for Pr 3d, Pr^{3+} and Pr^{4+}. PL results showed 4f-4f emission of Pr^{3+} under excitation of a broad band around 250 nm. The 4f-4f emission confirmed that Pr^{3+} ions were successfully incorporated into the Y^{3+} ions' positions of the YOF host lattice. The nature of the broad excitation band at 250 nm was ascribed to the 4f-5d transition of Pr^{3+} based on PL excitation and emission results obtained from a YOF:Ce^{3+} sample. The YOF:Ce^{3+} sample was specifically synthesized to confirm the existence of the Pr^{3+} 4f-5d level in order to contradict previous investigations that attributed the 250 nm excitation band to a Pr^{4+} charge transfer band.

The optimum Pr^{3+} concentration for PL emission was recorded for the sample doped with 0.3 % of Pr^{3+} as concentration quenching occurred at higher concentrations through cross relaxation processes. The low intensity NIR emission of YOF:Pr^{3+} is within the effective

response range for Si-SC and revealed a DS mechanism. YOF:Pr^{3+} is therefore an appropriate candidate to enhance the spectral response of Si-SC. The decay life times revealed the order of the life times in the range of μs which is consistent with other reported values of Pr^{3+} doped materials. The current investigations done on the YOF:Pr^{3+} phosphor material revealed a promising material for optoelectronic applications such as for UV-LED, SC and scintillators.

The YOF:Pr^{3+}, Yb^{3+} phosphors were investigated for DC applications for Si-SC. XPS peak deconvolutions showed the presence of both Pr^{3+} and Pr^{4+} for the Pr 3d peak. It also showed only the Yb 4d peak of Yb^{3+}. Visible PL results showed 4f-4f emission of Pr^{3+} upon 250 nm excitation. The IR excitation showed the typical Pr^{3+} 4f-5d band as well as the 4f-4f transitions upon 907 nm emission of Pr^{3+}. The existence of a new band at 225 nm during 971 nm emission of Yb^{3+} was interpreted in respect to YOF:Ce^{3+}. Theoretical investigations were also done in order to determine the nature of the 225 nm band and it was attributed to be a charge transfer band of Yb^{3+}. IR emission was due to Pr^{3+} and Yb^{3+} transitions upon excitation of 250 nm. Only emission due to the Yb^{3+} transitions was detected during excitation of 225 nm. Quenching of the Pr^{3+} IR emission during excitation of 225 nm was due to the cross-relaxation [$^1D_2$ (Pr^{3+}) + $^2F_{7/2}$ (Yb^{3+}) → $^3F_4$ (Pr^{3+}) + $^2F_{5/2}$ (Yb^{3+})] process that favors the 971 nm Yb^{3+} emission. The optimum Yb^{3+} concentration for IR emission was recorded for the sample co-doped with 2 mol % of Yb^{3+} as concentration quenching occurred at higher concentrations through cross relaxation processes. The obtained IR emission of YOF:Pr^{3+},Yb^{3+} was within the effective response range for Si SC. YOF:Pr^{3+},Yb^{3+} is therefore an appropriate candidate for Si SC enhancement. The decay times were in order of μs which is consistent with other reported values of Pr^{3+},Yb^{3+} doped materials.

AES results confirmed that Bi was homogeneously distributed on the surface of the YOF:Bi^{3+} sample. Two pairs of peaks could be fitted to the XPS data for the Bi 4f peak. The peaks were attributed to Bi^{3+} and Bi metal. PL studies revealed a broad UV emission band centered at 314 nm that originated from the $^3P_1 \rightarrow {}^1S_0$ A band with a symmetric excitation of 267 nm that corresponded to the $^1S_0 \rightarrow {}^3P_1$ A band of Bi^{3+}.

In order to explain the excitation and emission mechanism, investigations and theoretical calculations were done to predict the MMCT band. The MMCT excitation band was calculated to be situated at approximately 274 ± 26 nm that was in the same range than the A band. The emission peak at 314 nm was attributed to the $^3P_1 \rightarrow {}^1S_0$ A band transition. During excitation

to the MMCT band and to both the A band levels, non-radiative decay occurs from the MMCT to the emitting $^3P_1$ level. The interconfigurational nature of the transition and the presence of defects could result in the broadening of the excitation and emission peaks. The decay times obtained were in the microsecond range and showed the presence of Bi^{3+} centres perturbed by nearby defects. The measured quantum yield was measured to be 60 % by using the integrating sphere. According to the PL investigations the YOF:Bi^{3+} phosphor is therefore an appropriate candidate for optoelectronic applications such as for UV-LED, SC and scintillators, or to be applied as a sensitizer with other Ln^{3+} ions.

The YOF: 0.4 mol % Bi^{3+}, x mol % Ho^{3+} (x = 0.8, 1.4, 2, 3, 4 and 5) were investigated for a possible enhancement of IR emission of Ho^{3+}. XPS investigations showed an overlap of Bi 4f and Ho 4d peaks in the Y 3d peak. Visible PL results showed both the $^3P_1 \rightarrow {}^1S_0$ emission of Bi^{3+} and the 4f-4f transitions of Ho^{3+} under excitation of 265 nm and 449 nm. The broad excitation band that peaked at 265 nm was ascribed to the $^1S_0 \rightarrow {}^3P_1$ transition of Bi^{3+} whereas, the excitation peak at 449 nm was ascribed to the $^5I_8 \rightarrow {}^5F_1$, $^5G_6$ transition of Ho^{3+}. The UV (250 – 450) emission part at 314 nm originated from the $^3P_1 \rightarrow {}^1S_0$ transition of Bi^{3+}. The green (450 – 800 nm) emission part that peaked at 538 nm and 753 nm originated from Ho^{3+} and were ascribed to the $^5F_4$,$^5S_2 \rightarrow {}^5I_8$ and $^5F_4$,$^5S_2 \rightarrow {}^5I_7$ transitions of Ho^{3+}. The optimum Ho^{3+} concentration for visible PL emission was recorded for the sample co-doped with 2 mol % of Ho^{3+}. The IR emission was recorded for both 449 nm and 265 nm excitations with optimum concentration of about 3 mol % of Ho^{3+}. The IR emission that peaked at 1014 nm and 1200 nm were ascribed to the $^5F_4$,$^5S_2 \rightarrow {}^5I_6$ and $^5I_6 \rightarrow {}^5I_8$ transitions of Ho^{3+}. Population of the $^5I_6$ level might occur through the $^5S_2$, $^5I_8 \rightarrow {}^5I_7$, $^5I_7$, $^5I_6$ cross-relaxation process. The decay times for all emissions were in order of μs. The Bi^{3+}-Ho^{3+} co-doped YOF phosphor is therefore an appropriate candidate to enhance the spectral response of Si SC. Despite the efficient energy conversion in the Bi^{3+}, Ho^{3+} system, enhancement of the energy flow from Bi^{3+} to Ho^{3+} needs to be considered. This will reduce the dissipated energy into many unnecessary manifolds of Ho^{3+} and direct it to the range of spectral absorption of Si-SC.

The YOF: x mol % Bi^{3+} (x = 0.3, 0.4, 0.5, 0.6 and 0.8) and YOF: 0.4 mol % Bi^{3+}, x mol % Ho^{3+} (x = 0.8, 1.4, 2, 3, 4 and 5) phosphors were also investigated under electron beam irradiation (5 keV). XPS survey investigation for both the YOF: 5 mol % Bi^{3+} and YOF: 0.4 mol % Bi^{3+}, 5 mol % Ho^{3+} samples showed the C 1s, Y 3d, O 1s, F 1s and Bi 4d binding energy

peaks with Bi 4f and Ho 4d in the same energy range as Y 3d. CL results for the YOF: x mol % Bi^{3+} samples showed both the $^3P_1 \rightarrow {}^1S_0$ emission of Bi^{3+} at 316 nm and the $^2P_{3/2}$ (1) $\rightarrow {}^2P_{1/2}$ transition of Bi^{2+} emission at 624 nm. Bi^{2+} was a result from ionization due to the high electron energy radiation.

The YOF: 0.4 mol % Bi^{3+}, x mol % Ho^{3+} co-doped samples showed UV (250 – 450 nm) CL emission at 316 nm that originated from the $^3P_1 \rightarrow {}^1S_0$ transition of Bi^{3+} under 5 keV electron beam irradiation. The green (450 – 580 nm) CL emission that peaked at 540 nm originated from the $^5F_4$,$^5S_2 \rightarrow {}^5I_8$ transition of Ho^{3+}. The red (580 – 800 nm) CL emission that peaked at 624 nm originated was ascribed to the $^2P_{3/2}$ (1) $\rightarrow {}^2P_{1/2}$ transition of Bi^{2+}. The optimum Ho^{3+} concentration for visible CL emission was recorded for the sample co-doped with 4 mol % of Ho^{3+}. The fitted CIE coordinates showed tunable emission for different YOF: 0.4 mol % Bi^{3+}, x mol % Ho^{3+} co-doped samples from green to yellow and orange. The Bi^{3+} single doped and Bi^{3+}-Ho^{3+} co-doped YOF phosphor is therefore an appropriate candidate for optoelectronic applications such as for UV-LEDs and scintillators.

9.2 Future work

This research study investigated possible DC candidates as luminescent layers. Additional investigations are, however, needed on the enhancement of SC as well as on the application in UV-LEDs:

- Detailed investigation of the luminescence of Ce^{3+} in the YOF host for possible application as a sensitizer.
- Investigation of more luminescent ions like Sm^{3+} or Tm^{3+} in YOF host aiming at the Si-SC enhancement.
- Detailed XPS investigation on the YOF:Bi^{3+} and YOF:Bi^{3+}, Ho^{3+} samples after electron beam irradiation during CL measurements.
- Investigation of different co-doping combinations for Si-SC enhancement.
- Preparing thin films of the obtained phosphors to examine their performance on Si and on Si-SC substrates and to study the energy efficiencies.

Appendix A

Inokuti-Hirayama (I-H) model

Another way to calculate the critical distance is by using the I-H model.

The I-H model is a model that can be used to determine information such as the type of multipolar interaction (s), the energy transfer parameter (α), the critical distance (R_c) and the critical concentration (C_0) [1]. The aim here is to calculate the critical distance. The decay function according to the I-H model can be expressed as follows [1]:

$$\mathbf{I(t) = I_0 \exp\left[\frac{-t}{\tau_0} - \alpha\left(\frac{t}{\tau_0}\right)^{\frac{3}{s}}\right]} \quad \mathbf{\ldots\ldots\ldots\ldots\ldots\ldots\ldots\ldots\ldots\ldots\ldots\ldots\ldots\ldots(1).}$$

I(t) is the intensity at time t of the sample, I_0 is the intensity at time t = 0, τ_0 is the lifetime of the sample, α is the macroscopic parameter which determine the effect of the multipolar interaction on the decay curve, s is the type of the multipolar interaction and can have values of 6, 8 and 10 for dipole-dipole, dipole-quadrupole and quadrupole-quadrupole interactions respectively. Figure 1 shows the emission decay curve for the YOF:0.4 mol % Bi^{3+} sample and a theoretical least squares fit done by using the I-H equation 1 with multipolar interaction value s = 8 for dipole-quadrupole interaction. All the other samples were fitted by using the value s = 8 for the multipolar interaction (not shown).

The critical distance (Rc) can be determined from an expression for α [1]:

$$\mathbf{\alpha = \frac{4\pi}{3}\Gamma\left(1 - \frac{3}{s}\right) C_A R_c^3} \quad \mathbf{\ldots\ldots\ldots\ldots\ldots\ldots\ldots\ldots\ldots\ldots\ldots\ldots(2).}$$

$\Gamma\left(1 - \frac{3}{s}\right)$ is a gamma function as a function of the multipolar strength s and C_A is the concentration of the ions per cm^3. The value of the gamma function for the multipolar interaction s = 8 takes the value 1.43 for dipole-quadrupole interaction [1].

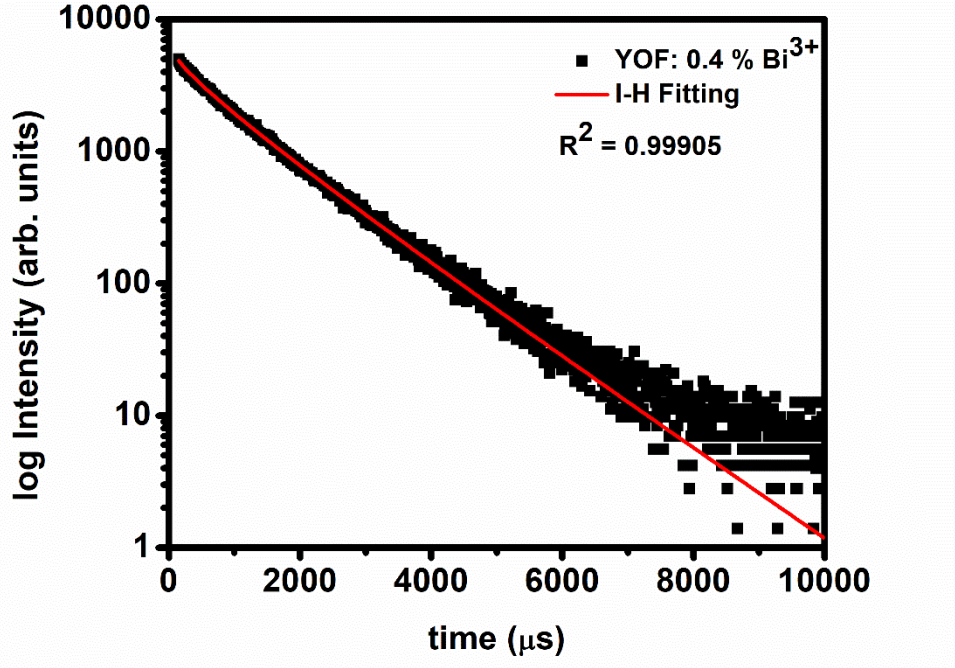

Figure 1: Emission decay curve for YOF: 0.4 mol % Bi^{3+} (λ_{em} = 31 800 cm^{-1}) and a theoretical fit using the Inokuti-Hirayama equation.

C_A can be obtained through the relation [2]:

$$C_A = \frac{\rho N_A C}{M_m} \text{.....(3),}$$

where ρ is the density of the host lattice (5.18 g/cm^3), N_A is Avogadro's number, C is the concentration in mole percent and M_m (123.903 g/mol) is the molar mass of the host lattice [3, 4]. In order to obtain R_c a linear fit for α versus $\frac{4\pi}{3}\Gamma(1 - \frac{3}{s})C_A$ for all the samples, with the slope equal to R_c^3 were done and is shown in figure 2. The slope was obtained to be around 2.10x10^{-21} cm^3 and R_c was then calculated to be 1.28 nm.

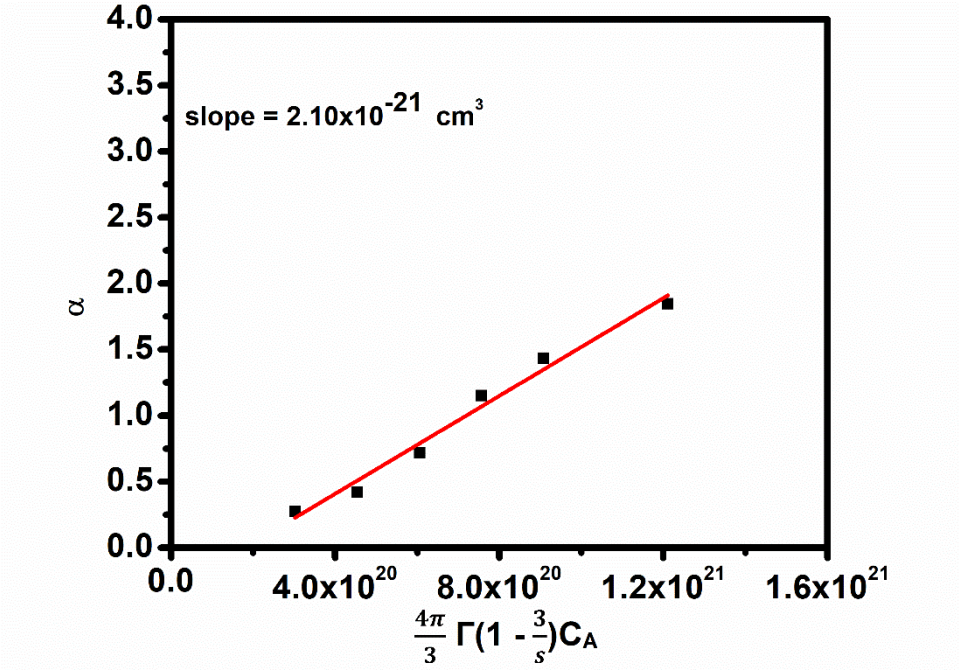

Figure 2: A plot of α versus $\frac{4\pi}{3}$ Γ(1 - $\frac{3}{s}$)C_A for all the samples, with a linear fit.

The critical concentration was then calculated for the R_c value by using a derived equation 4:

$$C_0 = \frac{3}{4\pi R_c^3} \quad \text{.....(4).}$$

This equation is derived from the I-H model's equation 1 [1] and was found to be 1.38 $\times 10^{20}$ cm^{-3}. This corresponded to 0.45 mol %. The increase in α with increasing dopant concentration corresponded to more energy being transferred between the Bi^{3+} ions. Although the same type of interaction for the 0.4 mol % sample was also obtained from Van Uitert's report (chapter 6, section 6.3) the value for R_c obtained by equation $R_c = 2[\frac{3V}{4\pi X_C N}]^{\frac{1}{3}}$ was different [5]. It is therefore concluded that it is more accurate to obtain the critical distance by using the I-H model since the I-H model depends on analysing the decay curves accompanied with the energy transfer mechanism in the system. Van Uitert's model determined the type of the interaction based on the crystal structure and the emission intensity.

The I-H model is characterized as a continuum approximation to relate the donor-acceptor distances in a random distribution in the sample and to calculate the average donor emission [1]. Whereas, the Van Uitert model is directly related to changes in the emission intensity of the acceptor's concentration [6, 7]. Interpretation of the decay curves is difficult as it involves many modes. Interpretation of the decay curves by using the I-H model can give clear

information on the dependencies of the donors and acceptors in the system that are only valid for multi-components. Van Uitert's model can give only limited information in terms of the type of multipolar interaction and it is very difficult to analyze the decay time by using this model. Van Uitert's model is only true if the decay function is a single exponential without interactions between RE ions [6, 7].

Table 1: The calculated values for the concentration per cm^3 (C_A), the macroscopic parameter (α) and the decay time (τ_0) obtained from I-H model for YOF:Bi^{3+}.

x mol % Bi^{3+}	τ_0	α	$C_A \times 10^{20}$ cm^{-3}
0.2	1.5	0.275	0.5055
0.3	1.45	0.421	0.7582
0.4	1.4	0.72	1.012
0.5	1.4	1.15	1.263
0.6	1.36	1.435	1.516
0.8	1.3	1.847	2.022

References

[1] M. Inokuti and F. Hirayama, J. Chem. Phys. 43 (1965) 1978 - 1989.

[2] IUPAC, Compendium of Chemical Terminology, 2nd ed. (the "Gold Book") (1997). Online corrected version: (2014).

[3] T. Petzel, V. Marx and B. Hormann, J. Alloys Compd. 200 (1993) 27 - 31.

[4] A.W. Mann and D.J.M. Bevan, Acta Cryst. B26 (1970) 2129 - 2131.

[5] G. Blasse, Philips Res. Rep. 24 (2) (1969) 131 - 144.

[6] L.G. Van Uitert, J. Electrochem. Soc. 114 (1967) 1048 - 1053.

[7] L. Ozawa and P.M. Jaffe, J. Electrochem. Soc. 118 (1971) 1678 - 1679.

Appendix B

B.1 Publications

This thesis is based on the following publications. The help of co-authors in preparing these publications is gratefully acknowledged:

1. N.A.M. Saeed, E. Coetsee and H.C. Swart, Photoluminescence studies of a YOF phosphor synthesized by the pyrolysis method, Optical Materials, **96** (2019) 109331.
2. N.A.M. Saeed, E. Coetsee, R.E. Kroon, M. Bettinelli and H.C. Swart, Photoluminescence Studies of Bi^{3+} Doped YOF phosphor, in preparation.
3. N.A.M. Saeed, E. Coetsee and H.C. Swart, Down-conversion of YOF:Pr^{3+},Yb^{3+} phosphor, in preparation.
4. N.A.M. Saeed, E. Coetsee and H.C. Swart, Infrared emission enhancement through Ho^{3+} co-doped YOF:Bi^{3+} Phosphor, in preparation.
5. N.A.M. Saeed, E. Coetsee and H.C. Swart, Tunable Ho^{3+} co-doped YOF:Bi^{3+} emission through cathodoluminescence, in preparation.

B.2 Conference proceeding:

1. N.A.M. Saeed, E. Coetsee and H.C. Swart, Structural studies of YOF synthesized by hydrothermal and pyrolysis of trifluoroacetate precursor methods, South African Institute of Physics, UFS, Bloemfontein, June 2018. (Poster).

B.3 International conference presentation:

1. N.A.M. Saeed, R.E. Kroon, H.C. Swart and E. Coetsee-Hugo, Photoluminescent studies of YOF:Bi^{3+} phosphor, 8^{th} South African Conference on Photonic Materials (SACPM), 6 - 10 May 2019 @ Kariega Game Reserve. (Oral Presentation.)